Even Wilberg Hovig

Anisotropy in Metals Processed by Laser Powder Bed Fusion

Elastic and plastic anisotropy in static and dynamic mechanical loading

Doctoral thesis

NTNU
Norwegian University of Science and Technology
Thesis for the Degree of
Philosophiae Doctor
Faculty of Engineering
Department of Mechanical and Industrial
Engineering

NTNU
Norwegian University of
Science and Technology

Even Wilberg Hovig

Anisotropy in Metals Processed by Laser Powder Bed Fusion

Elastic and plastic anisotropy in static and dynamic mechanical loading

Thesis for the Degree of Philosophiae Doctor

Trondheim, December 2021

Norwegian University of Science and Technology
Faculty of Engineering
Department of Mechanical and Industrial Engineering

NTNU
Norwegian University of
Science and Technology

Preface

This thesis is submitted as partial fulfilment of a PhD at Department of Manufacturing and Industrial Engineering at the Norwegian University of Science and Technology, NTNU. The PhD project was started in 2016 as an integrated MSc/PhD and finalised in 2021. The PhD project has been supervised by Professor Knut Sørby at the Department of Manufacturing and Industrial Engineering, NTNU, and co-supervised by Dr. Amin Azar at SINTEF Industry, and Dr. Klas Boivie at SINTEF Manufacturing.

Acknowledgments

I want to thank my supervisor Knut Sørby for continued support in both my MSc and PhD. I feel privileged to have worked with a supervisor who is trusting, fair, and supporting. I also thank my co-supervisor Amin Azar for helping me get off to a great start with especially the first article appended as Paper 1 in this thesis. Amin has been a great sparring partner and especially helpful in matters of material science. I also want to thank co-supervisor Klas Boivie for collaboration in several projects, both at NTNU and SINTEF Manufacturing. Klas has really shown me the importance of standardisation for industrial adoption of AM technology.

The PhD project is funded by the MKRAM project, which is financed by the Norwegian Research Council through the BIA programme. I would like to thank the project manager Erik Andreassen at SINTEF Industry for organising the project.

Appended Paper 3 and 6 are partly funded by the TROJAM3DC project via the Interreg A/ENI programme. I appreciated the interesting discussions led by Dr. Harlin and Dr. Feitosa at Sandvik AMC.

I want to thank all the co-authors of the appended papers. I would also like to thank my colleagues at SINTEF Manufacturing for the support in the final years of this PhD project, with special thanks to Vegard Brøtan, Olav Åsebø Berg, Johan Fahlström and Klas Boivie.

Finally, I would like to thank my wife Else, who has been supporting me throughout the PhD project.

Summary

This thesis is addressed to engineers and researchers working with powder bed fusion (PBF) additive manufacturing (AM) and provides insight into anisotropic mechanical properties for metals subjected to static and dynamic loading. Three common AM materials are investigated; Inconel 718, AlSi10Mg, and maraging steel grade 300. The thesis highlights the need to account for anisotropy when performing finite element analysis and provides methodology for determining anisotropic material models.

The focus is on PBF metals subjected to appropriate heat treatments commonly used in the industry. In the case of static loading the focus is on anisotropy caused by either preferred crystallographic orientation or alignment of inclusions, defects, or particles in the microstructure. In the case of dynamic loading, the focus has been on the contribution of surface roughness on fatigue life reduction.

The objective is to determine robust anisotropic material models in an efficient way. Digital image correlation (DIC) in combination with tensile testing is used to investigate the strain fields on rectangular tensile specimens in uniaxial tension. This is complimented with microstructural evaluation with scanning electron microscopy and fractography with both optical and electron microscopy. For dynamic loading, a combination of experimental results and numerical results are analysed to benchmark build orientations in an effort to maximise fatigue life.

The main scientific contributions are presented in the form of six peer-reviewed articles published in international journals. The main contributions are summarised as:

- A method for determining anisotropic elastic constants using DIC and an optimisation algorithm in Matlab.
- A significant reduction of anisotropy in AlSi10Mg by elevating the process temperature in the PBF process.
- A description of how the melt pool boundaries causes anisotropy, and how this can be reduced by proper heat treatment.
- A methodology for benchmarking the fatigue life of AM components based on simple surface roughness measurements and numerical analysis.
- A methodology and software suite that can optimise part orientation in the PBF build chamber to maximise fatigue life.
- A novel fatigue test specimen that experimentally captures the effect of as-built surface roughness on fatigue life.

The contributions in this thesis can be applied by researchers and engineers when designing parts for manufacturing with AM. Anisotropic elastic constants can be used directly in finite element analysis to optimise design for AM. Future work can

be done to improve the models for fatigue life estimation. The methodology for benchmarking orientations based on surface roughness are only valid when fatigue initiation stems from the as-built surface. Experimental fatigue data gathered with the novel test specimen can be used to further improve this methodology.

Contents

1. Introduction

1.1. Background of PhD Project

This PhD project started in the fall of 2016 as part of the Material Knowledge for Robust Additive Manufacturing (MKRAM) project funded by the BIA programme by the Norwegian Research Council (grant number 248243). The MKRAM consortium consists of SINTEF Industry, SINTEF Manufacturing, The Norwegian University of Science and Technology (NTNU), GKN Aerospace Norway, Kongsberg Automotive, Nammo Raufoss, OM BE Plast, and Sandvik Teeness. The goal of the MKRAM project is to understand the effective material properties of materials processed with AM technology, as well as providing design-tools for engineers creating components manufactured with AM in the form of robust material models for finite element analysis (FEA). Knowledge of a wide range of material properties are required for successful numerical analysis of structural components depending on the application. Several different AM technologies are available, each with different application areas and limitations. Based on the available resources at NTNU, the AM technology of Laser Based Powder Bed Fusion (LB-PBF) was chosen as the main technology to manufacture AM test coupons. Further limitation of the focus of the PhD was done by narrowing down the range of materials to what the industry partners of the MKRAM project thought most promising. The materials focused on in this PhD are the aluminium alloy AlSi10Mg, the tool steel 18Ni300, and the Nickel-base super alloy Inconel 718. During the first months of the PhD period, the candidate identified a research need on the *anisotropy* often associated with LB-PBF. Anisotropy is a feature in materials where properties depend on the direction of loading. If the material properties do not depend on the direction of loading, the material is said to be *isotropic.* A common example of an anisotropic material is wood, which is much easier to split along the grain compared to across the grain. This property is also found in metals, especially when processed in ways which introduce directionality in the microstructure (e.g. forging, rolling, and additive manufacturing) [1]. Anisotropic properties are not limited to mechanical properties, but can also be seen in magnetic, conductive, and electrical properties. The latter three are considered out of scope for this PhD project, which is limited to anisotropy in static and dynamic mechanically loaded LB-PBF metals.

1.2. Motivation and scope

One of the barriers for widespread adaptation of additive manufacturing in the Norwegian industry is the high cost associated with creating components. As a result of the high cost, AM is currently used as a manufacturing technology mainly in applications where conventional manufacturing processes are already costly, such as aerospace, medical applications, and tooling. The possibilities enabled by AM allows designers to add value to the components, which can far exceed the

added manufacturing cost. The added value can be in terms of e.g. enhanced performance of tools [2,3], weight reduction [4], or lead time reduction [5]. To capitalise on the capabilities, reliable material models are required. As discussed in the background chapter, anisotropic material models are required to optimise component design.

Additive Manufacturing technology enables engineers and designers to create light-weight components with high complexity with few design limitations compared to conventional manufacturing techniques such as casting, forging and subtractive machining. In order to capitalise on the capabilities robust material models are required. The material models for AM materials should account for the anisotropic properties of the materials. The problem is then to create a framework for establishing anisotropic material models for any material developed for LB-PBF additive manufacturing.

The research partners in this project are developing topology optimisation algorithms which are used as tools for engineers and designers to find optimal designs with respect to e.g. weight or stiffness. With an isotropic model, compromises must be made, and typically the properties of the weakest direction are used throughout the material. With an anisotropic material model, no such compromises are required.

1.2.1. Research needs

Additive manufacturing of metals has matured significantly over the last decade. Nevertheless, compared to conventional manufacturing techniques, it can still be considered a relatively new technology. Even within the scope of this PhD, there is a vast number of interesting research topics. My interest is in laser beam powder bed fusion, partly due to the high level of detail and accuracy compared to other technologies, but also due to the simple fact that it is what I was exposed to during my MSc. During my mechanical engineering studies, I learnt that a better understanding of the relationship between processing parameters and final mechanical properties is necessary to bring additive manufacturing from prototyping to widespread industrial adoption. Numerous success stories are published where AM solves a specific problem and enhances the functionality and value of specific components. To be an accessible tool for more engineers, a deeper knowledge of the possibilities and limitations of AM is required. With the current cost of AM parts, high-value applications tend to be more suitable, which often requires classification and standardisation. As I see it, as part of the foundation for AM to take the leap to becoming a tool most engineers and manufacturing industries can capitalise on, reliable material models are necessary. From a functional perspective reliable material models are pertinent to design optimal structures, but it is equally important from a monetary standpoint. The perhaps

most effective way to reduce the cost of AM parts is to reduce the weight and volume. To do this efficiently, reliable material models for finite element analysis and topology optimisation is a requirement. Furthermore, the cost of scrapping a part in the AM process chain is very expensive and getting it right the first time is important.

Based on this a general research question is formulated: What is the relationship between LB-PBF processing parameters and final part properties? This question cannot be answered in a single PhD, so the scope is further limited by selecting key processing parameters, limiting the materials, and limiting the final part properties forming the following research question:

1. How does part orientation influence the mechanical properties of LB-PBF metals in uniaxial tensile tests?
2. How can we define material models that captures the unique anisotropic microstructures of LB-PBF metals?
3. How does part orientation influence the surface finish and fatigue life of LB-PBF metals?
4. How can the relationship between orientation-dependent surface roughness and fatigue life be modelled?

1.3. Structure of the thesis
This thesis is a collection of articles and is presented in two parts.

The first part introduces the PhD project and summarises the included papers. In the first chapter the project is introduced. In chapter two anisotropy in LB-PBF materials subjected to static loading is discussed. Paper 1, 2, and 3 are introduced and summarised in this chapter. In chapter three anisotropy in LB-PBF materials subjected to dynamic loading is covered. This chapter also introduces Paper 4, 5, and 6. Chapter four indicates industrial applications and proposed future work.

The second part consists of the six peer-reviewed papers, which makes up the scientific contribution of this PhD project. The summaries of the papers in part one covers the main contributions to this thesis, and the appended articles are intended as supplementary information.

1.3.1. Publications
The six included papers are listed below and illustrated in Figure 1. Paper 1, 2, and 3 relates to anisotropy in statically loaded materials, while Paper 4, 5, and 6 relates to anisotropy in dynamically loaded materials.
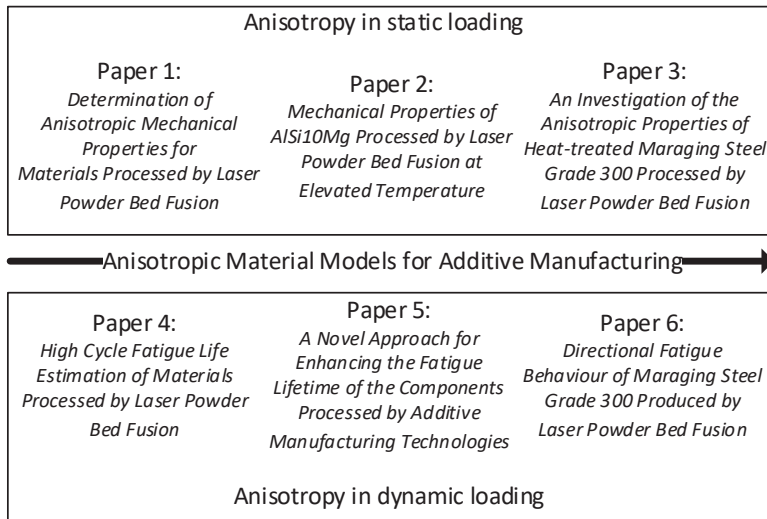
Figure 1 Outline of the papers included in this thesis.

Paper 1: Hovig E W, Azar A, Grytten F, Sørby K, Andreassen E (2018) Determination of Anisotropic Mechanical Properties for Materials Processed by Laser Powder Bed Fusion. Advances in Materials Science and Engineering. https://doi.org/10.1155/2018/7650303

Paper 2: Hovig E W, Azar A S, Mhamdi M, Sørby K (2020) Mechanical Properties of AlSi10Mg Processed by Laser Powder Bed Fusion at Elevated Temperature. In: The Minerals, Metals & Materials Society (eds) TMS 2020 149th Annual Meeting & Exhibition Supplemental Proceedings. The Minerals, Metals & Materials Series. Springer, Cham. https://doi.org/10.1007/978-3-030-36296-6_37

Paper 3: Hovig EW, Azar AS, Solberg K, Sørby K (2021) An Investigation of the Anisotropic Properties of Heat-Treated Maraging Steel Grade 300 Processed by Laser Powder Bed Fusion. The International Journal of Advanced Manufacturing Technology. 114:1359–1372. https://doi.org/10.1007/s00170-021-06938-2

Paper 4: Hovig E W, Azar A S, Sunding M F, Andreassen E, Sørby K (2019) High Cycle Fatigue Life Estimation of Materials Processed by Laser Powder Bed Fusion. Fatigue & Fracture of Engineering Materials & Structures 42:1454–1466. https://doi.org/10.1111/ffe.12982

Paper 5: Azar A S, Reiersen M, Hovig E W, Mhamdi M, Diplas S, Pedersen M M (2021) A Novel Approach for Enhancing the Fatigue Lifetime of the Components Processed by Additive Manufacturing Technologies. Rapid Prototyping Journal 27:256–267. https://doi.org/10.1108/RPJ-02-2020-0030

Paper 6: Solberg K, Hovig E W, Sørby K, Berto F (2021) Directional Fatigue Behaviour of Maraging Steel Grade 300 Produced by Laser Powder Bed Fusion. International Journal of Fatigue 149:. https://doi.org/10.1016/j.ijfatigue.2021.106229

In addition to the included publications, the candidate has published additional works related to the PhD work. These works are not included in the thesis, since they lead up to the included papers.

Hovig E.W., Holm H.D., Sørby K. (2019) Effect of Processing Parameters on the Relative Density of AlSi10Mg Processed by Laser Powder Bed Fusion. In: Wang K., Wang Y., Strandhagen J., Yu T. (eds) Advanced Manufacturing and Automation VIII. IWAMA 2018. Lecture Notes in Electrical Engineering, vol 484. Springer, Singapore. https://doi.org/10.1007/978-981-13-2375-1_34

Hovig E.W., Sørby K. (2020) Influence of Laser Scan Speed on the Relative Density and Tensile Properties of 18Ni Maraging Steel Grade 300. In: Wang Y., Martinsen K., Yu T., Wang K. (eds) Advanced Manufacturing and Automation IX. IWAMA 2019. Lecture Notes in Electrical Engineering, vol 634. Springer, Singapore. https://doi.org/10.1007/978-981-15-2341-0_58

Hovig Even W, Azar Amin S, Sunding Martin F, et al (2018) High cycle fatigue life estimation of AlSi10Mg processed by laser powder bed fusion. MATEC Web Conf 188. https://doi.org/10.1051/matecconf/201818803015

1.4. Contributions

The main findings of the six papers included in this thesis are described in chapter 2 and 3. This section briefly summarises the contributions to the scientific community for each of the included papers. The first three papers are related to research question 1 and 2 from section 1.2.1, while the final three are related to research question 3 and 4.

Paper 1: The main contribution in Paper 1 is a novel method for determining anisotropic elastic material models for AM materials. The proposed method uses digital image correlation and an optimisation algorithm to evaluate tensile test data from specimens built in different orientations. The method can provide statistically valid data that captures crystallographic effects at orientations other than 0°, 45°, and 90° angles with respect to the build plate. Additional value is found in the elastic constants for LB-PBF/Inconel 718 presented in the article.

Paper 2: The second paper investigates LB-PBF/AlSi10Mg processed at elevated temperature. The main contribution is the reduction of residual stresses associated with the AM process. This was achieved by implementing a high temperature heating system in a Concept Laser M2 Cusing PBF machine, which allows processing at 200°C. Increasing the processing temperature reduces the thermal gradient

between the melt pool and the preceding layers. In addition to reducing the effective residual stresses by 40%, the effect of crystallographic texture on the mechanical properties were reduced, leading to isotropic behaviour.

Paper 3: In Paper 3 the methodology developed in Paper 1 is applied to maraging steel grade 300 (18Ni300). The main contribution of Paper 3 is the description of how the alignment of load bearing melt pool boundaries causes anisotropy in elastic strain. This effect was reduced by performing a solution annealing heat treatment prior to ageing, demonstrating the usefulness of including this step. Skipping this step has been suggested by recent authors, but this result shows that care should be taken if this is considered.

Paper 4: The main contribution of Paper 4 is a method to benchmark the fatigue life of as-built AM surfaces built at different orientations. Numerical analysis indicates that for LB-PBF materials where surface defects acts as fatigue initiation, the fatigue life can be increased by an order of magnitude by selecting the proper orientation for critical surfaces.

Paper 5: In Paper 5 the methodology developed in Paper 4 is implemented in a fatigue analysis toolbox, Fatlab. The paper demonstrates how anisotropic surface properties affects the fatigue life and proposes a method for optimising part orientation in the PBF machine to maximise fatigue life.

Paper 6: In Paper 6 the fatigue life of heat-treated LB-PBF/18Ni300 with as-built surface finish is investigated. The main contribution is a novel specimen geometry that promotes failure in the as-built surface. A strong correlation between surface roughness and fatigue life was demonstrated, supporting the assumptions in Paper 4 and 5. For specimens with smoother surfaces however, cracks initiate from other defects indicating that the methodology presented in Paper 4 and 5 needs further development.

2. Anisotropy in static loading PBF-L/M

Anisotropic material properties are properties which depend on the axis of measurement, as opposed to isotropic properties which are uniform in every direction. A majority of physical material properties can be anisotropic, such as mechanical properties, thermal properties, electrical properties, and optical properties. The focus of this thesis is the anisotropy in mechanical properties of engineering metals, and an overview of anisotropic properties under static loading will be presented in this chapter. This section introduces Paper 1 through 3. First there will be a general introduction to the factors influencing anisotropic behaviour, before three materials, Inconel 718, AlSi10Mg, and 18Ni300 maraging steel grade 300, will be considered in more detail.

A more specific definition of anisotropic mechanical properties can be that the material responds differently to mechanical loads in different directions. A common example used is fibre glass composite. Consider a fibre glass composite with long fibres aligned in one principal direction, with epoxy resin as the binding matrix. In fibrous materials the material is generally strong in the fibre direction, while weaker in the matrix. The difference lies in which constituent of the microstructure absorbs the loading. For loading with the grain, the fibres and the matrix must be deformed for bulk deformation to happen. For loads perpendicular to the fibre direction only the matrix must be deformed for bulk deformation to happen.

In metals, anisotropy are typically caused by either preferred crystallographic orientation or alignment in the microstructure by particles such as precipitates or inclusions [1]. LB-PBF/M is known to introduce both sources of anisotropy in a range of materials [1,6–10].

2.1. Preferred crystallographic orientation

To understand preferred crystallographic orientation, also called *texture*, consider a cubic polycrystalline metal. When the metal solidifies from the molten state, seed crystals, or nuclei, starts to form. Assuming a degree of supercooling crystals grow from the nuclei, and the direction of growth is dictated by the heat flow vector. In LB-PBF/M the temperature difference between the melt pool and the preceding layers are typically in the order of several thousand kelvins with cooling rates in the order of 10^6 to 10^7 K/s [11]. This creates a strong heat flux moving from the focal point of the laser to the cooler regions of the preceding layers. Consider Figure 2, which represents a melt pool created by a laser traveling into the plane of the page (indicated by the y-direction in a right hand coordinate system).
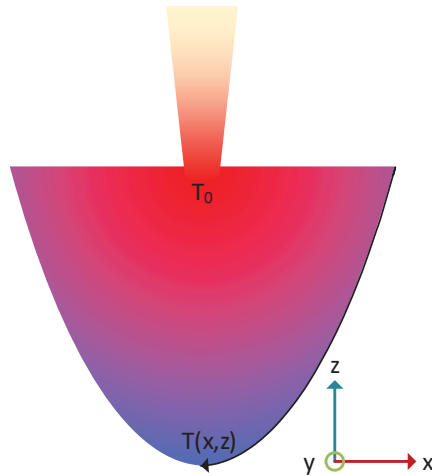
Figure 2 Schematic of a laser melt pool where the laser travels in the y-direction (into the plane). Colors indicate temperature, where blue is cold and red/white is hot.

The temperature of the melt pool is at its highest at the focal point of the laser beam, indicated by T_0. The temperature at the melt pool boundary (MPB) is a function of x and z, $T(x,z)$. The temperature is assumed to increase with z, due to the increased influence of the neighbouring melt track. The heat flow will travel from the highest temperature towards the lowest temperature as indicated by the colour gradient. Fluid motion is neglected in this example. Due to the high temperature in the laser spot relative to the low temperature in the preceding layers, the heat flow vector tends to align with the build direction. Crystals then starts to grow at nuclei at the melt pool boundary and grows towards the laser spot.

Figure 3 shows the difference in grain growth kinetics for a low cooling rate (a), and a high cooling rate (b) which is dominant in LB-PBF/m. The figure also indicates an arbitrary load in the z-direction, denoted F. In the case of the low cooling rate the load is close to the crystallographic <111>, and in the case of the higher cooling rate the loading is close to <100>. When most of the grains align with the build direction, the mechanical properties of LB-PBF/M parts can heavily depend on the orientation of the part relative to the build direction. In metals with cubic crystal structure, this is less dominant, due to the numerous slip planes available.
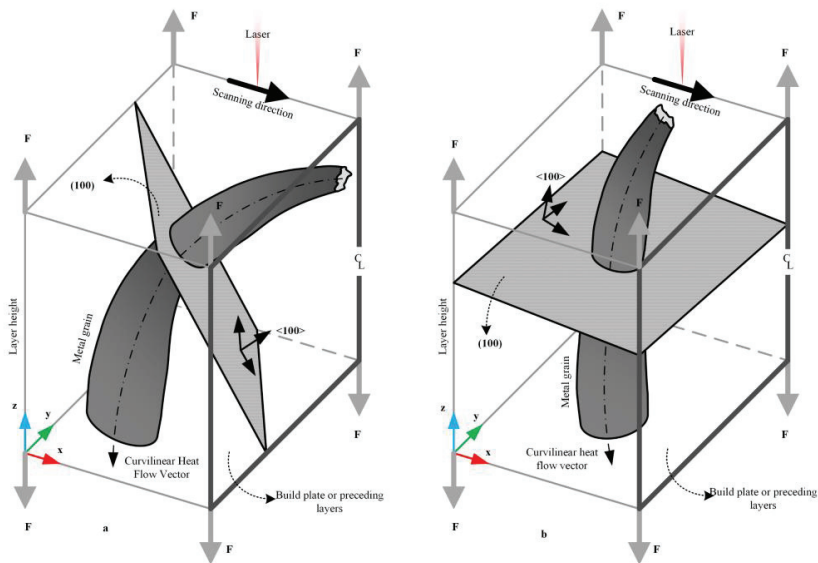
Figure 3 Differences in growth kinetics of metal grains along maximum heat flow. In a) the loading is close to the crystallographic <111> while in b) the loading is close to <100>. Figure from paper 1.

2.2. Alignment in the microstructure

Alignment in the microstructure is often the dominant cause of plastic anisotropy[1], and in LB-PBF/M there are several ways the microstructure can be decorated in a patterned way. Decoration by micro-segregation is one possibility[12]. Microsegregation is where certain elements segregate from the melt and form inclusions of a different chemical composition than the bulk material. In LB-PBF/M this can be influenced by the scan strategy [13], and lead to a patterned dispersion of defects as observed in the candidates work [Paper 3, 6]. Other defects, such as porosity due to poor PBF parameters can also lead to patterned defects, e.g., if the hatch spacing is too high, a repeated pattern of lack-of-fusion defects can be present [15]. Keyhole pores can also lead to similar patterned defects [16]. Xiong et al. [17] observed that fracture occurred along the melt pool boundaries, and that the number of melt pool boundaries in the cross section of the material being loaded depends on the build orientation. This is further investigated in Paper 3.

2.3. Elastic modelling

Elastic anisotropy is typically modelled with Hooke's law in matrix form, expressed as $\boldsymbol{\sigma} = \boldsymbol{C}\boldsymbol{\epsilon}$, where $\boldsymbol{\sigma}$, is the stress tensor, $\boldsymbol{C}$ is the stiffness matrix, and $\boldsymbol{\epsilon}$ is the strain

tensor. Equation (1) shows Hooke's Law written out for a linear elastic anisotropic material with principal axes 1, 2, and 3.

$$
\begin{bmatrix} \sigma_{11} \\ \sigma_{22} \\ \sigma_{33} \\ \sigma_{23} \\ \sigma_{13} \\ \sigma_{12} \end{bmatrix} =
\begin{bmatrix}
c_{11} & c_{12} & c_{13} & c_{14} & c_{15} & c_{16} \\
c_{21} & c_{22} & c_{23} & c_{24} & c_{25} & c_{26} \\
c_{31} & c_{32} & c_{33} & c_{34} & c_{35} & c_{36} \\
c_{41} & c_{42} & c_{43} & c_{44} & c_{45} & c_{46} \\
c_{51} & c_{52} & c_{53} & c_{54} & c_{55} & c_{56} \\
c_{61} & c_{62} & c_{63} & c_{64} & c_{65} & c_{66}
\end{bmatrix}
\begin{bmatrix} \epsilon_{11} \\ \epsilon_{22} \\ \epsilon_{33} \\ 2\epsilon_{23} \\ 2\epsilon_{13} \\ 2\epsilon_{12} \end{bmatrix}
\tag{1}
$$

It can be shown that the stiffness matrix must be symmetric [18], and Equation (1) can be reduced to Equation (2), reducing the number of elastic constants from 36 to 21.

$$
\begin{bmatrix} \sigma_{11} \\ \sigma_{22} \\ \sigma_{33} \\ \sigma_{23} \\ \sigma_{13} \\ \sigma_{12} \end{bmatrix} =
\begin{bmatrix}
c_{11} & c_{12} & c_{13} & c_{14} & c_{15} & c_{16} \\
c_{12} & c_{22} & c_{23} & c_{24} & c_{25} & c_{26} \\
c_{13} & c_{23} & c_{33} & c_{34} & c_{35} & c_{36} \\
c_{14} & c_{24} & c_{34} & c_{44} & c_{45} & c_{46} \\
c_{15} & c_{25} & c_{35} & c_{45} & c_{55} & c_{56} \\
c_{16} & c_{26} & c_{36} & c_{46} & c_{56} & c_{66}
\end{bmatrix}
\begin{bmatrix} \epsilon_{11} \\ \epsilon_{22} \\ \epsilon_{33} \\ 2\epsilon_{23} \\ 2\epsilon_{13} \\ 2\epsilon_{12} \end{bmatrix}
\tag{2}
$$

Further simplification of Hooke's Law requires certain physical conditions to be met. Most prominent are the assumptions of orthotropic elasticity (Equation (3)) and transversely isotropic elasticity (Equation (4)). Orthotropic elasticity requires three mutually perpendicular planes of symmetry. Transversely isotropic elasticity is found in materials with a principle material direction perpendicular to a plane of isotropic material properties.

$$
\begin{bmatrix} \sigma_{11} \\ \sigma_{22} \\ \sigma_{33} \\ \sigma_{23} \\ \sigma_{13} \\ \sigma_{12} \end{bmatrix} =
\begin{bmatrix}
c_{11} & c_{12} & c_{13} & 0 & 0 & 0 \\
c_{12} & c_{22} & c_{23} & 0 & 0 & 0 \\
c_{13} & c_{23} & c_{33} & 0 & 0 & 0 \\
0 & 0 & 0 & c_{44} & 0 & 0 \\
0 & 0 & 0 & 0 & c_{55} & 0 \\
0 & 0 & 0 & 0 & 0 & c_{66}
\end{bmatrix}
\begin{bmatrix} \epsilon_{11} \\ \epsilon_{22} \\ \epsilon_{33} \\ 2\epsilon_{23} \\ 2\epsilon_{13} \\ 2\epsilon_{12} \end{bmatrix}
\tag{3}
$$

$$
\begin{bmatrix} \sigma_{11} \\ \sigma_{22} \\ \sigma_{33} \\ \sigma_{23} \\ \sigma_{13} \\ \sigma_{12} \end{bmatrix} =
\begin{bmatrix}
c_{11} & c_{12} & c_{13} & 0 & 0 & 0 \\
c_{12} & c_{11} & c_{13} & 0 & 0 & 0 \\
c_{13} & c_{13} & c_{33} & 0 & 0 & 0 \\
0 & 0 & 0 & c_{44} & 0 & 0 \\
0 & 0 & 0 & 0 & c_{44} & 0 \\
0 & 0 & 0 & 0 & 0 & c_{11} - c_{12}
\end{bmatrix}
\begin{bmatrix} \epsilon_{11} \\ \epsilon_{22} \\ \epsilon_{33} \\ 2\epsilon_{23} \\ 2\epsilon_{13} \\ 2\epsilon_{12} \end{bmatrix}
\tag{4}
$$

In the case of orthotropic elasticity, a total of nine independent elastic constants are required to describe the material, while in the case of transversely isotropic elasticity the number of independent elastic constants are further reduced to five.

2.4. Determination of elastic constants using DIC.

2.4.1. Digital image correlation

Digital image correlation (DIC) is an image-based technique to capture surface strains during static or dynamic loading. In this thesis 3D commercial systems from Limess and Correlated Solutions are used (Vic3D). In short, two high resolution cameras are focused on two adjacent surfaces of flat tensile specimens, as illustrated in Figure 4.
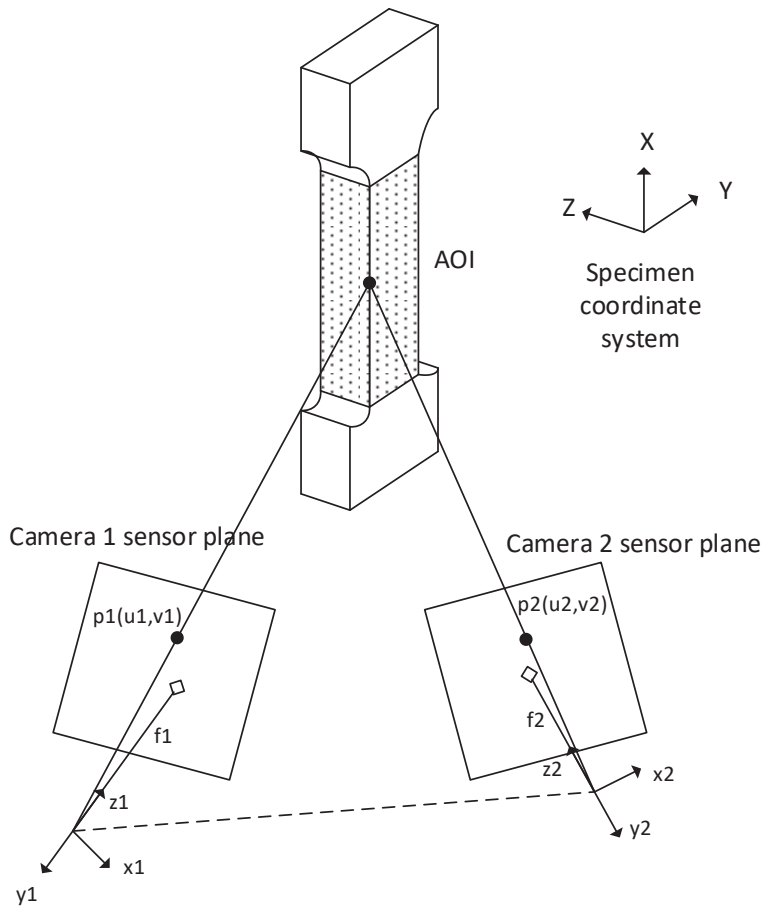

Figure 4 3D DIC schematic of a two-camera setup. Figure inspired by Grytten et al. [19].

The specimens are coated with a spatter pattern in the area of interest (AOI), and as the specimen is loaded the displacement is calculated by correlating the movement of the individual spatter points. Prior to each test run the cameras are calibrated with a grid of dots with known size and spacing. The key parameters of the cameras are determined based on the calibration. The analog data from the tensile test machine is logged at the same timestamp as the images are captured. A framerate of 2 frames per second is used in this thesis.

The correlation is performed after the physical experiment in the Vic3D software suite. The correlation is run with a subset size of 29 pixels, with a step of 5. A coordinate transformation is then done before calculating the Lagrange strain. The strains are then exported and further processed in Matlab. For most of the analyses the 'strain gauge' function is used in Vic3D to export the average strain over a line within the AOI for each frame. Other options include averaging the entire AOI or a selected area within the AOI. It is also possible to export the strain for each individual pixel within the AOI, but this is computationally expensive, and based on trial and error found to be unnecessary for the purposes of this thesis. The 'strain gauge' function captures a representative average and avoids surface effects due to roughness in the sample or spatter pattern. The full strain field for selected frames can also be of interest, and an example can be seen in Paper 3 (Figure 24).

2.4.2. Elastic constants

With sufficient experimental data the elastic constants can be determined directly from the elastic properties of tensile tests oriented at different orientations. If the material is assumed to be transversely isotropic in the XY plane, Hooke's law can be expressed as Equation (5).

$$
\begin{bmatrix} \varepsilon_{xx} \\ \varepsilon_{yy} \\ \varepsilon_{zz} \\ \varepsilon_{yz} \\ \varepsilon_{xz} \\ \varepsilon_{xy} \end{bmatrix} =
\begin{bmatrix}
\frac{1}{E_{xx}} & -\frac{v_{xy}}{E_{xx}} & -\frac{v_{zx}}{E_{zz}} & 0 & 0 & 0 \\
-\frac{v_{xy}}{E_{xx}} & \frac{1}{E_{xx}} & -\frac{v_{zx}}{E_{zz}} & 0 & 0 & 0 \\
-\frac{v_{xz}}{E_{xx}} & -\frac{v_{xz}}{E_{xx}} & \frac{1}{E_{zz}} & 0 & 0 & 0 \\
0 & 0 & 0 & \frac{1}{2G_{xz}} & 0 & 0 \\
0 & 0 & 0 & 0 & \frac{1}{2G_{xz}} & 0 \\
0 & 0 & 0 & 0 & 0 & \frac{1}{2G_{xy}}
\end{bmatrix}
\begin{bmatrix} \sigma_{xx} \\ \sigma_{yy} \\ \sigma_{zz} \\ \sigma_{yz} \\ \sigma_{xz} \\ \sigma_{xy} \end{bmatrix}
\tag{5}
$$

The E_{xx} and E_{yy} can easily be found using standard tensile tests built in the ZX and XZ orientations respectively. The Poisson's ratios are determined according to ASTM E132. The shear modulus in the plane of isotropy can be expressed as $G_{xy} = E_{xx}/2(1 + v_{xy})$. G_{xz} can be calculated using an off-axis tension test, e.g. a sample built in the XZ plane with a rotation of $\phi = 45°$ about the Y-axis. This assumes negligible shear strain, and is shown in Equation (6) [20].

$$G_{12} = \frac{\sin^2 \phi \cos^2 \phi}{\frac{1}{E_\phi} - \frac{\cos^4 \phi}{E_1} - \frac{\sin^4 \phi}{E_2} + \left(\frac{v_{21}}{E_1} + \frac{v_{12}}{E_2}\right)\sin^2 \phi \cos^2 \phi} \tag{6}$$

2.5. Determination of elastic constants using an optimisation algorithm.

The 'DIC method' requires only three tensile test orientations in order to determine the elastic constants, but as will be shown in Paper 1 this does not accurately describe the behaviour of the material. An optimisation algorithm is implemented to improve the significance of measurements at other orientations than 0°, 45°, and 90°, as well as reduce the number of repetitions necessary at each orientation for statistically valid data.

Consider the transversely isotropic case for which Hooke's law can be expressed as Equation (5). Each pair of strain and stress is related by the compliance matrix and a transformation matrix K, as derived by e.g. p. 54-55 in Ting [21]. Hooke's law transforms to $\epsilon' = S'\sigma'$, where $\sigma' = K\sigma$, and $S' = (K^{-1})^T SK^{-1}$, which leads to $\epsilon' = (K^{-1})^T SK^{-1}K\sigma = (K^{-1})^T S\sigma$. S' and S are the transformed and original compliance matrices. When a relationship between stress and strain is established, the strain tensor can be expressed as $\epsilon^* = (K^{-1})^T SK^{-1}\sigma$.

The objective of the optimisation problem is to minimise a cost function $J(\theta)$. A common cost function for problems of this nature is the root-sum-of-squares function $J(\theta) = \sum_{i=1}^{m} \sqrt{\epsilon^2 - \epsilon'^2}$, where ϵ is the measured strain in the elastic region. An optimisation problem like this can be implemented by e.g. the function `fmincon` in Matlab. The material is assumed to increase in volume and contract in the transverse directions when undergoing tensile stress. This constrains the Poisson's ratio in any orientation to be bound by $0 < v_{ij} < 0.5$. Since the elastic moduli in the 0°, 45° and 90° orientations are known, the problem is reduced to determining the Poisson's ratios.

2.6. Paper 1 - Determination of Anisotropic Mechanical Properties for Materials Processed by Laser Powder Bed Fusion

In Paper 1 the anisotropic behaviour of Inconel 718 processed by LB-PBF is investigated with microscopy and tensile tests with DIC. A novel method for determining elastic constants for use in FEM analysis is proposed.

2.6.1. Introduction

Inconel 718 is a nickel base superalloy with high corrosion resistance and service temperatures up to 760°C [22]. The nominal chemical composition for the material used in this thesis is provided in Table 1.

Table 1 Nominal chemical composition of Inconel 718 used in this thesis.

Element	Ni	Cr	Fe	Al	Mo	Nb	Ti
wt%	50-55	17-21	Bal.	0.2-0.8	2.8-3.3	4.75-5.5	0.6-1.1

The microstructure constitutes a solid γ phase and can be hardened through precipitation of γ' (Ni$_3$[Al,Ti], fcc) and γ'' (Ni$_3$Nb, bct). Precipitation ageing is typically done in a two-step process designed to favour formation of γ'', as γ' is a brittle phase. As the temperature increases, other brittle phases such as δ and σ can form, and as such the service temperature is limited by the formation of those phases. Figure 5 shows the time-temperature transformation diagram for calculated (left-hand side) and experimentally determined Inconel 718. Note the narrow temperature window between γ' and γ'', highlighting the need for careful heat treatment.
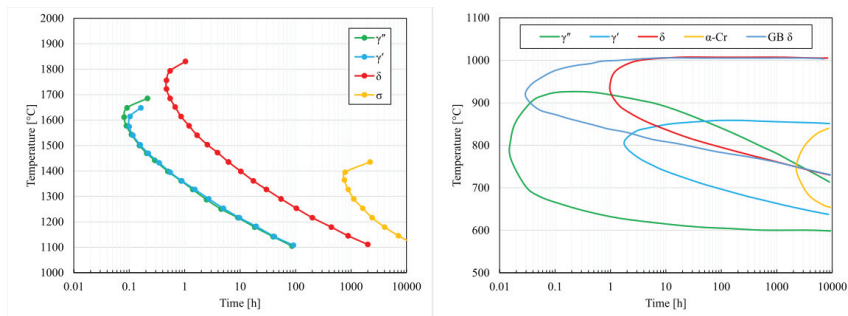

Figure 5 Time-temperature transformation (TTT) diagram for calculated (left) and experimentally determined [23,24] (right) Inconel 718.

To investigate the anisotropy in LB-PBF/Inconel 718 three sets of tensile specimens were produced in an SLM 280 PBF machine at several different orientations in the build chamber. The processing parameters were supplied by SLM Solutions, and the laser power was 275 W, layer thickness 0.05 mm, hatch spacing 0.12 mm, and

scan speed 805 mm/s. The tensile specimens are flat, with a gauge length of 10 mm, width of 2.5 mm and thickness of 1.5 mm. Three sets of specimens, each with 11 unique orientations, were produced and left with an as-built surface finish. Figure 6 shows the layout of the tensile specimens in the build chamber. The colour codes in Figure 6 refer to the orientation of the specimen, blue indicates a specimen parallel to the build direction, green is for specimens aligned with either the x or y-axis of the machine, while red is for specimens oriented at an angle of 45° to the build plane.
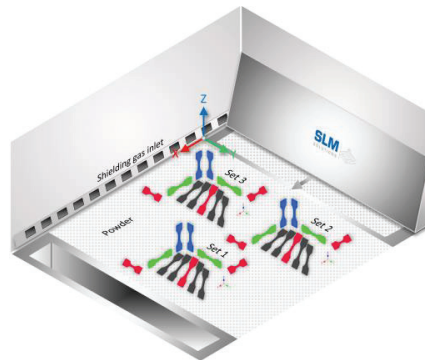

Figure 6 Layout of Inconel 718 specimens in the build chamber. Figure from Paper 1.

Each set was heat treated in a different way. Set 1 was given a solution treatment (S), set 2 was solution treated followed by a two-step ageing process (S+A), while the third set was hot isostatically pressed (HIP) after solution treatment and before ageing (S+H+A). Details of the heat treatment can be found in Paper 1. The specimens were characterised with scanning electron microscopy (SEM), electron backscatter diffraction (EBSD), and white light interferometry (WLI) in addition to the tensile tests. The tensile tests were carried out in a Zwick tensile machine with a 50 kN load cell. The strain fields on two perpendicular surfaces on the gauge length of the tensile specimens were captured using DIC, as described in section 2.4.1.

2.6.2. Results and discussion

In the solution treated condition, the microstructure constitutes of elongated grains in the build direction with a dendritic γ+γ'' lamellae structure, indicating texture. There are visible fusion lines, and some process induced defects were found. Microsegregation was observed in the inter-dendritic regions. In the aged condition δ and η phase was observed on the grain boundaries. In the HIP + aged condition the microstructure was effectively reconstructed, with grain boundary precipitates on the primary γ grains. The EBSD analysis confirms that the solution treated specimens has a clear preferred crystallographic orientation of <100> along

the build direction. The micrographs and inverse pole figures can be found in Figure 10 and Figure 11 in Paper 1. The strong texture is a clear indication that the material will have an anisotropic response to mechanical loading. The tensile tests further confirm this.

The stress-strain curves are shown in Figure 7, where it is evident that the ageing treatment significantly increases the strength at the cost of ductility. HIP before ageing reduces the strength compared to just ageing but increases the ductility. To get a better understanding of the anisotropy, selected tensile properties are plotted as a function of build orientation.
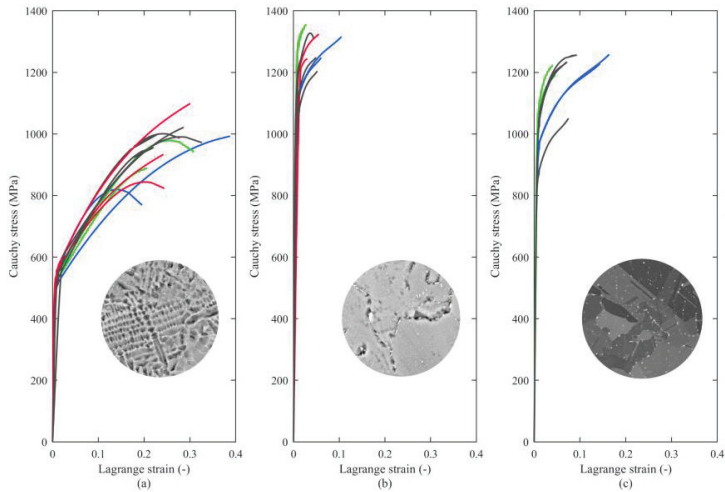

Figure 7 Stress-strain curves for Inconel 718 with three different heat treatments; a) solution treatment (S), b) solution treatment plus ageing (S+A), c) solution treatment plus HIP plus ageing (S+H+A). Figure from Paper 1.
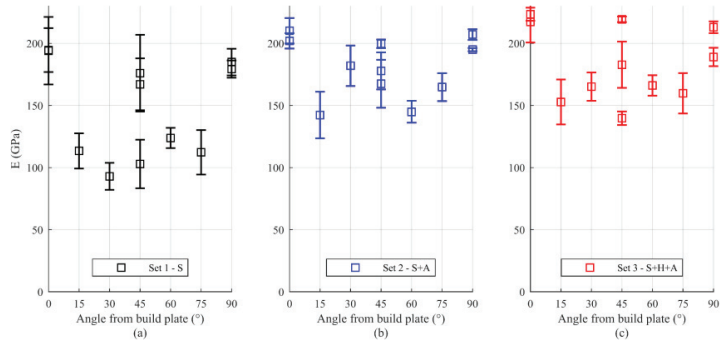
Figure 8 Elastic modulus as a function of build orientation for a) S, b) S+A, c) S+H+A. Figure from Paper 1.

Figure 8 shows the elastic modulus with respect to build orientation. In set 1 the material is stiffest in the 0° orientation, and then drops as the material is raised towards 45°. There is a large scatter in the 45° data, which is attributed to the difference in orientation of the 45° specimens. Two of the specimens have a secondary rotation among the among the load axis. These are denoted XZ-45B and YZ+45A according to ISO/ASTM52921:2013E, while the last specimen is denoted XY+45B. Since the cross section area is rectangular, the projection of the specimen cross section along the z-axis of the machine is w/cos(45°) for the XZ-45B and YZ+45A specimens, and t/cos(45°) for the XY+45B specimen. When loading the specimens built at 45° the grain boundaries will either align with the slip line and cause de-cohesion, or twin subgrains will form – resulting in twinning induced plasticity [25]. The results indicate that for the two former specimens subgrains are formed, while for the latter the grains align with the slip line and the plasticity is higher. When the specimens are raised further, the elastic modulus increases until 90° where it is comparable to the 0° orientation. The elastic modulus of the two aged conditions shows similar trends, but the lowest modulus is at a higher baseline.
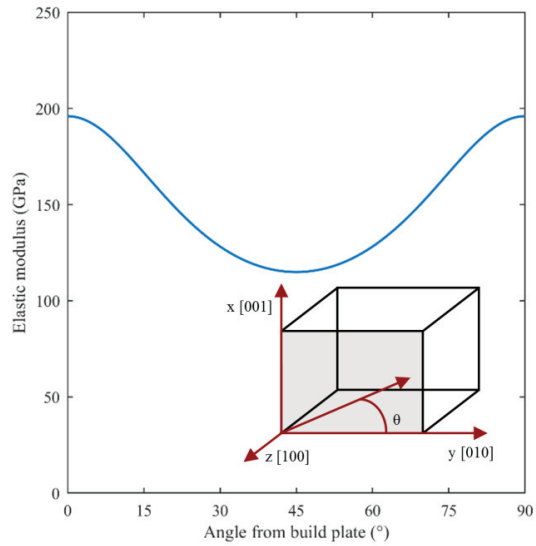
Figure 9 Elastic modulus according to [26], with a value for $E_{<100>} > E_{<111>}$ measured with DIC for set 1. Inset: {100} plane in an FCC crystal with xyz and corresponding (hkl) coordinates. Figure from Paper 1.

The strong fibre texture, especially in set 1, even allows for single crystal theory to be applied to the material. The elastic modulus in any particular crystallographic direction can be calculated [26], which conforms well to the observed experimental data. Details about the calculation can be found in section 4.3. in Paper 1.

Figure 10 shows the yield strength, ultimate tensile strength, and elongation at break for the three sets. A reference value (from machined rolled and aged Inconel 718) is indicated with a green line. For set 1 the yield stress is at the maximum at a 60° angle with respect to the build plate, which corresponds well with crystallographic theory for materials with strong texture.
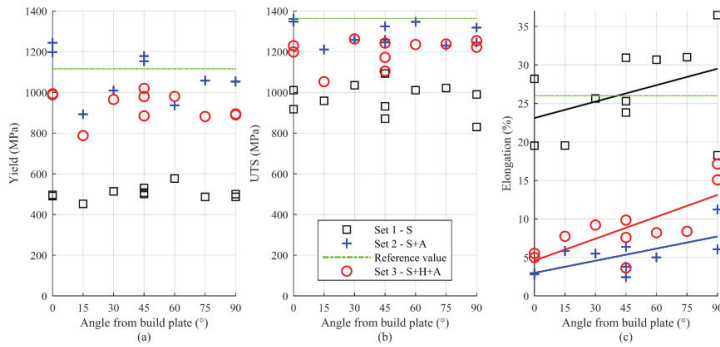
Figure 10 Yield strength (0.02%), ultimate tensile strength, and elongation at break for the three different heat treatment conditions of Inconel 718. Reference specimens values shown in the green line. Figure from Paper 1.
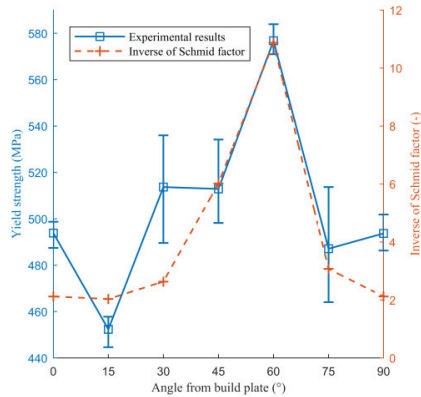
Figure 11 Yield stress for set 1 compared with the inverse Schmid factor for set 1. Figure from Paper 1.

In Figure 11 the inverse of the Schmid factor is plotted along with the yield strength. The observed trend is remarkable, although with some deviation as would be expected with as-built surface finish. For further detail about the significance of the Schmid factor the reader is referred to Paper 1 section 4.3. The trend seen in set 1 is not observed in set 2 and set 3, indicating that the ageing heat treatment reduces the anisotropy of the material.

The ultimate tensile strength is significantly increased with the ageing treatment, and it is noted that the UTS is slightly lower when HIP is performed prior to ageing. In set 2 and set 3 the yield strength and UTS have significant scatter, which is

attributed to random errors rather than anisotropic effects, due to the as-built surface finish.

The elongation at break shows a clear trend to increase with build orientation for all three sets. This indicates that different failure modes dominate, depending on the specimen build orientation. The angle between the axial load and the texture depends on the orientation, and for specimens in the 0° orientation mode 1 type failure is dominating. As the angle between the load and the texture changes, the possibility for mode 1 type failure decreases and a maximum elongation at failure can be observed at 90°.

The main contribution from this paper is the method for determining elastic constants based on DIC in combination with an optimisation algorithm. The material is assumed to be transversely isotropic and the methodology from sections 2.4 and 2.5 is applied to find the constants. The elastic constants are given in Table 2.

Table 2 Elastic constants for LB-PBF/Inconel 718 from the DIC method and the optimisation method.

	DIC method			Optimisation method		
Set	1 (S)	2 (S+A)	3 (S+H+A)	1 (S)	2 (S+A)	3 (S+H+A)
E_{xx}	194	206	217	194	206	217
E_{zz}	182	201	201	182	201	201
v_{xy}	0.4339	0.4748	0.4718	0.3612	0.4994	0.3888
v_{xz}	0.4029	0.3650	0.4019	0.3158	0.4999	0.4563
v_{zx}	0.3909	0.2045	0.2172	0.3745	0.4877	0.4927
G_{xz}	47	48	55	31	56	49
G_{xy}	68	65	75	71	69	78

The elastic constants can be used directly in FEM tools to predict anisotropic elastic behaviour of a three-dimensional part, as long as the build orientation is known. It can be a very useful tool in topology optimisation systems in order to not only find an optimised geometry, but also find an optimised build orientation. The elastic constants are verified by FE analysis in Abaqus, and the numerically determined elastic moduli are compared to the measured elastic moduli in Figure 12. With both approaches the elastic modulus follows a 4th order polynomial, with E(0°)>E(90°)>E(45°). The DIC method appears to over-estimate the stiffness at the 15°, 30°, 60°, and 90° orientation, while the optimisation method provides a more conservative prediction.

It is necessary to briefly discuss the uncertainty due to the as-built surface finish, which can be found in Paper 1 section 3.4. In summary, the average error of the calculated stress is 0.57%, 0.19% and 0.19% for set 1, set 2, and set 3 respectively.

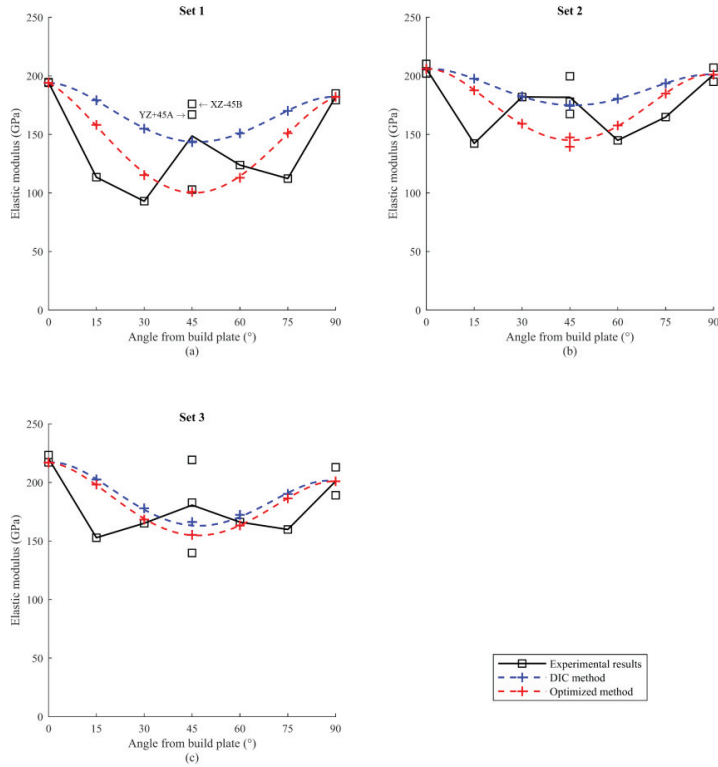Due to the relatively low error, only average values have been used when finding the elastic constants.

Figure 12 Elastic modulus in the load direction as measured directly, calculated using the DIC method, and calculated using the optimisation method for a) S, b) S+A, and c) S+H+A. Figure from Paper 1.

2.6.3. Concluding remarks

To summarise, Paper 1 describes a method for obtaining anisotropic elastic constants for metals processed by LB-PBF. This method is demonstrated using Inconel 718, which was shown to be highly anisotropic, particularly in the elastic part of the flow curve. The material had a clear preferred crystallographic orientation in the {100} direction along the build direction, to an extent that single crystal theory can be applied to describe the material. The results highlight the need for anisotropic material models when designing for additive manufacturing.

2.7. Paper 2 - Mechanical Properties of AlSi10Mg Processed by Laser Powder Bed Fusion at Elevated Temperature

In Paper 2 the methodology developed in Paper 1 was applied to LB-PBF/AlSi10Mg. Leading up the manufacturing of the specimens, the candidate, in collaboration with SINTEF Manufacturing AS developed a high temperature heating system which was retrofitted to the LB-PBF machine (Concept Laser M2 Cusing, installed 2009). This allowed for continuous heating of the building plate, which resulted in a significant change to the microstructure of the material. As of the time of writing this thesis (2021), this has become standard equipment in most new LB-PBF machines, but at the time of development (2017-2018), this completely changed the way we think about LB-PBF/AlSi10Mg. The effect of (pre-) heating the build platform on the microstructure and mechanical properties of LB-PBF/AlSi10Mg and AlSi12Mg had been reported in previous studies, with main findings suggesting a reduction of internal defects and residual stress [27–29].

2.7.1. Introduction

LB-PBF/AlSi10Mg is known to have a high degree of residual stresses and anisotropy in the as-built condition [30–34]. Heat treatments such as T6 (solution treatment plus artificial ageing) can reduce both the residual stress and anisotropy, but due to grain growth in the solution treatment this comes at the cost of strength and hardness [31,34]. An alternative to T6 heat treatment in LB-PBF is a stress relief treatment (SR), which reduces the residual stress while leaving the microstructure intact [35]. The latter does not restructure the microstructure, and the effect of SR on anisotropy is limited.

In this paper three sets of 14 tensile specimens were prepared by LB-PBF at 200°C and subjected to three different heat treatments. As in Paper 1, the strain fields were captured using DIC to capture anisotropic straining. In addition to the tensile test's calibration beams were produced to measure the residual stress when processing at 200° and room temperature.

The specimens were prepared in a Concept Laser M2 Cusing, and the powder feedstock was supplied by Concept Laser (CL31Al). The laser power was 200 W, hatch spacing 0.0975 mm, scan speed 1400 mm/s, and layer thickness 0.03 mm. Each layer was preheated by the laser at 50 W, with the same hatch spacing and scan speed. The scan strategy was the 'island' scan strategy by Concept Laser with island size of 2 mm, angular shift of 45°, and X/Y shift of 0.4 mm. The processing parameters were determined in a previous study and produces parts with a relative density of 99.9% [27].

The tensile specimens were prepared as rectangular blocks and machined to dog-bone specimens with gauge length of 32 mm and a quadratic cross section of

6x6 mm^2. The specimens were built at seven different orientations from 0° to 90° with 15° increments with respect to the build platform. The first set of the tensile specimens were given no heat treatment, denoted as AB. The second set was stress relieved at 300°C for 2 hours (SR), and the third set was given a T6 heat treatment. The T6 procedure was as follows: solution treatment at 536°C for 2 hours in argon, followed by water quench; artificial ageing at 160°C for 12 hours, followed by air cooling to room temperature. The tensile tests were carried out in a Zwick/Roell Z250 with a 50 kN load cell with a displacement rate of 1 mm/min.

Two cantilever beams for residual stress measurement were built on the same build platform as the tensile bars, and two additional cantilever beams were built separately at room temperature. For the cantilever beams built at room temperature the scan speed was reduced to 1200 mm/s to account for the lower process temperature. The two beams were aligned with either the X or Y direction of the machine. Figure 13 shows the geometry of the cantilever beam.
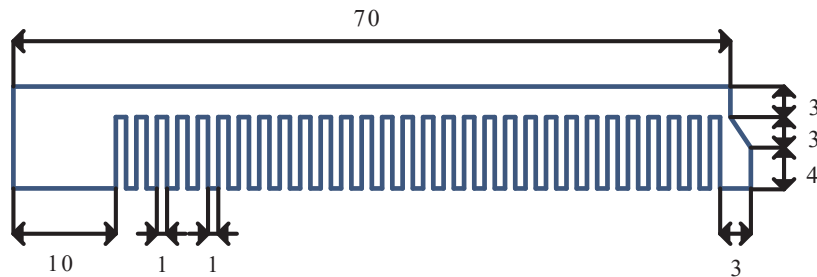

Figure 13 Cantilever beam geometry. All measurements in mm. Thickness 12 mm.

The residual stresses were calculated using the calibration feature of Simufact Additive 4.0 with an element size of 0.5 mm and the iterative sparse solver. The beams were first measured in a coordinate measurement machine (CMM) before the supports in the beam were cut using wire electron discharge machining at a height of 2.5 mm from the substrate plate. The deflection of the beam was then measured with the CMM.

The microstructure was characterised with SEM and EDS in an FEI Nova NanoSEM 650 with and X-Max 50 mm^2 EDS detector from Oxford Instruments.

2.7.2. Results and discussion

SEM images of the loaded cross-section of the as-built and T6 microstructure are shown in Figure 14. In the AB microstructure (a,b,c) the melt pool boundaries (MPB) are clearly visible. During the T6 heat treatment the microstructure is recrystallised and the MPBs are no longer visible. Figure 15 shows the same heat treatment

conditions in higher magnification. In the as-built condition a fine-grained cellular-dendritic structure is seen, with Si-rich cell-boundaries. T
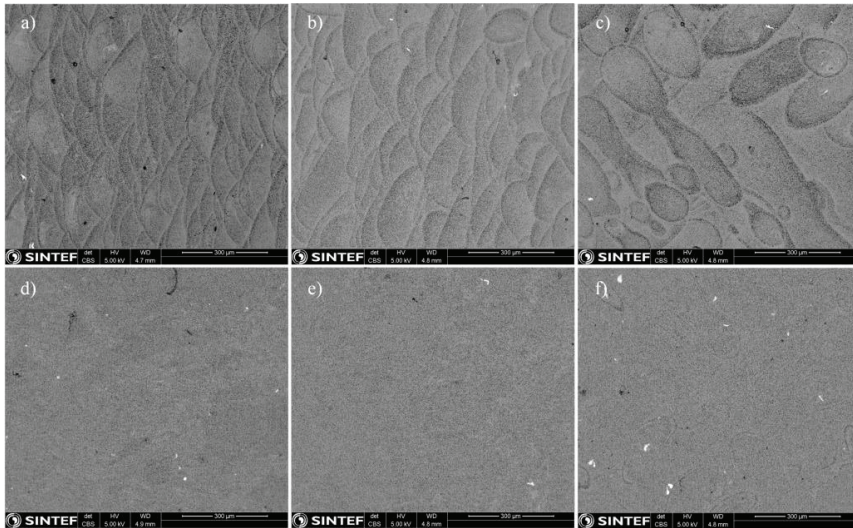
Figure 14 SEM Images of a) AB 0°, b) AB 45°, c) AB 90°, d) T6 0°, e) T6 45°, f) T6 90°.

Figure 15 shows the same heat treatment conditions in higher magnification. In the as-built condition a fine-grained cellular-dendritic structure is seen, with Si-rich cell-boundaries. A coarser cell-structure is seen on the right-hand side of the image, closer to the melt pool boundary. This is consistent with findings from other authors [31]. In the T6 condition (b) the cellular structure is transformed into eutectic AlSi decorated with Si-rich particles (c).

Figure 15 SEM images of a) AB 0°, b) T6 0° c) EDS map of Al (red), Si (cyan).

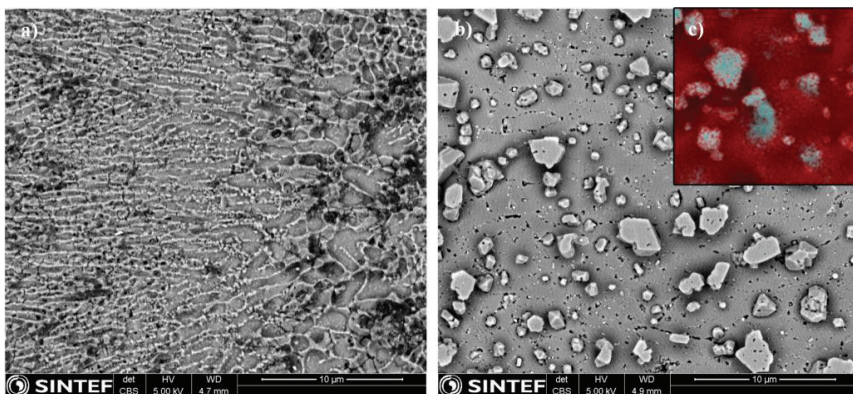The flow curves for the 14 specimens of each set is plotted in Figure 16. The AB and SR heat treatment conditions behave similarly with high strength, but low ductility. The T6 treatment increases the ductility at the cost of strength.
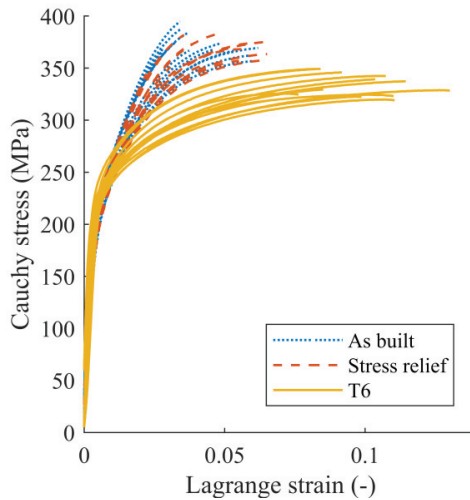

Figure 16 Stress-strain curves for AlSi10Mg for all 14 specimens for each of the three heat treatment conditions.

Selected tensile properties are plotted against the orientation with respect to the build plate in Figure 17. The elastic modulus does appear to depend on the build orientation, although there is significant scatter. This suggest that there is limited preferred crystallographic orientation when processing at 200°C, which is consistent with Tang et al. [32] and Hitzler et al. [33]. In the AB and SR condition there is no clear correlation between strength and build orientation, but in the T6 condition the strength increases with the specimen angle, and then drops at 90°. In the AB and SR condition the elongation at break increases with specimen angle, as seen with Inconel 718 in Paper 1. This is not seen in the T6 condition. This plastic anisotropy is attributed to different failure modes, as described in Paper 1.
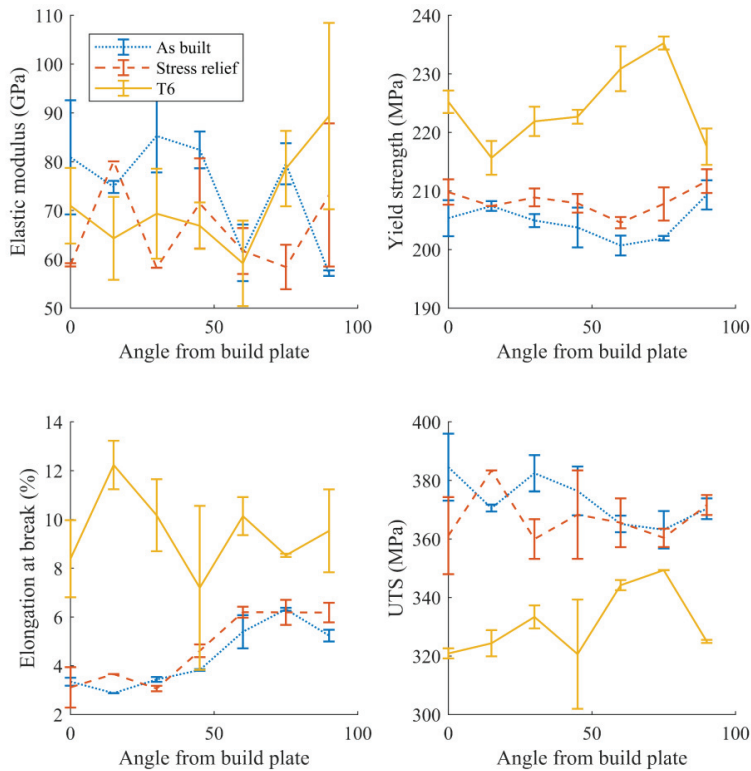
Figure 17 Tensile properties of AlSi10Mg plotted as a function of specimen orientation.

The displacement of the cantilever beams after cutting was measured to 2.723 mm and 2.808 mm at room temperature for the beams in X and Y direction respectively. When processed at 200°C the deflection was 0.22 mm and 0.23 mm. Using the inherent strain method in Simufact Additive the calculated residual stress is 370 MPa at room temperature, and 210 MPa at 200°C. Figure 18 shows the calculated and experimental displacement and calculated residual stress for the room temperature condition (a) and 200°C (b). The effective stress is reduced by approximately 40% when processing at elevated temperature. The benefits of such a reduction in stress is obvious when comparing the displacement in Figure 18 a) and b). The higher processing temperature reduces the thermal gradient, and difference in thermal expansion, between the melt pool and the preceding layers and build plate. The displacement is reduced to such an extent that geometries which required solid support structures at room temperature now can be

manufactured with lightweight supports and removed from the build plate prior to heat treatment.
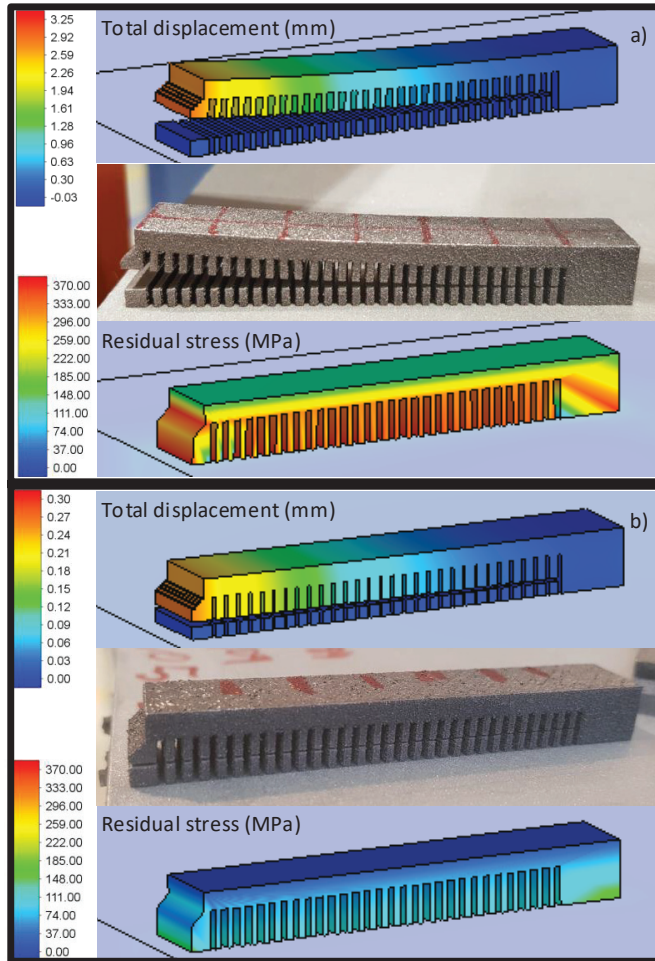
Figure 18 Total displacement and calculated residual stress for LB-PBF/AlSi10Mg at a) room temperature, and b) 200°C.

2.7.3. Concluding remarks

In LB-PBF/AlSi10Mg no elastic anisotropy was observed in tensile tests in either AB, SR or T6 heat treatment condition when processed at 200°C. SEM analysis revealed a cellular microstructure whose coarseness depends on the distance from the melt pool boundaries. After T6 heat treatment the microstructure consists of eutectic AlSi decorated with Si-rich particles. Plastic anisotropy was observed in yield strength and ultimate tensile strength in the T6 condition, and in the elongation at

break in the AB and SR condition. Processing at elevated temperature significantly reduces the residual stresses from the PBF process to an extent where post-processing SR treatment might not even be necessary. For FEM purposes an isotropic elastic analysis using the lower bound for elastic modulus seems appropriate. Elastic constants for the three heat treatment conditions can be found in Table 1 in Paper 2.

2.8. Paper 3 – An Investigation of the Anisotropic Properties of Heat-treated Maraging Steel Grade 300 Processed by Laser Powder Bed Fusion

In this paper the methodology from Paper 1 is further developed to understand anisotropic straining in the plastic region of the flow curve. As with the previous two papers, tensile specimens are produced at different orientations and subjected to different heat treatments. The tensile tests are performed with DIC to capture the strain fields. To compliment the tensile test results, SEM analysis with electron backscatter diffraction (EBSD) is performed. The main finding in this paper is a correlation between the fraction of load bearing melt pool boundaries in a specific direction and anisotropic straining in the transverse direction to the loaded axis.

2.8.1. Introduction

Maraging steels are FeNi alloys with a martensitic microstructure at room temperature than can be hardened through precipitation hardening (ageing), hence the name. The steel is graded by the nominal axial tensile strength in imperial unit ksi, which depends on the chemical composition. In AM, maraging steel grade 300 is the most commonly used variation, with a nominal tensile strength of 300 ksi or about 2000 MPa [36]. The steel is also known as 18% Ni maraging 300 (USA), 1.2709 (Europe), and X3NiCoMoTi18-9-5 (Germany). In this thesis the steel is denoted as 18Ni300. The steel is easily machined in the soft annealed condition, while exhibiting high strength and hardness in the aged condition [37,38].

The mechanical properties of LB-PBF 18Ni300 depends on several factors including, feedstock properties, PBF processing parameters, and post-processing conditions. Several authors have investigated the influence of different processing conditions with resulting strength in the range of 1700-2100 MPa, elastic modulus between 142.5 and 219 GPa, and elongation at break between 1.7% and 6.1% [6,39–45]. Most authors test either a single orientation, or up to a maximum of three orientations (0°, 45°, 90°). This might be insufficient to describe the anisotropic response of the material, as will be discussed in this paper. Both sources of anisotropy can be expected in LB-PBF/18Ni300, although in metals with a cubic crystal structure the plastic anisotropy resulting from preferred crystallographic orientation is limited because of the numerous slip planes that can be activated in different orientations. This suggests that alignment in the microstructure could be more dominant in this material.

The heat treatment for 18Ni300 is typically a two-stage process with solution treatment followed by precipitation hardening. The precipitation of inter-metallics requires fully dissolved hardening elements in solid solution [46], which in LB-PBF/18Ni300 is readily available due to the high cooling rates associated with the process. Because of this direct ageing has been suggested by several authors

[6,40,43,45,46]. In this study both direct ageing, and a more conventional two step heat treatment process is investigated.

Plastic anisotropy in LB-PBF/18Ni300 is studied previously by other authors, with especially Mooney et al. [6,46] doing interesting work. This paper expands on the knowledge and provides a systematic investigation of the strain behaviour in both the elastic and plastic regions of the flow curve.

In this study two sets of 21 tensile specimens were produced in a Concept Laser M2 Cusing with a laser power of 180W, hatch spacing of 0.105 mm, scan velocity of 650 mm/s and layer thickness 0.03 mm. The 'island' scan strategy was used with island size of 5 mm, angular shift of 45° and X/Y shift of 1 mm. The specimens were built in two separate builds and heat treated before removal from the build platform. The same seven orientations were built as in Paper 2 (0° to 90° with 15° increments), but the cross section of the gauge area was reduced to 4.5x4.5 mm^2 to ensure that a 50 kN load cell could pull until failure. The two heat treatment procedures were direct ageing (DA) at 500°C for 5 hours, and solution annealing at 815°C for one hour followed by the same ageing (SA+A). The specimens were cut from the build plate and machined after heat treatment. Figure 19 shows the layout of the tensile specimens on the build plate.
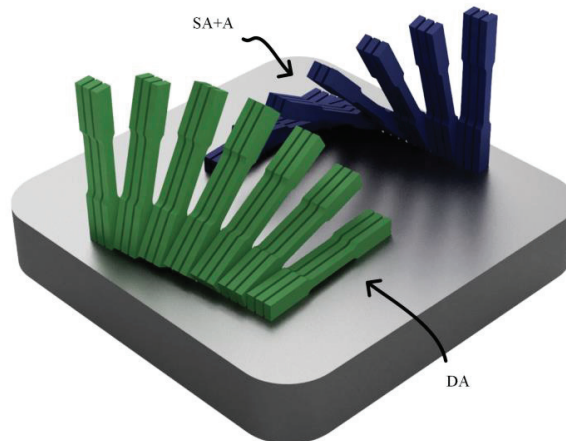
Figure 19 Illustration of the 18Ni300 tensile specimens on the building plate. In reality the two sets were built on separate build plates.

The tensile tests were performed in an MTS 809 Axial Test System with a 100 kN load cell. SEM was done after electro-etching the samples using Struers A2 electrolyte solution.

2.8.2. Results and discussion

The stress-strain curves for a selected specimen of each orientation is shown in Figure 20. The flow curves are relatively homogeneous with respect to both heat treatment and orientation, except for elongation at fracture for the 90° orientation in the SA+A condition. The elongation at fracture is also significantly lower for the 15° orientation in both heat treatment conditions.
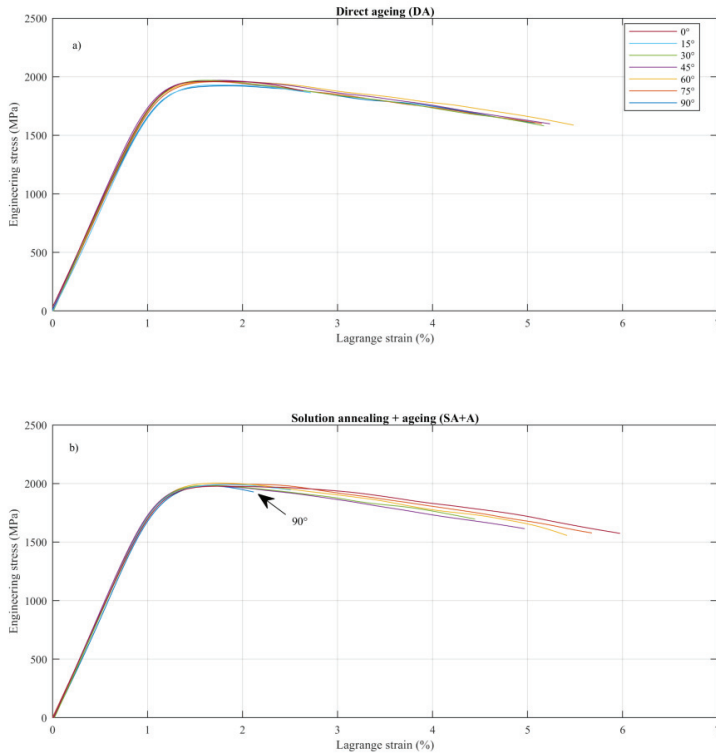
Figure 20 Stress-strain curve for a selected specimen of each orientation for the DA (a) and SA+A (b) condition.

Selected tensile properties plotted against build orientation is shown in Figure 21. The elastic modulus is slightly lower than the reference value, and in the DA condition, there is a clear variation with orientation. A similar trend can be seen in the SA+A condition, although less pronounced. The material appears to be stiffer when loaded in the 45°/60° orientation. There is no obvious correlation between strength and build orientation, but the elongation at fracture shows a trend similar

to what has been observed in Inconel 718 and AlSi10Mg in Paper 1 and Paper 2. For rolled bar stock the reference value for elongation is 4% for 0° and 5% for 90° orientation, indicating a similar trend for forged 18Ni300.
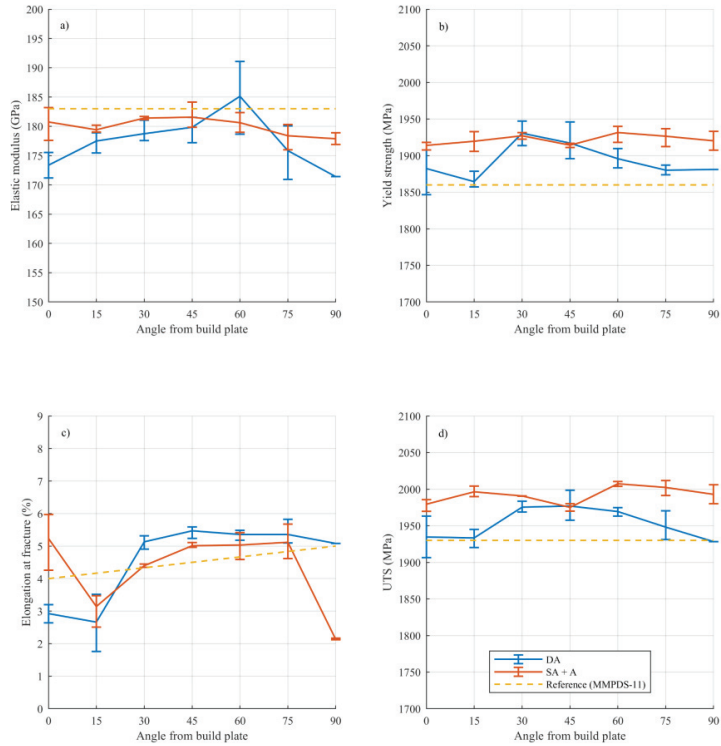
Figure 21 Elastic modulus (a), yield strength (b), elongation at break (c), and ultimate tensile strength (d) for both heat treatment conditions. The reference value is for bar stock aged at 482°C [47].

To further investigate the anisotropy the strain fields captured with DIC are analysed in detail. Each specimen is given a local coordinate system. The X-axis is aligned with the axial direction, the Y-axis perpendicular in the flat plane of the specimen, and the Z-axis to complete the right-hand coordinate system. Two perpendicular surfaces (area of interest – AOI) on each specimen are captured by the DIC system and the strain fields are analysed. Figure 22 shows the specimen with the AOIs and local coordinate system.

Figure 22 Dimensions of the tensile specimens in mm. AOI 1 and 2 indicates the area of interest where the strain fields are captured with DIC.

The ratio of the strains transverse to the axial direction, i.e. the strain in the local Y and Z direction, are called the transverse strain ratio, or in the plastic region of the flow curve, the Lankford coefficient [48]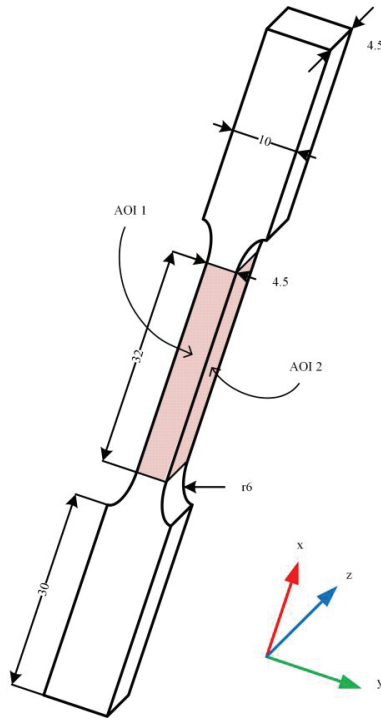. The Lankford coefficient has been used to quantify plastic anisotropy in sheet metal since the early 1950s, and can be expressed as $r = \Delta\epsilon_Y/\Delta\epsilon_Z$ for an axial load in the X-direction. If the Lankford coefficient is not equal to one, the material is considered anisotropic. Recent work by Mooney et al. [6,46] have used the Lankford coefficient to quantify plastic anisotropy in LB-PBF/18Ni300. A similar approach is adopted in this paper but expanded to include elastic strain as well. Figure 23 shows elastic and plastic transverse strain ratios for both heat treatment conditions. The measured plastic transverse strain ratios are indicated with solid lines, while the elastic transverse strain ratios are indicated with dashed lines. The dotted lines show the estimated elastic strain ratios using elastic constants determined by the 'DIC method' presented in Paper 1.
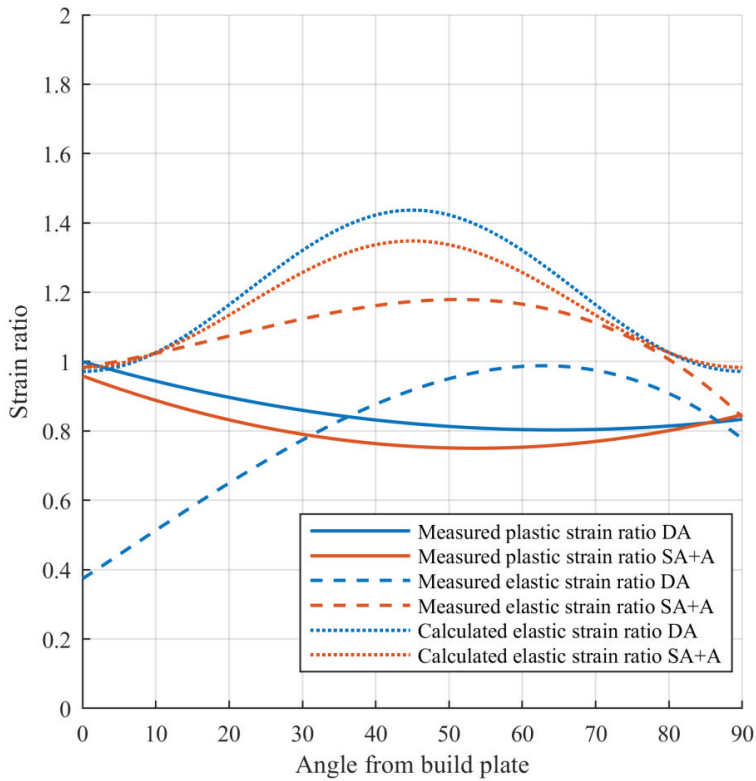
Figure 23 Elastic and plastic transverse strain ratios as a function of build orientation shown with polynomial fits. An isotropic material would have a transverse strain ratio of 1.

The transverse strain ratios tell us that the material prefers straining in particular directions, and that the direction of loading decides whether that straining is isotropic or not. In the 0° orientation the plastic transverse strain ratio is close to 1 for both heat treatment conditions. As the specimen are raised the transverse strain ratio is reduced, until it increases again and approaches 1 when the specimen orientation approaches 90°. The trend is in line with observations by Mooney et al. [6], although in this study the material is generally less anisotropic (transverse strain ratio close to 1). The anisotropic straining is highlighted in Figure 24. Note the high strain in the Y direction (ϵ_{yy}) compared to the Z direction in the DA 45° specimen. Even though the strength does not vary significantly with build orientation, the material favours straining in certain directions, which again depends on the build orientation.

Figure 24 Transverse strain fields of DA 45° specimen in the plastic region. Note the high strain in the Y direction compared to the Z direction.
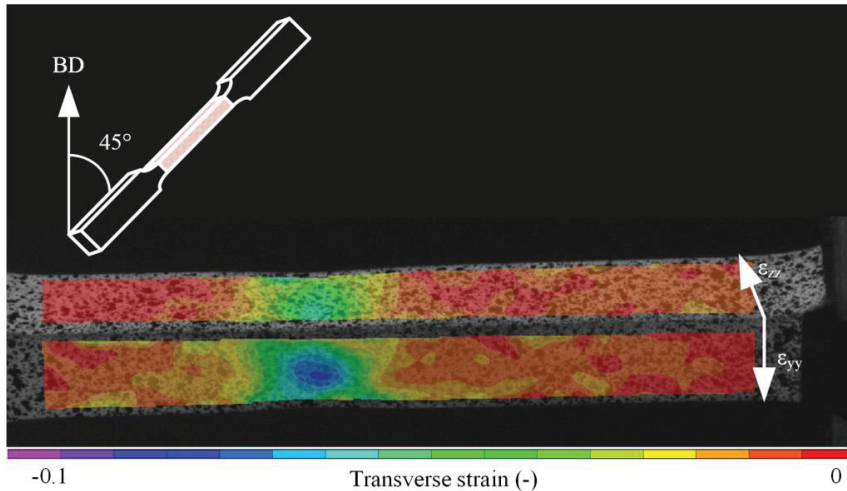
The measured elastic transverse strain ratio depends on both heat treatment and build orientation. In the SA+A the elastic transverse strain ratio equals one at 0° orientation and is higher than one for specimens between 15° and 75°, it then dips below 1 for 90°. In the DA condition, the material heavily favours straining in one particular direction in the 0°, with a transverse strain ratio of approx. 0.4, before it increases to almost 1 at 60° and then dips down to approx. 0.8 at 90°. This does not match the calculated elastic transverse strain ratio, which assumes transverse isotropy ($\epsilon_{xx} = \epsilon_{yy}$ in the *machine* coordinate system). The calculated elastic transverse strain ratios are included however, to highlight this particular property. In Paper 1 the assumption of transverse isotropy held true for Inconel 718, but in the case of DA 18Ni300 this assumption is invalid.

The preferred direction of the elastic strain observed in the low angle DA specimens can be explained by alignment of defects and particles in the microstructure. More specifically it seems related to the fraction of load bearing melt pool boundaries (MPB) in the specific directions. The number of MPBs in the specimen Y and Z directions can be approximated geometrically. Consider the inset in Figure 25, where the laser tracks are indicated on a section of a square specimen. The number of laser tracks in the build plane can be expressed by the specimen height, *H*, specimen width, *w*, layer thickness, *t*, hatch spacing, *h*, and the angle from the build plate, θ. For any θ between 0° and 90° the number of MPBs in the Y-direction can be expressed as $H/t * sin\theta + w/h * cos\theta$. The number of MPBs in the specimen Z direction can simply be expressed as w/h. This assumes only one MPB for each laser line, but since only the fraction of MPBs in a particular direction is considers,

this does not alter the results. The fraction of MPBs in the specimen Y-direction over the specimen Z-direction is plotted over build orientation in Figure 25. The measured elastic transverse strain ratio in the DA condition matches the fraction of MPBs in Y over Z remarkably well. This gives a clear indication that when the fraction of MPBs in the specimen Y direction is low, the material favours straining in that direction. As the fraction of MPBs increases the straining is more uniform.
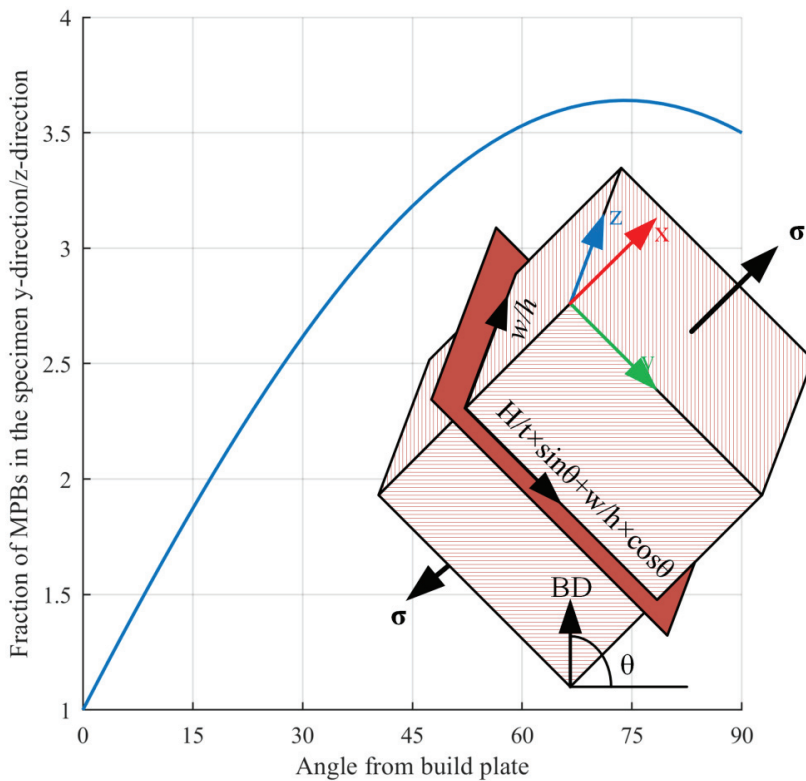
Figure 25 Fraction of load bearing melt pool boundaries in the specimen Y direction over specimen Z direction as a function of specimen orientation.

It can be seen in Figure 26 that the melt pool boundaries are clearly visible in the DA condition, and that the martensite plates align with the direction of the heat flow (arrows). In the SA+A condition, the MPBs are no longer visible, but the original orientation of the martensite plates remain. The solution treatment before ageing reduces the elastic anisotropy, especially when considering the transverse strain ratios. The dissolution of the MPBs supports the hypothesis that the fraction of

loadbearing MPBs influences the preferred direction of straining. A more detailed investigation of the microstructure is available in Paper 3, including EBSD analysis and fracture analysis. The EBSD analysis with Taylor factor mapping confirms that there is no significant contribution to anisotropy from preferred crystallographic orientation in LB-PBF/18Ni300, although local texture is observed. The high number of available slip planes, and the 24 directions available for martensite transformation (K-S relationship [49]) results in a stochastic grain orientation. For this reason, the detailed analysis and discussion is omitted from this section of the thesis.
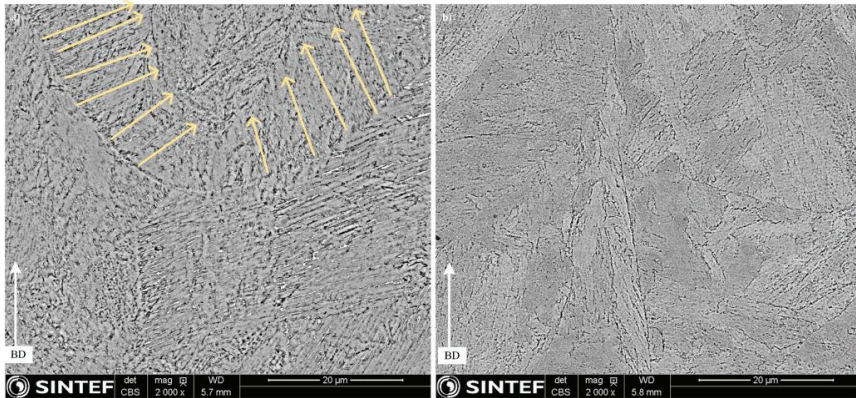
Figure 26 SEM images of a) DA condition and b) SA+A condition. Arrows in (a) suggests the solidification direction.

2.8.3. Concluding remarks

The main contribution to the thesis in this paper is the expanded method of using the transverse strain ratios to better understand the anisotropic straining. Further work can be done on improving the scan strategy to even out the number of MPBs in any particular direction. Furthermore, the analysis revealed that the assumption of transverse isotropy does not hold for 18Ni300. If the methodology developed in Paper 1 is to be used on 18Ni300, it must be modified to at least account for orthotropic behaviour.

3. Anisotropy in dynamic loading LB-PBF/m

This section concentrates on anisotropy in dynamically loaded metals processed by LB-PBF. Paper 4 focuses on the effect of surface roughness on fatigue life, with proposed methodology to estimate the fatigue life of AM components. In Paper 5 the methodology developed in Paper 4 is implemented in an open source software package for numerical fatigue analysis, Fatlab. In Paper 6, the surface characteristics of LB-PBF/18Ni300 is investigated and coupled with experimental fatigue testing.

In crystalline metallic materials fatigue cracks initiates by an irreversible slip process on the surface [50]. The state of local stress, crystal orientation and texture with respect to the external stimuli, grain boundaries type and lengths, microstructure clusters and inclusions are among the factors that play central roles in fatigue life [51–55]. Among these parameters the stress state is the backbone of the fatigue failure, in the absence of which no damage will take place. Local stress can be much higher than applied external stress due to topological inhomogeneities acting as stress concentrations. Extensive work has been done on this topic, especially in machining and milling and it is well understood that surface defects causes stress concentrations that reduces the fatigue life [56,57]. Figure 27 indicates typical surface roughness for selected metal processing technologies.
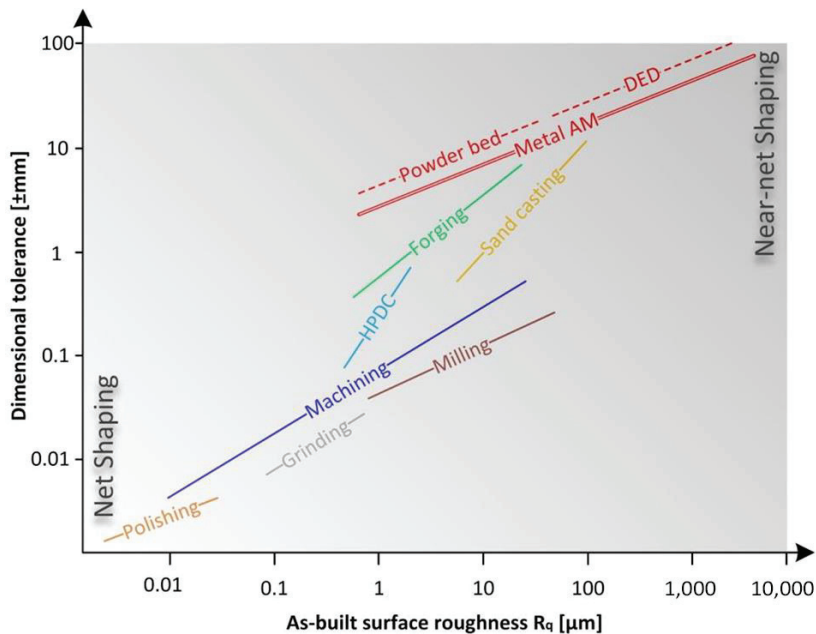
Figure 27 Surface roughness characteristics of selected metal processing technologies. Figure from Paper 5.

Powder bed fusion typically achieves a roughness of approximately Ra = 4-10 μm, an order of magnitude rougher than what can be expected from surface machining. In powder bed fusion, phenomena such as the 'stair-case' effect can influence the fatigue life. The stair case effect is a result of the discretisation of the 3D geometry, and is represented schematically in Figure 44 in section 3.3.2. Whereas in subtractive machining the surface roughness depends on the machining parameters, in LB-PBF it largely depends on the build orientation, as will be demonstrated in Paper 4 and 6.

LB-PBF materials are in general inferior to cast and wrought counterparts when it comes to fatigue life. Several factors influence the fatigue life of materials, and in this thesis the focus is on surface roughness. Other important factors, especially in AM, are internal defects and notches, and to some extent the causes for anisotropy covered in the previous chapter. Preferred crystallographic orientation and alignment in the microstructure will change the stress distribution within a component but is considered less efficient at creating stress concentrations compared to surface defects and internal defects.

3.1. Paper 4 – High Cycle Fatigue Life Estimation of Materials Processed by Laser Powder Bed Fusion

In this paper a method for determining stress concentration factors for fatigue life estimation based on surface roughness is presented. It utilises white light interferometry (WLI) on specimens with as-built surface built at several different angles with respect to the build plate. The results are validated numerically and should thus be considered a tool to benchmark different orientations with respect to fatigue life reduction from surface effects only.

3.1.1. Introduction

Predicting the fatigue life of a component requires an appropriate definition of a stress concentration factor (SCF). We can distinguish between the SCF of the nominal geometry, and the SCF from process induced defects. The SCF is defined as the maximum observed stress divided by the externally applied, or nominal, stress in Equation (7).

$$k_t = \sigma_{max}/\sigma_{nom} \qquad (7)$$

For a U-shaped surface defect under uniaxial loading the SCF can be estimated according to Equation (8), where d is the distance from the surface to the tip of the defect and ρ is the radius at the tip [57].

$$k_t = 1 + 2\sqrt{\frac{d}{\rho}} \qquad (8)$$

Based on the type and size of defects in the component either internal or external defects will play a dominant role. Internal defects can be characterised by non-destructive methods such as micro-CT or by destructive methods such as microscopy. Surface defects are typically characterised with microscopy or interferometry. There are several studies regarding fatigue life estimation based on AM defects. Ramona et al. proposed a model based on internal defects to predict both high-cycle and low-cycle fatigue [29,58]. Yadollahi et al. applied a similar method to describe the effect of surface texture and defects [59]. The latter suggests using the maximum valley depth of the surface profile (*Rv*) as the initial crack length for fatigue life modelling. This approach, however, does not account for the geometry of the defect. Yamashita et al. studied the effect of internal defects, and concludes that the area of defect must be seen in relation with other defects in near proximity for a more accurate prediction [60]. Zhou et al. studied the effect of texture on low-cycle fatigue [61], and found that a columnar grain structure parallel to the build direction influences the fatigue life.

This study aims to provide a tool for estimating the impact on fatigue life from surface roughness only, as a low-cost option for benchmarking different orientation. It is well documented in the literature that the as-built surface roughness of PBF materials has a negative effect on the fatigue life of AM components [31,62–65]. With this in mind, two approaches are proposed to estimate the fatigue life of LB-PBF components. One approach uses white light interferometry to characterise the surface roughness, while the other uses a stylus-type measurement for surface roughness characterisation.

Surface roughness measurements were performed on the Inconel 718 and AlSi10Mg tensile specimens described in Paper 1 and Paper 2. The white light interferometry characterisation was performed in a Wyko NT-9800 and analysed in Veeco Vision 4.2. Two areas of 1.7x2.3 mm^2 were investigated on each orientation and filtered with a long wavelength pass Gaussian filter with a spatial cut-off of 20 µm.

The fatigue life is estimated by determining an expected stress concentration factor (SCF) from the surface roughness profile. The SCF can then be applied to the relevant surfaces in FEA software. In this paper a static preload was simulated in Abaqus CAE and dynamic loading, including the SCF was carried out in FE-Safe. To estimate the SCF consider the schematic in Figure 28, which shows a cross section of three layers in a PBF process where the scanning direction alternates between the layers. Each semi-circle represents a laser track. The hatch spacing is indicated with h, the layer thickness with t, and the angle of the surface with θ. The radius at the depth of the valley, ρ, can be calculated according to Equation (9).
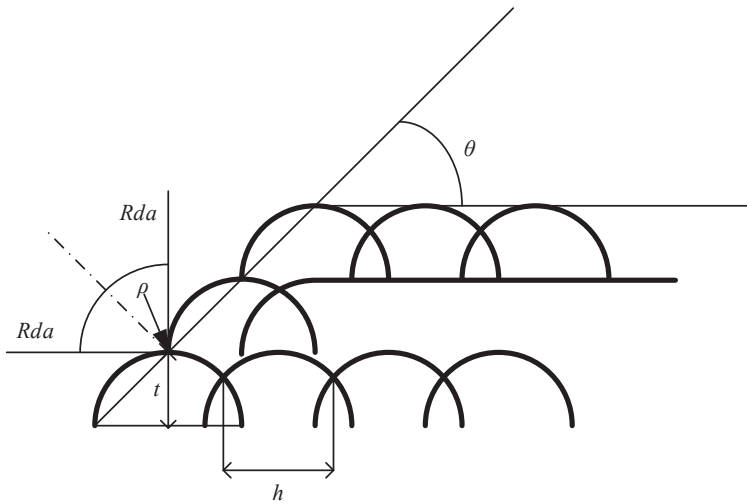

Figure 28 Schematic of three layers of a LB-PBF process with relevant surface parameters indicated.

$$\rho = \frac{L - tan(Rda)\,Rz}{1 - tan(Rda)} \tag{9}$$

In Equation (9) *L* is the peak-to-peak distance measured as *S*. The value of *Rda*, *Rz*, and S can be determined by line analysis with WLI or with a perthometer. The SCF for surface defects can then be calculated by inserting Equation (9) into Equation (8). This method is referred to as the 'stylus method'. An alternative approach is to calculate the SCF of surface defects using the mapped topography from WLI. The surface topography is represented in a matrix with each element (Z_{XY}) corresponding to the height of the pixel indicated by the row (X) and column (Y). The horizontal radius of curvature at each point can then be obtained using a quadratic fit though that point and the adjacent points. If the data is fit to $Z(X,Y) = aZ(X,Y)^2 + bZ(X,Y)^2 + c$, the spherical radius of curvature at (X,Y) is approximately $\rho \cong (2a)^{-1}$. The SCF for each point can then be estimated using Equation (8). This approach is referred to as the 'WLI method'.

3.1.2. Results and discussion

The results for Inconel 718 will be shown in this chapter. In the appended Paper 4 additional results for AlSi10Mg are also included.

Selected surface roughness measurements for as-built Inconel 718 is shown in Figure 29. The arithmetic mean deviation from the *Ra*, average depth of the valleys Rvm, average distance between the peaks *Rz*, and the average absolute slope measured in radians *Rda*, all follows the same general trend line. The smoothest surface is found on the 0° orientation, and the surface roughness quickly increases as the specimen is tilted to 15°. The surface roughness becomes smoother as the specimen are further tilted towards 90°. The surface roughness for HIPed Inconel 718 follows the same trend. The results for HIP can be found in Paper 4.
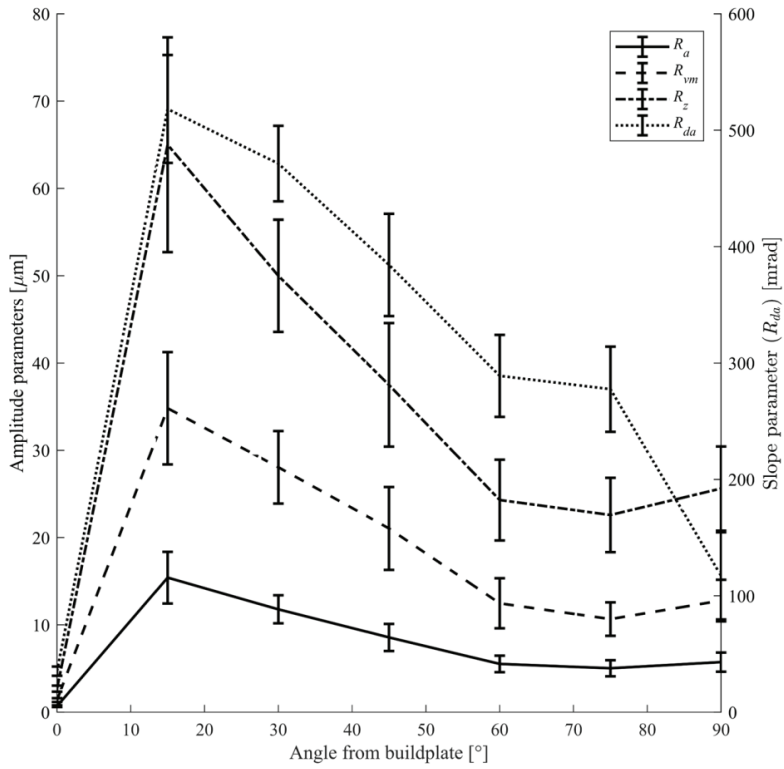
*Figure 29 Selected roughness measurements for the as-built Inconel 718 specimens oriented from 0°
to 90° with 15° increments with respect to the build plate.*

The surface roughness along with the laser scan parameters are then used to calculate SCF for the different surface orientations. Figure 30 shows the SCF, k_t, for Inconel 718 in both as-built and HIP + aged heat treatment condition. The WLI method is shown with solid lines, and the stylus method with dashed lines.
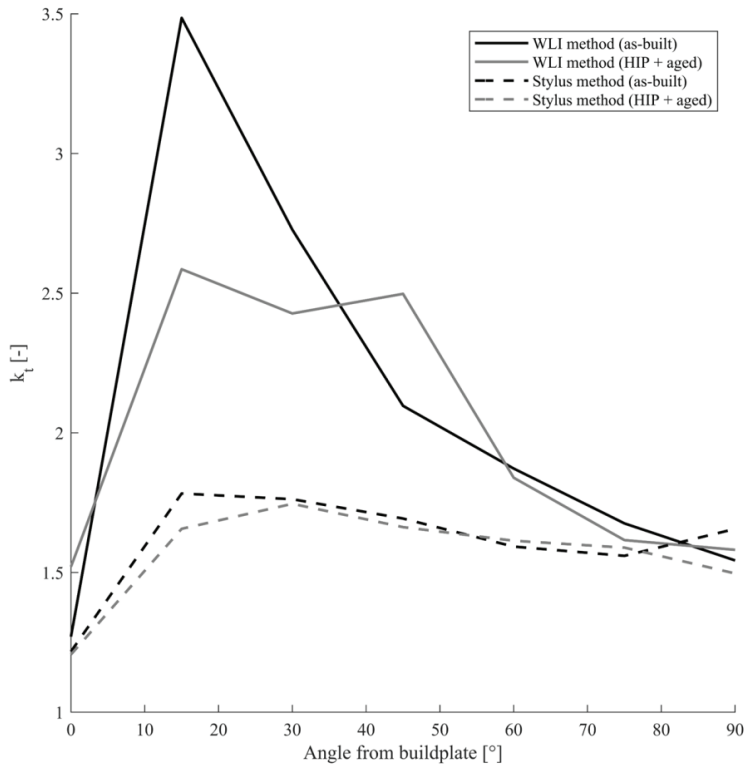
Figure 30 Estimated stress concentration factors for surface defects in Inconel for as-built and HIP + aged heat treatment condition.

As expected, the SCF follows the trend of the surface roughness. There is a large discrepancy between the WLI and stylus methods, except for the low surface roughness specimens at 0° and 75°/90°. The WLI method is sensitive to local high-spots which in LB-PBF can be e.g. partially fused powder particles. This is especially true for inclined surfaces, such as the 15° specimen shown in Figure 31. The presence of such particles will strongly affect the roughness extremes but can be avoided when using a stylus method to measure a single line.
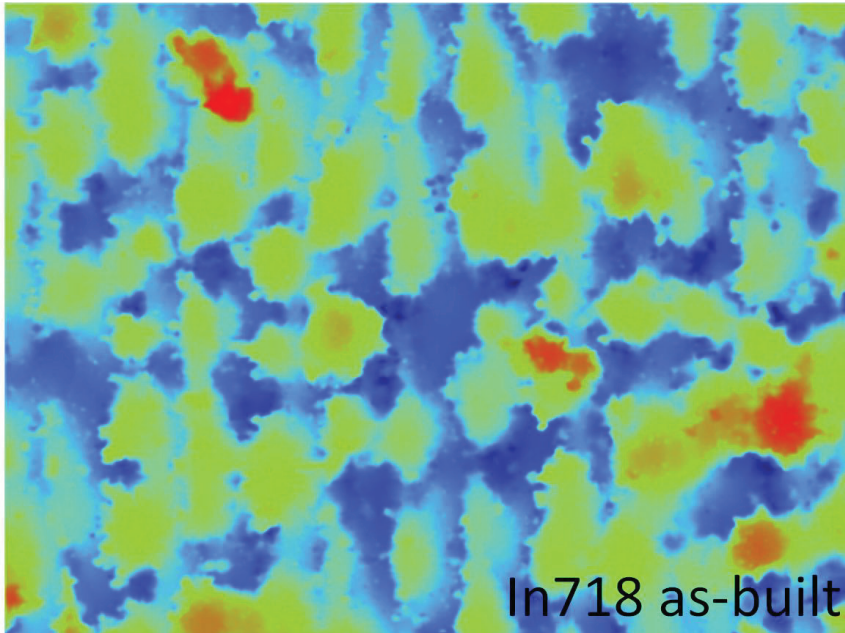
Figure 31 Unmasked WLI image of the 15° as-built Inconel 718 specimen. The area investigated is 1.7 mm by 2.3 mm.

This method only considers surface defects in the form of surface roughness. To evaluate if internal defects contribute to a reduction in fatigue lifetime FEM analysis is performed on an idealised geometry. The inset in Figure 32 shows the relative geometry of a groove with a nominal SCF of 4.5. A generic material is loaded in uniaxial tension with a pore of diameter 50, 100, or 150 μm with distance *a* from the tip of the U-shaped groove. The curves show that if sub-surface pores are present at a certain critical distance from the surface defect the internal defects will play a larger role than surface defects in reducing fatigue life.
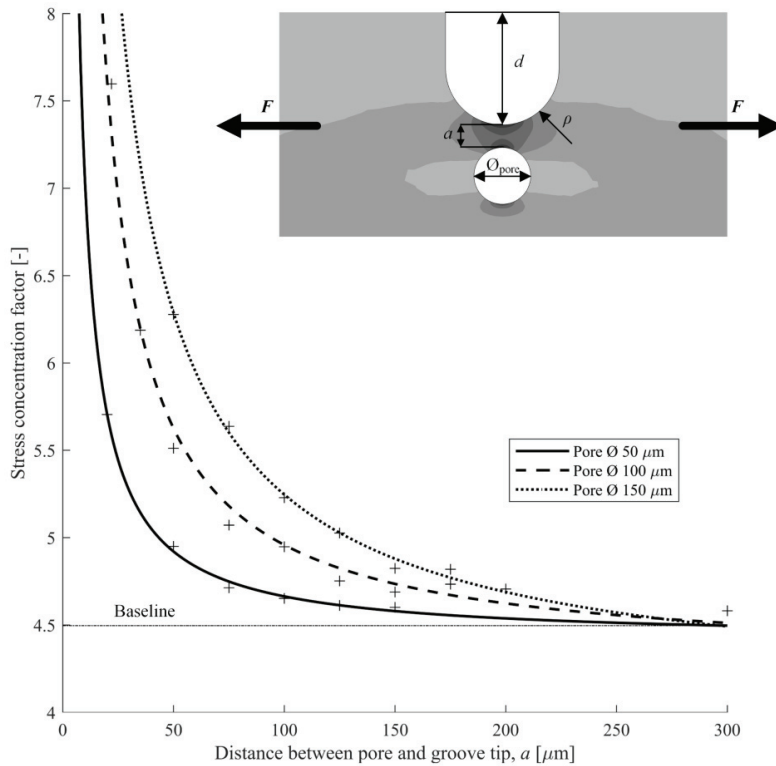
Figure 32 The effect of pore diameter and distance between pore and crack tip on a U-shaped surface defect with nominal SCF of 4.5.

To demonstrate the effect of surface roughness on high cycle fatigue life a series of numerical simulations were performed in Abaqus and FE-safe. A dog bone geometry was loaded in tension and compression at 10% of the materials yield strength in Abaqus. After which it was subjected to a cyclic load (R=-1) in FE-Safe. The model is based on an experimentally determined SN curve, and the fatigue life is calculated for different SCF based on the surface roughness. The material data for aged Inconel 718 from Paper 1 is used for the preload in Abaqus, while an SN curve based on machined and aged Inconel 718 was used[65]. Figure 33 shows the expected number of cycles before failure for Inconel 718 with a cyclic load of 10% of the yield strength for different surface conditions. The lifetime is reduced by approximately one order of magnitude for the 45° orientation compared to the 0° orientation.
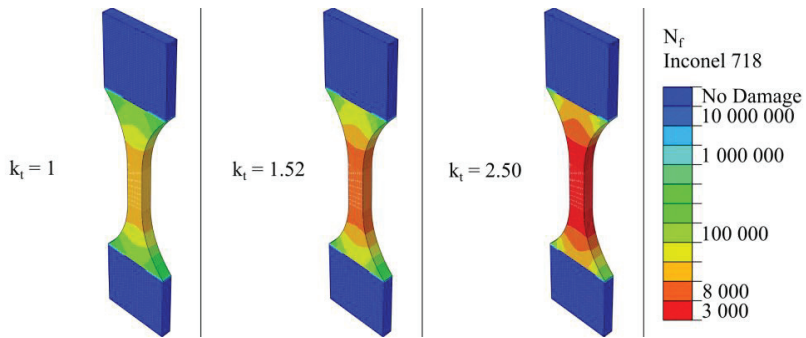
Figure 33 Fatigue life estimation of LB-PBF aged Inconel 718 with different surface conditions. Polished surface (k_t=1), 0° orientation (k_t=1.52), and 45° orientation (k_t=2.5). The legend shows expected number of cycles to failure. The SCFs were selected from the WLI method.

3.1.3. Concluding remarks

The SCFs are taken from the more conservative WLI method, and the fatigue life would be expected to be higher in reality. As a tool for benchmarking different orientations with respect to fatigue life, the proposed method can be useful, especially when dealing with complex geometries. As will be presented in the next section, this methodology can be applied to optimise part orientation in the PBF build chamber with respect to fatigue life.

3.2. Paper 5 – A Novel Approach for Enhancing the Fatigue Lifetime of the Components Processed by Additive Manufacturing Technologies

Paper 5 is a collaboration between SINTEF Industry, the University of Oslo, Aarhus University, and the Norwegian University of Science and Technology. The ideas from Paper 4 are implemented in an open source, free to use, metal fatigue toolbox (Fatlab[1]) developed by Mikkel M. Pedersen at Aarhus University. The examples shown in this section are developed by Magnus Reiersen and Amin Azar. My contribution is mainly the methodology for characterisation of the material for the input to the Fatlab toolbox, or the left-hand side of Figure 34. The methodology is described in detail in the previous section, and thus this section will focus on the implementation in Fatlab, including an example analysis of a complex geometry.

3.2.1. Implementation

Fatlab is a postprocessing tool for fatigue analysis from FE analysis. Paper 5 describes how the toolbox is expanded to integrate anisotropy in the fatigue analysis of AM components. The concept is visualised in Figure 34. During the analysis Fatlab determines the angle of the surface of each node with respect to a reference direction (e.g. the build direction). The fatigue strength of each node is then scaled based on the orientation according to a table of fatigue strength scaling factors. The first rectangular box and the left-hand side of Figure 34 is there to determine the table of fatigue strength scaling factors. The shrink-wrap step on the right hand-side of Figure 34 is beneficial as it generates smooth transitions between geometrical features from e.g. topology optimised geometries. The surface is represented as discrete triangles defined by three points and a normal vector. The angle of the normal vector with respect to the reference direction can be mapped for each triangle and used in the analysis to find the optimal orientation in the AM process. When the characterisation and modelling is done the fatigue, analysis is performed.

Fatigue analysis in Fatlab consists of setting up the loads, the model, and the SN curve before the analysis can be run. Setting up the loads and the model is well documented in the toolbox (http://fatiguetoolbox.org/fatlab/documentation). The SN curve setup includes defining a SN curve as well as mean stress handling. For metallic (ductile) materials the Gerber parabola is recommended. The SN curve should be of a defect free (i.e. polished) material when implementing anisotropy from surface roughness. In this step the anisotropy is defined, and the fatigue strength is scaled relative to the defined SN curve and reference direction vector in a table. The scaling can be based on anything, not just surface roughness as in this

---

[1] http://fatiguetoolbox.org/fatlab

example. The fatigue strength could be scaled on experimental fatigue data, or other models than the one presented in Paper 4.
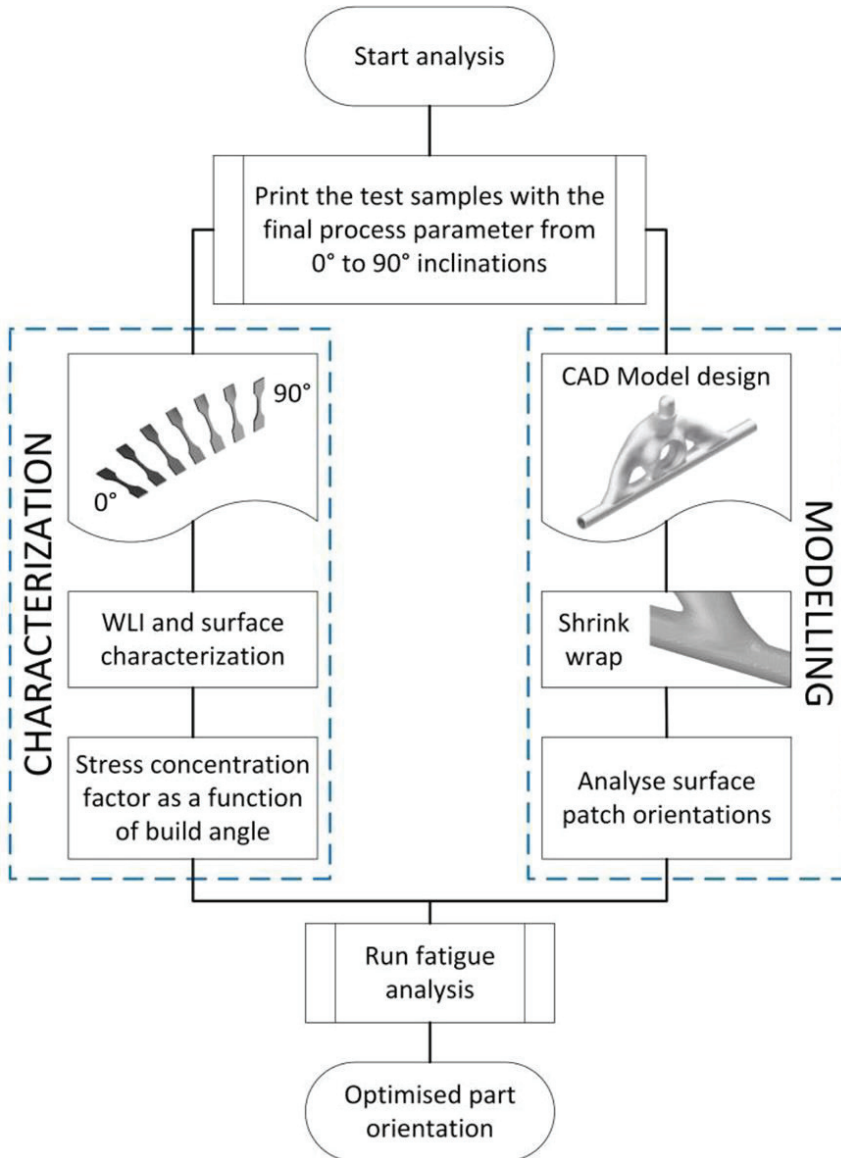
Figure 34 Flowchart showing the steps of the data processing in Fatlab.

To evaluate the design, a quantity named the utilisation ratio (UR) is used. The UR is the ratio between the applied stress range and the fatigue strength at the same number of cycles. A value of UR=1 means that the material fails exactly at the given number of load cycles, while UR<1 means the design is conservative. UR>1 means the design fails prematurely and should be improved. The UR value tells the designer how to adjust the stresses in critical locations by modifying the geometry or re-orienting the component to introduce a different surface topography distribution.

3.2.2. Example

An example of optimisation of a complex geometry will be given in this section. The geometry is a topology optimised skateboard 'truck', which is the structural component connecting the board to the wheels. The material selected is AlSi10Mg. The topology optimised model was shrink wrapped before FE analysis was performed in Abaqus CAE. Figure 35 shows the topology optimised geometry of the skateboard truck with boundary conditions and loading in Abaqus. The load is 1 kN and it is applied to the three extremities on the truck where the wheels and skateboard are attached. The centre of the geometry is full constrained.

Figure 35 Boundary conditions and loading in Abaqus.

The equivalent stresses are shown from the front, back, and side in Figure 36. The stress is mainly distributed on the lower axle, and above the central hole.
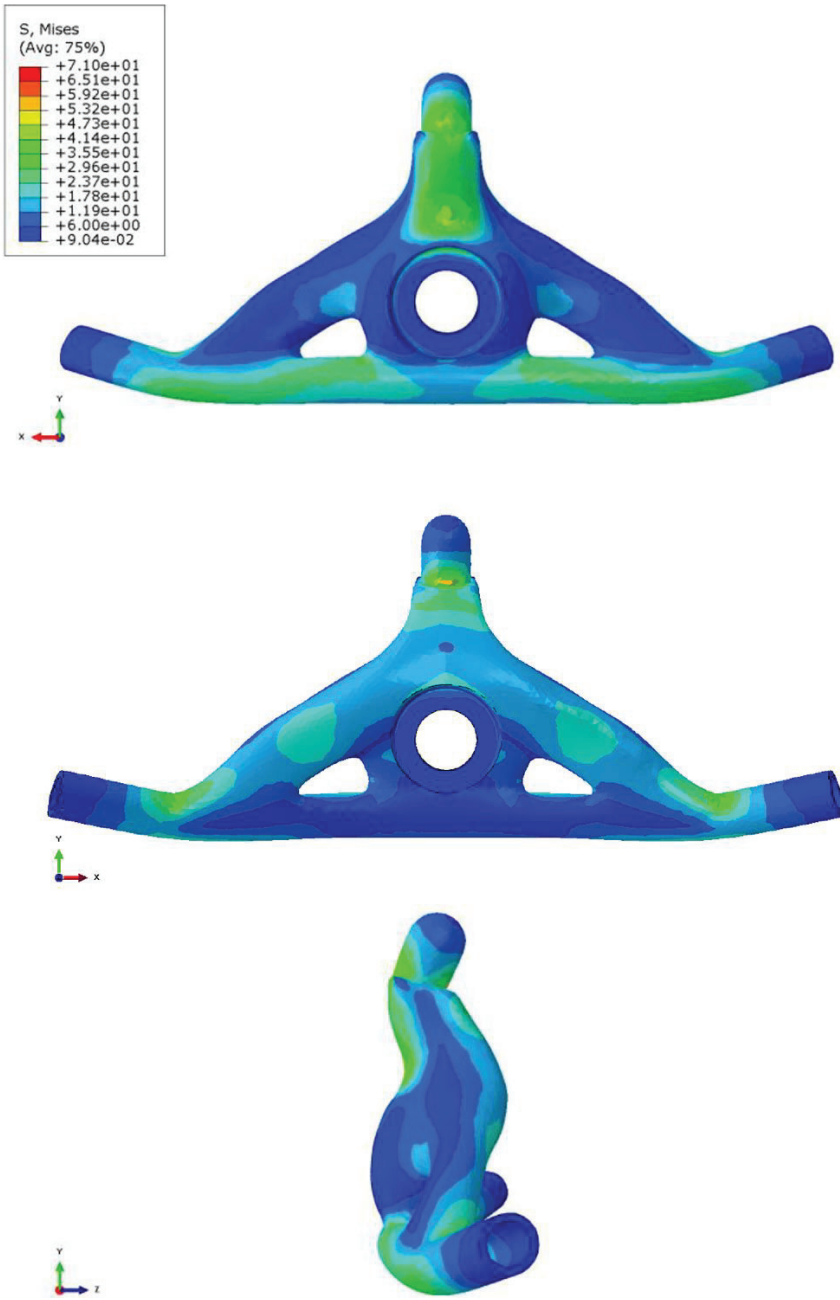
Figure 36 Equivalent stresses at a unit load of 1 kN. Deformation scaled 200 times.

The load is setup as a sine curve with amplitude corresponding to a load of 80kg, repeated for 3×10^5 cycles. The SN curve is defined as a two-step curve with a primary slope of 6.5 and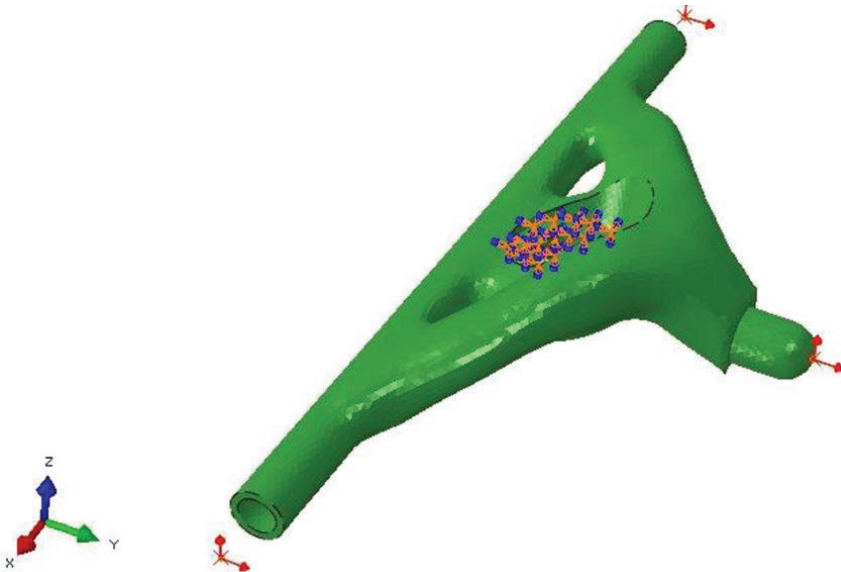 a secondary slope of 22. The fatigue strength is set to 215 MPa at 10,000 cycles, and the knee point is at 200,000 cycles with a stress of 50 MPa. A safety factor of 2.7 is then applied, and the allowable damage set to one. The mean stress is handled as a Gerber parabola with mean stress sensitivity 0.2, yield strength of 230 MPa, and tensile strength of 345 MPa. For further details the reader is referred to Figure 10 and Figure 20 in the appended Paper 5. The anisotropy is implemented by considering the experimental data from Paper 4 and given as input as per the table in Figure 37.

Reference direction vector: [0 0 –1]

Enter fatigue strength scaling factors:

Angle	Scaling
0	0.5714
15	0.5556
30	0.5405
45	0.2857
60	0.3448
75	0.3509
90	0.4444
105	0.3509
120	0.3448
135	0.2857
150	0.5405
165	0.5556
180	0.5714
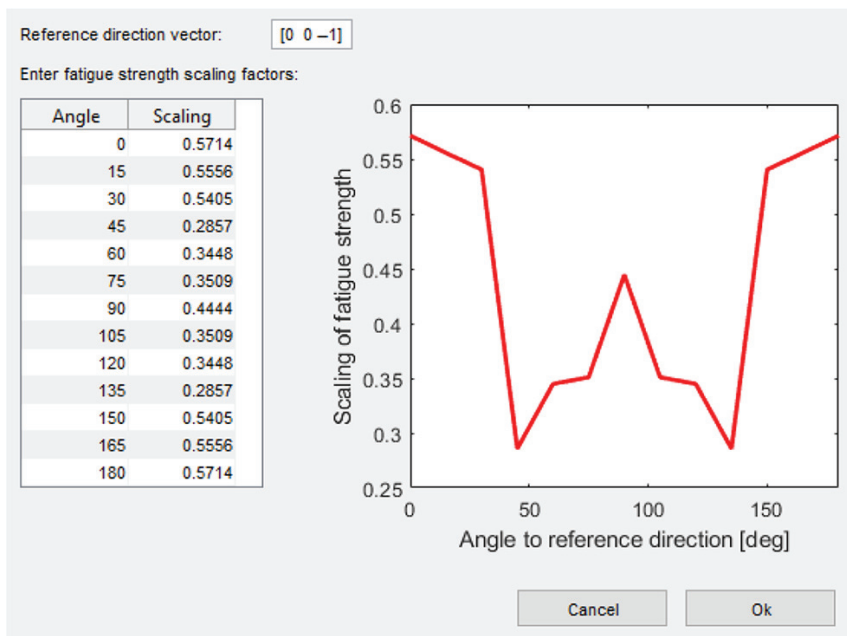
Figure 37 Fatigue strength scaling for AlSi10Mg.

An isotropic reference analysis (smooth surface) is performed first and showed in Figure 38. From the static analysis a hot spot was seen in the top dome of the geometry (orange in Figure 36). After 3×10^5 cycles, damage is caused in this region. The worst node in this region has a UR of 1.01, which corresponds to 281,256 cycles. Another major stress concentration can be seen directly beneath this hot-spot from the static analysis (red colour in the left hand side of Figure 38). No extensive fatigue damage is seen under the given conditions, however.
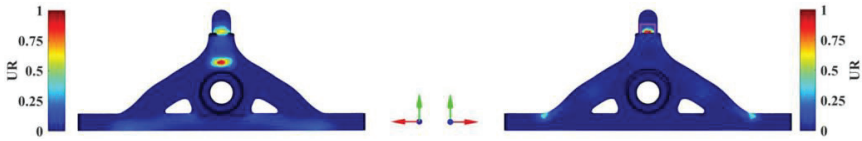
Figure 38 Isotropic reference fatigue analysis.

When anisotropy is introduced, significant damage is observed in the model. Figure 39 shows the UR of the anisotropic analysis where the build direction is set to the negative Z-axis in the global coordinate system. The magnitude of the UR is doubled in the hot spot below the top dome, and new hot spots evolve at the lower axle. The worst node has a UR of 2.779, which decreases the expected lifetime to just 391 cycles, a significant reduction in lifetime compared to the isotropic analysis. When the build direction is changed to the negative Y-axis (Figure 40), the location and UR of the hot spots also change. Although the number of nodes with high UR is higher in Figure 40 compared to Figure 39 the expected lifetime of the component when the build direction is along the negative Y-axis is 624 cycles. This is an increase of 60%, and the latter orientation is preferrable.
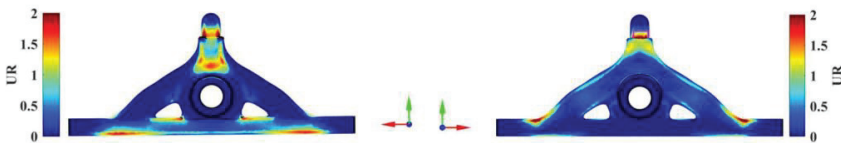
Figure 39 Anisotropic analysis where the build direction is set to the negative Z-axis in the global coordinate system (out of plane view).
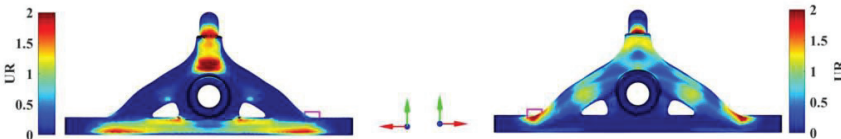
Figure 40 Anisotropic analysis where the build direction is set to the negative Y-axis in the global coordinate system (opposite direction of the green arrow).

For complex geometries such as the skateboard truck the optimal orientation cannot be deduced intuitively. Fatlab can find the optimal orientation by sweeping all possible build directions to minimise the UR of the worst node. The design space is represented as a spherical coordinate system, where the reference direction vector is expressed as $\vec{u} = [sin\phi cos\theta, sin\phi sin\theta, cos\phi]$. The task is then to sweep θ bound by 0 and 2π and ϕ bound by 0 and π. The sweep is done with angular increments of 1.8° resulting in 5000 different possible orientations. Figure 41 shows the UR of the design space, with a red dot indicating the optimal reference vector with respect to minimising the UR of the worst node.
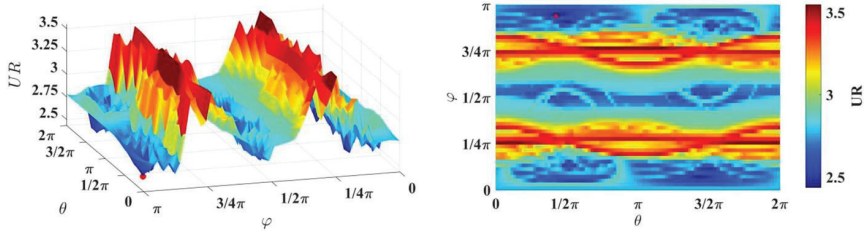
Figure 41 Sweep of the design space to find the optimal orientation with respect to fatigue life.

The corresponding fatigue analysis is shown in Figure 42, where the reference direction is shown with the cyan arrow. The corresponding UR for the worst node is 2.406 which corresponds to 998 lifecycles, up by 155% compared to the first orientation investigated in Figure 39.
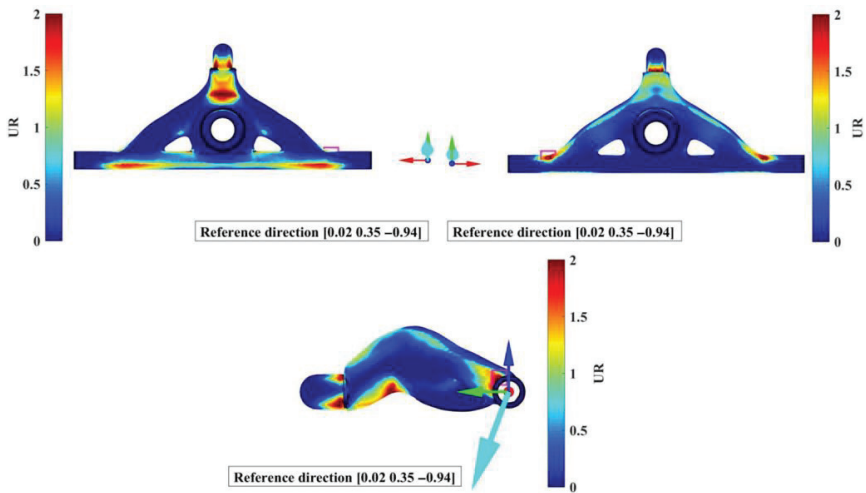
Figure 42 Anisotropic fatigue analysis for the optimal orientation. The reference direction is indicated by the cyan arrow and the text box.

3.2.3. Concluding remarks

The Fatlab toolbox with the added functionality presented in this paper gives engineers and designers a tool to evaluate the fatigue life of components with respect to build direction in e.g. LB-PBF processes. A good design for additive manufacturing accounts for the build direction early in the design stage, and this toolbox can be used to efficiently benchmark build directions. Other factors might also influence the choice of build direction, such as residual stresses, the need for support structure, and build plate packing for cost reduction. The more informed a designer is, the better the resulting design will be.

The effect of surface roughness on fatigue life is well established in the scientific community, but the methodology presented here is not limited to surface defects. The fatigue strength scaling can be based on experimental data, or other models incorporating e.g. preferred crystallographic orientation, microstructure alignment, internal defects, or combinations of these. The next paper demonstrates that other defects than measured surface roughness will influence the fatigue life of LB-PBF materials.

3.3. Paper 6 − Directional Fatigue Behaviour of Maraging Steel Grade 300 Produced by Laser Powder Bed Fusion

This paper concludes the section on anisotropy of dynamically loaded LB-PBF materials. The paper is the result of a collaboration between the Design, Analysis and Manufacturing (Solberg and Berto) and the Engineering Design & Production Technology (Hovig and Sørby) groups at the Department of Mechanical and Industrial Engineering at NTNU. The fatigue lifetime of LB-PBF 18Ni300 built at different orientations with as-built surface condition is investigated experimentally. This work presents experimental data which can be used to validate/improve the model presented in Paper 4. A detailed description of the material, processing conditions, and static tensile properties are available in Paper 3. My main contribution to this work is the design of experiment, specimen preparation, microstructure analysis, and manuscript preparation.

3.3.1. Introduction

By this point in the theses it is well documented that AM materials can have both internal and external defects, as well as anisotropic microstructures due to preferred crystallographic orientation and alignment of particles in the microstructure. Additionally, high tensile strength and hardness are often found to have high notch sensitivity in dynamic loading [66]. In AM, with as-built surface condition, Solberg and Berto demonstrates that fatigue usually initiates from surface defects [67]. When the surface is machined prior to fatigue loading, the fatigue initiates from internal defects [68]. Other post-processing treatments such as chemical etching and hot isostatic pressing can increase fatigue life [69–71]. Although the fatigue life can be improved by post-processing treatments, it is in many cases undesirable for AM applications. One of the major benefits of AM is the freedom of design, and if a surface requires machining post-AM the design is limited to the capabilities of the post-processing technique.

The fatigue life of LB-PBF/18Ni300 under uniaxial loading has been studied in the literature before, but limited to either horizontal or vertical build orientations [72–74]. Contradicting results are reported where Meneghetti et al. found that the fatigue life was higher in the horizontal orientation compared to the vertical orientation in 2017 [72], while in 2019 both Damon et al. [74] and Meneghetti et al. [73] reports higher fatigue life in the vertical build orientation. The difference is attributed to inherent strains in the vertical specimens causing deformations when the specimens were removed from the build plate – leading to bending stresses when clamped in the uniaxial fatigue test machine. The directional fatigue behaviour of AM materials is typically explained by either a stacking of internal defects, microstructure effects, or surface roughness effects. It is shown in Paper 1, Paper 3, and Paper 4 that these effects vary significantly with build orientation, and

that testing only a few orientations (0° and 90°) is insufficient to describe the anisotropic behaviour.

In this paper a novel fatigue test specimen is presented with one as-built surface. The specimens are built at 10 different orientations ranging from 0° to 135° with respect to the build plate. 3 specimens were built at each orientation. The as-built surface is either up-skin (surface facing upwards), or down-skin (surface facing downwards). The layout of the specimens is shown in Figure 43. The specimens were produced near-net shape and all surfaces except the indicated as-built surface were machined to the nominal geometry in the bottom right hand corner. The material was subjected to the direct ageing procedure described in Paper 3. The fatigue testing was performed with a load ratio of R = 0, and a frequency of 30 Hz on an MTS servo-hydraulic system with a 50 kN load cell. A single load level of 500 MPa was selected for all specimens, corresponding to approximately 10^5 cycles. In addition to fatigue testing the surface, fracture surface, and microstructures were characterised in an SEM. The microstructure analysis is discussed in more detail in Paper 3. The surface profiles were processed in python.
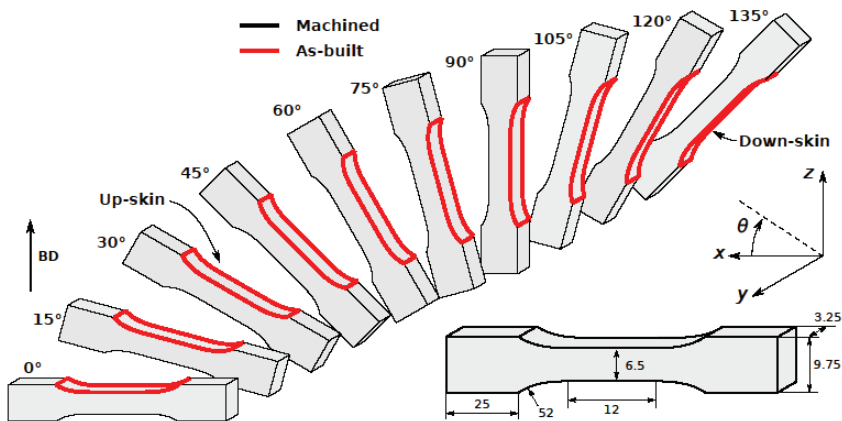
Figure 43 Specimen orientations and dimensions. BD indicates the build direction.

3.3.2. Results and discussion

The as-built surfaces are shown in Figure 44 for a selected specimen of each orientation. a) shows the side-view, b) the top-view, and c) a schematic representation of three different surface characteristics. For the 0° specimen the scan strategy is clearly visible in the top-view. For the 15° to 60° specimen the different build layers are visible, highlighting the staircase effect. Close to the vertical orientation a general roughness is seen which increases as the surface turns to downskin.

Three surface categories are identified and presented schematically in Figure 44 c):

    i.   Stair-case effect for orientations 0° - 45°.
    ii.   A general surface roughness for orientations 45° - 90°.
    iii.   Down-skin surface roughness for orientation > 90°.
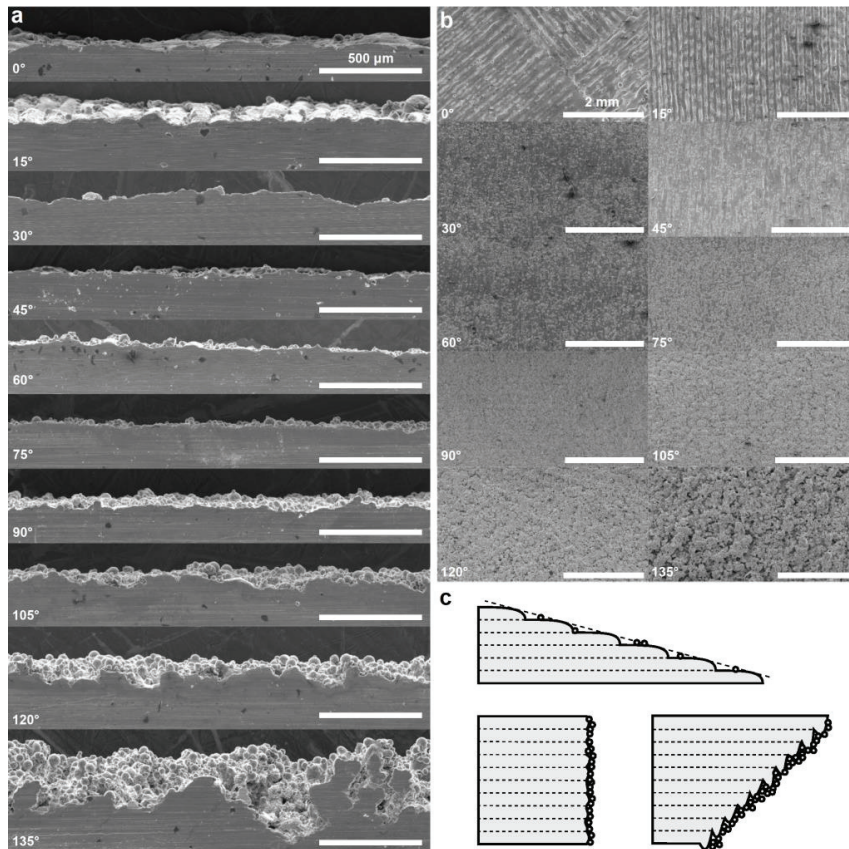
Figure 44 SEM of surface conditions of specimens a) machined cross section, b) as-built surface, c) schematic illustration.

The surface roughness parameters *Ra* and *Rz* were calculated from the profiles shown in Figure 44 and presented in Figure 45. For orientations between 0° and 90° both *Ra* and *Rz* are relatively homogeneous, before a steep increase in roughness as the surface turns to down-skin. The surface roughness for category (i) is dominated by the staircase effect and not equal in different directions (i.e. depends on the direction of the laser scanning). For case (ii) and (iii) the surface is uniform regardless of the direction of measurement. The main shift in surface roughness occurs when the specimens are tilted from vertical to down-skin. No sharp features

are observed in the surface profile in Figure 44 however. The up-skin surfaces display a waviness profile, especially visible in the 15° specimen. For the up-skin surfaces, the roughness manifests as notches defined along the thickness direction of the sample. On down-skin surfaces, the notches from the surface roughness are not constant along the thickness direction. This could explain why the 15° specimen has the lowest fatigue life, even though the roughness is much higher for the down-skin specimens.
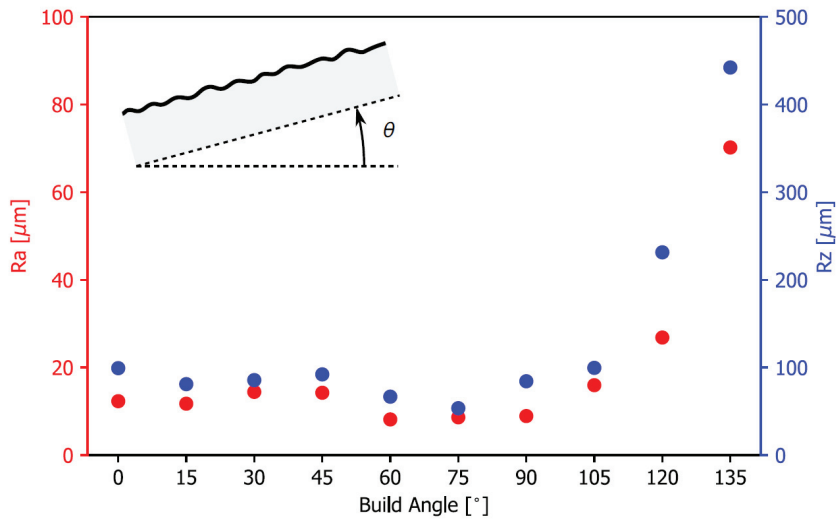
Figure 45 Surface roughness (Ra and Rz) as a function of build orientation.

The fatigue lifetime is shown in Figure 46, with tabulated values available in the appended Paper 6. The figure shows the number of cycles to failure for a nominal load level of 500 MPa, for each of the 10 orientations. It is immediately obvious that the fatigue life depends on the orientation of the specimen, and a clear trend is visible. The highest fatigue life is found for the 60° specimen. The down-skin specimens have a lower fatigue lifetime compared to the up-skin counterparts, e.g. 60° and 120°. Although comparing the 45° and 135° specimens, the fatigue life is in a similar range.

Figure 46 Fatigue data for different orientations.

The fatigue life is the lowest for the 15° specimen and increases as the build angle is increased to 60°. The fatigue life then decreases again as the specimens are tilted towards 90° and beyond in the down-skin category. When comparing the down-skin and up-skin specimens of similar orientation, $\theta' = \arcsin(\sin(\theta))$, the down-skin samples have consistently lower fatigue life. There is some overlap within the scatter for $\theta' = 75°$ and $\theta' = 45°$, however. There were geometrical deviations from the nominal dimensions, mainly due to the surface roughness. To account for this the applied load stress is re-calculated as $\sigma' = F/t(w - Rz)$, where t is the specimen thickness, w is the specimen width, and Rz is the maximum height of the surface profile. After the correction, the nominal stress increases slightly for the values between 0° and 105° and decreases for the 120° and 135° specimens. It is noted that not only the surface roughness, but also the dimensional tolerances, depends on the build orientation.

The fatigue data presented in Figure 46 assumes the load level to be constant. Since this is not the case, a correction is made based on the deviation from an assumed fatigue life curve. Fatigue data from this study is superimposed on Basquin curves from literature data in Figure 47 a). The slope, B, is taken from the 90° data in Meneghetti et al. [73]. In addition to the trend lines an assumed fatigue life curve for the current data is created. The assumed trend line is given a vertical shift, A, such that it intersects the mean value of the maximum and minimum number of cycles for tests performed at close to 500 MPa. The deviation from the assumed fatigue life is then given by $n\_i = \log\_10(N\_i) - \log\_10\big((\sigma\_i/A)^{1/B}\big)$. The

deviation from the regression line is then normalised by the maximum value, n_max, and shown in Figure 47 b). This comparison confirms that the fatigue life is lower for the down-skin region compared to the up-skin region.
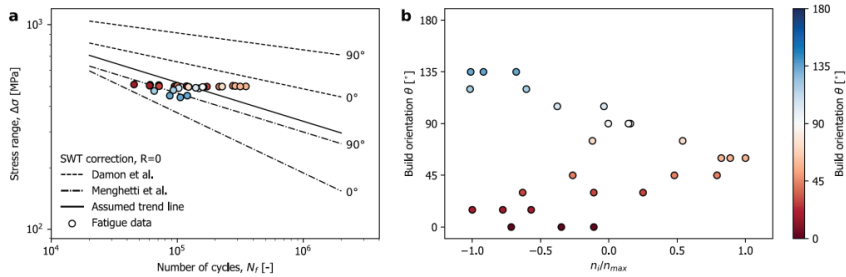

Figure 47 a) Comparison of the fatigue data presented in this study and regression lines of the fatigue data of LB-PBF/18Ni300 by Damon et al.[74] and Meneghetti et al.[73] b) Corrected fatigue data from this study.

The fracture surfaces analysed by SEM are shown in Figure 48. All specimens investigated had fatigue initiating from a defect, follow by crack propagation and a final rupture zone. Not all the specimens failed in the as-built surface. The different fracture modes are shown in Figure 48. In a) and b) a 0° specimen is shown. The fatigue initiation is from the centre of the as-built surface. The crack initiates in a defect that is approximately 70 µm deep. In c) and d) a 135° specimen is shown. This specimen also failed from the as-built surface, but from a corner rather than the centre. e) and f) shows a 60° specimen where fatigue initiated from an internal defect close to the machined surface. This is the orientation which had the highest fatigue life.
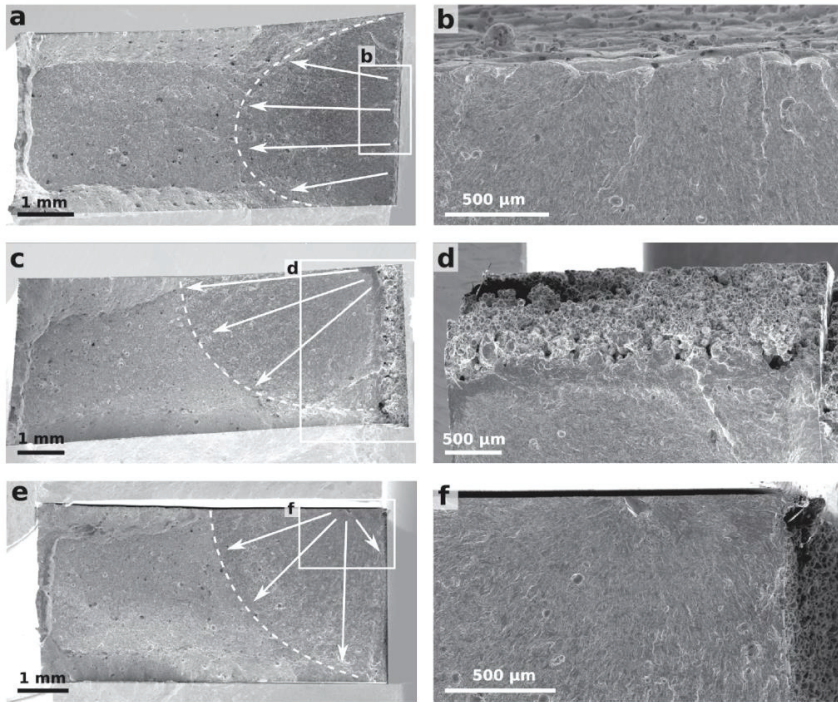
Figure 48 Fracture surfaces of three different fatigue initiations: (a and b) 0°, fatigue initiation from the centre of the AB surface, (c and d) 135°, fatigue initiation from the corner of the AB surface and (e and f), 60° fatigue initiation from internal defect.

3.3.3. Concluding remarks

This paper showcases a new fatigue specimen with an as-built surface for testing the influence of process-induced surface roughness on the fatigue life of LB-PBF materials. A clear trend is observed, where the orientation of the surface directly influences the fatigue life of 18Ni300. The fatigue life is found to be higher for specimens built close to the vertical orientation, with 60° orientation having the highest fatigue life. Specimens with as-built down-skin surfaces have a lower fatigue life compared to specimens with as-built up-skin surfaces. All the specimens, with the exception of the 60° orientation, failed from the as-built surface, supporting the assumptions made in Paper 4, and Paper 5. In a future work, the experimental data from this study can be incorporated in the methodology presented in Paper 5 for more accurate fatigue life prediction of complex geometries and build orientation optimisation for said geometries.

4. Applications and future work

4.1. Applications

The contributions and findings in this PhD can be used as tools for designers and engineers designing for manufacturing with LB-PBF. The methods proposed can be used for developing new AM materials, or for existing materials where there is a need for a deeper understanding.

The elastic constants provided in Paper 1 can be used directly in finite element method analysis. To maximise the potential of AM, topology optimisation algorithms can be used with anisotropic material models for minimum compliance problems. It should be noted however, that popular algorithms such as element density algorithms struggle with anisotropic models. Other algorithms such as the SIMP method developed by Bendsøe and Sigmund [75] may be better suited for anisotropic problems. Common practice today assumes the material isotropic, and elastic constants from the least stiff direction must be used. In the case of as-built Inconel 718 (Paper 1), this means a reduction of elastic modulus by 50%, leading to a significantly over dimensioned solution.

Commercially available software, such as Autodesk Fusion 360 with the generative design module, incorporates selected constrains for shape optimisation algorithms intended for additive manufacturing. The methodology developed in Paper 5 can be included in such problems to not only optimise for static properties, but also for fatigue life, or surface quality in general.

4.2. Future work

When working on problems on the same topic for several years you tend to find more questions than answers. In this section the most apparent future work will be mentioned.

In Paper 3 the transverse strain ratio was analysed, which revealed anisotropic straining in both the elastic and plastic part of the flow curve. This analysis could be done on the DIC strain fields for AlSi10Mg from Paper 2. There was no evidence of anisotropy in the tensile test results from AlSi10Mg when processed at elevated temperature, but as demonstrated in Paper 3 there can be anisotropic straining due to uneven alignment of melt pool boundaries. The same analysis can also be performed on the strain fields for Inconel 718 in Paper 1. In the latter case, the preferred crystallographic orientation is dominant, and in the elastic part of the flow curve, melt pool boundary effects are assumed to be minimal.

The experimental fatigue data in Paper 6 compliments the methodology developed in Paper 4 and 5. A natural extension of the work in Paper 6 is to validate the method for fatigue life prediction using stress concentration factors from surface

roughness profile data. Furthermore, the implementation of that method in Fatlab can be validated. The experimental result itself can also be used to define the anisotropy in Fatlab. This is a rather trivial task, and well documented in the Fatlab toolbox.

Additive manufacturing is growing rapidly, and new materials are regularly brought to the market. New materials require characterisation and understanding, and the contributions in this thesis can be extended to new alloy systems. AM is often used in applications where a significant value is added by reducing the weight, and to minimise this parameter, reliable material data is required. Material characterisation is time consuming and expensive, and the methods proposed here can be further refined to reduce the number of required test coupons, while still providing a statistically significant result. This is especially important when machine-to-machine repeatability is low, and material data from one specific machine may not be valid for a different machine.

5. References

[1]   B. Hutchinson, Critical assessment 16: Anisotropy in metals, Mater. Sci. Technol. (United Kingdom). (2015). https://doi.org/10.1179/1743284715Y.0000000118.

[2]   V. Brøtan, O.Å. Berg, K. Sørby, Additive Manufacturing for Enhanced Performance of Molds, Procedia CIRP. 54 (2016) 186–190. https://doi.org/http://dx.doi.org/10.1016/j.procir.2016.05.074.

[3]   E.W. Hovig, V. Brøtan, K. Sørby, H. Even Wilberg, B. Vegard, S. Knut, E.W. Hovig, V. Brøtan, K. Sørby, Additive Manufacturing for Enhanced Cooling in Moulds for Casting, Proc. 6th Int. Work. Adv. Manuf. Autom. (2016). https://doi.org/https://doi.org/10.2991/iwama-16.2016.11.

[4]   I. (Metal AM), Boeing 777X takes flight with reported 300 additively manufactured parts in each GE9X engine, (2020). https://www.metal-am.com/boeing-777x-takes-flight-with-reported-300-additively-manufactured-parts-in-each-ge9x-engine/ (accessed October 2, 2020).

[5]   D.-G. Ahn, Applications of laser assisted metal rapid tooling process to manufacture of molding & forming tools — state of the art, Int. J. Precis. Eng. Manuf. 12 (2011) 925–938. https://doi.org/10.1007/s12541-011-0125-5.

[6]   B. Mooney, K.I. Kourousis, R. Raghavendra, Plastic anisotropy of additively manufactured maraging steel: Influence of the build orientation and heat treatments, Addit. Manuf. 25 (2019) 19–31. https://doi.org/10.1016/j.addma.2018.10.032.

[7]   E. Hovig, A. Azar, F. Grytten, K. Sørby, Determination of Anisotropic Mechanical Properties for Materials Processed by Laser Powder Bed Fusion, Adv. Mater. Sci. Eng. 2018 (2018). https://doi.org/10.1155/2018/7650303.

[8]   E. Chlebus, K. Gruber, B. Kuznicka, J. Kurzac, T. Kurzynowski, Effect of heat treatment on the microstructure and mechanical properties of Inconel 718 processed by selective laser melting, Mater. Sci. Eng. A. 639 (2015) 647–655. https://doi.org/10.1016/j.msea.2015.05.035.

[9]   S. Mishra, K. Kulkarni, N.P. Gurao, Effect of crystallographic texture on precipitation induced anisotropy in an aluminium magnesium silicon alloy, Mater. Des. 87 (2015) 507–519. https://doi.org/10.1016/j.matdes.2015.08.008.

[10]   E. Brandl, U. Heckenberger, V. Holzinger, D. Buchbinder, Additive manufactured AlSi10Mg samples using Selective Laser Melting (SLM): Microstructure, high cycle fatigue, and fracture behavior, Mater. Des. 34

(2012) 159–169. https://doi.org/10.1016/j.matdes.2011.07.067.

[11]   P.A. Hooper, Melt pool temperature and cooling rates in laser powder bed fusion, Addit. Manuf. 22 (2018) 548–559. https://doi.org/10.1016/j.addma.2018.05.032.

[12]   E.A. Jägle, Z. Sheng, P. Kürnsteiner, S. Ocylok, A. Weisheit, D. Raabe, G. Requena, Comparison of Maraging Steel Micro- and Nanostructure Produced Conventionally and by Laser Additive Manufacturing, Materials (Basel). 10 (2016). https://doi.org/10.3390/ma10010008.

[13]   L. Thijs, J. Van Humbeeck, K. Kempen, E. Yasa, J.-P. Kruth, M. Rombouts, Investigation on the inclusions in maraging steel produced by selective laser melting, Innov. Dev. Virtual Phys. Prototyp. (2012) 297–304.

[14]   E.W. Hovig, A.S. Azar, M. Mhamdi, K. Sørby, Mechanical Properties of AlSi10Mg Processed by Laser Powder Bed Fusion at Elevated Temperature, in: TMS 2020 149th Annu. Meet. Exhib. Suppl. Proc., Springer International Publishing, Cham, 2020: pp. 395–404.

[15]   M. Tang, P.C. Pistorius, J.L. Beuth, Prediction of lack-of-fusion porosity for powder bed fusion, Addit. Manuf. 14 (2017) 39–48. https://doi.org/https://doi.org/10.1016/j.addma.2016.12.001.

[16]   M. Bayat, A. Thanki, S. Mohanty, A. Witvrouw, S. Yang, J. Thorborg, N.S. Tiedje, J.H. Hattel, Keyhole-induced porosities in Laser-based Powder Bed Fusion (L-PBF) of Ti6Al4V: High-fidelity modelling and experimental validation, Addit. Manuf. 30 (2019) 100835. https://doi.org/10.1016/j.addma.2019.100835.

[17]   Z.H. Xiong, S.L. Liu, S.F. Li, Y. Shi, Y.F. Yang, R.D.K. Misra, Role of melt pool boundary condition in determining the mechanical properties of selective laser melting AlSi10Mg alloy, Mater. Sci. Eng. A. 740–741 (2019) 148–156. https://doi.org/10.1016/j.msea.2018.10.083.

[18]   T.A. Wilson, Solid Mechanics, 2011. https://doi.org/10.1002/cphy.cp030303.

[19]   F. Grytten, H. Daiyan, M. Polanco-Loria, S. Dumoulin, Use of digital image correlation to measure large-strain tensile properties of ductile thermoplastics, Polym. Test. 28 (2009) 653–660. https://doi.org/10.1016/j.polymertesting.2009.05.009.

[20]   E. V. Morozov, V. V. Vasiliev, Determination of the shear modulus of orthotropic materials from off-axis tension tests, Compos. Struct. 62 (2003) 379–382. https://doi.org/10.1016/j.compstruct.2003.09.008.

[21]   T.C.T. Ting, Anisotropic Elasticity : Theory and Applications, Oxford University Press, New York, 1996.

[22] J.C. Lippold, S.D. Kiser, J.N. DuPont, Welding Metallurgy and Weldability of Nickel-Base Alloys, John Wiley and Sons, Hoboken, NJ, USA, 2011.

[23] S. Singh Handa, J. Andersson, M. Eynian, Precipitation of Carbides in a Ni-based Superalloy, Utskiljning Av Karbider i En Nickelbaserade Superlegering. (2014).

[24] N. Saunders, Z. Guo, A.P. Miodownik, J. Schillé, MODELLING THE MATERIAL PROPERTIES AND BEHAVIOUR OF NI- AND NIFE-BASED SUPERALLOYS, Superalloys. (2005) 571–580.

[25] J. Jung, J.I. Yoon, J.G. Kim, M.I. Latypov, J.Y. Kim, H.S. Kim, Continuum understanding of twin formation near grain boundaries of FCC metals with low stacking fault energy, Npj Comput. Mater. 3 (2017) 1–9. https://doi.org/10.1038/s41524-017-0023-1.

[26] K.M. Knowles, P.R. Howie, The Directional Dependence of Elastic Stiffness and Compliance Shear Coefficients and Shear Moduli in Cubic Materials, J. Elast. 120 (n.d.) 87–108. https://doi.org/10.1007/s10659-014-9506-1.

[27] E.W. Hovig, H.D. Holm, K. Sørby, Effect of processing parameters on the relative density of alsi10mg processed by laser powder bed fusion, 2019. https://doi.org/10.1007/978-981-13-2375-1_34.

[28] S. Siddique, M. Imran, E. Wycisk, C. Emmelmann, F. Walther, Influence of process-induced microstructure and imperfections on mechanical properties of AlSi12 processed by selective laser melting, J. Mater. Process. Technol. 221 (2015) 205–213. https://doi.org/https://doi.org/10.1016/j.jmatprotec.2015.02.023.

[29] S. Romano, A. Brückner-Foit, A. Brandão, J. Gumpinger, T. Ghidini, S. Beretta, Fatigue properties of AlSi10Mg obtained by additive manufacturing: Defect-based modelling and prediction of fatigue strength, Eng. Fract. Mech. 187 (2018) 165–189. https://doi.org/10.1016/j.engfracmech.2017.11.002.

[30] F. Trevisan, F. Calignano, M. Lorusso, J. Pakkanen, A. Aversa, E. Ambrosio, M. Lombardi, P. Fino, D. Manfredi, On the Selective Laser Melting (SLM) of the AlSi10Mg Alloy: Process, Microstructure, and Mechanical Properties, Materials (Basel). 10 (2017) 76. https://doi.org/10.3390/ma10010076.

[31] S. Bagherifard, N. Beretta, S. Monti, M. Riccio, M. Bandini, M. Guagliano, On the fatigue strength enhancement of additive manufactured AlSi10Mg parts by mechanical and thermal post-processing, Mater. Des. 145 (2018) 28–41. https://doi.org/10.1016/j.matdes.2018.02.055.

[32] M. Tang, P.C. Pistorius, Anisotropic Mechanical Behavior of AlSi10Mg Parts Produced by Selective Laser Melting, JOM. 69 (2017) 516–522.

https://doi.org/10.1007/s11837-016-2230-5.

[33]   L. Hitzler, C. Janousch, J. Schanz, M. Merkel, B. Heine, F. Mack, W. Hall, A. Öchsner, Direction and location dependency of selective laser melted AlSi10Mg specimens, J. Mater. Process. Technol. 243 (2017) 48–61. https://doi.org/10.1016/j.jmatprotec.2016.11.029.

[34]   P. Yang, M.A. Rodriguez, L. Deibler, B. Jared, J. Griego, A. Kilgo, A. Allen, D. Stefan, Effect of thermal annealing on microstructure evolution and mechanical behavior of an additive manufactured AlSi10Mg part, J. Mater. Res. 33 (2018) 1701–1712. https://doi.org/10.1557/jmr.2018.82.

[35]   N.E. Uzan, R. Shneck, O. Yeheskel, N. Frage, Fatigue of AlSi10Mg specimens fabricated by additive manufacturing selective laser melting (AM-SLM), Mater. Sci. Eng. A. 704 (2017) 229–237. https://doi.org/10.1016/j.msea.2017.08.027.

[36]   C. Turk, H. Zunko, C. Aumayr, H. Leitner, M. Kapp, Advances in Maraging Steels for Additive Manufacturing, BHM Berg- Und Hüttenmännische Monatshefte. 164 (2019) 112–116. https://doi.org/10.1007/s00501-019-0835-z.

[37]   A. Fortunato, A. Lulaj, S. Melkote, E. Liverani, A. Ascari, D. Umbrello, Milling of maraging steel components produced by selective laser melting, Int. J. Adv. Manuf. Technol. 94 (n.d.) 1895–1902. https://doi.org/10.1007/s00170-017-0922-9.

[38]   J.D. Roehling, W.L. Smith, T.T. Roehling, B. Vrancken, G.M. Guss, J.T. McKeown, M.R. Hill, M.J. Matthews, Reducing residual stress by selective large-area diode surface heating during laser powder bed fusion additive manufacturing, Addit. Manuf. (2019). https://doi.org/https://doi.org/10.1016/j.addma.2019.05.009.

[39]   T.H. Becker, D. Dimitrov, R.I. Campbell, R.I. Campbell, The achievable mechanical properties of SLM produced Maraging Steel 300 components, Rapid Prototyp. J. 22 (2016). internal-pdf://0861539755/Becker-Rapid.Prototype.J-2016.pdf.

[40]   J. Suryawanshi, K.G. Prashanth, U. Ramamurty, Tensile, fracture, and fatigue crack growth properties of a 3D printed maraging steel through selective laser melting, J. Alloys Compd. 725 (2017) 355–364. https://doi.org/10.1016/j.jallcom.2017.07.177.

[41]   C. Tan, K. Zhou, M. Kuang, W. Ma, T. Kuang, Microstructural characterization and properties of selective laser melted maraging steel with different build directions, Sci. Technol. Adv. Mater. 19 (2018) 746–758. https://doi.org/10.1080/14686996.2018.1527645.

[42]   C. Elangeswaran, K. Gurung, R. Koch, A. Cutolo, B. Van Hooreweder, Post-treatment selection for tailored fatigue performance of 18Ni300 maraging steel manufactured by laser powder bed fusion, Fatigue Fract. Eng. Mater. Struct. 43 (2020) 2359–2375. https://doi.org/https://doi.org/10.1111/ffe.13304.

[43]   W. Wu, X. Wang, Q. Wang, J. Liu, Y. Zhang, T. Hua, P. Jiang, Microstructure and mechanical properties of maraging 18Ni-300 steel obtained by powder bed based selective laser melting process, Rapid Prototyp. Journal. 26 (2020) 1379–1387. https://doi.org/10.1108/RPJ-08-2018-0189.

[44]   J. Vishwakarma, K. Chattopadhyay, N.C. Santhi Srinivas, Effect of build orientation on microstructure and tensile behaviour of selectively laser melted M300 maraging steel, Mater. Sci. Eng. A. 798 (2020) 140130. https://doi.org/https://doi.org/10.1016/j.msea.2020.140130.

[45]   A.R. Oliveira, J.A.A. Diaz, A.D.C. Nizes, A.L. Jardini, E.G. Del Conte, Investigation of Building Orientation and Aging on Strength–Stiffness Performance of Additively Manufactured Maraging Steel, J. Mater. Eng. Perform. 30 (2021) 1479–1489. https://doi.org/10.1007/s11665-020-05414-4.

[46]   B. Mooney, K.I. Kourousis, R. Raghavendra, D. Agius, Process phenomena influencing the tensile and anisotropic characteristics of additively manufactured maraging steel, Mater. Sci. Eng. A. 745 (2019) 115–125. https://doi.org/10.1016/j.msea.2018.12.070.

[47]   Battelle Memorial Institute, Metallic Materials Properties Development and Standardization (MMPDS-11), Battelle Memorial Institute, 2016.

[48]   W.T. Lankford, S.C. Snyder, J.A. Bauscher, New criteria for predicting the press performance of deep drawing sheets, in: Thrity-First Annu. Conv. Soc., 1949.

[49]   G. Kurdjumow, G. Sachs, Über den Mechanismus der Stahlhärtung, Zeitschrift Für Phys. (1930). https://doi.org/10.1007/BF01397346.

[50]   M.D. Sangid, The physics of fatigue crack initiation, Int. J. Fatigue. 57 (2013) 58–72. https://doi.org/https://doi.org/10.1016/j.ijfatigue.2012.10.009.

[51]   J.M. Barsom, R.C. McNicol, Effect of Stress Concentration on Fatigue-Crack Initiation in HY-130 Steel, in: P.C. Paris, G.R. Irwin (Eds.), Fract. Toughness Slow-Stable Crack., ASTM International, West Conshohocken, PA, 1974: pp. 183–204. https://doi.org/10.1520/STP38600S.

[52]   A.S. Azar, L.-E. Svensson, B. Nyhus, Effect of crystal orientation and texture on fatigue crack evolution in high strength steel welds, Int. J. Fatigue. 77

(2015) 95–104.
https://doi.org/https://doi.org/10.1016/j.ijfatigue.2015.03.008.

[53]   M.D. Sangid, H.J. Maier, H. Sehitoglu, The role of grain boundaries on
        fatigue crack initiation – An energy approach, Int. J. Plast. 27 (2011) 801–
        821. https://doi.org/https://doi.org/10.1016/j.ijplas.2010.09.009.

[54]   Y. Guilhem, S. Basseville, F. Curtit, J.-M. Stéphan, G. Cailletaud,
        Investigation of the effect of grain clusters on fatigue crack initiation in
        polycrystals, Int. J. Fatigue. 32 (2010) 1748–1763.
        https://doi.org/https://doi.org/10.1016/j.ijfatigue.2010.04.003.

[55]   Y. Murakami, Metal fatigue: effects of small defects and nonmetallic
        inclusions, Academic Press, 2019.

[56]   D. Arola, C.L. Williams, Estimating the fatigue stress concentration factor of
        machined surfaces, Int. J. Fatigue. 24 (2002) 923–930.
        https://doi.org/10.1016/S0142-1123(02)00012-9.

[57]   W.D. Pilkey, D.F. Pilkey, Peterson's stress concentration factors, 3rd ed.,
        John Wiley, Hoboken, NJ, USA, 2008. internal-
        pdf://103.150.28.183/Petersons_Stress_Concentration.pdf.

[58]   S. Romano, L. Patriarca, S. Foletti, S. Beretta, LCF behaviour and a
        comprehensive life prediction model for AlSi10Mg obtained by SLM, Int. J.
        Fatigue. 117 (2018) 47–62. https://doi.org/10.1016/j.ijfatigue.2018.07.030.

[59]   A. Yadollahi, M.J. Mahtabi, A. Khalili, H.R. Doude, J.C. Newman, Fatigue life
        prediction of additively manufactured material: Effects of surface
        roughness, defect size, and shape, Fatigue Fract. Eng. Mater. Struct. 41
        (2018) 1602–1614. https://doi.org/10.1111/ffe.12799.

[60]   Y. Yamashita, T. Murakami, R. Mihara, M. Okada, Y. Murakami, Defect
        analysis and fatigue design basis for Ni-based superalloy 718 manufactured
        by selective laser melting, Int. J. Fatigue. 117 (2018) 485–495.
        https://doi.org/10.1016/j.ijfatigue.2018.08.002.

[61]   Z. Zhou, H. Xu, C. Li, G. Chen, The effect of texture on the low cycle fatigue
        property of Inconel 718 by selective laser melting, MATEC Web Conf. 165
        (2018). https://doi.org/10.1051/matecconf/201816502007.

[62]   E. Beevers, A.D. BrandãO, J. Gumpinger, M. Gschweitl, C. Seyfert, P.
        Hofbauer, T. Rohr, T. Ghidini, Fatigue properties and material
        characteristics of additively manufactured AlSi10Mg – Effect of the contour
        parameter on the microstructure, density, residual stress, roughness and
        mechanical properties, Int. J. Fatigue. 117 (2018) 148–162.
        https://doi.org/10.1016/j.ijfatigue.2018.08.023.

[63]   P.F. Kelley, A. Saigal, J.K. Vlahakis, A. Carter, Tensile and Fatigue Behavior

of Direct Metal Laser Sintered (DMLS) Inconel 718, in: ASME 2015 Int. Mech. Eng. Congr. Expo., American Society of Mechanical Engineers, Houston, Texas, USA, 2015. internal-pdf://5.168.32.231/kelley2015.pdf.

[64]   R. Konečná, G. Nicoletto, L. Kunz, A. Bača, Microstructure and directional fatigue behavior of Inconel 718 produced by selective laser melting, in: 21st Eur. Conf. Fract. ECF21, Catania, Italy, 2016: pp. 2381–2388. internal-pdf://247.63.161.122/1-s2.0-S2452321616303092-main.pdf.

[65]   A.R. Balachandramurthi, J. Moverare, N. Dixit, R. Pederson, Influence of defects and as-built surface roughness on fatigue properties of additively manufactured Alloy 718, Mater. Sci. Eng. A. 735 (2018) 463–474. https://doi.org/10.1016/j.msea.2018.08.072.

[66]   S.A. McKelvey, A. Fatemi, Surface finish effect on fatigue behavior of forged steel, Int. J. Fatigue. 36 (2012) 130–145. https://doi.org/https://doi.org/10.1016/j.ijfatigue.2011.08.008.

[67]   K. Solberg, F. Berto, Notch-defect interaction in additively manufactured Inconel 718, Int. J. Fatigue. 122 (2019) 35–45. https://doi.org/https://doi.org/10.1016/j.ijfatigue.2018.12.021.

[68]   N. Sanaei, A. Fatemi, Analysis of the effect of internal defects on fatigue performance of additive manufactured metals, Mater. Sci. Eng. A. 785 (2020) 139385. https://doi.org/https://doi.org/10.1016/j.msea.2020.139385.

[69]   P. Jamshidi, M. Aristizabal, W. Kong, V. Villapun, Selective Laser Melting of Ti-6Al-4V : The Impact of Post-processing on the Tensile , Fatigue and Biological, (n.d.).

[70]   R. Molaei, A. Fatemi, N. Phan, Significance of hot isostatic pressing (HIP) on multiaxial deformation and fatigue behaviors of additive manufactured Ti-6Al-4V including build orientation and surface roughness effects, Int. J. Fatigue. 117 (2018) 352–370. https://doi.org/https://doi.org/10.1016/j.ijfatigue.2018.07.035.

[71]   S. Tammas-Williams, P.J. Withers, I. Todd, P.B. Prangnell, The Effectiveness of Hot Isostatic Pressing for Closing Porosity in Titanium Parts Manufactured by Selective Electron Beam Melting, Metall. Mater. Trans. A Phys. Metall. Mater. Sci. 47 (2016) 1939–1946. https://doi.org/10.1007/s11661-016-3429-3.

[72]   G. Meneghetti, D. Rigon, D. Cozzi, W. Waldhauser, M. Dabalà, Influence of build orientation on static and axial fatigue properties of maraging steel specimens produced by additive manufacturing, Procedia Struct. Integr. 7 (2017) 149–157. https://doi.org/10.1016/j.prostr.2017.11.072.

[73]   G. Meneghetti, D. Rigon, C. Gennari, An analysis of defects influence on axial fatigue strength of maraging steel specimens produced by additive manufacturing, Int. J. Fatigue. 118 (2019) 54–64. https://doi.org/https://doi.org/10.1016/j.ijfatigue.2018.08.034.

[74]   J. Damon, T. Hanemann, S. Dietrich, G. Graf, K.-H. Lang, V. Schulze, Orientation dependent fatigue performance and mechanisms of selective laser melted maraging steel X3NiCoMoTi18-9-5, Int. J. Fatigue. 127 (2019) 395–402. https://doi.org/https://doi.org/10.1016/j.ijfatigue.2019.06.025.

[75]   M.P. Bendsoe, O. Sigmund, Topology Optimization: Theory, Methods, and Applications, Second Edi, Berlin, Heidelberg: Springer Berlin / Heidelberg, Berlin, Heidelberg, 2003. https://doi.org/10.1007/978-3-662-05086-6.

6. Appended full text articles

6.1. Paper 1 - Determination of Anisotropic Mechanical Properties for Materials Processed by Laser Powder Bed Fusion

Research Article

Determination of Anisotropic Mechanical Properties for Materials Processed by Laser Powder Bed Fusion

Even W. Hovig [iD],[1] **Amin S. Azar** [iD],[2] **Frode Grytten** [iD],[2] **Knut Sørby** [iD],[1]
and Erik Andreassen [iD][2]

[1]*Norwegian University of Science and Technology (NTNU), Department of Production and Quality Engineering,*
Trondheim, Norway
[2]*SINTEF Industry, Oslo, Norway*

Correspondence should be addressed to Even W. Hovig; even.w.hovig@ntnu.no

Improving the success rate in additive manufacturing and designing highly optimized structures require proper understanding of material behaviour. This study proposes a novel experimental method by which anisotropic mechanical properties of additively manufactured materials can be assessed. The procedure is based on tensile testing of flat specimens, manufactured by laser powder bed fusion (LPBF) at different orientations relative to the build plate. In this study, the procedure was applied to the Inconel 718 alloy. Three identical specimen sets were built, each of which received complementary postprocessing treatments. The tensile tests were carried out on specimens with as-built surface finish. Digital image correlation was used to record the strain field evolution on two perpendicular surfaces of the tensile specimens under loading. An optimization algorithm is also proposed for determining the anisotropic elastic constants using only a few tensile test results. It was observed that both build orientation and postprocessing have strong influence on the anisotropic mechanical properties of the material. The effect of microstructure was also investigated and characterised. Consequently, three transversely isotropic compliance matrices were constructed, representing the effect of the different processing conditions.

1. Introduction

Most of the commercial additive manufacturing (AM) technologies can produce materials with relatively high density and decent mechanical properties, close to that of classical processing methods. Capability of manufacturing complex geometries by AM brought about new opportunities such as "topology optimization" and "design for additive manufacturing (DfAM)" and caused commencement of a new chapter in performance-oriented design of components. Several challenges, such as anisotropic behaviour [1–6] and effects of postprocessing steps [7–10], need to be addressed in the design phase to release the full potential of AM. Despite these facts, most of the current algorithms for generative design use isotropic material models or globally uniform and defect-free properties [11–13]. Thus, we propose a methodology for calibrating anisotropic constitutive material models based on systematic mechanical tests and as-built surface conditions. Inconel 718 (IN718) processed by laser powder bed fusion (LPBF) are the material and process of choice in this study.

1.1. Determination of Elastic Constants—Transversely Isotropic Elastic Materials. Anisotropic elasticity can be modelled using the generalized Hooke's law. If the material is assumed to be transversely isotropic, that is, isotropic in the XY plane, Hooke's law can be expressed as [14]

$$\begin{bmatrix} \varepsilon_{xx} \\ \varepsilon_{yy} \\ \varepsilon_{zz} \\ \varepsilon_{yz} \\ \varepsilon_{xz} \\ \varepsilon_{xy} \end{bmatrix} = \begin{bmatrix} \dfrac{1}{E_{xx}} & -\dfrac{\nu_{xy}}{E_{xx}} & -\dfrac{\nu_{zx}}{E_{zz}} & 0 & 0 & 0 \\[2mm] -\dfrac{\nu_{xy}}{E_{xx}} & \dfrac{1}{E_{xx}} & -\dfrac{\nu_{zx}}{E_{zz}} & 0 & 0 & 0 \\[2mm] -\dfrac{\nu_{xz}}{E_{xx}} & -\dfrac{\nu_{xz}}{E_{xx}} & \dfrac{1}{E_{zz}} & 0 & 0 & 0 \\[2mm] 0 & 0 & 0 & \dfrac{1}{2G_{xz}} & 0 & 0 \\[2mm] 0 & 0 & 0 & 0 & \dfrac{1}{2G_{xz}} & 0 \\[2mm] 0 & 0 & 0 & 0 & 0 & \dfrac{1}{2G_{xy}} \end{bmatrix} \begin{bmatrix} \sigma_{xx} \\ \sigma_{yy} \\ \sigma_{zz} \\ \sigma_{yz} \\ \sigma_{xz} \\ \sigma_{xy} \end{bmatrix}. \tag{1}$$

The E_{xx} and E_{zz} moduli can be found using standard tensile tests. The shear modulus in the plane of isotropy can be expressed as [14]

$$G_{xy} = \frac{E_{xx}}{2(1 + \nu_{xy})}. \tag{2}$$

G_{xz} can be calculated using an off-axis tension test to determine E_ϕ on a sample built in the XZ plane with a rotation of $\phi = 45°$ about the Y-axis. This E_ϕ, assuming negligible shear strain, can then be used to calculate G_{xz}, using the following equation [15]:

$$G_{12} = \frac{\sin^2 \phi \cos^2 \phi}{(1/E_\phi) - (\cos^4 \phi/E_1) - (\sin^4 \phi/E_2) + ((\nu_{21}/E_1) + (\nu_{12}/E_2))\sin^2 \phi \cos^2 \phi}, \tag{3}$$

where the principal directions 1 and 2 correspond to Y and Z, respectively, and E_ϕ is the measured elastic modulus in the off-axis tension test. Note that E_ϕ can only be determined using the off-axis tension test if the following inequality is satisfied [15]:

$$G_{12} \geq \frac{E_1}{2(1 + \nu_{21})}. \tag{4}$$

Another approach to determine the elastic constants is to implement the problem as an optimization problem by minimizing a function of several variables and constraints. A proposed solution for this is presented in Section 2.4.

1.2. Inconel 718. IN718 was developed in an effort to improve weldability and strain-aged cracking resistance. It is a hardenable alloy of Ni-Fe-Cr, which takes advantage of Ni$_3$[Al,Ti] (γ' phase, fcc) and Ni$_3$Nb (γ'' phase, bct) precipitates to increase the resistance to cracking because of slow formation kinetics of these constituents. This alloy is known to have excellent corrosion and fatigue properties at service temperatures up to 760°C [16]. Typical IN718 compositions for wrought and powder material are given in Table 1.

The precipitates are mostly coherent with the austenite matrix that increases the mechanical strength of the material by co-straining with the matrix under different loading conditions. However, some precipitates can adversely affect the performance of these alloys, especially when they are exposed to high temperatures for a relatively long period of time [18]. Figure 1 shows the calculated and experimentally determined TTT diagrams for IN718 that will be used to determine the heat treatment cycle later in this work. The formation kinetics and thermodynamics of

γ' and γ'' precipitates are analogous in these diagrams; γ' forms at a slightly higher temperature range, which is indicative of the importance of accurate temperature control in the ageing process. Despite that both the calculated and experimentally determined TTT curves are addressing the nominal IN718 material, slight variation in the chemical composition may result in discrepancy between the two approaches when exact formation kinetics of the γ' and γ'' are being investigated. In addition to solid solution strengthening, the strength can be obtained through formation of γ'' phase in this alloy. The γ' phase is brittle, and its formation is less preferred to increase the high and low temperature ductility. Other brittle phases such as δ may also form upon long exposure to elevated temperatures. Therefore, the service temperature of this alloy is limited by the formation of δ and σ phases.

1.3. Additive Manufacturing of Inconel 718. In laser powder bed fusion (LPBF), the starting point is a packed bed of powder material—usually prealloyed—that is fused locally using an adjustable laser heat source. Today's advanced machines spread the powder in layer thicknesses ranging from 30 to 200 μm [21, 22]. Selection of layer thickness is a trade-off between build rate and part quality, and the chosen layer thickness is a breakeven point for achieving the best built rate with satisfactory quality [23, 24].

There are several features that can cause anisotropy in AM materials. Porosity and pore shape [25], microstructure and texture [26–29], and surface finish [30, 31] of the AM material are among the most referred reasons for anisotropic behaviour. Previous studies have captured the anisotropic properties of various heat treatments of laser powder bed

TABLE 1: Chemical composition of a commercial wrought solution-treated IN718 [17] and the commercial IN718 powder used in this study (specifications from the supplier).

Element	Ni	Cr	Fe	Al	Mo	Nb (+Ta)	Ti
wt.%, commercial wrought	53	19	18.5	0.5	3.0	5.1	0.9
wt.%, commercial powder	50–55	17–21	Bal.	0.2–0.8	2.8–3.3	4.75–5.5	0.6–1.1

(a)

(b)
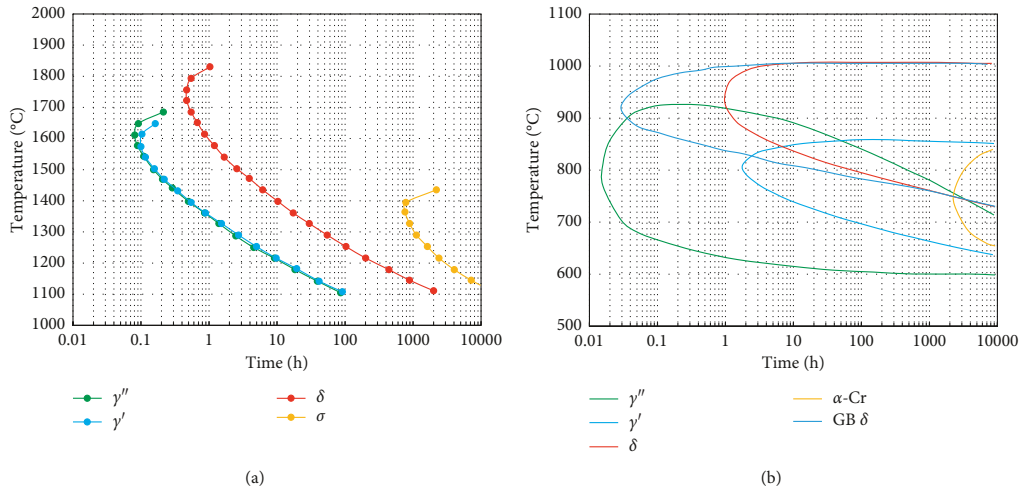
FIGURE 1: TTT diagram for IN718, calculated (a) and experimentally determined (b) [19, 20].

fusion Inconel 718 [11, 32–34]. The mentioned studies were not focused on determining anisotropic elastic properties, and thus excluded required orientations and mechanical properties (i.e., Poisson's ratio).

Since the powder bed surface is always set horizontally and parallel to the build plate, placement of the components at different angles will result in various grain growth orientations with reference to the local coordinate system of the component. Therefore, applying the same process parameters, including the laser scanning strategy, will cause evolution of disparate crystallographic textures depending on the build orientation [35]. Disregarding surface effects, this phenomenon is the major source of anisotropic behaviour in the same material that is processed at different build orientations. Figure 2 compares two possible grain growth directions induced by varied build parameters. These grains are assumed to undergo a biaxial loading in the presented direction annotated with F. It was also assumed that the grains are at one side of the melt pool and there is a symmetry in the growth shown by centreline annotation C_L. Moreover, the local coordinate system at each arbitrary location along the grain is indicated on the cross-cutting plane with <100> orientation as the normal vector. Figure 2 (a) schematically shows a slow cooling rate and Figure 2(b) presents a higher cooling rate. The latter is the dominant case in LPBF. After solidification, two differently oriented grains will be loaded along a certain crystal orientation. Therefore,

the mechanical response of the material would apparently differ if identical parts are produced with various relative orientations to the build plate.

Choi et al. [36], Wang et al. [37], and Keshavarzkermani et al. [38] are among the researchers who investigated the microstructure and texture of IN718, processed by LPBF. In all these studies, the matrix mainly consists of γ grains. The grains were oriented nearly in the same direction, almost like a single crystal. According to their reported electron backscatter diffraction (EBSD) analysis, the γ matrix grains were oriented with <100> parallel to the build direction. Azar et al. [39] showed that the cubic crystal growth along <100> follows the maximum heat flow direction in welding, which is perpendicular to the powder layers in the LPBF case. According to Azar et al. [39], depending on the heat source dynamics and solidification kinetics, the crystals can follow a curvilinear path where the <100> is rotating (Figure 2).

Murr et al. [40, 41] reported that HIP treating the IN718 alloy increases the ductility of the material significantly, which is related to reduction in the residual stresses and hardness of the precipitates. Wang et al. [42] summarised the heat treatment cycles that were applied by previous researchers for IN718 processed by AM. The major driving force for optimising the heat treatment procedure is to maximise the evolution of advantageous phases while suppressing the formation of the detrimental ones.
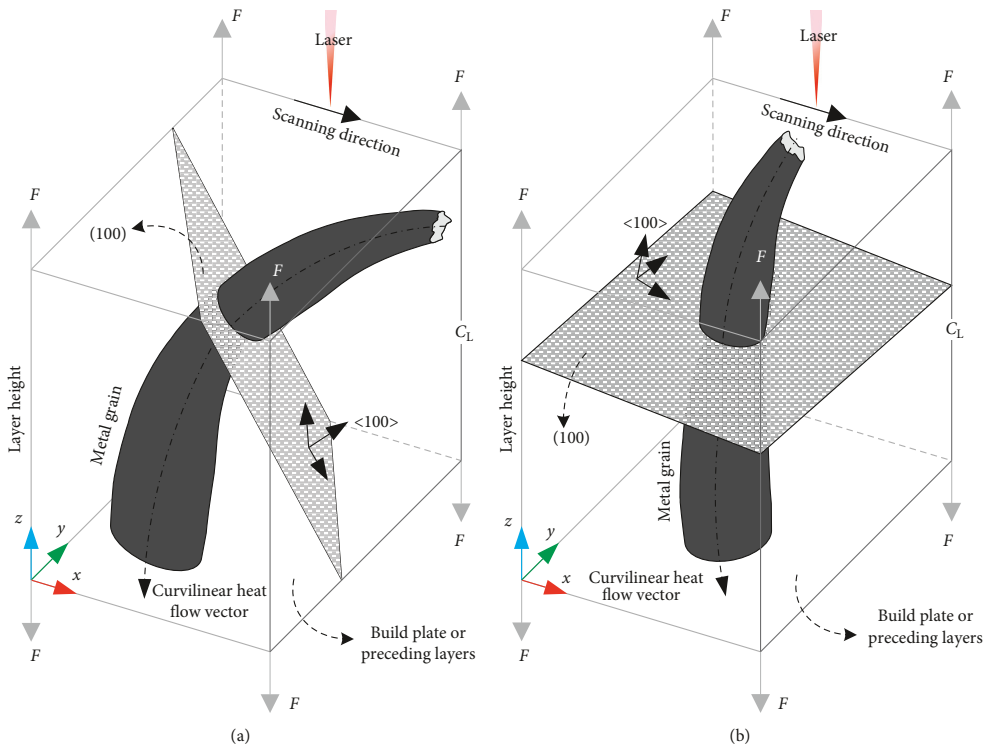
FIGURE 2: Differences in growth kinetics of metal grains along maximum heat flow. This schematic illustration shows two different grain positions with respect to the future loading conditions. In (a), the loading is close to the crystallographic <111> while in (b), the loading is close to <100>.

2. Materials and Methods

In order to investigate the anisotropy of the additively manufactured IN718 material, the tensile specimens were manufactured at various orientations with respect to the horizontal build plate. In this section, the entire chain from powder to postprocessing, and testing will be summarised.

2.1. IN718 Powder.
Prior to the LPBF processing, the powder morphology and chemistry were investigated. The powder used was from a recycled batch, which was sieved and dehumidified following standard practices. The morphology of the powder particles was determined using a Malvern G3 Morphology instrument in the dry dispersion mode. The powder was dispersed on a microscope slide and particles were captured for analysis one-by-one. About 33,000 particles were scanned in the analysis. The chemical composition of the powder was determined by energy-dispersive X-ray spectroscopy (EDS) mapping in a scanning electron microscope (SEM).

2.2. Laser Parameters and Sample Preparation.
The tensile samples were built in an LPBF machine (SLM 280 HL from

SLM Solutions, installed 2014), with process parameters for IN718 powder as supplied by SLM Solutions [43]. The main process parameters are given in Table 2.

The density of the specimen is related to the energy in the LPBF process [44], with the energy per area $(J \cdot m^{-2})$ defined as $E_A = P/vd$, where P is the laser power (W), v is the scanning velocity $(m \cdot s^{-1})$, and d is the hatch spacing (m). In this study, the energy density formula will be used to benchmark the build conditions against earlier published data. The relative density of the material was calculated on polished cross sections of the material using optical microscopy and an image-processing approach (ImageJ software).

Flat tensile specimens were produced in three sets, each consisting of 11 specimens built at different orientations. The sample orientation with respect to the build plate starts at horizontal (0°) increasing to vertical (90°) with 15° increments. Figure 3 shows the tensile specimen geometry, and Figure 4 shows the 11 specimen orientations for each set. The sample geometry and dimensions were initially designed for in situ tensile tests in an SEM, which is the subsequent study of this work. The colours correspond to the orientations in Table 3. The tensile specimens were not machined after LPBF, as the goal of the study is to assess

TABLE 2: Process parameters.

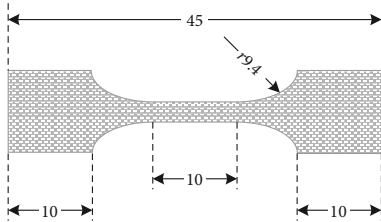| Laser power, P (W)	Layer thickness, t (μm)	Hatch spacing, d (μm)	Scan velocity, v (mm/s)
275	50	120	805

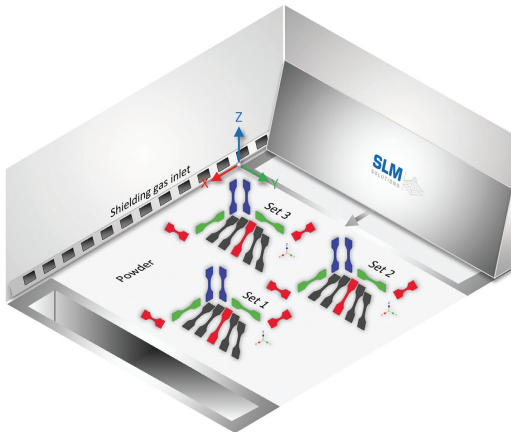FIGURE 3: Geometry of the tensile specimen. Dimensions are in mm.

FIGURE 4: Orientation of the specimens and their configuration in the LPBF build platform. The colours indicate the samples that are used for determining the elastic constants in Section 2.3. Orientations are according to Table 3.

TABLE 3: Codes for test specimen orientation corresponding to Figure 4, with similar choice of colours. Orientation annotation is according to ISO/ASTM 52921:2013E.

ZX	ZY		
XZ	YZ		
XZ − 45B	XY + 45B	YZ + 45A	
XY + 15B	XY + 30B	XY + 60B	XY + 75B

and classify the behaviour of LPBF components with as-built surfaces. In addition to the LPBF specimens, some reference specimens were machined from rolled and aged IN718.

Three different postprocessing routes (denoted as "sets") were designed. Each route was applied to a complete set of sample orientations. Tables 4–6 summarise the applied postprocessing parameters based on the instructions found in reference [45]. (S), (A), and (H) abbreviations were used to show the postprocessing steps of solution treatment, ageing, and HIP, respectively. The solution treatment was performed prior to the removal of the specimens from the build plate. HIP was performed by Bodycote AB.

2.3. Determination of Elastic Constants Using Digital Image Correlation. Using Digital Image Correlation (DIC) in combination with tensile testing [46] eliminates the need for strain gauges. It is sufficient to test at three orientations to determine the transversely isotropic compliance matrix. However, as shown in this study, it is necessary to increase the number of orientations to capture the mechanical response of the material. There are other methods available to capture anisotropy, such as magnetic resonance elastography [47] and nanoindentation [48]. However, these methods are dependent on the local properties of the materials and will only characterize the superficial surface layers.

A commercial DIC system (Vic3D) was used to determine the displacement fields during the tensile tests. The tensile tests were carried out using a Zwick tensile machine equipped with a 50-kN load cell. The cross-head speed was set to 1 mm/min. The cross-sectional area of each specimen was measured with a digital calliper and cross-checked with DIC to account for any deviation from the nominal dimensions. In addition, the surface roughness was measured with white light interferometry (WLI) to quantify the uncertainty of the measured cross-sectional area. Two cameras (2452 × 2052 pixels) equipped with Pentax 75 mm f/2.8 lenses were used. The cameras were mounted on a tripod such that two faces of the tensile sample were exposed to both cameras. This setup allows for the capture of out-of-plane displacements and in-plane displacements on the specimen surface. The correlation was performed with a subset of 29 pixels and a step size of 5 pixels. For a detailed description of the DIC setup, the reader is referred to reference [46].

The Lagrange strain was calculated using the Vic3D software, and the average principal and shear strains were exported for further processing in Matlab. For uniaxial loading of a specimen with gauge length L_0, the Lagrange strain can be written as

$$\varepsilon = \frac{\Delta L}{L_0} + \frac{1}{2}\left(\frac{\Delta L}{L_0}\right)^2. \tag{5}$$

Taking into account that the cross-sectional area varying as a load is applied, and introducing w as the current width, w_0 as the initial width, and similarly for the thickness t, the stress can be expressed as

TABLE 4: Set 1: instructions for solution treatment (S).

HT#	Description	Conditions	Holding temperature	Holding time	Cooling
1	Homogenization and solution treatment	Argon atmosphere. Fast heating to the target temperature	980°C	1 hr	Air cool

TABLE 5: Set 2: instructions for treatment (S + A).

HT#	Description	Conditions	Holding temperature	Holding time	Cooling
1	Homogenization and solution treatment	Argon atmosphere. Fast heating to the target temperature	980°C	1 hr	Air cool
2	Ageing	Vacuum/argon atmosphere. Fast heating to the target temperature	720°C	8 hr	Furnace cool to 620°C within 2 hours
3	Ageing	Vacuum/argon atmosphere. Fast heating to the target temperature	620°C	8 hr	Air cool

TABLE 6: Set 3: instructions for treatment (S + H + A).

HT#	Description	Conditions	Holding temperature	Holding time	Cooling
1	Homogenization and solution treatment	Argon atmosphere. Fast heating to the target temperature	980°C	1 hr	Air cool
2	HIP	100 MPa	1160°C	4 hr	Air cool
3	Ageing	Vacuum/argon atmosphere. Fast heating to the target temperature	720°C	8 hr	Furnace cool to 620°C within 2 hours
4	Ageing	Vacuum/argon atmosphere. Fast heating to the target temperature	620°C	8 hr	Air cool

$$\sigma = \frac{F}{A_0}\frac{w_0 t_0}{wt} = \frac{F}{A_0}\frac{1}{\sqrt{1 + 2\left[((w-w_0)/w_0) + \left((1/2)\left((w-w_0)/w_0\right)^2\right)\right]}\sqrt{1 + 2\left[((t-t_0)/t_0) + \left((1/2)\left((t-t_0)/t_0\right)^2\right)\right]}}, \tag{6}$$

or, in terms of strain, where subscript a denotes the axial direction:

$$\sigma_a = \frac{F}{A_0\left(\sqrt{1 + 2\overline{\epsilon}_w}\ \sqrt{1 + 2\overline{\epsilon}_t}\right)}. \tag{7}$$

Here, σ_a is the Cauchy stress, F is the current force, A_0 is the initial specimen cross-sectional area, and $\overline{\epsilon}_w$ and $\overline{\epsilon}_t$ are the average Lagrange strains [46] in the transverse directions for all points in the current cross section of the two AOIs, respectively. Thereafter, the Cauchy stress was used to find Young's moduli of the specimen in the load direction according to ASTM E111. Poisson's ratios were determined according to ASTM E132. With all the calculated terms, the compliance matrix can be constructed for a transversely isotropic material based on Equation (1) with colour codes corresponding to the samples in Figure 4.

2.4. Determination of Elastic Constants with an Optimization Algorithm. Determining anisotropic material data via direct measurements requires a large dataset to eliminate random errors in the measurements. To improve the significance of the measurements and reduce the number of test specimens,

an optimization algorithm is implemented. This algorithm determines the elastic constants as a complementary solution to direct measurement using DIC. As it will be shown in this article, the benefit of determining the elastic constants by such optimization is that the data will be less vulnerable to noise in the strain measurements, since the algorithm weighs all the stress-strain pairs equally.

In this study, a set of measured stresses and corresponding strains is known for the tensile specimens with respect to the principal material direction. An optimization algorithm was implemented to optimize the compliance matrix.

Consider the transversely isotropic case for which Hooke's law can be expressed as Equation (1). Each pair of strain and stress is related by the compliance matrix and a transformation matrix $\mathbf{K}$, as derived by e.g., pp. 54–55 in Ting [14]. Hooke's law transforms to $' = \mathbf{S}'\boldsymbol{\sigma}'$, where $\boldsymbol{\sigma}' = \mathbf{K}\boldsymbol{\sigma}$, and $\mathbf{S}' = (\mathbf{K}^{-1})^T\mathbf{S}\mathbf{K}^{-1}$, which leads to $' = (\mathbf{K}^{-1})^T\mathbf{S}\mathbf{K}^{-1}\mathbf{K}\boldsymbol{\sigma} = (\mathbf{K}^{-1})^T\mathbf{S}\boldsymbol{\sigma}$. $\mathbf{S}'$ and $\mathbf{S}$ are the transformed and original compliance matrix.

In the current study the Lagrange strain tensor is measured directly using DIC. The shear stress and strain were found to be negligible, allowing the procedure

described in Equation (3) to be used to calculate the shear moduli. When a relationship between stress and strain is established, the strain tensor can be expressed as

$$\epsilon^* = \left(\mathbf{K}^{-1}\right)^T \mathbf{S} \mathbf{K}^{-1} \boldsymbol{\sigma}, \tag{8}$$

where $\boldsymbol{\sigma}$ is the Cauchy stress tensor from Equation (7). The objective of the optimization problem is to minimize a cost function $J(\theta)$. A common cost function for problems like this is the root-sum-of-squares function shown in the following equation:

$$J(\theta) = \sum_{i=1}^{m} \sqrt{\epsilon^2 - \epsilon'^2}, \tag{9}$$

where ϵ is the measured strain in the elastic region. An optimization problem like this can be implemented by e.g., the function fmincon in Matlab. The material is assumed to increase in volume and contract in the transverse directions when undergoing tensile stress. This in turn constrains the Poisson's ratio in any orientation to be bound by $0 < \nu_{ij} < 0.5$. As the elastic moduli in the $0°$, $45°$ and $90°$ orientations are known, the problem is reduced to determining the Poisson's ratios. The elastic moduli in the compliance matrix (Equation (1)) are known and are used together with the constraints on the Poisson's ratios to determine ν_{xy}, ν_{xz}, and ν_{zx}. The shear moduli are determined based on Equations (2) and (3).

2.5. Electron Microscopy and Electron Backscattered Diffraction (EBSD) Analysis.

In order to investigate the effect of postprocessing conditions on the grain structure using SEM, the samples were prepared by means of mechanical grinding and polishing followed by etching. Glyceregia solution was used for etching the samples. In the interest of studying crystallographic texture and preferred crystallographic orientations, EBSD analysis was employed. For this purpose, the $90°$ ZY specimens from set 1 and set 3 were selected. These samples were also prepared by mechanical grinding and polishing, though, instead of final etching, Oxide Polishing Suspension (OP-S, $0.04\,\mu m$) from Struers was applied. The EBSD sample was extracted from the side wall of this specimen. The backscattered patterns were collected in offline mode using FEI NOVA NANOSEM 650 ultralow vacuum field emission gun scanning electron microscope (SEM). An EBSD detector (Oxford Instruments NordlysMax3) was used to record approximately 1000 offline patterns per second. The working distance was set to 11 mm with a tilt angle of $70°$ under a high-current electron beam. The accelerating voltage of the gun was 20 kV. An area of $800\,\mu m \times 800\,\mu m$ was scanned with step size 400 nm, accumulating crystallographic data for 4 million points for the selected area.

3. Results

3.1. Powder Characterization.
Figure 5 shows the statistical values for the particle analysis. The figure contains information about circle equivalent (CE) diameter, high sensitivity (HS) circularity, aspect ratio and elongation for the analysed

CE diameter mean (μm): 33.18 Vol.%
CE diameter mean (μm): 28.41 Nr%
HS circularity: >95%
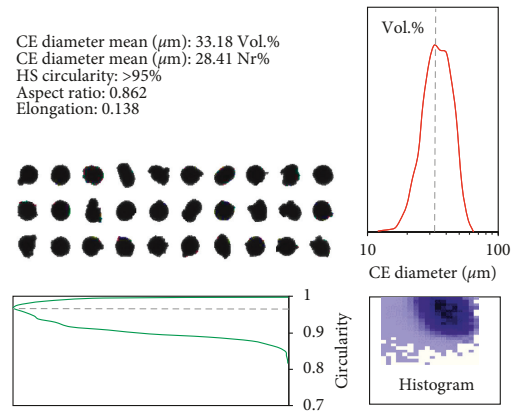Aspect ratio: 0.862
Elongation: 0.138

Figure 5: IN718 powder morphology analysis.

powder. Description of these entities is given in reference [49]. Moreover, selected individual particles in the vicinity of the peak of the distribution are shown in the figure. The vertical axis in the CE diameter figure is reported in arbitrary units (a.u.). The vertical and horizontal axes in the histogram figure are reflected in the upper and left figures in Figure 5.

Figure 6 shows the chemical composition mapping of the particles. Some particles are rich in Al-Co-Ni content and depleted in other elements. Although there are local inhomogeneities in the chemical composition of the particles, the mass composition of the powder is within the specifications of IN718 datasheet.

3.2. Microstructure.
Figure 7 shows SEM images of the XY + 45B tensile sample from set 1 at three locations. The observed steps are a result of the "stair-stepping" effect, and the distance between each step perpendicular to the page is the layer height. The edge steps were measured directly on the figure and the layer height was calculated based on the known nominal inclination ($45°$). The layer height was also checked and compared, both by focusing the scanning electron beam of the microscope on each two adjacent steps and measuring from the cross section. The results are tabulated in Table 7.

Figure 8 shows high-magnification SEM micrographs of a specimen from set 1. Figure 8(a) shows the fusion lines along the build direction, and Figure 8(b) shows the $\gamma + \gamma''$ lamellae structure at a higher magnification. White and blue arrows show some of the typical flaws in the matrix resulting from lack of fusion, and microsegregation in the interdendritic regions, respectively.

SEM micrographs of the aged specimens (SET 2) in Figure 9 show dendritic lamellae and grain boundary δ/η-phase evolution after ageing.

Figure 10(a) illustrates the acquisition conditions for the EBSD investigations. The build direction is along $Y0$ in the figure, leaving the LPBF layers perpendicular to $Y0$. Figure 10(b) presents the inverse pole figure $Y0$ (IPF-$Y0$) of the scanned area. In this frame, north of the figure is $X0$ and east

(a)   (b)   (c)

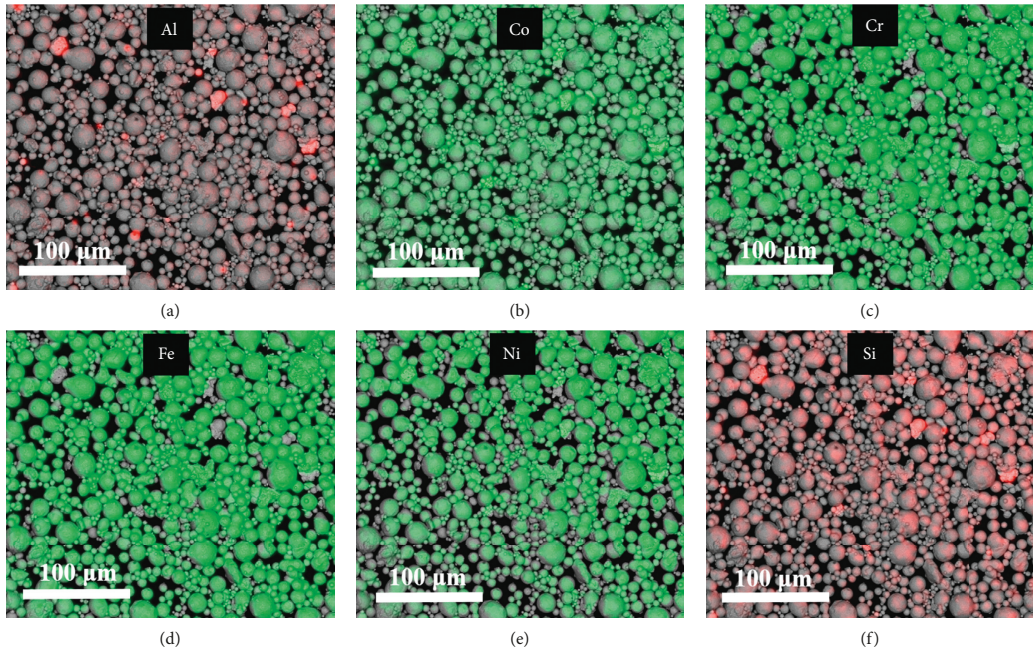(d)   (e)   (f)

FIGURE 6: EDS chemical composition mapping of the used IN718 powder.
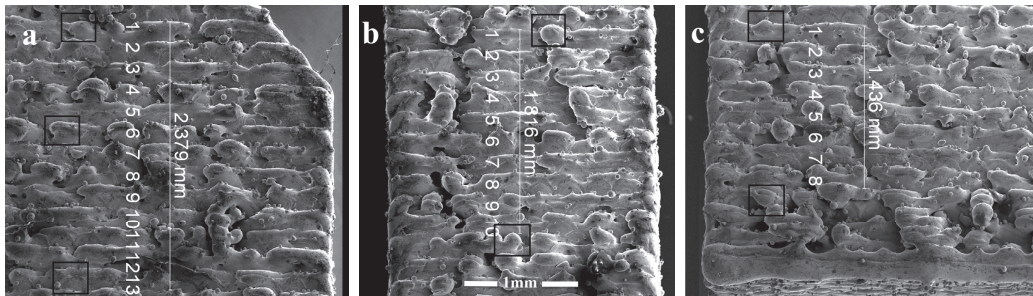

FIGURE 7: Surface topography of the upwards facing surface of the $XY + 45B$ specimen from set 1 at the (a) top; (b) middle; and (c) bottom of the tensile sample.

TABLE 7: Layer and edge step measurements.

Site	Layers	Total width (μm)	Width of single layer (μm)	Layer height (μm)
a	13	2379	183.0	49.0
b	10	1816	181.6	48.7
c	8	1436	179.5	48.1

of the frame is $Y0$. The dataset was rotated 90° counter-clockwise to capture the texture of the material correctly.

Figures 11(a) and 11(b) show the inverse pole figures of the scanned area for samples from set 1 and set 3. It can be seen that the preferred orientation of {100}<100>||$Y0$ is dominating in set 1 as a result of the build conditions. In other words, the {100} family of planes is preferably oriented

towards the build orientation if the sample is set at 90° with respect to the build platform. Traces of texture components in the samples from set 3 can still be seen. However, due to extensive recrystallization and ageing after postprocessing (HIPing + ageing), the texture is weakened. This can be observed by comparing the orientation clustering densities in the legend of both figures.

Figure 12 shows the orientation distribution function (ODF) space of the scanned area for the sample from set 1. The ideal texture component of <100>||$Y0$ was also plotted in each section. It is apparent that the hot spots on different sections of $\phi2$ Euler angle coincide well with the presented ideal orientation, suggesting that there is a dominating texture component in the specimen.
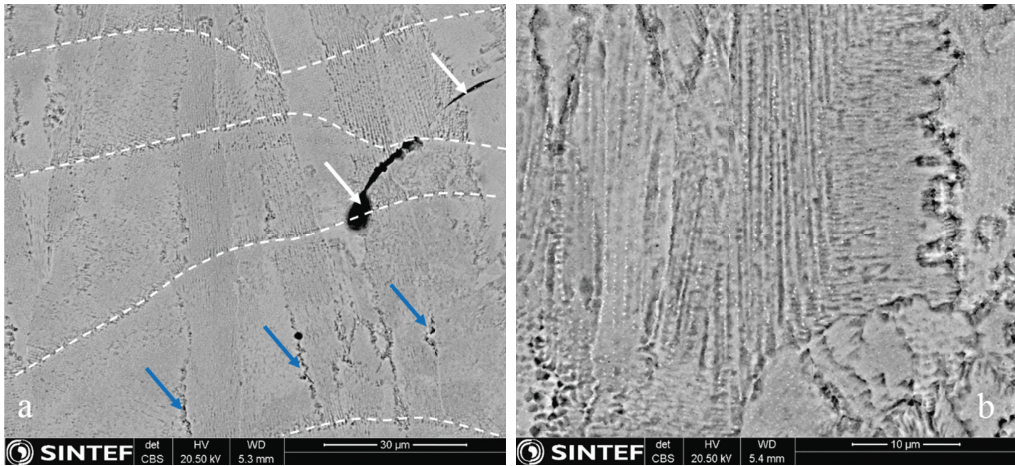
Figure 8: SEM micrographs from the solution-treated samples (Set 1) (a) showing the fusion lines, white arrows show the lack of fusion due to laser parameters and blue arrows show the inter-dendritic regions. (b) showing the dendritic $\gamma + \gamma''$ lamellae structure.
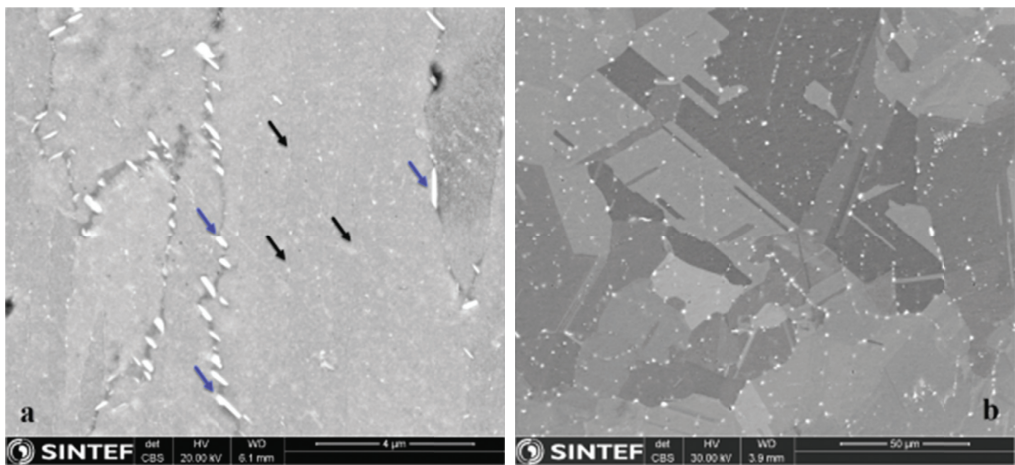

Figure 9: SEM micrograph of (a) aged IN718, and (b) HIPed and aged IN718. Black arrows show the interdendritic $\gamma + \gamma''$ lamellae, and blue arrows show the evolution of grain boundary δ/η-phase upon ageing. Extensive reconstructions of the grain structure, and grain boundary precipitates mostly on the prior boundaries of γ grains can be seen in (b).

3.3. Mechanical Properties. The relative density was measured to be 99.97% (set 1) and 99.98% (set 3). Figure 13 shows Cauchy stress versus Lagrange strain for set 1 (a), set 2 (b) and set 3 (c), with postprocessing as described in Tables 4–6, respectively.

Figure 14 shows the elastic modulus for set 1 (a), set 2 (b), and set 3 (c) for all build orientations. The error bars indicate the standard deviation of the strain field, as captured by DIC, in each specimen. Due to surface effects and porosity, the strain field on each specimen is not homogeneous. The elastic moduli are determined for the average strain

(box), and for the average strain plus/minus the standard deviation (error bars).

Figure 15 shows the yield strength (a), ultimate tensile strength (b), and elongation at break (c) for all build orientations and heat treatment conditions. The average strain of each specimen is considered when determining the respective properties. The average value of the reference specimens is indicated with the green line.

The tensile properties of the IN718 specimens manufactured by LPBF, averaged over all the build orientations, are shown in Table 8. For comparison, the values for the
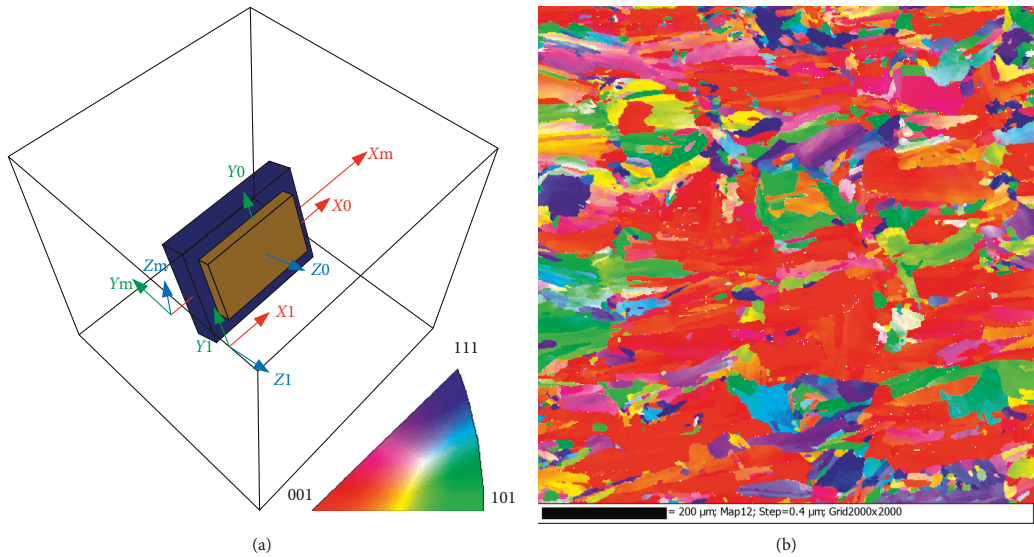
(a)

(b)

FIGURE 10: (a) Sample configuration and principal axes in the microscope chamber and (b) IPF-$Y0$ inverse pole figure grain map of the scanned area on the side wall of the sample oriented at 90° with respect to the build plate. The EBSD patterns were acquired with 0.4 μm step size.
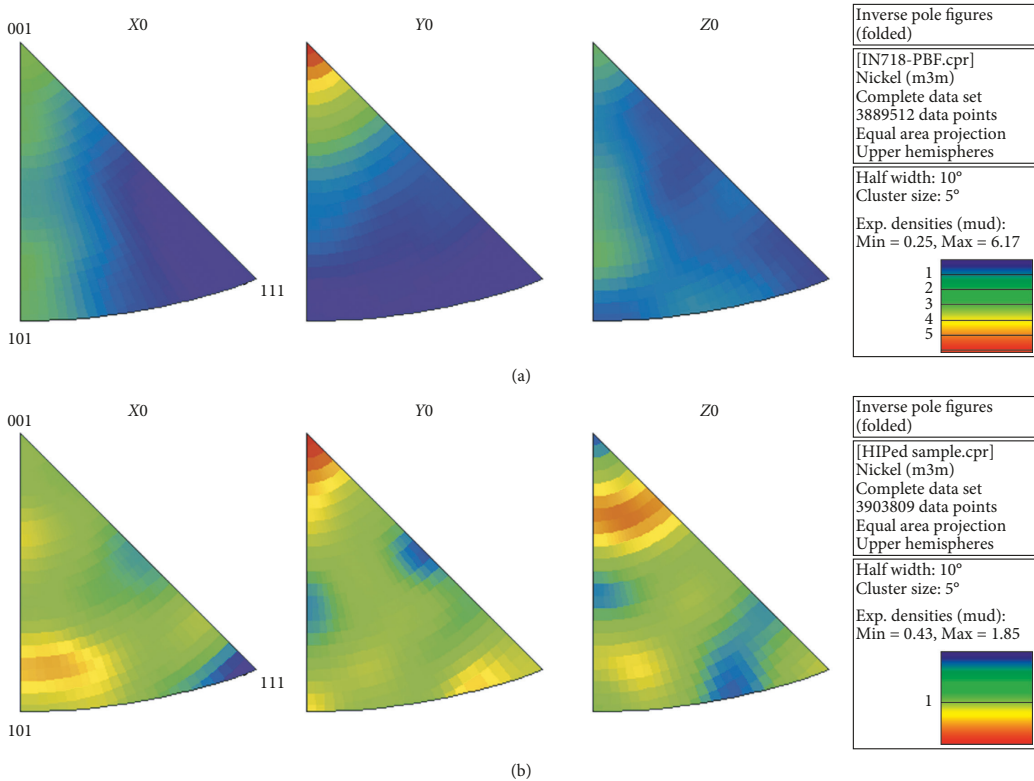

(a)

(b)

FIGURE 11: Inverse pole figure constructed based on 4 million data-points from the scanned area along the sample principal axes $X0$, $Y0$, and $Z0$ for (a) solution-treated and (b) HIP-treated sample.
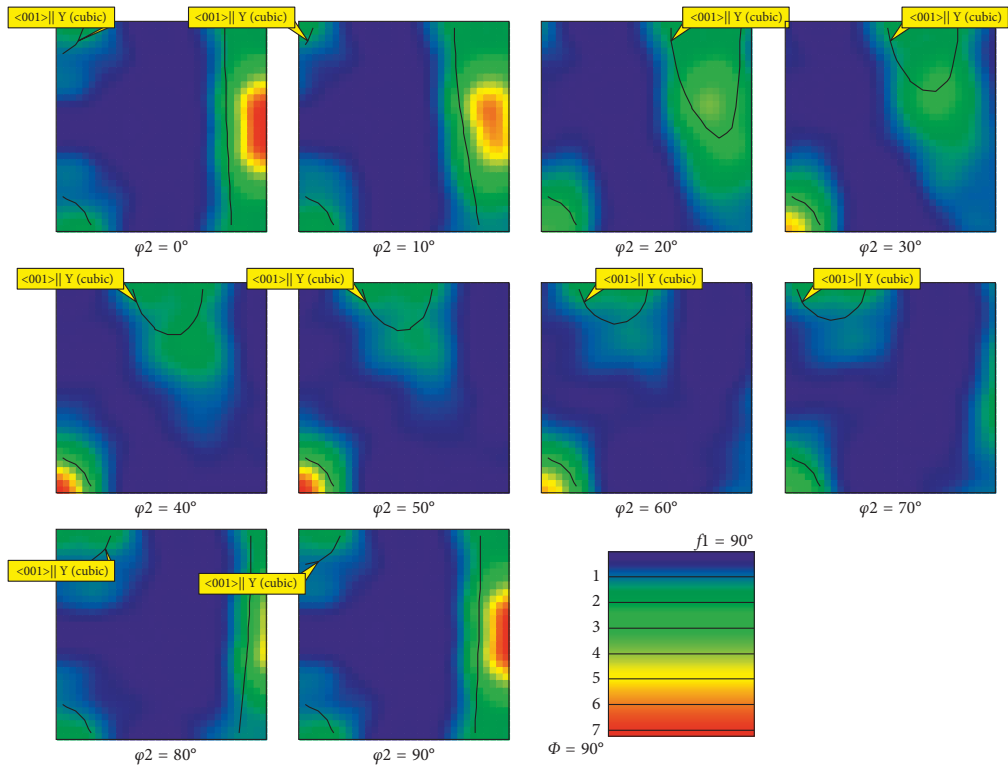
FIGURE 12: ODF sections of the scanned area. The boundaries of <001>||$Y0$ ideal texture components is shown with black solid line in different $\phi2$ sections.

reference specimens (machined from rolled and aged IN718) are included in parenthesis.

3.4. Elastic Constants. The elastic constants, assuming transverse isotropy, acquired from the DIC strain fields are given in Table 9.

Table 10 shows the elastic constants obtained using the optimization algorithm described in Section 2.4 assuming transverse isotropy.

It is important to note that there are uncertainties associated with the calculated elastic constants. The elastic constants are determined from a calculated stress (Equation (7)), which is a function of the initial cross section area, the current transverse strain, and the applied force. The surface roughness is measured to be less than Ra = 1 μm for the 0° specimens, while peaking at the specimen oriented at 15° with Ra = 16 μm. The roughness then decreases to Ra = 5 μm as the specimens are raised towards 90°. HIP appears to reduce the surface roughness of the roughest surfaces by approximately 60%. The maximum uncertainty in the measurement of the initial cross section area due to the surface roughness is in the order of 80 μm^2, or 0.002% of the nominal cross section, introducing

negligible uncertainty. The standard deviation of the transverse strain has a much larger contribution to the uncertainty. The measured force is assumed to be accurate followed by load cell calibration certificate. The error of the calculated stress can be quantified by introducing the uncertainty of the initial cross-sectional area and the standard deviation of the transverse strain to Equation (7). The average error of the calculated stress is 0.57%, 0.19%, and 0.19% for set 1, set 2, and set 3, respectively. Due to the low error, only average values have been used to determine the elastic constants.

4. Discussion

The presented anisotropic material data, and the general methodology to obtain these, provide a basis for improved numerical modelling (finite element analysis) of the mechanical response of components produced by LPBF without postproduction machining. Even if machining is required for tolerances and surface finish, complex geometries with large inaccessible surface areas will remain the weakest link, and this justifies the method for obtaining the mechanical properties of the unmachined specimens as proposed in this study.
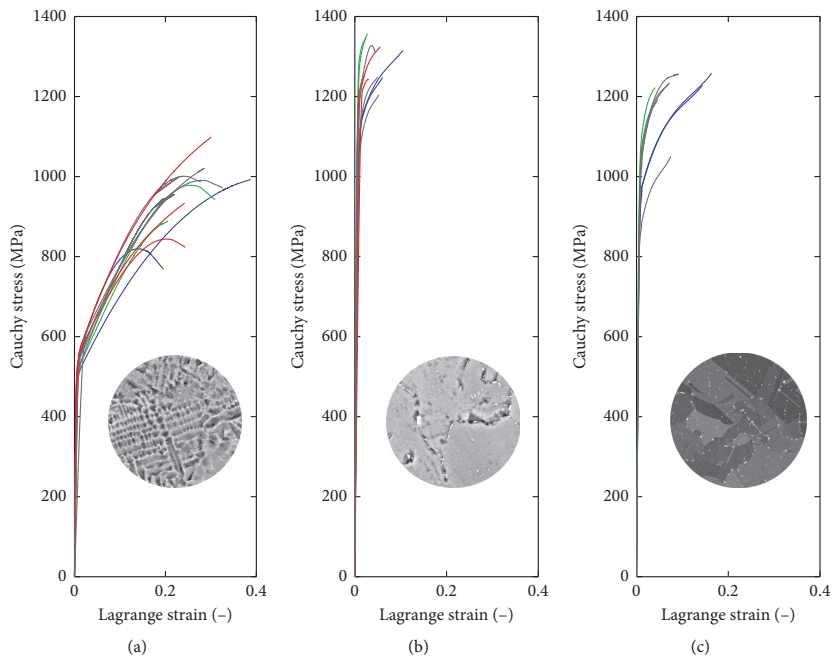
(a)

(b)

(c)

Figure 13: Cauchy stress plotted versus Lagrange strain for (a) S condition, (b) S + A condition, (c) S + H + A condition. Colours are according to Table 3.
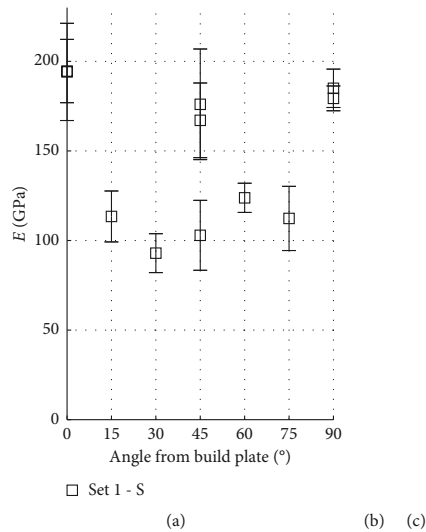

□ Set 1 - S

(a)   (b)   (c)

Figure 14: Mechanical properties of Set 1 (postprocessing "S"), Set 2 ("S + A"), and Set 3 ("S + H + A") with respect to orientation angle from build plate. Points indicate measured values (3×11 in each diagram), while the lines are either 2nd order polynomial fits (a), connecting lines (b and c) or least square fits (d), indicating the trend.

4.1. Powder, Laser, and Density Characteristics. Despite local inhomogeneities in the particle scale (Figure 6), the overall chemical composition of the powder is uniform. The

presented defects in Figure 8(a), arising from metallurgical phenomena such as segregation or formation of eutectic phases, can possibly be related to local impurity enrichment
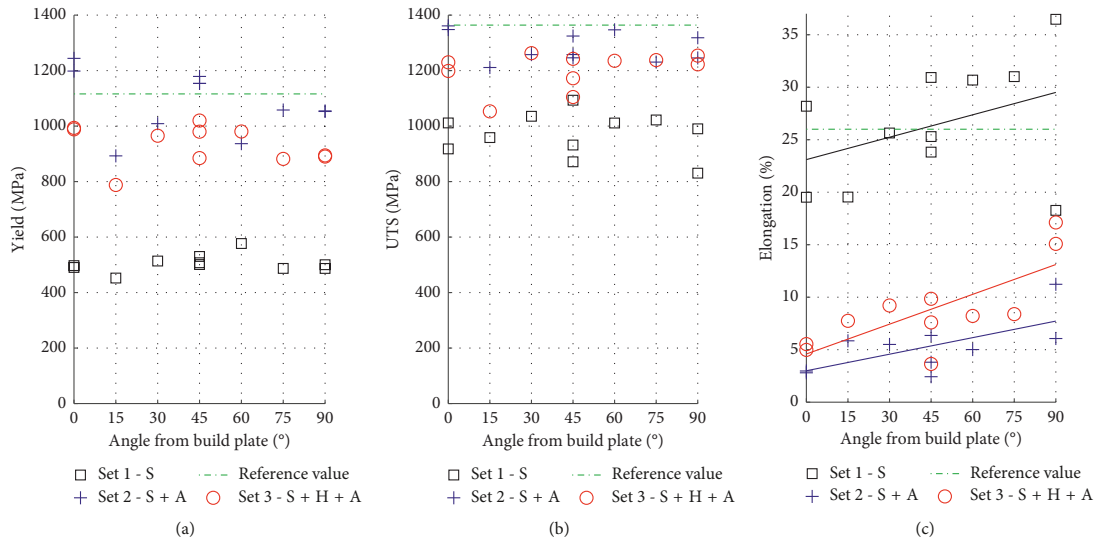
Figure 15: Yield strength (a), ultimate tensile strength (b), and elongation at break (c) of set 1, set 2, and set 3 with respect to orientation angle from build plate. Points indicate measured values while the lines in elongation indicate the least square fit.

Table 8: Average tensile properties for all eleven orientations. Values for the reference specimens (machined from rolled and aged IN718) are given in parenthesis.

	E (GPa)	UTS (MPa)	Yield stress (MPa)	Elongation at break (%)
SET 1	149 ± 40	970 ± 74	504 ± 30	26 ± 6
SET 2	181 ± 24 (193 ± 9)	1286 ± 52 (1364 ± 21)	1085 ± 106 (1116 ± 27)	5 ± 2 (26 ± 5)
SET 3	184 ± 30	1201 ± 63	933 ± 67	9 ± 4

Table 9: Elastic constants from DIC, for a transversely isotropic material model. This model is referred to as "DIC method" in figures below.

Elastic constants	Set 1 (S)	Set 2 (S + A)	Set 3 (S + H + A)
E_{xx} (GPa)	194	206	217
E_{zz} (GPa)	182	201	201
ν_{xy} (−)	0.4339	0.4748	0.4718
ν_{xz} (−)	0.4029	0.3650	0.4019
ν_{zx} (−)	0.3909	0.2045	0.2172
G_{xz} (GPa)	47	48	55
G_{xy} (GPa)	68	65	75

Table 10: Constants of optimized elastic model.

Elastic constants	Set 1 (S)	Set 2 (S + A)	Set 3 (S + H + A)
E_{xx} (GPa)	194	206	217
E_{zz} (GPa)	182	201	201
ν_{xy} (−)	0.3612	0.4994	0.3888
ν_{xz} (−)	0.3158	0.4999	0.4563
ν_{zx} (−)	0.3745	0.4877	0.4927
G_{xz} (GPa)	31	56	49
G_{xy} (GPa)	71	69	78

originating from non-IN718 powder particles. For instance, the presence of Al-rich particles (Figure 6) in the powder may result in anomalies and, therefore, proper cleaning of the build envelope, and powder-handling units play an important role in LPBF processing. Despite being recycled, the powder morphology and chemistry were well maintained (Figure 5), and the morphology measurements show no major deviations from the virgin powder specifications. The layer height after processing of the material decreased by 2–4% by comparing measured values in Table 7 with nominal values in Table 2. The source of such differences can be dependent on several parameters such as powder fusion and

densification, or shrinkage and dilution between each two adjacent layers [50]. On the one hand, a small difference between the measured and nominal values implies a relatively high packing ratio of the powder particles prior to fusion. On the other hand, it may also imply limited dilution between two adjacent layers. The latter case can be detrimental if low dilution leads to lack of fusion between the layers and cause formation of cracks. Lack of fusion was rarely found in the large areas being investigated, although Figure 8(a) proves the presence of such anomalies. In these cases, subsequent HIP will be required. Full closure of the crack will depend on the local chemistry, location and morphology of the anomaly, type of trapped gas inside cavities (pores), and the HIP parameters for that specific material. It is worth mentioning that

porosity in the powder particles may also play a central role in the evolution of postfusion porosity, since powder defects may retain throughout the entire process [51].

In this study, the energy per area (E_A) was 2.85 MJ/mm^2 (c.f. Table 2). Jia and Gu [52] achieved a relative density of 98.4% with an energy per area of 4.64 MJ/mm^2. Chlebus et al. [11] achieved a relative density in excess of 99.7% with an energy per area of 6.48 MJ/mm^2. According to the presented results in this work, high density can be achieved even with a low energy per area compared with the predecessor's applied parameters. Adjusting the process to build at high energy per area increases the baseline temperature and may cause the heat cycle to affect several layers below the last fusing surface. Depending on the peak temperature and the susceptibility of the material to form new phase constituents or anomalies, running the process at high temperature can be detrimental. Lower energy per area will confine the extent of the heat-affected zone (HAZ) in the previously fused layers.

4.2. Macro- and Microstructure. Beyond the effects of powder and part surface topography, the microstructure is also playing a significant role in determining the mechanical properties. Figures 8 and 9 show how the microstructure of a single alloy may change upon heat treatment. The grains are growing epitaxially throughout several layers before they are overgrown by other larger grains. The dendritic solidification pattern and $\gamma + \gamma''$ lamellae structure are visible in the microstructure. Observations of η and δ precipitates at the grain boundary were reported by several early researchers [42, 53, 54]. Their results unanimously propose that a small amount of these two phases may improve the notch sensitivity and resistance to intergranular crack propagation. The ageing of solution-treated IN718 is already showing these phases in the current study, and its indirect effect on the mechanical properties is shown in Figure 9(a). The benefit of HIP in eliminating anomalies was discussed earlier in Section 4.1. In addition to densification, the microstructure recrystallizes at high temperature during HIP, and the architecture of the grains and grain boundaries is largely affected [53–55]. According to Figure 9(b), the recrystallised grain boundaries transcend the primary γ grains, and subsequent ageing leads to the formation of precipitates not only on the recrystallised γ grains but also on the primary γ grains [26]. The presence of evenly distributed precipitates, even within the grains, seems to unitedly hamper the dislocation movements and causes a more uniform response of the material as can be seen when comparing set 1 with set 2 and set 3 in Figure 14(a).

In Figure 10(b), it was also illustrated that LPBF is a directional processing route that influences the grain structure, the grain morphology, and the crystallographic texture of the material. Preferred alignment of <100> along the build direction may weaken the material if it is built at an angle. The curvilinear heat flow vector argument is shown to be the dominant growth mechanism for high and low cooling kinetics [39]. The evolution of <100> along the build direction is primarily due to low layer thickness that embodies fewer grains within each layer, and high processing

speed (i.e., laser scanning speed), which determines the range of grain growth kinetics. In such conditions, unlike welding, for example, the grains are not given sufficient time to bend behind the heat source (see e.g., Figure 2(a)).

4.3. Mechanical Properties. Consider the stress-strain curves presented in Figure 13. Ageing (Figures 13(b) and 13(c)) increases the yield stress and ultimate tensile strength at the expense of elongation, compared with the nonaged specimens in Figure 13(a). HIP before ageing will somewhat reduce the yield strength and ultimate tensile strength and increase the elongation (Figures 13(b) and 13(c)).

Figure 14 shows the elastic moduli for all three sets as function of the specimens' build angle relative to the build platform. For set 1, the elastic modulus is highest for the specimen built at 0° with respect to the build plate. It then drops as the specimens are raised towards 45°. The elastic modulus then increases as the angle is raised further up to 90°. The three measured values for the specimens at 45° are 167 ± 20.8 GPa, 103 ± 19.5 GPa, and 176 ± 30.1 GPa, for orientations *XZ-45B*, *XY + 45B*, and *YZ + 45A*, respectively. A possible explanation of the large variation in the 45° data is given in Section 4.4. As can be seen in Figure 14, ageing will increase the modulus of the material significantly. The average modulus is 149 ± 40 GPa, 181 ± 24 GPa, and 184 ± 30 GPa for set 1, set 2, and set 3, respectively.

Recall that the microstructure in set 1 primarily consists of FCC γ-phase with slip system {111} <1$\bar{1}$0>, and that the material exhibits a strong {100} fibre texture (Figures 11 and 12). Consider, for arguments sake, the material as single crystal FCC. The elastic modulus in any particular crystallographic direction can then be calculated using the following equation [56]:

$$
\frac{1}{E_{[hkl]}} = \frac{1}{E_{<100>}}
$$
$$
- 3\left(\frac{1}{E_{<100>}} - \frac{1}{E_{<111>}}\right)(\alpha^2\beta^2 + \alpha^2\gamma^2 + \beta^2\gamma^2), \tag{10}
$$

where $E_{<100>}$ and $E_{<111>}$ are the moduli in the <100> and <111> directions, respectively, and α, β, and γ describe a unit vector $\mathbf{v} = [\alpha \ \beta \ \gamma]$ within the crystallographic plane of interest where α, β, and γ are the direction cosines with respect to [100], [010], and [001]. In the current study, we are interested in the modulus in the {100} plane under different loading angles. The inset in Figure 16 shows the {100} plane in a cubic system with the unit vector $\mathbf{v} = [0 \cos(\theta) \sin(\theta)]$, and the blue line (Equation (10)) shows the moduli under different load angles with values for $E_{<100>}$ being greater than $E_{<111>}$ as measured with DIC for set 1. The calculated modulus in Figure 16 compares well with the observed behaviour of the material as seen in Figure 14(a).

Figure 15(a) shows the yield stress for all specimens as a function of build angle. For set 1, the yield stress is at its maximum at a 60° angle to the build plate. Although the sample size for set 1 is small, and thus not statistically significant, crystallographic theory supports the observed
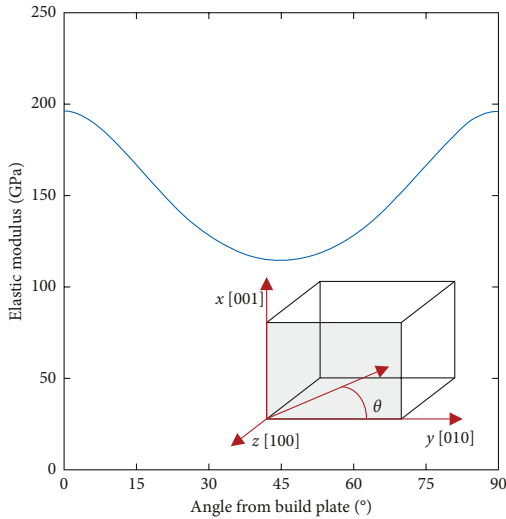
FIGURE 16: Elastic modulus is according to Equation (10) with a value for $E_{<100>} > E_{<111>}$ as measured with DIC for set 1. Inset: {100} plane in a FCC crystal with xyz and corresponding (hkl) coordinates.

FIGURE 17: Yield stress for set 1 compared with the inverse Schmid factor for set 1.

maxima close to the theoretical maxima at 54°, as will be shown in the next paragraph. In the aged and HIP + aged condition, the scatter in the data is large and no clear anisotropic trends are observed. However, it is clear that the average yield stress increases as the material is aged, and HIP before ageing reduces the average yield stress somewhat.

Consider again the material as single-crystal FCC. The Schmid factor can then be employed to describe the anisotropic behaviour with respect to build angle, as previously done by Ni et al. [32], for the same material and process as in the present study. The yield stress can be expressed as

$$\sigma_{\text{yield}} \geq \frac{\tau_c}{\cos(\phi)\cos(\beta)}, \quad (11)$$

where τ_c is the critical resolved shear stress in slip systems, φ is the angle between the axial load and the normal direction of the slip plane, and β is the angle between the axial load and the slip direction. The term $\cos(\phi)\cos(\beta)$ is known as the Schmid factor. With the current slip system φ and β sum to 90° and the Schmid factor can be expressed as $(1/2)\sin(2\phi)$. For set 1, the yield stress and the inverse of the Schmid factor are plotted as function of build angle in Figure 17. The error bars represent the standard deviation of the strain field for each specimen. The general trend for the inverse Schmid factor and the yield stress is the same. If the material did not exhibit the strong texture observed in this study, Taylor's factor may be employed to estimate the deformation instead of the Schmid factor. However, with the texture exhibited in the present material the Taylor factor and the Schmid factor will be comparable.
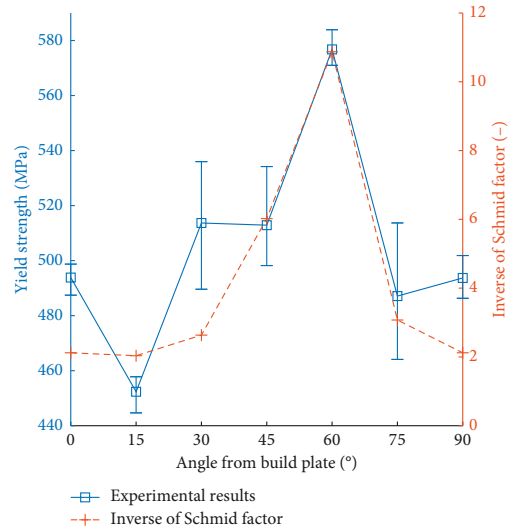
The trend of the yield strength of set 1 corresponds with the Schmid factor, as shown in Figure 17, with a minimum in yield strength at a 15° angle from the build plate and a maximum yield strength at a 60° angle from the build plate. This trend is not observed for set 2 and set 3.

After ageing, and after HIP and ageing, the average yield stress increases to 1085 ± 106 MPa and 933 ± 67 MPa, respectively. The precipitation hardening that occurs during ageing will increase the yield stress due to the pinning of grain boundaries and the stopping of dislocation movement. The standard deviation of the yield stress is reduced when HIP is done prior to ageing, indicating a homogenization effect. The magnitude of the yield stress is also slightly reduced when HIP is done before ageing, most likely due to recrystallization and evolution of twin grain boundaries.

Figures 15 and 14(b) show the ultimate tensile strength for the three different heat treatment sets as function of build angle. Again, it is obvious that ageing increases the materials strength. The ultimate tensile strength in set 1 is significantly lower compared with the aged variants. It is observed that the ultimate tensile strength is lower when the material has undergone HIP processing, as was the case for yield stress. Further analysis of ultimate tensile strength is considered unnecessary for this material as its main application is in aerospace where plastic deformation would be considered as failure.

Figure 15(c) shows the elongation at break for the three different heat treatment sets as function of build angle. The average elongation at break for set 1 is 26 ± 5%, with increasing elongation at break as the build angle increases. The same trend is observed for the heat-treated samples, but the magnitude of the elongation at break is greatly reduced. The

elongation at break for set 3 (S + H + A) is higher compared with the elongation at break for set 2 (S + A). This is attributed to a reduction in the residual stresses and hardness of the precipitates after HIP.

The angle between the axial load and the material texture will determine the failure mode. For the tensile specimens with main loading axis in the build plate plane (0°), the columnar grains are perpendicular to the loading direction (c.f. growth mechanisms in Section 1.3), promoting mode I type failure. For the specimens with main axis along the perpendicular to the build plate (90° build angle), the columnar grains are in general parallel to the load direction. This will limit the possibility of mode I failure. The lowest elongation at break should then be observed for the 0° specimens and increase gradually to a maximum for the 90° specimens. This hypothesis is supported by the data seen in Figure 15(c).

Consider the average mechanical properties for all orientations in Table 8. The results for the aged specimens (set 2) compare well with those of the reference specimens (machined from rolled and aged IN718). The specimens of set 2 have average modulus, yield stress, and UTS that are 94%, 94%, and 97% of the reference's values, respectively. However, the elongation at break is significantly higher for the reference specimens than for the set 2 specimens.

4.4. Elastic Constants. The elastic constants given in Tables 9 and 10 can be used in FE analysis (e.g., Abaqus) directly to predict the anisotropic elastic behaviour of a general three-dimensional part with a certain build orientation. Next, the model is discussed and verified by performing simulations with load conditions simulating the physical experiments. The first approach of determining the elastic constants, based on direct DIC measurements, is referred to as the "DIC method," while the approach employing the optimization algorithm is referred to as the "optimized method."

Figure 18 shows the elastic modulus numerically determined with the DIC method and the optimized method, compared with the experimental results for each heat treatment condition (sets 1, 2, and 3). When using the DIC method, the elastic modulus follows a 4th order polynomial as discussed in the previous section (Equation (10) with $E(0°) > E(90°) > E(45°)$). The same trend is observed with the optimized method, which follows the experimentally determined data more closely. This is a result of how the optimization algorithm treats each individual stress/strain pair equally, and thus the high values at 45° are given less weight.

The experimentally determined elastic moduli deviate from the calculated moduli, with higher modulus for the 45° angle, particularly for the two specimens with orientation *XZ*-45B and *YZ* + 45A, which are not simply rotated from a "flat" orientation such as *XY* + 45B (Figure 4 and Table 3). For the orientations *XZ*-45B and *YZ* + 45A, the projection of the specimen cross section along the *Z* axis (of the build chamber) is $w/\cos(45°)$, where w is the width of the sample (2.5 mm in the gauge section). On the other hand, for the

orientation *XY* + 45B, the projection of the specimen cross section along the *Z* axis is $t/\cos(45°)$, where t is the thickness of the sample (1.5 mm). When loading specimens with 45° build angle, the grain boundaries will either align with the slip line and cause de-cohesion, or twin subgrains will form, which will introduce twinning-induced plasticity [57]. The experimental results shown in Figure 18(a) might indicate that for the orientations *XZ*-45B and *YZ* + 45A, subgrains are formed, while for *XY* + 45B, the grains align with the slip line and the plasticity is higher. Chlebus et al. [11] reported values for moduli in the solution treated only condition (set 1) with the trend $E(45°) > E(0°) > E(90°)$, which is in line with activation of slip lines under loading. Considering the magnitude of the moduli for specimens oriented at angles 15°, 30°, 60°, and 75° in the present study, the data suggest the worst-case scenario should be assumed, where the grains align with the slip line. This will in turn give a more conservative model. There are also significant differences between the study by Chlebus et al. and the present study when it comes to laser parameters, alloy composition, and heat treatment procedures. The spread in the $E(45°)$ data is far larger than the spread in the data for $E(0°)$ and $E(90°)$ for all three sets, which indicates that some competing effect—like the one described in this paragraph—might be the source of the presented disparity.

Using the DIC method, the modulus is calculated to be higher than the experimental values for 15°, 30°, 60°, and 75°, resulting in a possibility to overestimate the stiffness in components with walls, etc. oriented in this range of angles.

Both the DIC method and the optimized method predict moduli higher than the observed values for 15°, 30°, 60°, and 75°, with the exception of set 2 at 30° and set 3 at 30° and 60°. However, the optimized method is not as strongly influenced by the apparent outliers at 15°, 60°, and 75° compared with the DIC method. This in turn suggests that the optimized method is less vulnerable to noise in the data. For all heat treatment conditions, the optimized method gives a more conservative estimate of the moduli.

5. Conclusions

(i) A method has been demonstrated for obtaining anisotropic (transverse isotropic) elastic constants for material processed by laser powder bed fusion (LPBF). The method is based on building a set of tensile specimens, oriented in a systematic manner on the build plate, and using digital image correlation (DIC) during the tensile tests. The current study is focused on the response of nonmachined specimens, inspired by the fact that in complicated AM geometries, postmachining may be difficult or even impossible.

(ii) Extensive tensile testing of a single specimen geometry built with different orientations shows that the LPBF process induces mechanical anisotropy.
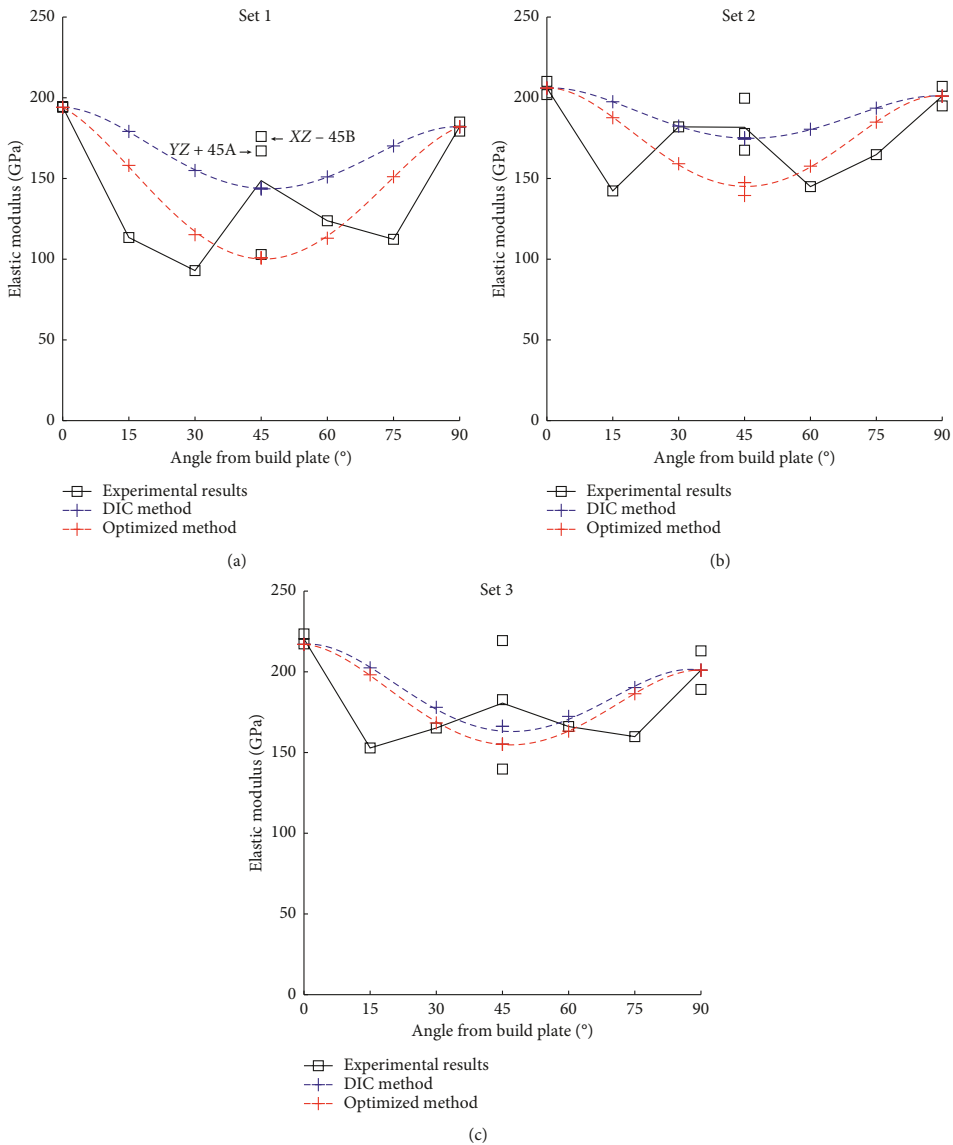
(a)

(b)

(c)

FIGURE 18: Elastic modulus in the load direction as measured directly, calculated based on the DIC measurements, and calculated based on the optimized elastic model for (a) as built condition, (b) aged condition, and (c) HIP + aged condition.

Therefore, care should be taken when orienting components in the build chamber to maximize the mechanical properties.

(iii) Two approaches for determining the anisotropic elastic constants are presented in this study. In the future, more experimental data will be included to consolidate the reliability and robustness of the determined elastic constants.

(iv) While all the tensile properties are influenced by the build angle of the test specimen relative to the build plate, the elastic modulus and the elongation at break show the highest dependence on build angle.

(v) Ageing has a large effect on the mechanical properties; it improves the elastic modulus, yield stress, and ultimate tensile strength, but reduces the elongation at break. Hot isostatic pressing (HIP)

before ageing increases the elongation at break at the expense of a reduction in elastic modulus, yield stress, and ultimate tensile strength. Furthermore, HIP does not reduce the scatter in mechanical properties among the tested samples, and evidence of the initial structure and texture is still apparent.

(vi) This study confirms that LPBF processing of IN718 introduces texture, and the variation in mechanical properties can be explained by crystallographic theories such as Schmid's theory.

Data Availability

The raw data required to reproduce these findings cannot be shared at this time as the data also form part of an ongoing study. The processed data required to reproduce these findings cannot be shared at this time as the data also form part of an ongoing study.

Conflicts of Interest

The authors declare that there are no conflicts of interest regarding the publication of this paper.

Authors' Contributions

The authors Even W. Hovig and Amin S. Azar contributed equally to this work.

Acknowledgments

References

[1] B. E. Carroll, T. A. Palmer, and A. M. Beese, "Anisotropic tensile behavior of Ti–6Al–4V components fabricated with directed energy deposition additive manufacturing," *Acta Materialia*, vol. 87, pp. 309–320, 2015.

[2] W. E. Luecke and J. A. Slotwinski, "Mechanical properties of austenitic stainless steel made by additive manufacturing," *Journal of research of the National Institute of Standards and Technology*, vol. 119, p. 398, 2014.

[3] T. Wang, Y. Zhu, S. Zhang, H. Tang, and H. Wang, "Grain morphology evolution behavior of titanium alloy components during laser melting deposition additive manufacturing," *Journal of Alloys and Compounds*, vol. 632, pp. 505–513, 2015.

[4] J. J. Lewandowski and M. Seifi, "Metal additive manufacturing: a review of mechanical properties," *Annual Review of Materials Research*, vol. 46, no. 1, pp. 151–186, 2016.

[5] L. Thijs, M. L. M. Sistiaga, R. Wauthle, Q. Xie, J.-P. Kruth, and J. Van Humbeeck, "Strong morphological and

[6] F. List, R. R. Dehoff, L. E. Lowe, and W. J. Sames, "Properties of Inconel 625 mesh structures grown by electron beam additive manufacturing," *Materials Science and Engineering: A*, vol. 615, pp. 191–197, 2014.

[7] N. Gardan and A. Schneider, "Topological optimization of internal patterns and support in additive manufacturing," *Journal of Manufacturing Systems*, vol. 37, pp. 417–425, 2015.

[8] C. C. Swan and I. Kosaka, "Voigt-Reuss topology optimization for structures with nonlinear material behaviors," *International Journal for Numerical Methods in Engineering*, vol. 40, no. 20, pp. 3785–3814, 1997.

[9] B. Vrancken, L. Thijs, J.-P. Kruth, and J. Van Humbeeck, "Heat treatment of Ti6Al4V produced by selective laser melting: microstructure and mechanical properties," *Journal of Alloys and Compounds*, vol. 541, pp. 177–185, 2012.

[10] T. Vilaro, C. Colin, and J.-D. Bartout, "As-fabricated and heat-treated microstructures of the Ti-6Al-4V alloy processed by selective laser melting," *Metallurgical and Materials Transactions A*, vol. 42, no. 10, pp. 3190–3199, 2011.

[11] E. Chlebus, K. Gruber, B. Kuźnicka, J. Kurzac, and T. Kurzynowski, "Effect of heat treatment on the microstructure and mechanical properties of Inconel 718 processed by selective laser melting," *Materials Science and Engineering: A*, vol. 639, pp. 647–655, 2015.

[12] T. Trosch, J. Strößner, R. Völkl, and U. Glatzel, "Microstructure and mechanical properties of selective laser melted Inconel 718 compared to forging and casting," *Materials Letters*, vol. 164, pp. 428–431, 2016.

[13] D. Tomus, Y. Tian, P. A. Rometsch, M. Heilmaier, and X. Wu, "Influence of post heat treatments on anisotropy of mechanical behaviour and microstructure of Hastelloy-X parts produced by selective laser melting," *Materials Science and Engineering: A*, vol. 667, pp. 42–53, 2016.

[14] T. C. T. Ting, *Anisotropic Elasticity: Theory and Applications*, Oxford University Press, New York, NY, USA, 1996.

[15] E. V. Morozov and V. V. Vasiliev, "Determination of the shear modulus of orthotropic materials from off-axis tension tests," *Composite Structures*, vol. 62, no. 3-4, pp. 379–382, 2003.

[16] J. C. Lippold, S. D. Kiser, and J. N. DuPont, *Welding Metallurgy and Weldability of Nickel-Base Alloys*, John Wiley and Sons, Hoboken, NJ, USA, 2011.

[17] R. Cozar and A. Pineau, "Morphology of γ'and γ" precipitates and thermal stability of inconel 718 type alloys," *Metallurgical Transactions*, vol. 4, no. 1, pp. 47–59, 1973.

[18] S. Singh Handa, J. Andersson, and M. Eynian, *Precipitation of carbides in a Ni-based superalloy*, Ph.D. thesis, Department of Engineering Science, University West, Trollhättan, Sweden, 2014.

[19] N. Saunders, Z. Guo, X. Li, A. Miodownik, and J.-P. Schille, "Modelling the material properties and behaviour of Ni-based superalloys," in *Proceedings of the 10th International Symposium on Superalloys*, pp. 849–858, Champion, PA, USA, September 2004.

[20] A. Oradei-Basile and J. F. Radavich, "A current TTT diagram for wrought alloy 718," in *Proceedings of Superalloys 718, 625 and Various Derivatives*, pp. 325–335, Pittsburgh, PA, USA, June 1991.

[21] A. Simchi, "Direct laser sintering of metal powders: mechanism, kinetics and microstructural features," *Materials Science and Engineering: A*, vol. 428, no. 1, pp. 148–158, 2006.

[22] M. E. Aydinöz, F. Brenne, M. Schaper et al., "On the microstructural and mechanical properties of post-treated additively manufactured Inconel 718 superalloy under quasistatic and cyclic loading," *Materials Science and Engineering A*, vol. 669, pp. 246–258, 2016.

[23] D. L. Bourell, H. L. Marcus, J. W. Barlow, and J. J. Beaman, "Selective laser sintering of metals and ceramics," *International Journal of Powder Metallurgy*, vol. 28, no. 4, pp. 369–381, 1992.

[24] M. Dressler, M. Röllig, M. Schmidt, A. Maturilli, and J. Helbert, "Temperature distribution in powder beds during 3D printing," *Rapid Prototyping Journal*, vol. 16, no. 5, pp. 328–336, 2010.

[25] D. H. Smith, J. Bicknell, L. Jorgensen et al., "Microstructure and mechanical behavior of direct metal laser sintered Inconel alloy 718," *Materials Characterization*, vol. 113, pp. 1–9, 2016.

[26] K. Amato, S. Gaytan, L. Murr et al., "Microstructures and mechanical behavior of Inconel 718 fabricated by selective laser melting," *Acta Materialia*, vol. 60, no. 5, pp. 2229–2239, 2012.

[27] X. Zhao, J. Chen, X. Lin, and W. Huang, "Study on microstructure and mechanical properties of laser rapid forming Inconel 718," *Materials Science and Engineering: A*, vol. 478, no. 1-2, pp. 119–124, 2008.

[28] F. Liu, X. Lin, C. Huang et al., "The effect of laser scanning path on microstructures and mechanical properties of laser solid formed nickel-base superalloy Inconel 718," *Journal of Alloys and Compounds*, vol. 509, no. 13, pp. 4505–4509, 2011.

[29] A. Simchi and H. Pohl, "Effects of laser sintering processing parameters on the microstructure and densification of iron powder," *Materials Science and Engineering: A*, vol. 359, no. 1-2, pp. 119–128, 2003.

[30] B. N. Turner and S. A. Gold, "A review of melt extrusion additive manufacturing processes: II. Materials, dimensional accuracy, and surface roughness," *Rapid Prototyping Journal*, vol. 21, no. 3, pp. 250–261, 2015.

[31] W. E. Frazier, "Metal additive manufacturing: a review," *Journal of Materials Engineering and Performance*, vol. 23, no. 6, pp. 1917–1928, 2014.

[32] M. Ni, C. Chen, X. Wang et al., "Anisotropic tensile behavior of in situ precipitation strengthened Inconel 718 fabricated by additive manufacturing," *Materials Science and Engineering: A*, vol. 701, pp. 344–351, 2017.

[33] O. Scott-Emuakpor, T. George, C. Holycross, J. Bruns, and A. Zearley, "Bending fatigue life comparison between DMLS and cold-rolled nickel alloy 718," in *Proceedings of the Prognostics and Health Management Solutions Conference (MFPT 2014)*, Virginia Beach, VA, USA, May 2014.

[34] M. M. Kirka, D. Greeley, C. Hawkins, and R. Dehoff, "Effect of anisotropy and texture on the low cycle fatigue behavior of Inconel 718 processed via electron beam melting," *International Journal of Fatigue*, vol. 105, pp. 235–243, 2017.

[35] V. Badiru Vhance and D. A. B. Liu, *Valencia, Additive Manufacturing Handbook: Product Development for the Defense Industry*, CRC Press Inc., Boca Raton, FL, USA, 2017.

[36] J.-P. Choi, G.-H. Shin, S. Yang et al., "Densification and microstructural investigation of Inconel 718 parts fabricated by selective laser melting," *Powder Technology*, vol. 310, pp. 60–66, 2017.

[37] X. Wang, T. Keya, and K. Chou, "Build height effect on the Inconel 718 parts fabricated by selective laser melting," *Procedia Manufacturing*, vol. 5, pp. 1006–1017, 2016.

[38] A. Keshavarzkermani, M. Sadowski, and L. Ladani, "Direct metal laser melting of Inconel 718: process impact on grain formation and orientation," *Journal of Alloys and Compounds*, vol. 736, pp. 297–305, 2018.

[39] A. S. Azar, E. Østby, and O. M. Akselsen, "Effect of hyperbaric chamber gas on transformation texture of the API-X70 pipeline weld metal," *Metallurgical and Materials Transactions A*, vol. 43, no. 9, pp. 3162–3178, 2012.

[40] L. Murr, S. Li, Y. Tian, K. Amato, E. Martinez, and F. Medina, "Open-cellular Co-base and Ni-base superalloys fabricated by electron beam melting," *Materials*, vol. 4, no. 4, pp. 782–790, 2011.

[41] L. E. Murr, E. Martinez, S. Gaytan et al., "Microstructural architecture, microstructures, and mechanical properties for a nickel-base superalloy fabricated by electron beam melting," *Metallurgical and Materials Transactions A*, vol. 42, no. 11, pp. 3491–3508, 2011.

[42] X. Wang, X. Gong, and K. Chou, "Review on powder-bed laser additive manufacturing of Inconel 718 parts," in *Proceedings of ASME 2015 International Manufacturing Science and Engineering Conference*, p. V001T02A063, American Society of Mechanical Engineers, Charlotte, NC, USA, 2015.

[43] SLM Solutions, "3D METALS, discover the variety of metal powders," October 2018, https://slm-solutions.com/sites/default/files/downloads/201en171023-01-001-powder_web.pdf.

[44] D. D. Gu, W. Meiners, K. Wissenbach, and R. Poprawe, "Laser additive manufacturing of metallic components: materials, processes and mechanisms," *International Materials Reviews*, vol. 57, no. 3, pp. 133–164, 2012.

[45] S. Ernst, "Postweld heat treatment of nonferrous high-temperature materials," in *ASM Handbook*, vol. 6, pp. 572–574, ASM International, Geauga County, OH, USA, 1993.

[46] F. Grytten, H. Daiyan, M. Polanco-Loria, and S. Dumoulin, "Use of digital image correlation to measure large-strain tensile properties of ductile thermoplastics," *Polymer Testing*, vol. 28, no. 6, pp. 653–660, 2009.

[47] R. Miller, A. Kolipaka, M. P. Nash, and A. A. Young, "Estimation of transversely isotropic material properties from magnetic resonance elastography using the optimised virtual fields method," *International Journal for Numerical Methods in Biomedical Engineering*, vol. 34, no. 6, article e2979, 2018.

[48] J. J. Vlassak and W. D. Nix, "Measuring the elastic properties of anisotropic materials by means of indentation experiments," *Journal of the Mechanics and Physics of Solids*, vol. 42, no. 8, pp. 1223–1245, 1994.

[49] A. Vogel, S. Diplas, A. Durant et al., "Reference dataset of volcanic ash physicochemical and optical properties," *Journal of Geophysical Research: Atmospheres*, vol. 122, no. 17, pp. 9485–9514, 2017.

[50] V. Gunenthiram, P. Peyre, M. Schneider, M. Dal, F. Coste, and R. Fabbro, "Analysis of laser–melt pool–powder bed interaction during the selective laser melting of a stainless steel," *Journal of Laser Applications*, vol. 29, no. 2, article 022303, 2017.

[51] M. Zhang, C.-N. Sun, X. Zhang et al., "Fatigue and fracture behaviour of laser powder bed fusion stainless steel 316L: influence of processing parameters," *Materials Science and Engineering: A*, vol. 703, pp. 251–261, 2017.

[52] Q. Jia and D. Gu, "Selective laser melting additive manufacturing of Inconel 718 superalloy parts: densification, microstructure and properties," *Journal of Alloys and Compounds*, vol. 585, pp. 713–721, 2014.

[53] A. Casanova, N. Martín-Piris, M. Hardy, and C. Rae, "Evolution of secondary phases in alloy ATI 718Plus® during processing," *MATEC Web of Conferences*, vol. 14, article 09003, 2014.

[54] E. McDevitt, S. Oppenheimer, R. Kearsey, and J. Tsang, *Crack Growth Behavior in ATI 718Plus® Alloy, Materials Science Forum*, Trans Tech Publications, Zürich, Switzerland, 2012.

[55] X. Wang, X. Gong, and K. Chou, "Review on powder-bed laser additive manufacturing of Inconel 718 parts," *Proceedings of the Institution of Mechanical Engineers, Part B: Journal of Engineering Manufacture*, vol. 231, no. 11, pp. 1890–1903, 2017.

[56] K. M. Knowles and P. R. Howie, "The directional dependence of elastic stiffness and compliance shear coefficients and shear moduli in cubic materials," *Journal of Elasticity*, vol. 120, no. 1, pp. 87–108, 2014.

[57] J. Jung, J. I. Yoon, J. G. Kim, M. I. Latypov, J. Y. Kim, and H. S. Kim, "Continuum understanding of twin formation near grain boundaries of FCC metals with low stacking fault energy," *NPJ Computational Materials*, vol. 3, no. 1, p. 21, 2017.

6.2. Paper 2 - Mechanical Properties of AlSi10Mg Processed by Laser Powder Bed Fusion at Elevated Temperature

Mechanical Properties of AlSi10Mg Processed by Laser Powder Bed Fusion at Elevated Temperature

Even W. Hovig, Amin S. Azar, Mohammed Mhamdi and Knut Sørby

Abstract AlSi10Mg processed by laser powder bed fusion is expected to have remarkable mechanical properties due to the dominant cellular microstructure. Nevertheless, the as-processed material is known to contain significant residual stresses, as well as a textured microstructure resulting in anisotropic mechanical properties. To mitigate these problems, a retrofitted heating system was used to elevate the process temperature to 200 °C. The characterization results show low levels of porosity, anisotropy, and residual stress. Furthermore, the effect of three heat treatment conditions (as-built, stress relief, and T6) on the tensile properties was investigated. For this purpose, 14 tensile samples were built in seven different orientations. Digital image correlation was used to understand the deformation mechanism for each heat treatment condition. It was observed that the as-built material has comparable properties to the stress relieved condition, while T6 heat treatment resulted in increased ductility. Based on the results, LPBF processing of AlSi10Mg at elevated temperature can potentially eliminate the need for post-process stress relief heat treatment.

Keywords Powder bed fusion · Laser melting · Additive manufacturing · Residual stress · Tensile properties · Anisotropy · Digital image correlation

Introduction

AlSi10Mg processed by laser powder bed fusion (LPBF) has received significant attention in the scientific community. Challenges with respect to microstructure, heat treatment, and anisotropy are still limiting the adaptation in the industry, however [1]. The material is known to have a high degree of residual stresses and anisotropy in the as-built condition [1–5]. T6 heat treatment (solution treatment plus artificial ageing) is known to reduce both the residual stresses and the anisotropy at the cost of strength

E. W. Hovig (✉) · K. Sørby
Norwegian University of Science and Technology, Trondheim, Norway
e-mail: even.w.hovig@ntnu.no

A. S. Azar · M. Mhamdi
SINTEF Industry, Oslo, Norway

and hardness, due to the recrystallization and grain growth of the microstructure [2, 5]. Stress relief is another commonly used heat treatment, as suggested by some of the major powder suppliers [6–8], which reduces the residual stresses and leaves the microstructure intact [9].

The effect of (pre-) heating the build platform on the microstructure and mechanical properties of AlSi10Mg and the similar alloy AlSi12Mg has been reported in several studies [10–12]. The main findings suggest that pre-heating the build platform can reduce the quantity and size of internal defects, reduce the residual stresses, and consequently increase the usability of the process and material.

In this work, we cover the microstructure, residual stresses, and tensile properties of AlSi10Mg processed by laser powder bed fusion at elevated bed temperature. To investigate the effect of the elevated temperature on the anisotropy of the material, tensile specimens processed at different orientations are studied.

Materials and Method

Specimen Preparation

The AlSi10Mg specimens was prepared by the Concept Laser M2 Cusing machine. The AlSi10Mg powder feedstock was supplied by the machine vendor (CL31Al by Concept Laser). The following processing parameters were used: laser power $P = 200$ W, laser scan velocity $v = 1400$ mm/s, layer thickness $t = 30\ \mu$m, hatch spacing $h = 97.5\ \mu$m. Prior to the layer fusion, each layer was pre-heated by a 50 W pre-scan. The build platform was heated from below using a retrofitted heating system to keep the build platform at 200 °C throughout the entire process. The employed scan strategy was the 'island' type by Concept Laser, with 2 mm islands with an angular shift of 45° and an XY-shift of 0.4 mm between each layer. The processing parameters were selected based on the previous study of the same machine and material which resulted in a relative density of 99.90% [13].

Three sets of 14 rectangular blocks were processed by LPBF at seven different orientations (0° to 90° at 15° increments with respect to the build platform). The blocks were then heat treated before machined to rectangular cross-sectional tensile specimens as shown in Fig. 1a. Two cantilever beams aligned in the X and Y direction
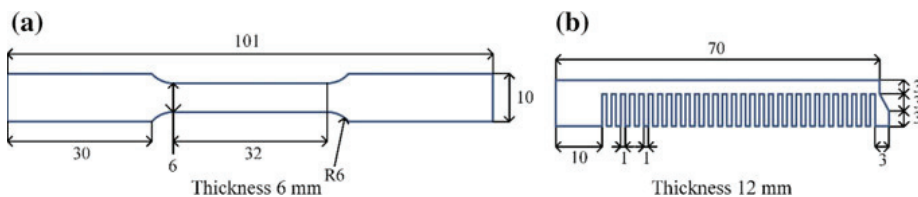
Fig. 1 Dimensions of tensile specimens (**a**), and cantilever beams (**b**). All units in mm

of the LPBF machine (Fig. 1b) were manufactured to measure the magnitude of the released residual stresses. An additional set of two cantilever beams were manufactured using a laser scan speed of 1200 mm/s without heating in the build plate, to act as a control for the residual stress investigations.

Heat Treatment

Each of the three sets of tensile specimens was subjected to different heat treatments. The first set received no heat treatment (denoted as AB), while the second set was stress relieved at 300 °C for 2 h following air cooling to room temperature (denoted as SR). The last set was solution annealed at 536 °C for 2 h in argon atmosphere followed by water quenching, before an artificial ageing at 160 °C for 12 h followed by air cooling to room temperature (denoted as T6).

Residual Stress

To get insight into the residual stresses of the material, the deflection in Z-direction in the cantilever beams after cutting with wire-EDM was measured with a portable CMM (Leica AT960). The inherent strains and stresses were calculated with the calibration feature in the Simufact Additive 4.0 analysis software using an element size of 0.5 mm and the iterative sparse solver.

Tensile Test

The tensile tests were carried out in a Zwick/Roell Z250 with a 50 kN load cell at a displacement rate of 1 mm/min. The displacement field on two perpendicular sides of each specimen was captured with a commercial DIC system (VIC 3D). A detailed description of the DIC system and set-up is given in [14].

Microscopy

For SEM imaging and EDS investigations, the samples were prepared by mechanical grinding and polishing, followed by a single step electropolishing using standard Struers recipe. The microscope is an FEI Nova NanoSEM 650 ultralow vacuum field emission gun scanning electron microscope (SEM) equipped with an X-Max 50 mm^2 EDS detector from Oxford Instruments.

## Results and Discussion

Residual Stress

The deflection in Z-direction after cutting the cantilever beams processed at 200 °C was measured to 0.22 and 0.23 mm for the beams aligned with the X and Y direction, respectively. The corresponding displacements in the cantilever beams processed at room temperature were measured to 2.723 and 2.808 mm. The calibration process in Simufact Additive 4.0 estimates the inherent strains before calculating the displacement after the cutting process. The inherent strains are then changed as the calibration process iterates until the least-squares error is below 3%. The resulting inherent strains are $\in_x = -0.00025$, $\in_y = -0.00033$ at 200 °C and $\in_x = -0.00458$, $\in_y = -0.00600$ at room temperature. Note that the inherent strains are specific to the current process parameters and material. The simulated residual stresses, corresponding to the measured displacement for the two processing conditions, are shown in Fig. 2.

The effective stress distribution in the specimens built at 200 °C is reduced by approximately 40%, down from a maximum of 370 MPa when processed at room temperature to a maximum of 210 MPa. The reduction of residual stress is attributed to the lower temperature gradient between the melt pool and substrate or previously fused layers, reducing the difference in thermal expansion throughout the component. The indications of the reduced residual stress can be inferred from the displacement after the cantilever beam is cut from its supports. The displacement is calculated based on the inherent strains, which in turn are estimated from the measured displacement. The error between measured displacement and calculated displacement is less than 3% for both processing conditions.

According to simulations by Sehrt et al. [15], a temperature of 300 °C is necessary to reduce residual stresses. This is dependent on the remaining parameters, however, and as demonstrated here, 200 °C seems sufficient to significantly reduce the residual stresses with the current process parameters. Bagherifard et al. [2] demonstrate that the laser parameters may be adjusted such that a substrate temperature of 150 °C provides a reduction of residual stresses.

Tensile Properties

Figure 3 plots the Cauchy stress against the Lagrange strain as calculated based on the DIC displacement fields for all specimens. Details about DIC, Cauchy stress, and Lagrange strain can be found in [14]. As can be seen, the AB and SR heat treatment conditions behave similarly with a relatively high yield strength and ultimate tensile strength (UTS) and low elongation at break. As expected, the T6 heat treatment condition increases the elongation at break at the cost of strength.
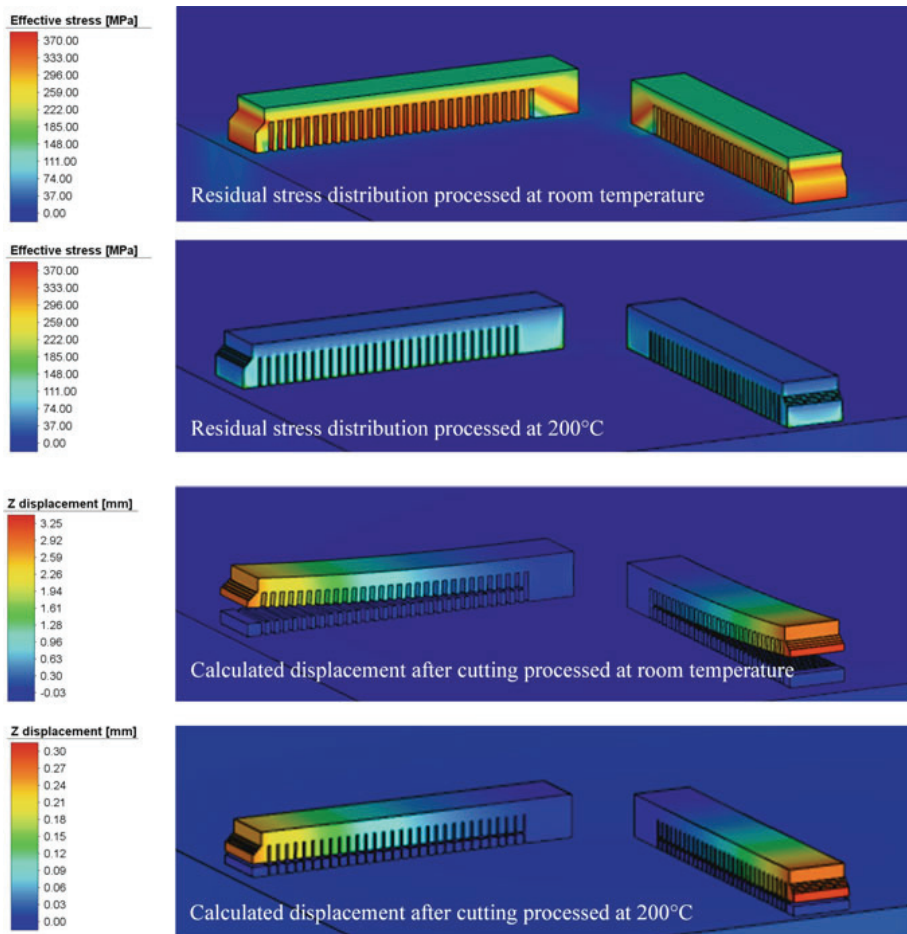
Fig. 2 Residual stress distribution and calculated displacement after cutting for AlSi10Mg processed at room temperature and at 200 °C

Figure 4 shows selected tensile properties plotted against the build orientation for each specimen. The build orientation does not appear to alter the elastic modulus for the applied heat treatment conditions, although the scatter in the data is substantial. This suggests that the crystallographic texture, if any, has a limited effect on the elastic anisotropy. Hitzler et al. [4] found the elastic modulus to be sensitive to the orientation when processed at elevated temperature, but this is attributed to deviations in their applied laser scan patterns. Tang et al. [3] report no significant sensitivity in the elastic modulus with respect to orientation, which further suggests that the crystallographic texture is insignificant with respect to anisotropy in the elastic behavior.

The yield strength and UTS appear to take a dip at 15° before steadily increasing as the specimens are raised towards 75° for the T6 heat treatment condition, which can be a result of retained melt pool boundaries even after recrystallization. There is no apparent correlation between build orientation and strength for the AB and

Fig. 3 Cauchy stress plotted against the Lagrange strain for all 14 samples from each of the three heat treatment conditions
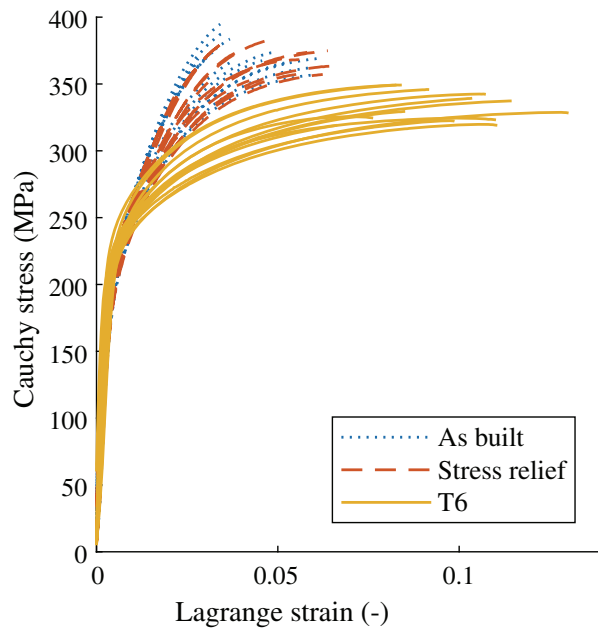
SR heat treatment conditions. Interestingly, the elongation at break increases as the specimens are tilted from 0° (parallel to the build plate) to 90° (perpendicular to the build plate) in the AB and SR heat treatment conditions. This plastic anisotropy suggests that a crystallographic textured microstructure might influence the failure mode, as observed on, e.g. LPBF Inconel 718 by [14, 16]. As the specimens are raised from 0° to 90°, the angle between the load direction and the assumed preferred orientation in the microstructure changes, either promoting or limiting mode I type failure. Another explanation of the plastic anisotropy can be the effect of the melt pool boundaries, and how they align with the load direction, which is discussed in the next section.

The average tensile properties for each heat treatment condition are listed in Table 1. As mentioned, the AB and SR heat treatment conditions show no significant difference in tensile properties. This is attributed to the elevated temperature in the build plate during LPBF processing, resulting in a great reduction of residual stresses. Consequently, SR treatment might be considered superfluous, eliminating a step in the process chain. The average elongation at break is doubled after T6 treatment, but the yield strength and UTS are reduced by approximately 10% as compared to AB and SR. Both the elastic and plastic Poison's ratios are slightly reduced in the T6 condition as well. The Poisson's ratio in the elastic region is determined according to ASTM E132-17. The Poisson's ratio in the plastic region is the average of the local Poisson's ratios for each data point for each point above the yield strength (~175 points).
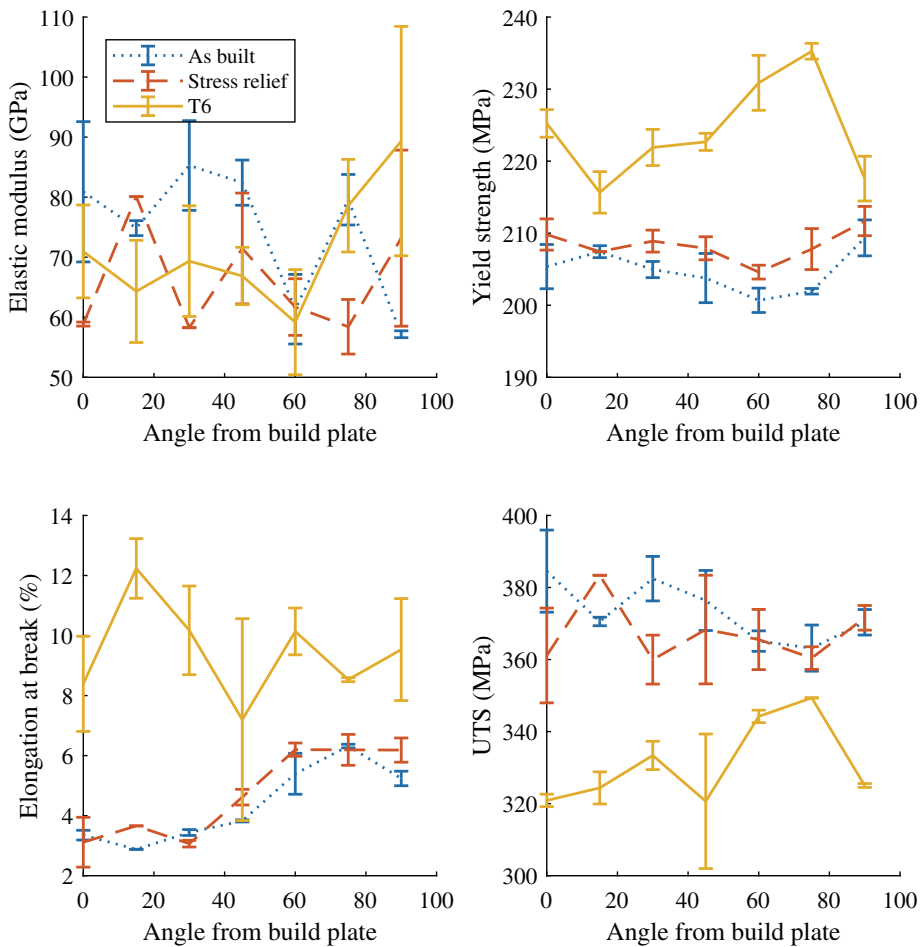
Fig. 4 Tensile properties plotted as a function of specimen orientation with respect to the build platform

Microstructural Investigations

Figure 6 shows SEM images of the loaded cross section at low magnification for AB and T6 heat treatment at 0°, 45°, and 90° orientation. The T6 heat treatment (d–f) mostly homogenizes the microstructure and removes the melt pool boundaries which are clearly visible in the AB condition (a–c).

In the as-built condition, the microstructure is fine-grained with a cellular-dendritic structure, with Si-rich cell-boundaries (Fig. 6a). During T6 heat treatment, the microstructure is recrystallized, and the eutectic Si structure formed spheroidized particles during the artificial ageing (Fig. 6b, c). The findings are comparable to [2, 17] where the LPBF specimens were processed both at room temperature and at elevated temperature. Bagherifard et al. report that the grain size is finer in the melt
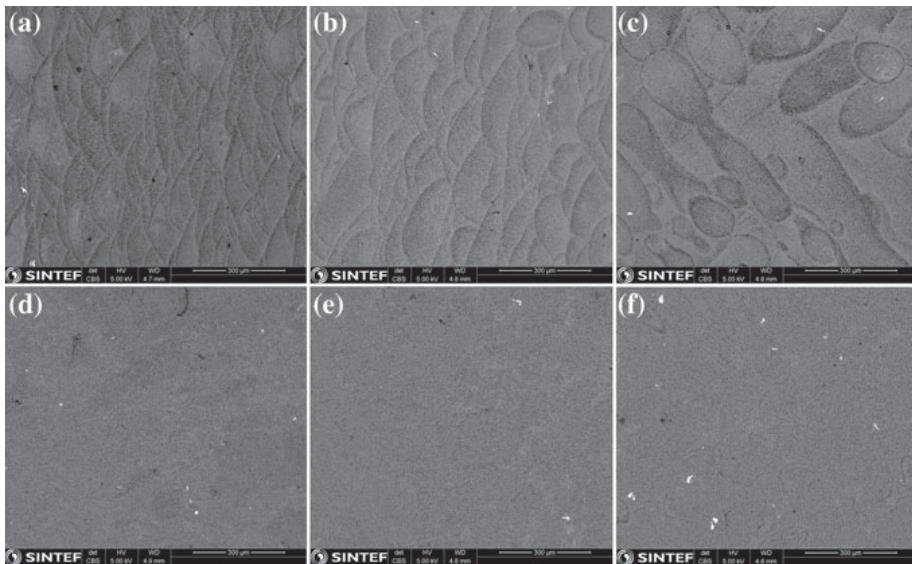
Fig. 5 SEM images of **a** AB 0°, **b** AB 45°, **c** AB 90°, **d** T6 0°, **e** T6 45°, **f** T6 90°

Table 1 Average tensile properties for each heat treatment condition

Condition	E (GPa)	Yield (MPa)	UTS (MPa)	ε (%)	$v_{\text{elastic}}(-)$	$\overline{v}_{\text{plastic}}(-)$
As-built (AB)	74.5 ± 12.3	204.8 ± 3.6	373.2 ± 10.4	4.35 ± 1.28	0.355 ± 0.026	0.459 ± 0.006
Stress relieved (SR)	66.0 ± 11.2	208.3 ± 2.8	367.2 ± 12.1	4.72 ± 1.48	0.350 ± 0.029	0.459 ± 0.004
T6	71.2 ± 14.3	224.2 ± 7.2	331.1 ± 13.56	9.46 ± 2.36	0.343 ± 0.041	0.437 ± 0.014
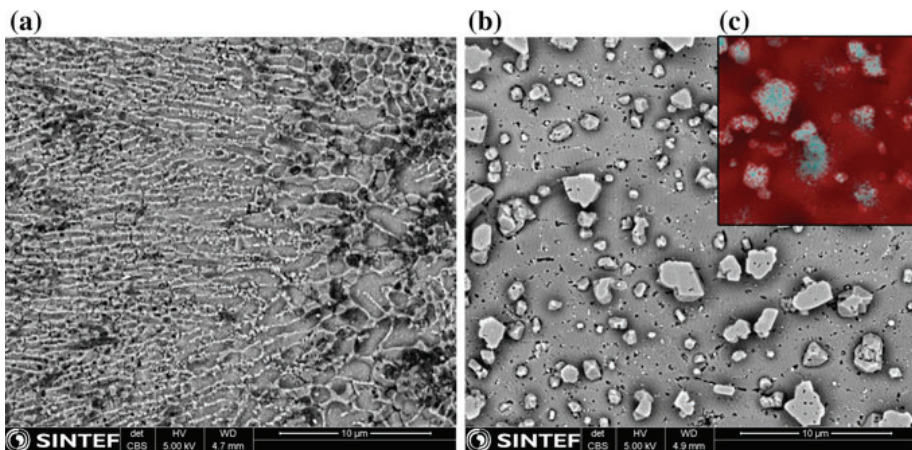
Fig. 6 SEM images of **a** as-built heat treatment condition—0° specimen, **b** T6 heat treatment condition—0° specimen, **c** EDS map of Al (red) and Si (cyan) of the T6 condition (same scale)

pool and coarser on the boundary of the melt pool only when processing at room temperature [2]. The complete homogenization of the microstructure observed by [2] when processing at elevated temperature is not observed in this study. As can be seen in Fig. 6a, the microstructure is still coarser at the right-hand side of the image, corresponding to the boundary of the melt pool. Brandl et al. [17] also report a slightly inhomogeneous microstructure even when processed at 300 °C. According to Xiong et al. [18], anisotropic tensile properties are driven by the distribution of the melt pool boundaries on the load bearing cross section, irrespective to the microstructural texture. Even though the melt pool boundaries in the AB condition is clearly visible, no definitive elastic anisotropy is observed in this study. The elongation at break indicates plastic anisotropy, which as mentioned can be attributed to the melt pool boundaries observed in the AB condition Fig. 5a–c.

Summary and Conclusions

This study demonstrates the effect of elevating the build plate temperature during LPBF processing of AlSi10Mg on the build stresses, tensile properties, and microstructure. Elevating the build plate temperature has several positive effects, such as:

- An estimated reduction in the effective residual stress by approximately 40%.
- Potentially eliminating the need for SR treatment of AlSi10Mg components processed by LPBF. For parts where toughness is considered more important than strength, T6 heat treatment can increase the ductility at the cost of a reduction in strength.
- Any crystallographic texture appears to be insignificant in the elastic part of the flow curve, as there is no apparent relationship between elastic modulus and build orientation. In a future work, the material should be investigated with EBSD to get a better understanding of the (preferred) grain orientation.

The elongation at break in the AB and SR conditions is linearly dependent on build orientation. Specimens built parallel to the build plate exhibits the lowest elongation at break. The recrystallization of the microstructure after T6 heat treatment eliminates the sensitivity to build orientation and effectively doubles the elongation at break, at the cost of a slight reduction in strength.

References

1. Trevisan F, Calignano F, Lorusso M, Pakkanen J, Aversa A, Ambrosio E, Lombardi M, Fino P, Manfredi D (2017) On the selective laser melting (SLM) of the AlSi10Mg alloy: process, microstructure, and mechanical properties. Materials 10(1):76
2. Bagherifard S, Beretta N, Monti S, Riccio M, Bandini M, Guagliano M (2018) On the fatigue strength enhancement of additive manufactured AlSi10Mg parts by mechanical and thermal post-processing. Mater Des 145:28–41
3. Tang M, Pistorius PC (2017) Anisotropic mechanical behavior of AlSi10Mg parts produced by selective laser melting. JOM 69(3):516–522
4. Hitzler L, Janousch C, Schanz J, Merkel M, Heine B, Mack F, Hall W, Öchsner A (2017) Direction and location dependency of selective laser melted AlSi10Mg specimens. J Mater Process Technol 243:48–61
5. Yang P, Rodriguez MA, Deibler L, Jared B, Griego J, Kilgo A, Allen A, Stefan D (2018) Effect of thermal annealing on microstructure evolution and mechanical behavior of an additive manufactured AlSi10Mg part. J Mater Res 33(12):1701–1712
6. Renishaw plc., Data sheet: AlSi10Mg-0403 (200 W) powder for additive manu-facturing, 2019. https://resources.renishaw.com/en/details/data-sheet-alsi10mg-0403-200-w-powder-for-additive-manufacturing–73121. Accessed 20 Aug 2019
7. EOS GmbH, EOS Aluminium AlSi10Mg (2019). https://cdn0.scrvt.com/eos/f3f4bf485d78f2dd/b010c05abe97/AlSi10Mg-090-M400_Flexline_Material_data_sheet_09-15_en.pdf. Accessed 20 Aug 2019
8. edmit inc., Material Data Sheet CL 30AL/ CL 31AL Aluminium alloy (2019). http://edmitinc.com/download/EDMIT_ALUMINUM_AlSi12_AlSi10Mg.pdf. Accessed Aug 20 2019
9. Uzan NE, Shneck R, Yeheskel O, Frage N (2017) Fatigue of AlSi10Mg specimens fabricated by additive manufacturing selective laser melting (AM-SLM). Mater Sci Eng A 704:229–237
10. Hovig EW, Holm HD, Sørby K (2019) Effect of processing parameters on the relative density of AlSi10Mg processed by laser powder bed fusion. Singapore, Springer Singapore, pp 268–276
11. Siddique S, Imran M, Wycisk E, Emmelmann C, Walther F (2015) Influence of process-induced microstructure and imperfections on mechanical properties of AlSi12 processed by selective laser melting. J Mater Process Technol 221:205–213
12. Romano S, Brückner-Foit A, Brandão A, Gumpinger J, Ghidini T, Beretta S (2018) Fatigue properties of AlSi10Mg obtained by additive manufacturing: defect-based modelling and prediction of fatigue strength. Eng Fract Mech 187:165–189
13. Reiersen M (2019) Microstructural analysis of SLM AlSi10Mg and Al7075 alloys—topology optimisation in redesigning novel parts to be produced by SLM, Department of Chemistry, University of Oslo
14. Hovig EW, Azar AS, Grytten F, Sørby K, Andreassen E (2019) Determination of anisotropic mechanical properties for materials processed by laser powder bed fusion. Adv Mater Sci Eng
15. Sehrt JT, Witt G, Müller B, Töppel T, Hoeren KPJ, Reinarz B (2015) Less residual stresses in laser beam melting by investigating on supports, powder layer properties, powder preheat-ing and scanning strategies. In: Presentation held at International Symposium on Additive Manufacturing, February 25th-26th, 2015, ISAM, Dresden
16. Ni M, Chen C, Wang X, Wang P, Li R, Zhang X, Zhou K (2017) Anisotropic tensile behavior of in situ precipitation strengthened Inconel 718 fabricated by additive manufacturing. Mater Sci Eng A 701:344–351
17. Brandl E, Heckenberger U, Holzinger V, Buchbinder D (2012) Additive manufactured AlSi10Mg samples using selective laser melting (SLM): microstructure, high cycle fatigue, and fracture behavior. Mater Des 34:159–169
18. Xiong ZH, Liu SL, Li SF, Shi Y, Yang YF, Misra RDK (2019) Role of melt pool boundary condition in determining the mechanical properties of selective laser melting AlSi10Mg alloy. Mater Sci Eng A 740–741:148–156

6.3. Paper 3 - An investigation of the anisotropic properties of heat-treated maraging steel grade 300 processed by laser powder bed fusion

ORIGINAL ARTICLE

An investigation of the anisotropic properties of heat-treated maraging steel grade 300 processed by laser powder bed fusion

Even W. Hovig[1] · Amin S. Azar[2] · Klas Solberg[1] · Knut Sørby[1]

Abstract

In order to explore the possibilities enabled by laser beam powder bed fusion of metals (PBF-LB/M), reliable material models are necessary to optimize designs with respect to weight and stiffness. Due to the unique processing conditions in PBF-LB/M, materials often develop a dominating microstructure that leads to anisotropic mechanical properties, and thus isotropic material models fail to account for the orientation-dependent mechanical properties. To investigate the anisotropy of 18Ni300 maraging steel, tensile specimens were built in seven different orientations. The specimens were heat treated at two different conditions and tested for their tensile properties using digital image correlation (DIC) technique. The microstructure and fracture surfaces are investigated with scanning electron microscope and electron backscatter diffraction. The tensile properties are typical for the material, with a yield strength in the range of 1850 MPa to 1950 MPa, and ultimate tensile strength in the range of 1900 MPa to 2000 MPa. The elastic modulus is 180 GPa, and the elongation at fracture is in the range of 2–6% for all specimens. The strain fields analysed with DIC reveals anisotropic straining in both the elastic and plastic parts of the flow curve for both direct ageing and solution treatment plus ageing specimens. In the former condition, the elastic anisotropy is dictated by the fraction of melt pool boundaries on the transverse surfaces of the specimens. When the material is solution treated prior to ageing, the melt pool boundary effect was supressed.

1 Introduction

Maraging steels are categorized as FeNi alloys with dominating martensitic microstructure at room temperature. This class of alloys can be hardened through a uniform precipitation mechanism, reflecting the name maraging steel (martensitic + ageing). Maraging steels are usually graded by the nominal axial tensile strength in the imperial unit *ksi* (or sometimes in *MPa*), which depends on the chemical composition. In additive manufacturing (AM), specifically laser beam powder bed fusion (PBF-LB/M), maraging steel grade 300 is the most commonly used grade [1]. The steel is also known as 18% Ni maraging 300 (USA), 1.2709 (Europe), and X3NiCoMoTi 18-9-5 (Germany). The material is easily machined in its

annealed state, while higher strength and hardness can be obtained after proper ageing heat treatment [2, 3], making it suitable for several applications. Among other applications, the PBF-LB/M material is used in the tooling industry such as injection moulding [4] and aluminium casting [5–7].

The mechanical properties of maraging steel grade 300 (hereafter denoted as 18Ni300) processed by PBF-LB/M depends on several variables in the AM process chain. In the AM value chain, three factors, namely, feedstock properties, PBF-LB/M process parameters, as well as post-processing conditions, influence the mechanical response of the material. Feedstock properties such as particle size distribution and morphology, chemical composition, and apparent density directly affect the processability of the material [8], while laser processing parameters such as laser power (P), laser scan velocity (v), hatch spacing (h), layer thickness (t), and scan strategy influence the relative density, microstructure, and mechanical properties. Post-processing such as solution annealing will soften the material and allow for easy machining [2], while precipitation hardening will increase the hardness and strength [9, 10] at the expense of bulk ductility.

✉ Even W. Hovig
   even.w.hovig@ntnu.no

1   Department of Mechanical and Industrial Engineering, Norwegian University of Science and Technology, Trondheim, Norway

2   SINTEF Industry, Oslo, Norway

Unique to AM and PBF-LB/M in particular, materials develop a fine-grained columnar microstructure due to the rapid and directional cooling conditions and epitaxial growth [10]. Because of the disproportional grain geometry, the columnar microstructure may result in anisotropic behaviour [11–13]. Due to increased geometrical complexity, understanding the influence of build orientation on the mechanical response of the additively manufactured materials is of great importance. Table 1 summarizes the tensile properties of PBF-LB/18Ni300. There is significant variation in elastic modulus, yield strength, ultimate tensile strength, and elongation at fracture between the different studies. Build orientation, processing parameters, and heat treatment schemes all influence the mechanical properties. Mooney et al. [9] investigated the influence of build orientation and heat treatments on the plastic anisotropy of PBF-LB/18Ni300 and observed considerable anisotropy in the material, especially in the as-built condition. They reported that tailored heat treatments can reduce the anisotropy at the expense of material's yield strength. Vishwakarma et al. [14] demonstrates how the ductility can be significantly approved (elongation at fracture above 10%), but at the cost of a large reduction in strength. With the exception of the latter study, the elongation at fracture ranges between 1.7 and 6.1%. The yield strength and ultimate tensile strength are in the range of 1700–2100 MPa. The elastic modulus ranges from 142.5 GPa found by Wu et al. [15] to 219 GPa found by Becker et al. [16]. The ageing temperature of 550 °C in the latter study might explain the low elastic modulus.

There are two main sources of anisotropy: preferred crystallographic orientation and alignment in the microstructure of secondary phases and inclusions [21]. The latter is typically the main contributor to plastic anisotropy, while the former is often observed in elastically anisotropic materials. The PBF-LB/M is known to bring on both sources of anisotropy in a range of materials [9, 11, 13, 21–23]. In metals with cubic crystal structure, the plastic anisotropy resulting from preferred crystallographic orientation is limited because of numerous slip planes that can be activated in different orientations. This suggests that microstructural alignment of the secondary phases and inclusions are more likely to prevail. Xiong et al. observed that the fracture occurred along the melt pool boundaries (MPB) and that the fraction of load-bearing MPBs in the cross-section can be a source of anisotropic plastic tensile response [24].

The heat treatment for PBF-LB/18Ni300 is typically (as suggested by material vendors) a two-stage treatment starting with a solution treatment followed by ageing. The standards are not developed for AM applications. However, the recommended solution treatment, ageing temperatures, and holding times might not be appropriate for the PBF-LB/M material. Bai et al. [10] investigates the effect of temperature and holding time for solution treatment and ageing of PBF-LB/18Ni300 and finds that a good combination of hardness and strength is achieved with a direct ageing at 520 °C for 6 h. As shown by Mooney et al. [9], this heat treatment scheme also reduces the plastic anisotropy, yet higher strength can be achieved with lower ageing temperatures.

Table 1 Summary of orientation-dependent tensile properties of PBF-LB/18Ni300

Process	Orientation	E [GPa]	Yield [MPa]	UTS [MPa]	ε_f [%]	HT	Reference
Forged bar	0°/90°[2]	183	1861	1930	5 / 4	Aged (482 °C)	MMPDS-11 (2016) [17]
PBF-LB	0°	219	1720	1800	4.5	Annealed + aged (490 °C)	Becker et al. (2016) [16]
	90°	217	1750	1850	5.1		
PBF-LB	0°	-	1953	2216	3.2	Aged (480 °C)	Suryawanshi et al. (2017) [18]
	90°	-	1833	2088	3.1		
PBF-LB	0°	-	1882	1943	5.6	Annealed + aged (490 °C)	Tan et al. (2018) [12]
	90°	-	1818	1898	4.8		
PBF-LB	0°	178	1901	1958	5.9	Aged (490 °C)	Mooney et al. (2019) [9]
	45°	183	1925	1984	4.4		
	90°	178	1893	1958	6.1		
PBF-LB	90°	-	1744	1786	5	Annealed + Aged (480 °C)	Elangeswaran et al. (2020) [19]
PBF-LB	90°	142.5	2065	2225	4.2	Aged (550 °C)	Wu et al. (2020) [15]
PBF-LB	0°	-	920	1529	10.6	Annealed + aged (520 °C)	Vishwakarma et al. (2020) [14]
	45°	-	830	1568	12.7		
	90°	-	886	1552	10.7		
PBF-LB	0°	177	1701	1822	3.3	Aged (480 °C)	Oliveira et al. (2021) [20]
	45°	144	1714	1727	1.7		
	90°	145	1710	1741	4.3		

[2] Orientation for bar stock refers to longitudinal (90°) and transverse (0°) direction of the forged bar

Table 2 Nominal chemical composition of 18Ni300

Element	Fe	C	Mn	Si	Cr	Ni	Mo	Co	Ti	Al
Wt%	Bal.	<0.03	<0.1	<0.1	<0.3	18.0	4.8	9.0	0.7	0.1

Although plastic anisotropy of PBF-LB/18Ni300 is set forth in preceding articles, this study provides a systematic investigation of the strain behaviour in both the elastic and plastic regions of the flow curve of tensile specimens built in seven different orientations in the PBF-LB/M process subjected to two different heat treatments. Digital image correlation (DIC) is utilized to capture the strain fields on the surface of rectangular tensile specimens. By using tensile tests with DIC combined with microstructure investigation, this study demonstrates how the fraction of load bearing melt pool boundaries directly influences the transverse strain anisotropy. Furthermore, it is demonstrated how this effect can be minimized by opting for a solution annealing heat treatment prior to precipitation hardening.

2 Material and methods

2.1 Specimen preparation

A total of 42 tensile specimens were prepared in a Concept Laser M2 Cusing PBF-LB/M machine in a nitrogen atmosphere with monitored oxygen content below 0.2%. The feedstock material was supplied by Sandvik Osprey®. The nominal chemical composition is provided in Table 2. The powder morphology was analysed with a Malvern Morphologi G3 system. A particle size distribution with a mean diameter of 24 μm, a lower cut-off at 5 μm, and upper cut-off at 63 μm was characterized. The average circularity of the powder particles is 0.93, where a circularity of 1 indicates a perfect circle [25]. Laser parameters for the PBF-LB/18Ni300 specimens were determined in a previous study [26] and are summarised in Table 3.

The tensile specimens were prepared in two sets of 21 specimens, subjected to different heat treatments (HT). Within each set, three identical specimens were prepared at 0°, 15°, 30°, 45°, 60°, 75°, and 90° angles with respect to the building plate. The specimens were built using the 'island' scan strategy from concept laser with 5 mm × 5 mm islands with an angular shift of 45° and XY shift of 1 mm. Following PBF-LB/M processing, the tensile specimens were machined to target standard dimensions according to Fig. 1 in order to preclude the process induced surface roughness effects. The two different heat treatments are solution treatment (815 °C, 1

Fig. 1 Dimensions of tensile specimens. All dimensions in mm. AOI 1 and 2 indicate the strain fields captured with the digital image correlation system

h) plus ageing (500 °C, 5 h), denoted as SA + A, and direct ageing (500 °C, 5 h), denoted as DA. All specimens were rotated 5° around the Z-axis to avert the re-coater colliding with long flat edges of the samples, intending to mitigate powder coating failures. The specimens were built in two separate builds, depending on the HT. Overhanging samples were built with block-type support structures, which were removed using electrical discharge machining (EDM). Figure 2 illustrates the orientations of all the specimens.
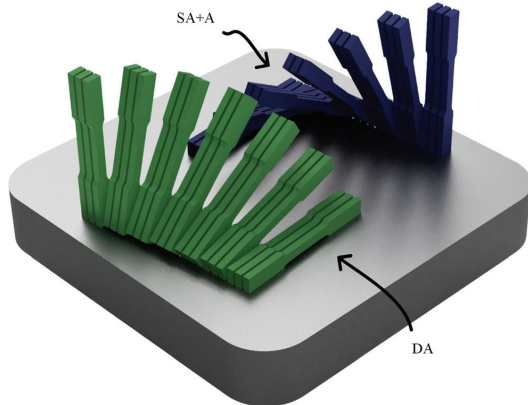
Table 3 Processing parameters [26]

Laser power [W]	Hatch spacing [mm]	Scan velocity [mm/s]	Layer thickness [mm]
180	0.105	650	0.03

Fig. 2 Illustration of the specimens on the build plate

2.2 Mechanical evaluation

The tensile tests were carried out in an MTS 809 Axial Test System with a 100 kN load cell at room temperature, equipped with a DIC system from Vic3D to capture the evolution of strain fields. A detailed description of the DIC setup is provided in [27]. Post-processing of the DIC data was performed in a combination of Vic3D Version 7 and self-developed MATLAB code.

2.3 Microstructure investigation

The microstructure was characterised using scanning electron microscopy (SEM) after electro-etching of the samples using Struers A2 electrolyte solution with vendor's recommended steel etching parameters. The fracture surfaces after tensile testing were also investigated by SEM. A selective area of the material in the SA + A was investigated by the electron
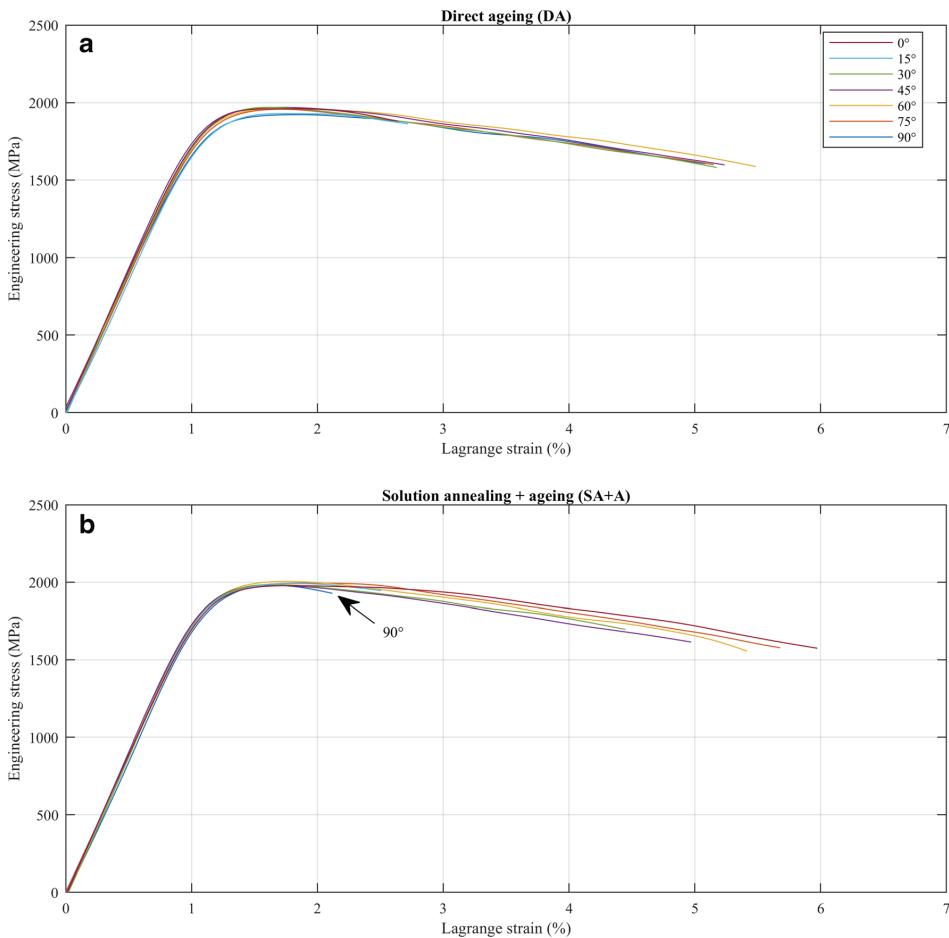
Fig. 3 Engineering stress and Lagrange strain plotted for a selected specimen of each orientation for direct ageing (**a**) and solution treatment + ageing (**b**)

backscattered diffraction (EBSD) technique to understand the crystal orientation and microstructure of the material. The EBSD maps were acquired from an area of 300 μm × 300 μm and scanned with a step size of 200 nm corresponding to 2000 datapoints. The details of the microscopy and EBSD methods are given in [11] by the current authors.

3 Results and discussion

3.1 Mechanical properties

Figure 3 shows the engineering stress and Lagrange strain for one tensile specimen for each orientation for direct ageing (a) and solution treatment + ageing (b). Except for elongation at fracture, the flow curves are relatively homogeneous with

respect to HT and orientation. The elongation at fracture is comparable for the two HT conditions, except for the 90° orientation in the SA + A condition, which is significantly lower compared to the DA condition. The elongation at fracture for the 15° orientation is also significantly lower compared to the other orientations for both HT conditions.

Figure 4 shows selected tensile properties plotted against the build orientation for the two HT conditions. The average elastic modulus is 179 ± 5.0 GPa and 180 ± 2.0 GPa for DA and SA + A conditions respectively, slightly below the reference value at 183 GPa for bar stock aged at 482 °C [17]. The results suggest that the build orientation slightly influences the elastic modulus in the DA condition. It appears that the material is slightly stiffer when loaded at angles around 45°. Both the magnitude and orientation dependency of the elastic modulus are consistent with previously reported findings with
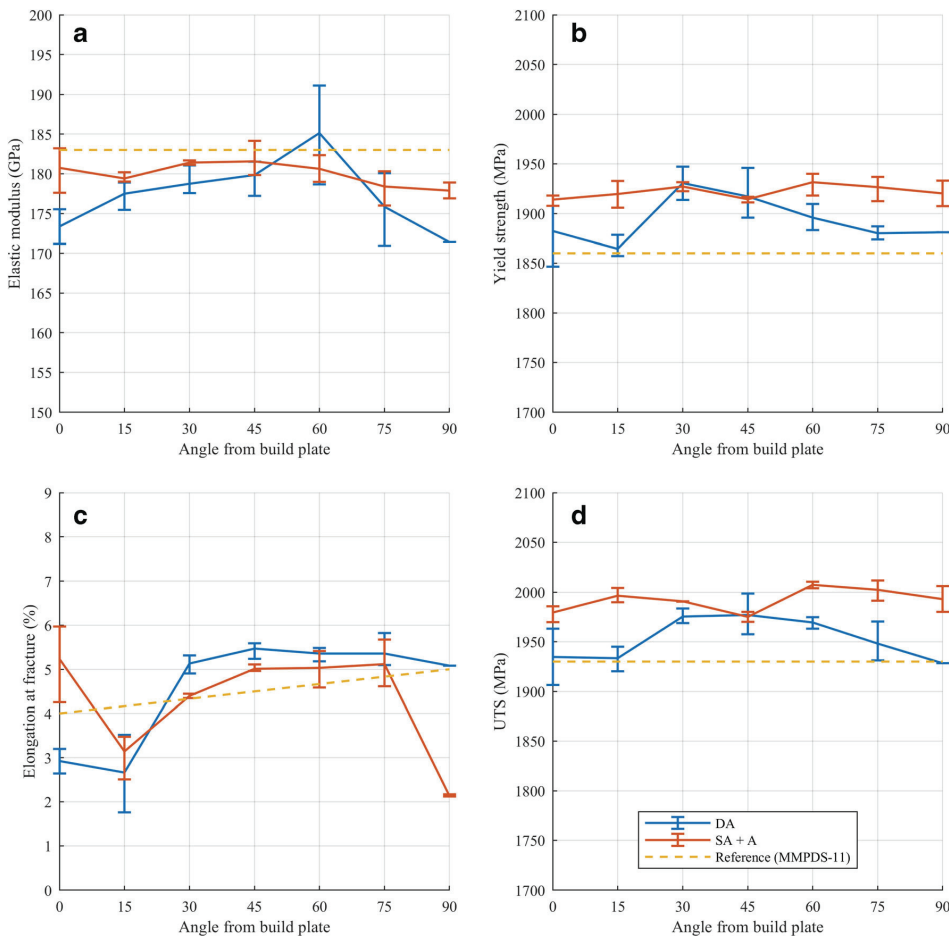
Fig. 4 Elastic modulus (**a**), yield strength (**b**), elongation at fracture (**c**), and ultimate tensile strength (**d**) plotted against build orientation for both HT conditions. Reference values are for bar stock aged at 482 °C [17]
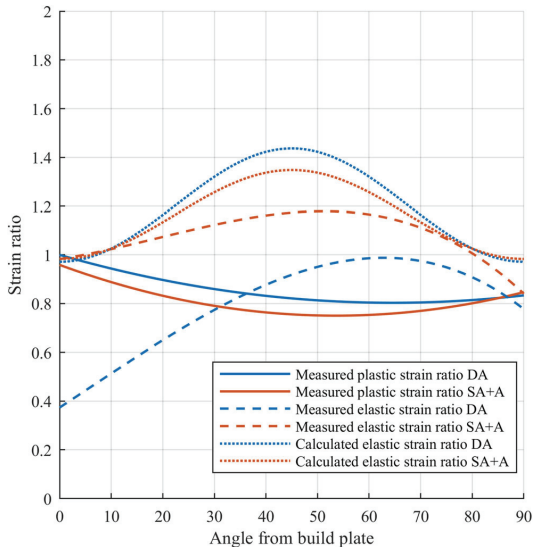
Fig. 5 Elastic and plastic strain ratios as a function of build orientation, shown with polynomial fits. An isotropic material would have a transverse strain ratio of 1

similar HT procedures [9]. The stiffest orientation (60°) is approximately 8% stiffer compared to the least stiff orientation at 90°. In the plastic region of the flow curve, a yield strength of 1900 ± 30 MPa and 1920 ± 10 MPa and ultimate tensile strength of 1960 ± 30 MPa and 1990 ± 20 MPa for DA and SA + A conditions respectively are observed. This is within the expected values reported in the literature (Table 1) and compares well with the reference values in the Metallic Materials Properties Development and Standardization (MMPDS-11) report [17]. There is no obvious dependency on build orientation in the yield strength and ultimate tensile strength. The elongation at fracture is $4.23 \pm 1.83\%$ and $4.24 \pm 1.48\%$ for DA and SA + A respectively,

with a significant variation at certain orientations. In the literature elongation at fracture, values are reported in a range between 1.7 and 6.1% depending on HT and processing conditions (Table 1), with a design value indicated at 4% at 0° increasing to 5% at 90° [17]. The elongation at fracture at 15° orientation is considerably lower compared to the remaining orientations (except for SA + A 90°).

Due to the relatively homogeneous elastic and plastic tensile properties with respect to orientation, it is hard to draw any conclusions about anisotropy based on the tensile tests as shown in Fig. 3 and Fig. 4. Further investigation of the DIC strain fields as well as SEM imaging with EBSD is needed to shed light on the subject.

3.2 Strain field analysis

To investigate the anisotropy, the strain fields captured by DIC are analysed. The DIC setup captures the strains in the local X, Y, and Z directions of the specimens as indicated in Fig. 1. Each specimen is oriented such that the local XY plane of each specimen is parallel to the build direction, and the local YZ surface is built at the indicated angles (Fig. 2). In an isotropic material, the transverse strains in the specimen Y and Z directions should be equal, in both the elastic and plastic regions of the flow curve. The transverse strain ratio, or Lankford coefficient, in the plastic range of the flow curve has been used to quantify anisotropy in sheet metal since the early 1950s [28]. The Lankford coefficient, r, can be expressed as $r = \Delta \epsilon_y / \Delta \epsilon_z$ for an axial load in the X direction, where $\Delta \epsilon_y$ is the change in strain in the specimen Y direction and $\Delta \epsilon_z$ is the change in specimen Z direction (see specimen directions in Fig. 1). If the Lankford coefficient is unequal to one, the material must be considered anisotropic in the plastic region. Recent works by Mooney et al. have utilized the Lankford coefficient to quantify plastic anisotropy in PBF-LB/18Ni300 [9, 29]. A similar approach is shown in Fig. 5

Fig. 6 Transverse strain field of DA 45° specimen in the plastic region. Note the high strain in the y direction compared to the z direction
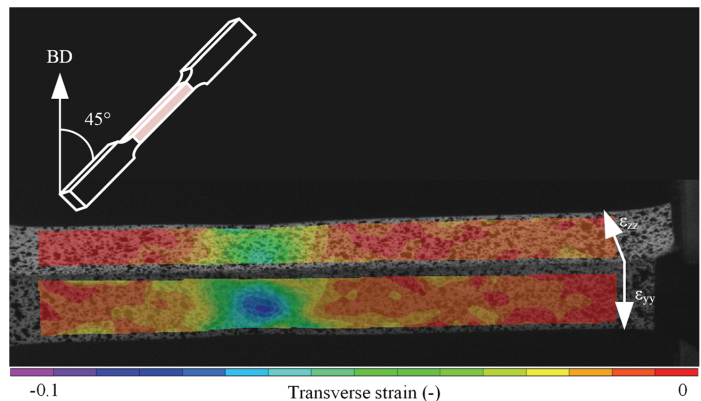
where the measured plastic strain ratio is shown with solid lines (measured between the yield strength and 2% elongation for each sample). The dashed lines in Fig. 5 represent the elastic strain ratios measured in the elastic part of the flow curve for each sample. The calculated elastic strain ratios (dotted lines) are estimated from the elastic constants of the compliance matrix in Hooke's law [30], using the relationship described in Eq. (1) assuming $\epsilon_{xx} = \epsilon_{yy}$ in the machine coordinate system.

$$r_{el}(\theta) = \frac{cos^2(\theta)sin^2(\theta)\left(\frac{2}{E_{xx}} - \frac{2}{G_{xy}}\right) + (cos^4(\theta) + sin^4(\theta))\frac{-\nu_{xy}}{E_{xx}}}{cos^2(\theta)\frac{-\nu_{xz}}{E_{zz}} + sin^2(\theta)\frac{-\nu_{zx}}{E_{zz}}} \quad (1)$$

In Eq. (1), E_{xx} is the elastic modulus of the 0° specimen, and E_{zz} is the elastic modulus of the 90° specimen. θ is the specimen build angle with respect to the build plate. $G_{xy} = E_{xx}/2(1 + \nu_{xy})$, and ν_{xy}, ν_{zx}, ν_{xz} are Poisson ratios determined using the strains in the respective directions according to the different specimen orientations. The measured elastic strain ratios are determined as $R_{el} = \Delta\epsilon_z/\Delta\epsilon_y$, where z and y denote the local specimen directions indicated in Fig. 1.

3.2.1 Plastic transverse strain ratios

The plastic strain ratios of the 0° specimens are close to $r_{pl} = 1$ for both HT conditions, indicating isotropic straining at this orientation. r_{pl} takes a value of approximately 0.8 at 45° for the DA HT condition, and $r_{pl} = 0.75$ for the SA + A HT condition. For the 90° specimens, the plastic strain ratio is slightly higher than $r_{pl} = 0.8$ for both HT conditions. Mooney et al. [9] reports plastic

strain ratios of approximately 0.6 for the 0° specimens and between 0.5 to 0.6 for the 90° specimens depending on the HT condition. The same trend is observed, where the plastic strain ratio for the 45° specimens is lower compared to the 0° and 90° specimens. Figure 6 shows the transverse strain field of a DA45° specimen, where it is clearly indicated that the transverse strain in the specimen Y direction is significantly higher than the Z direction in the plastic part of the flow curve. Even though the tensile properties do not indicate plastic anisotropy, the DIC strain fields reveal that the material favours straining in certain directions depending on the build orientation.

3.2.2 Elastic transverse strain ratios

The calculated elastic strain ratio is estimated based on the assumption that the material is transversely isotropic, i.e., $\epsilon_{xx} = \epsilon_{yy}$ in the machine coordinate system. This leads to $r_{el,c} = 1$ for the 0° and 90° specimens. As illustrated in Fig. 5, this assumption is not valid for either of the HT conditions at 90° since the measured transverse strain ratio is unequal to one. Even though $\nu_{xy} \neq \nu_{zx}$, the calculated transverse strain ratio for the 0° specimens suggests isotropic straining. The latter holds true for the SA + A HT condition, but for the DA condition, the material heavily favours straining on the surface parallel to the build direction, particularly for the low angle specimens. In the DA condition, the material has close to isotropic straining in the 60° build orientation, whereas the SA + A condition has close to isotropic straining in the 0° build orientation.

A potential explanation to the favoured straining can be found in the number of melt pool boundaries (MPB) in the different directions. The number of MPBs in the specimen Y
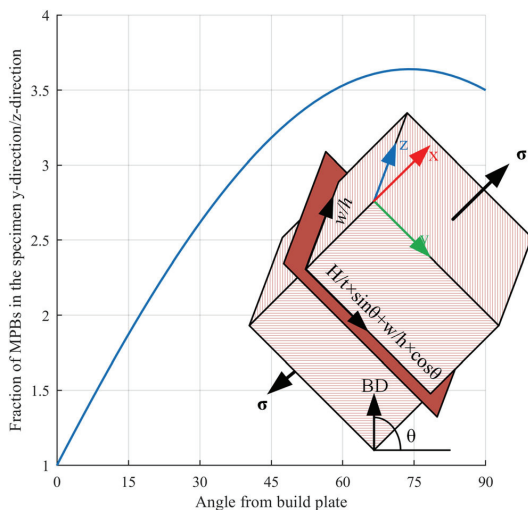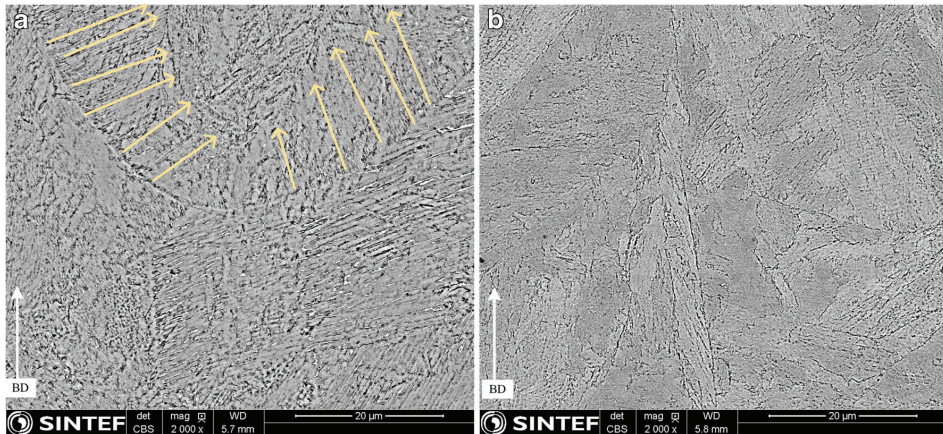

Fig. 7 Fraction of MPBs in the specimen *Y* direction over specimen *Z* direction as a function of specimen orientation

Fig. 8 SEM image of the as-built microstructure. (1) Indicates a fine cellular structure; (2) indicates a heat affected zone with cell growth; (3) shows a melt pool boundary; (4) precipitates in the AB condition
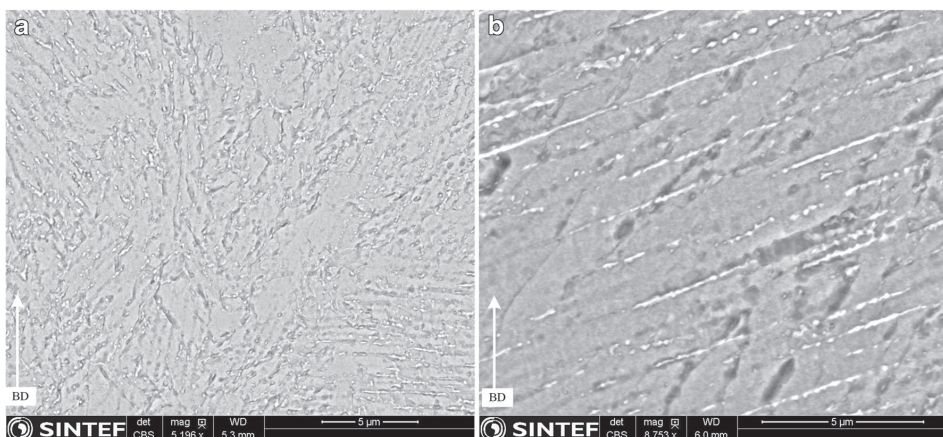
Fig. 9 SEM images of **a** DA condition; **b** SA + A condition. Arrows in (**a**) suggest the solidification direction

and Z directions can be approximated geometrically. Consider the schematic in Fig. 7 where the laser tracks are indicated on the specimen surface. The number of laser tracks in the build plane can be expressed by the specimen height, H, specimen width, w, layer thickness, t, hatch spacing, h, and the angle from the build plate θ. For any θ between 0° and 90°, the number of MPBs in the specimen Y direction can be expressed as $H/t \times sin\theta + w/h \times cos\theta$. The number of MPBs in the specimen Z direction can be expressed as w/h. Note that this assumes only one MPB for each laser line, since only the fraction of MPBs are of interest. The fraction of MPBs in the specimen Y direction over MPBs in the specimen Z direction is shown in Fig. 7. The measured elastic transverse strain ratio in the DA condition (Fig. 5) clearly indicates that when the fraction of MPBs in the specimen Y direction is low, the material favours straining in that direction, and as the fraction of

MPBs increase, the straining is more uniform in the two directions. As will be discussed later, the MPBs are clearly present in the DA condition, while not visible in the SA + A condition. A consequence of this observation is that the anisotropy cannot be accurately modelled under the assumption that the material is transversely isotropic, with symmetry around the axis of the build direction.

The solution treatment before ageing appears to partially reduce the elastic anisotropy, although it is not eliminating it completely. In the plastic part of the flow curve, the solution treatment seems to have a negligible effect on the anisotropic straining. A potential explanation for why the elastic anisotropy is reduced by solution treatment is that the microstructure is textured in the as-built condition, which is recrystallized in the SA treatment, and thus the texture strength is reduced. This would also explain why

Fig. 10: SEM image of **a** DA condition; **b** SA + A condition at higher magnification showing precipitation along the martensite plates

only the elastic anisotropy is reduced by SA treatment, assuming that the source of the plastic anisotropy is strongly related to MPB or grain boundary decoration and not texture.

3.3 Microstructure investigation

To understand the underlying mechanism of unequal straining, the microstructure has been investigated using SEM and EBSD. Figure 8 shows a micrograph of the as-built microstructure, with several distinct process induced features. A cellular microstructure is observed, and the coarseness of the structure is dependent on the thermal cycling history of the specific area. Arrow 1 shows a fine cellular structure that is formed in the middle of the fused area, namely, the molten pool, while arrow 2 shows a coarser structure. Arrow 3 shows a melt pool boundary (fusion line) crossing a previously molten area. In the vicinity of the fusion line, the material undergoes a thermal cycle without being melted. In those regions, the temperature reaches the austenitization temperature of the material, and the grains transform to austenite. For the given time interval, the grains grow, and upon martensite transformation, coarser microstructure is formed. Such coarsening could be observed between the fusion lines in the illustrated cross section. Arrow 4 points to precipitates assumed to form only when the material is kept above a critical temperature for an extended period of time [31]. The precipitates observed in the microstructure are likely contributing to the anisotropy, as reported by several authors [9, 21, 22], where the precipitates are dispersed along elongated grain boundaries and block the movement of dislocations within the crystal structure.

When the material is heat treated, some of the process induced features tend to abate. Figure 9 shows the microstructure after DA (a) and SA + A (b) heat treatments. In the direct ageing condition, the melt pool boundaries are still distinctive, but not to the extent that was observed in the as-built condition. Furthermore, the microstructure is composed of lamellas, which appears to align with the heat flux direction during initial solidification (indicated by arrows in Fig. 9a). This provides a potential reason for the anisotropy in the angled specimens. When the material first solidifies during the PBF-LB/M process, the high atomic density vector <110> of the primary austenite face-centred cubic (FCC) crystal structure aligns with the direction of the heat flux [32]. As martensite transformation happens during cooling, the orientations of the martensite plates are directed by the Kurdjumov-Sachs (K-S) orientation relationship [33], and the martensite plates align with the heat flux direction. Furthermore, as seen in Fig. 10 a and b, the precipitates formed during ageing are dispersed on the martensite plates, acting as barrier against dislocation movement along the heat flux direction. This is exemplified in the DA0° specimen, which favoured elastic straining on the surface parallel to the build plate, perpendicular to the martensite plates, as can be seen from the transverse strain ratio in Fig. 5. Even though there is local anisotropy, there is no significant variation in yield stress with respect to build orientation (Fig. 4). Only one component of the stress tensor is influenced by this, and the overall yield stress of the differently oriented specimens conforms to the same magnitude.

When the material is solution treated before ageing, the microstructure recrystallizes, and the melt pool boundaries are no longer vividly visible. Nevertheless, the strain ratios still indicate plastic anisotropy, likely due to the precipitates dispersed on the martensite plates. The solution treatment
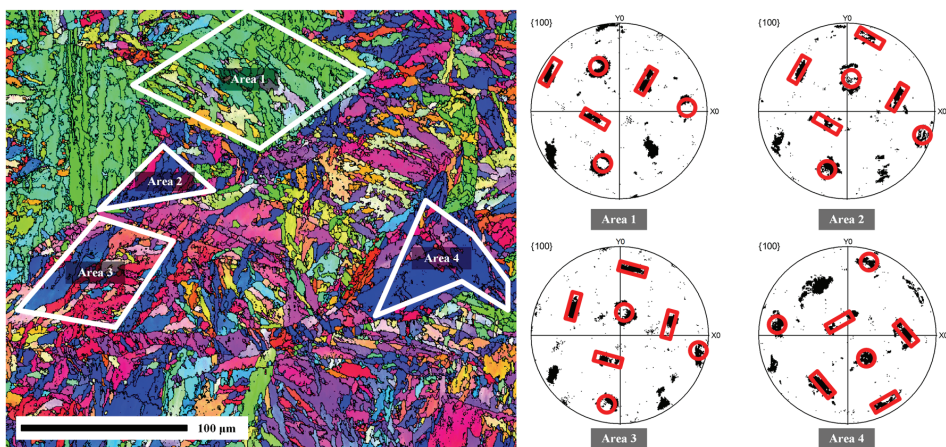
Fig. 11 Inverse pole figure (IPF-Z) orientation map of a selective area from the AB sample. Smaller pockets of the transformed material show K-S orientation relationship as shown in their pole figures
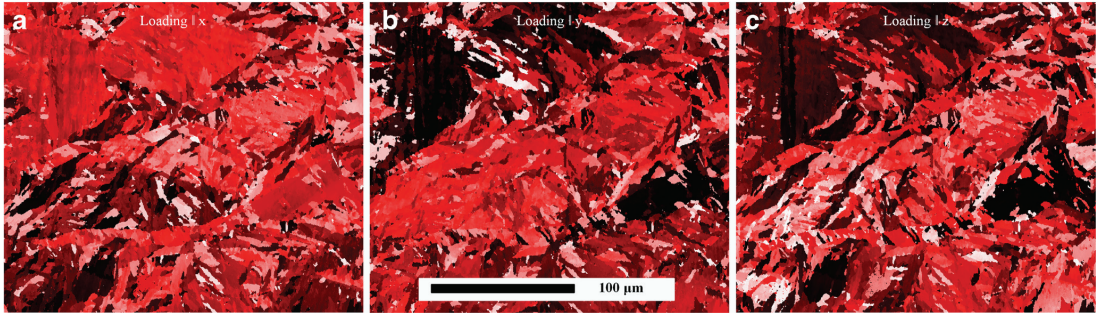
Fig. 12 Taylor factor mapping of the mapped area when loaded along X direction (**a**), loaded along Y direction (**b**), and loaded along the Z direction. The darker red colour shows higher Taylor factor (more difficult to deform), and the brighter colour is representing the weaker grains under the given loading direction

brings the material up to a temperature allowing for complete austenite reversion. However, the observed carbide precipitates in the as-built condition are not expected to dissolve at that temperature range and dwelling time. Due to the crystal orientation of the primary austenite grains, martensitic transformation has a memory effect. This means that the martensite laths will remain in the same orientation, morphology, and location over several numbers of austenitization and martensite transformation episodes [34]. The martensite lath boundaries will become preferred sites for precipitation, and therefore the precipitates will align along the morphological orientation of the plates, which have a relationship with the primary austenite grains, which are originally affected by the solidification conditions affected by the heat flux direction.

Figure 11 shows an inverse pole figure orientation map of a selected area from an 'as-built' sample of the material. It is clear that there is texture in the individual pockets, as highlighted in areas 1 to 4. The K-S orientation relationship [32] for the respective areas is shown as individual pole figures on the right-hand side of the figure and corresponds well with the theoretical pattern indicated in red. As previously mentioned, the <110> direction of the primary austenite aligns with the direction of the heat-flux, and the K-S orientation relationship dictates the direction of the martensite plates. The texture is limited to individual pockets, which orientations are affected by the laser scan strategy, giving a stochastic global microstructure, thus isotropic behaviour.

Figure 12 shows the Taylor factor mapping of the same area as Fig. 11. In polycrystalline materials, the arithmetic mean of the Taylor factors (M) is calculated from the ratio between the material's flow stress over the critical resolved shear stress. Therefore, grains with low M will deform more easily than the ones with higher M. However, grains with low M cannot deform until the harder ones are also deforming plastically. Moreover, the grains with high M will not deform unless a combination of stress and work hardening conditions are met.

The weighted average of the Taylor factors along X, Y, and Z are shown in Fig. 13. The frequency of grains with high Taylor factors indicates that the investigated area is approximately 3.2% stronger if loaded in the Y direction compared to the X direction, and approximately 1% weaker if loaded in the Z direction compared to the X direction. These values suggest that there is a mild anisotropy in the microstructure level.

### 3.3.1 Fracture surface analysis

The strain ratios captured by the DIC system indicates anisotropic straining, but this is only observed in the
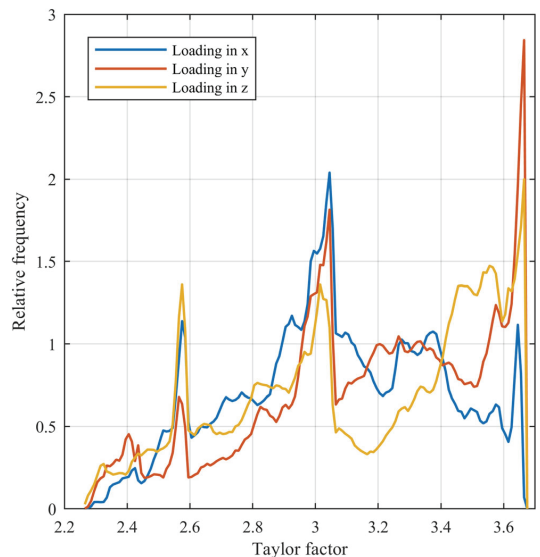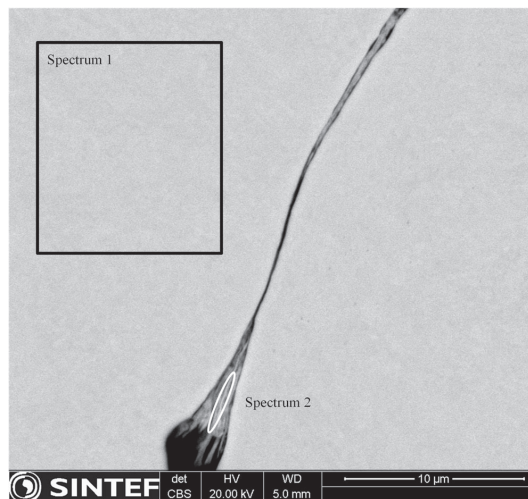

Fig. 13 Histogram of the Taylor factor when the mapped area is loaded along X, Y, and Z. When the external load is aligned along Y direction, the frequency of grains with high M increases

tensile tests for the elastic part of the flow curve. The variation in yield strength, ultimate tensile strength, and elongation at failure with respect to build orientation is not systematic enough to draw conclusions about anisotropy. The yield strength and ultimate tensile strength are fairly uniform, but there is significant scatter in the elongation at failure. To better understand the root cause of scattering, fracture surface analysis was carried
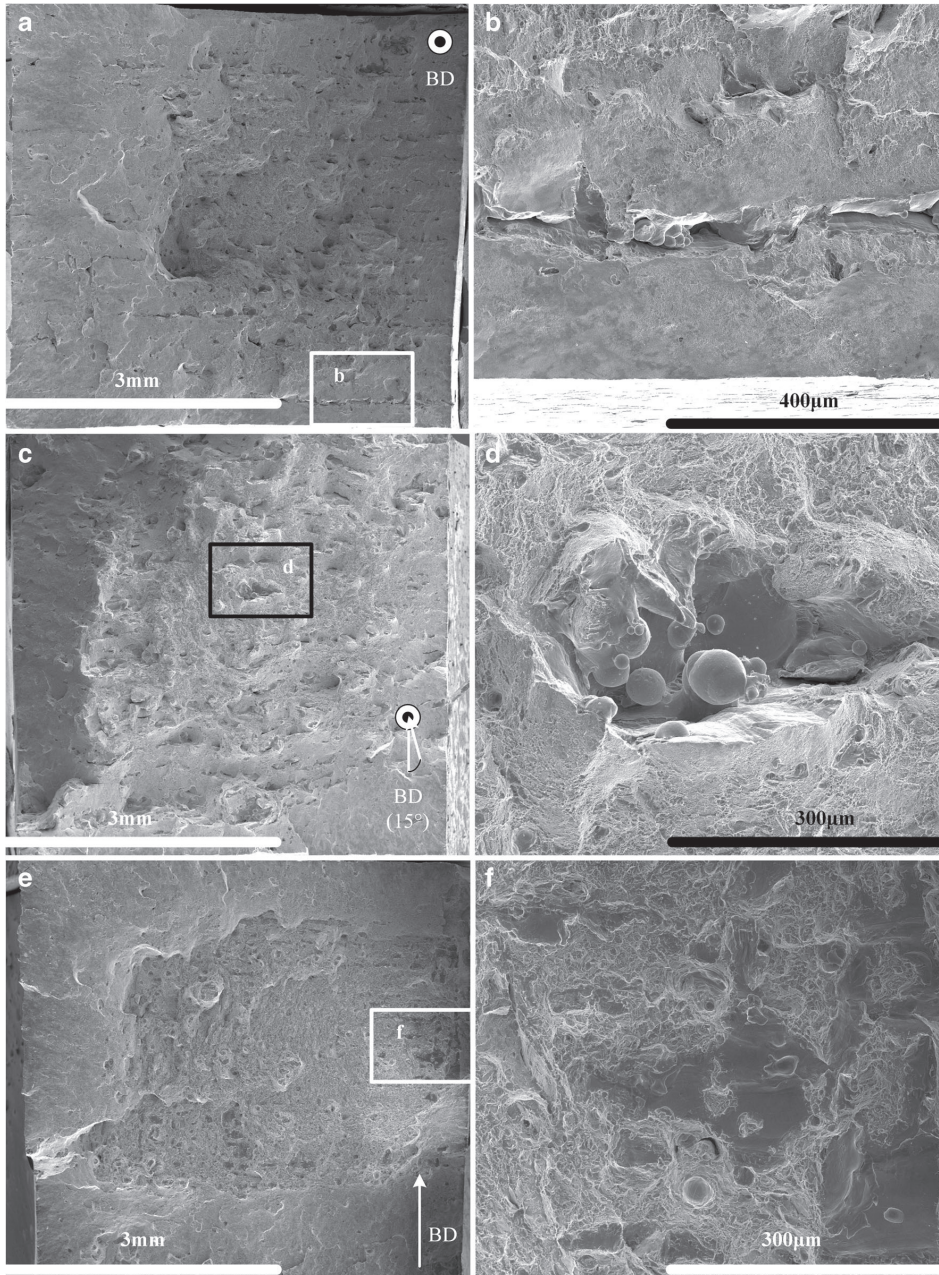
Fig. 14 SEM images of the fracture surfaces of the tensile tests. **a–b** DA 0°, **c–d** DA 15°, and **e–f** SA + A 90° specimens

Fig. 15 Polished SEM image with corresponding EDS spectrum of a DA-0° after fracture

Table 4 Chemical composition of EDS spectra as indicated in Fig. 15

Elements	Spectrum 1		Spectrum 2	
	Wt%	Standard deviation	Wt%	Standard deviation
O	0.45	0.24	4.83	0.37
Al	0.05	0.12	0.77	0.14
Ti	0.62	0.12	7.54	0.22
Fe	Bal.	-	Bal.	-
Co	8.96	0.41	8.05	0.4
Ni	18	0.45	15.1	0.44
Mo	5.35	0.4	4.6	0.38

out on the specimens performing poorly. The specimens selected were the 0° and 15° from the DA condition, and the 90° specimen from the SA + A condition. SEM images of the fracture surfaces of the respective specimens are compiled in Fig. 14.

Figure 14 a, c, and e show low magnification images of the fracture surface. The surfaces have flat regions in the centre and pronounced shear lips around the edges, typically seen when there is a large reduction in cross-section area prior to failure [35]. Even though the relative density is measured to be above 99.94%, traces of porosity are visible on all the surfaces. The higher magnification images reveal process specific defects in addition to the porosity. In the DA-0° specimen, lines parallel to the layers are visible throughout the cross-section, highlighted in Fig. 14b. The defect extends for lines with lengths of approximately 3 mm and appears to be process-parameter related, as they are evenly spaced and parallel to each other. At first glance, the defects appear to be lack-of-fusion (LOF) defects, but further investigation suggests that it could be a result of micro-segregation. Figure 15 shows the fracture surface after polishing, and Table 4 shows the corresponding EDS spectra and chemical composition. The EDS analysis reveals a higher concentration of Ti and O in the defect. Micro-segregation in PBF-LB/18Ni300 has been reported by several authors [36–38], where certain elements, such as Ti, segregate towards the front of the melt pool. Furthermore, Ti has one of the highest affinities to oxygen of the remaining elements composing the 18Ni300 material [39]. When a sufficiently high concentration of oxygen is present, Ti-oxides can form. As described in section 2.1, the material is processed with the 'island' scan strategy with an

island size of 5 mm. The contour of each island is scanned in a continuous line, consistent with the lines observed in the fracture surface of the 0° specimen. Thijs et al. [40] also observed a higher concentration of oxides at the contour of the islands. Based on the EDS spectra and the length and spacing of the defects in Fig. 14 a and b, a compelling argument can be made that the defects are a result of micro-segregation leading to Ti-oxide formation, in combination with a laser scan strategy where the phenomena are amplified. Furthermore, this type of defect is only observed in the 0° orientation specimen, where the loading direction is within the plane of the islands.

Defects are observed in the DA-15° and SA + A-90° specimens as well. In the DA 15° specimen, a defect is found with what appears to be partially melted powder particles. This could in fact be a LOF defect, if for instance a re-coater issue leads to a high local layer thickness. In the SA + A-90° specimen, a LOF region of approximately the same size is observed, despite that non-melted powder particles are not present. In addition to the LOF defect, a crack is visible. Defects of this sort highlight the importance of process-parameter optimization. The defects are assumed to not be detrimental for the yield strength but are expected to influence the fatigue life of the material.

4 Conclusions

In this study, the anisotropy of PBF-LB/18Ni300 maraging steel subjected to two different heat treatments has been investigated using techniques such as tensile testing, digital image correlation (DIC), and microstructure and fracture surface analysis with scanning electron microscopy. Strain field analysis with DIC reveals elastic and plastic anisotropy for both direct ageing (DA) and solution treatment + ageing (SA+A) heat treatment conditions.

Based on the results and discussions in this study, it is concluded that the elastic anisotropy is likely a result of process induced features such as melt pool boundaries (MPB)

decorated with precipitates, which limits the dislocation movement. In addition, the martensite plates decorated with precipitates align with the primary austenite grain orientation, which is related to the direction of the heat flux during solidification. In the DA condition, the elastic anisotropy is significant, and the elastic modulus varies with the build orientation. In the SA + A condition, the MPBs are no longer vividly visible, and the elastic modulus has only a very slight dependency on the specimen build orientation. The DIC analysis reveals anisotropic straining, which cannot be represented by Hooke's law under the assumption that PBF-LB/M materials are transversely isotropic.

The EBSD analysis shows a strong texture within individual pockets, but the global microstructure appears to be heterogeneous. This further supports the conclusion that the anisotropy is due to process induced features related to the MPBs and that there is no globally preferred crystallographic orientation causing anisotropic tensile properties.

Plastic anisotropy was observed in the strain field analysis but did not have a significant influence on the yield strength and ultimate tensile strength. The elongation at fracture was significantly lower for specimens at low-angle orientations, which is mainly attributed to MPB effects.

Based on the results presented for grain orientation and transformation relationships, future work can include in-depth studies to delineate the effect of transformation-induced crystal plasticity on the anisotropic behaviour. The results in this study contribute to establishing computational models, where the effect of anisotropy, transformation-induced plasticity, and residual stresses can be studied in isolation to provide a better understanding of the thermal cycles and pre-heating conditions for AM parameter optimization in phase transforming steels of similar type.

Declarations

Conflict of interest The authors declare no competing interests.

References

1. Turk C, Zunko H, Aumayr C et al (2019) Advances in Maraging Steels for Additive Manufacturing. BHM Berg- und Hüttenmännische Monatshefte 164:112–116. https://doi.org/10.1007/s00501-019-0835-z

2. Fortunato A, Lulaj A, Melkote S et al (n.d.) Milling of maraging steel components produced by selective laser melting. Int J Adv Manuf Technol 94:1895–1902. https://doi.org/10.1007/s00170-017-0922-9

3. Roehling JD, Smith WL, Roehling TT et al (2019) Reducing residual stress by selective large-area diode surface heating during laser powder bed fusion additive manufacturing. Addit Manuf. https://doi.org/10.1016/j.addma.2019.05.009

4. Combrinck J, van As B, Booysen GJ, de Beer DJ (2019) Cost-effectiveness of direct metal laser sintered maraging steel inserts for plastic injection moulding process. South African J Ind Eng 30:52–62. https://doi.org/10.7166/30-3-2263

5. Brøtan V, Berg OÅ, Sørby K (2016) Additive manufacturing for enhanced performance of molds. Procedia CIRP 54:186–190. https://doi.org/10.1016/j.procir.2016.05.074

6. Pereira M, Kunene G, Spiering A, Du Preez WB (2009) Performance of LaserCUSING® metal powder specimens under aluminium high pressure die-casting process conditions. In: 10th Annual RAPDASA International Conference

7. Hovig EW, Brøtan V, Sørby K et al (2016) Additive manufacturing for enhanced cooling in moulds for casting. Proc 6th Int Work Adv Manuf Autom. https://doi.org/10.2991/iwama-16.2016.11

8. Tan JH, Wong WLE, Dalgarno KW (2017) An overview of powder granulometry on feedstock and part performance in the selective laser melting process. Addit Manuf 18:228–255. https://doi.org/10.1016/j.addma.2017.10.011

9. Mooney B, Kourousis KI, Raghavendra R (2019) Plastic anisotropy of additively manufactured maraging steel: Influence of the build orientation and heat treatments. Addit Manuf 25:19–31. https://doi.org/10.1016/j.addma.2018.10.032

10. Bai Y, Wang D, Yang Y, Wang H (2019) Effect of heat treatment on the microstructure and mechanical properties of maraging steel by selective laser melting. Mater Sci Eng A 760:105–117. https://doi.org/10.1016/j.msea.2019.05.115

11. Hovig EW, Azar AS, Grytten F et al (2018) Determination of anisotropic mechanical properties for materials processed by laser powder bed fusion. Adv Mater Sci Eng:2018. https://doi.org/10.1155/2018/7650303

12. Tan C, Zhou K, Kuang M et al (2018) Microstructural characterization and properties of selective laser melted maraging steel with different build directions. Sci Technol Adv Mater 19:746–758. https://doi.org/10.1080/14686996.2018.1527645

13. Chlebus E, Gruber K, Kuznicka B et al (2015) Effect of heat treatment on the microstructure and mechanical properties of Inconel 718 processed by selective laser melting. Mater Sci Eng A 639:647–655. https://doi.org/10.1016/j.msea.2015.05.035

14. Vishwakarma J, Chattopadhyay K, Santhi Srinivas NC (2020) Effect of build orientation on microstructure and tensile behaviour of selectively laser melted M300 maraging steel. Mater Sci Eng A 798:140130. https://doi.org/10.1016/j.msea.2020.140130

15. Wu W, Wang X, Wang Q et al (2020) Microstructure and mechanical properties of maraging 18Ni-300 steel obtained by powder bed based selective laser melting process. Rapid Prototyp J 26:1379–1387

16. Becker TH, Dimitrov D, Campbell RI, Campbell RI (2016) The achievable mechanical properties of SLM produced Maraging Steel 300 components. Rapid Prototyp J 22

17. Battelle Memorial Institute (2016) Metallic Materials Properties Development and Standardization (MMPDS-11). Battelle Memorial Institute

18. Suryawanshi J, Prashanth KG, Ramamurty U (2017) Tensile, fracture, and fatigue crack growth properties of a 3D printed maraging steel through selective laser melting. J Alloys Compd 725:355–364. https://doi.org/10.1016/j.jallcom.2017.07.177

19. Elangeswaran C, Gurung K, Koch R et al (2020) Post-treatment selection for tailored fatigue performance of 18Ni300 maraging steel manufactured by laser powder bed fusion. Fatigue Fract Eng Mater Struct 43:2359–2375. https://doi.org/10.1111/ffe.13304

20. Oliveira AR, Diaz JAA, Nizes ADC et al (2021) Investigation of building orientation and aging on strength–stiffness performance of additively manufactured maraging steel. J Mater Eng Perform 30:1479–1489. https://doi.org/10.1007/s11665-020-05414-4

21. Hutchinson B (2015) Critical assessment 16: Anisotropy in metals. Mater Sci Technol (United Kingdom). https://doi.org/10.1179/1743284715Y.0000000118

22. Mishra S, Kulkarni K, Gurao NP (2015) Effect of crystallographic texture on precipitation induced anisotropy in an aluminium magnesium silicon alloy. Mater Des 87:507–519. https://doi.org/10.1016/j.matdes.2015.08.008

23. Brandl E, Heckenberger U, Holzinger V, Buchbinder D (2012) Additive manufactured AlSi10Mg samples using Selective Laser Melting (SLM): Microstructure, high cycle fatigue, and fracture behavior. Mater Des 34:159–169. https://doi.org/10.1016/j.matdes.2011.07.067

24. Xiong ZH, Liu SL, Li SF et al (2019) Role of melt pool boundary condition in determining the mechanical properties of selective laser melting AlSi10Mg alloy. Mater Sci Eng A 740–741:148–156. https://doi.org/10.1016/j.msea.2018.10.083

25. Grace JR, Ebneyamini A (2021) Connecting particle sphericity and circularity. Particuology 54:1–4. https://doi.org/10.1016/j.partic.2020.09.006

26. Hovig EW, Sørby K (2020) Influence of laser scan speed on the relative density and tensile properties of 18Ni maraging steel grade 300. Lect Notes Electr Eng 634:466–472. https://doi.org/10.1007/978-981-15-2341-0_58

27. Grytten F, Daiyan H, Polanco-Loria M, Dumoulin S (2009) Use of digital image correlation to measure large-strain tensile properties of ductile thermoplastics. Polym Test 28:653–660. https://doi.org/10.1016/j.polymertesting.2009.05.009

28. Lankford WT, Snyder SC, Bauscher JA (1949) New criteria for predicting the press performance of deep drawing sheets. Thirty-first Annual Convention of the Society

29. Mooney B, Kourousis KI, Raghavendra R, Agius D (2019) Process phenomena influencing the tensile and anisotropic characteristics of additively manufactured maraging steel. Mater Sci Eng A 745:115–125. https://doi.org/10.1016/j.msea.2018.12.070

30. Daniel D, Jonas JJ, Bussière J (1992) The elastic strain ratio, the lüders strain ratio and the evolution of r-value during tensile deformation. Textures Microstruct 19:175–188. https://doi.org/10.1155/tsm.19.175

31. Tewari R, Mazumder S, Batra IS et al (2000) Precipitation in 18 wt% Ni maraging steel of grade 350. Acta Mater 48:1187–1200. https://doi.org/10.1016/S1359-6454(99)00370-5

32. Azar AS, Østby E, Akselsen OM (2012) Effect of hyperbaric chamber gas on transformation texture of the API-X70 pipeline weld metal. Metall Mater Trans A Phys Metall Mater Sci. https://doi.org/10.1007/s11661-012-1157-x

33. Kurdjumow G, Sachs G (1930) Über den Mechanismus der Stahlhärtung. Zeitschrift für Phys. https://doi.org/10.1007/BF01397346

34. Shirazi H, Miyamoto G, Hossein Nedjad S et al (2018) Microstructure evolution during austenite reversion in Fe-Ni martensitic alloys. Acta Mater 144:269–280. https://doi.org/10.1016/j.actamat.2017.10.068

35. ASM Handbook Comittee (1987) ASM handbook, volume 12. Fractography

36. Jägle EA, Sheng Z, Kürnsteiner P et al (2016) Comparison of maraging steel micro- and nanostructure produced conventionally and by laser additive manufacturing. Materials (Basel):10. https://doi.org/10.3390/ma10010008

37. Kempen K, Yasa E, Thijs L et al (2011) Microstructure and mechanical properties of selective laser melted 18Ni-300 steel. Phys Procedia 12:255–263. https://doi.org/10.1016/j.phpro.2011.03.033

38. Jägle EA, Choi P-P, Van Humbeeck J, Raabe D (2014) Precipitation and austenite reversion behavior of a maraging steel produced by selective laser melting. J Mater Res 29:2072–2079

39. Hong T, DebRoy T (2001) Effects of time, temperature, and steel composition on growth and dissolution of inclusions in liquid steels. Ironmak Steelmak 28:450–454

40. Thijs L, Van Humbeeck J, Kempen K et al (2012) Investigation on the inclusions in maraging steel produced by selective laser melting. Innov Dev Virtual Phys Prototyp:297–304

6.4. Paper 4 - High cycle fatigue life estimation of materials processed by laser powder bed fusion

WILEY **FFEMS** Fatigue & Fracture of Engineering Materials & Structures

High cycle fatigue life estimation of materials processed by laser powder bed fusion

Even W. Hovig[1] 🟢 | Amin S. Azar[2] 🟢 | Martin F. Sunding[2] 🟢 | Erik Andreassen[2] 🟢 |
Knut Sørby[1] 🟢

[1] Department of Mechanical and Industrial Engineering, Norwegian University of Science and Technology, Trondheim, Norway

[2] SINTEF Industry, Oslo, Norway

Correspondence
Even W. Hovig, Norwegian University of Science and Technology, Trondheim, Norway.
Email: even.w.hovig@ntnu.no

Funding information
SINTEF, Grant/Award Number: SIP-LAMINA; Research Council of Norway, Grant/Award Number: 248243

Abstract

The fatigue life of metal components is known to depend on the surface topography. For components made by laser powder bed fusion, the roughness of the as-built surfaces depends on the orientation of the component surface with respect to the build plate. Surface topographies of AlSi10Mg and Inconel 718 specimens built at 0° to 90° inclination, with 15° increments, were characterised by white light interferometry. Two methods for calculating the stress concentration factor using the surface roughness data are proposed, and the results of each approach are presented and compared. Moreover, a finite element model was developed, in order to analyse the stress field when subsurface porosity is present. The fatigue lifetime estimates suggest that the lifetime of components may differ up to two orders of magnitude, depending on the build orientation.

KEYWORDS

additive manufacturing, AlSi10Mg, fatigue, Inconel 718, laser melting, powder bed fusion, stress concentration factor

1 | INTRODUCTION

Additive manufacturing (AM) is a process where material is added, typically layer by layer, to form a three-dimensional part. The most common AM process for

Nomenclature: d, Distance from main surface down to the tip of a defect (eg, crack or groove); h, Laser scanning hatch spacing; k_t, Stress concentration factor; L, Peak to peak distance of a surface profile; N_f, Number of fatigue cycles to failure; P, Laser power; R, Min-to-max stress ratio in fatigue test; R_a, Arithmetic mean deviation of surface profile; R_{da}, Average absolute slope of the surface profile within the sampling length; R_v, Maximum valley depth of a surface profile in the evaluation length; R_{vm}, Average maximum valley depth of surface profile of each sample length within an evaluation length; R_z, Average distance between the highest peak and lowest valley of a surface profile; S, Mean spacing between adjacent local peaks of a surface profile; t, Layer thickness used in the powder bed fusion process; T_s, Substrate temperature; v, Laser scan velocity; σ, Stress amplitude; σ_{max}, Maximum local stress; σ_{nom}, Nominal global stress; ρ, Radius at tip of defect; ν, Poisson's ratio

metals is laser metal powder bed fusion (LPBF), in which a layer of the feedstock material, typically a prealloyed powder, is distributed over a substrate, and then, the layer is selectively melted by a laser to build a certain geometry and fuse with the previous layer. A number of materials and alloys for LPBF are commercially available, and process parameters have been optimised for each machine type and material system.[1] In this study, one aluminium alloy and one iron-nickel–based superalloy are considered. AlSi10Mg is typically used in casting of parts with complex geometry and thin walls, eg, automotive applications. Inconel 718 is a high-temperature alloy that is typically used in aerospace where excellent mechanical properties at elevated temperatures are critical. Additive manufacturing of these alloys allows for complex geometries, but there are some issues compared with their cast or wrought counterparts, such as higher surface roughness, different microstructures, and higher porosity. Therefore, specific knowledge of AM material

performance is of great importance for demanding applications such as automotive and aerospace.

The fatigue life of AM components is affected by several features: component size, surface characteristics, internal porosity, subsurface porosity, and microstructure. Predicting the fatigue life of a component with defects requires appropriate definition of stress concentration factors (SCF). We can distinguish between the SCFs of the nominal geometry and those of process-induced defects (defects at the surface or in the bulk of the component). The stress concentration factor is defined as

$$k_t = \sigma_{max}/\sigma_{nom} \tag{1}$$

where k_t is the SCF, σ_{max} is the maximum stress in the component, and σ_{nom} is the externally applied stress. For a U-shaped surface defect under uniaxial loading, the SCF can be estimated according to Equation 2,

$$k_t = 1 + 2\sqrt{\frac{d}{\rho}} \tag{2}$$

where d is the distance from the surface to the tip of the defect and ρ is the radius at the tip.[2] Depending on the cumulative stress concentration, based on the type and size of defects in the component, either internal or surface defects will play a dominant role. Internal defects can be characterized by nondestructive methods (eg, X-ray microcomputed tomography (μ-CT)[3]) or destructive methods (eg, microscopy of cross sections, etc), while surface defects are usually characterized by microscopy or interferometry.

There are several studies on estimating the fatigue life of AM components based on internal and external defects.[4-8] Romano et al[4,5] proposed a model based on internal defects to predict both low-cycle and high-cycle fatigue in AlSi10Mg, based on assumptions regarding defect size, geometry, and occurrence. Yadollahi et al[6] applied a similar method to describe the effect of surface texture and defect features on the fatigue life of Inconel 718. The latter article suggested using the maximum valley depth of the surface profile (R_v) as the initial crack length for fatigue life modelling. However, this approach does not account for the geometry of the defect. Yamashita et al[7] studied the effect of internal defects on fatigue life of Inconel 718. They concluded that the area of a defect must be seen in relation with other defects in the immediate proximity and expanded the model to give a more accurate prediction. Zhou et al[8] investigated the effect of texture on low-cycle fatigue of Inconel 718. Along with other studies on the microstructure of LPBF Inconel 718,[9-11] they found that the as-built microstructure consists of a predominantly columnar grain structure

parallel to the build direction. This structure will result in an anisotropic mechanical response, making the fatigue life dependent on build orientation in addition to internal and external defects.

The models mentioned in the previous paragraph use internal defect geometry as input to estimate the fatigue life. In an effort to eliminate the need for destructive testing such as microscopy, or high-cost equipment such as μ-CT to characterize internal defects, this paper propose models based on only surface roughness measurements. However, if subsurface porosity is present, internal defects must be accounted for, as will be demonstrated in Section 3.2.

Several experimental studies on the fatigue life of AlSi10Mg alloys with respect to different LPBF processing parameters have been conducted in the recent years.[12-16] Among the findings, the key conclusions suggest that elevating the substrate temperature during LPBF processing, and post-LPBF heat treatment (T6) of the as-built samples, increases the fatigue life significantly. The microstructure will recrystallize upon solution heat treatment, which in turn will mitigate the anisotropic effect of the as-built columnar microstructure. A more comprehensive summary of the experimental studies is available in Hovig et al.[17] Furthermore, machining and shot peening of the surfaces increase the lifetime compared with the as-built performance. Bagherifard et al[18] demonstrates how sand blasting and shot peening can significantly increase the fatigue strength of AlSi10Mg LPBF specimens, and Beevers et al[19] investigated the effect of various processing parameters and posttreatments. The latter study showed that LPBF processing without contour scan, and postprocessing with vibration polishing, increased the fatigue life of net-shape specimens to the level of machined specimens.

There have also been several experimental studies on the fatigue life of LPBF Inconel 718. Scott-Emuakpor et al[20] reported fatigue life of polished samples built in parallel with the LPBF build direction before and after hot isostatic pressing (HIP) treatment. The results indicate that HIP marginally increases the fatigue lifetime for high fatigue loads, while no apparent difference is seen in low fatigue loads (high cycle fatigue). Kelley et al[21] reported fatigue life of Inconel 718 based on orientation for both machined and rough samples built both parallel and perpendicular to the build direction and demonstrates that the fatigue life drastically decreases when no surface treatment is done post-LPBF processing. Konečná et al[22] reported fatigue life of three sets of rough surface-aged samples built in three different orientations. The study shows how surface roughness and orientation influence the fatigue life, where the smoothest surfaces yielded the highest fatigue life also for aged samples.

Balachandramurthi et al[23] demonstrated how the fatigue life of samples built in parallel to the build direction responds to heat treatments and surface machining for both electron beam melting and LPBF. It was shown that HIP treatment followed by ageing and surface machining improved the fatigue life of the components significantly.

As for AlSi10Mg, ageing Inconel 718 increases the low cycle fatigue life compared with only surface machining. Nevertheless, machining the surface still significantly increases the fatigue life, especially at low stress levels (high cycle fatigue). When comparing the fatigue life data from the literature, it becomes apparent that the machine-to-machine repeatability is low. The fatigue life of the same alloy built by different vendors does not have comparable tensile properties, surface roughness, and consequently fatigue lives.

Having established the significance of surface roughness on the high cycle fatigue life for both AlSi10Mg and Inconel 718, it becomes critical to account for surface roughness when designing LPBF components. In order to capitalize on the design freedom offered by LPBF, surface machining is often impractical, or even impossible. In this study, we propose two approaches for determining the stress concentration factors due to process-induced roughness, for flat surfaces of specimens made by LPBF. One approach uses white light interferometry to characterize the surface roughness, while the other approach utilizes a stylus-type measurement for surface roughness characterization.

2 | MATERIALS AND METHODS

The AlSi10Mg specimen was fabricated with a Concept Laser M2 cusing machine. The powder feedstock was supplied by GE Additive (CL31AL). The processing parameters for AlSi10Mg were developed by optimizing the relative density of the material. The Inconel 718 specimens were built with an SLM 280 HL machine with process parameters for Inconel 718 powder as supplied by the machine manufacturer. The nominal chemical compositions of the AlSi10Mg and Inconel 718 alloys can be seen in Tables 1 and 2, respectively. The main processing parameters are listed in Table 3.

The fabricated parts were miniature flat tensile test specimens (length 45 mm, width in the reduced area section 2.5 mm, thickness 1.5 mm) as shown as inset in

Figure 1. The specimens made from AlSi10Mg were processed with the island scan strategy (island size of 5 × 5 mm^2, X and Y shift of 1 mm, and angular shift of 45°). One additional contour scan was used, on the inside of the specimen surface perimeter. Each layer was first scanned with a low laser power of 50 W to dry and preheat the powder. Argon gas was used to shield the build chamber. The specimens made from Inconel 718 were produced according to the machine manufacturers' specification.

For both materials, specimens with seven different build orientations were selected for surface topography characterization by white light interferometry (WLI) using a Wyko NT-9800 instrument.

Table 4 shows the selected specimens with annotation according to ISO/ASTM 52921:2013E.

The AlSi10Mg specimens were first solution annealed at 538°C followed by artificial ageing at 160°C for 12 hours (T6). Both sets of the Inconel 718 specimens received solution treatment, and one set was HIPed and aged. The heat treatment procedure for the Inconel 718 specimens can be found in Hovig et al.[24]

The upward facing as-built surfaces were characterized by WLI and analysed in the Veeco Vision 4.2 software. Two areas of 1.7 × 2.3 mm^2 were captured in the reduced area region of each of the specimens. The raw data were filtered with a long wavelength pass Gaussian filter and spatial cutoff of 20 μm. Initial investigation revealed that partially melted powder particles were fused to the surface; therefore, the upper "tail" of the distribution of the surface height was masked for the SCF estimation. Further analysis of the filtered topography was carried out with in-house MATLAB scripts.

3 | RESULTS AND DISCUSSION

3.1 | Roughness measurements

Figure 1 shows selected surface roughness measurements for the AlSi10Mg specimens, as captured by WLI. The arithmetic mean deviation of the roughness profile (R_a) is at the lowest for the samples oriented at 0°, 15°, and 30°, before a steep increase in surface roughness at 45°, followed by a decline in surface roughness as the samples are "raised" to 90° inclination. The average depth of the valleys (R_{vm}), the average distance between the peaks

**TABLE 1** Chemical composition of the AlSi10Mg powder feedstock as given by the supplier

Element	Si	Mg	Fe	Mn	Ti	Cu	Zn	C	Al
wt%	9.0-11.0	0.2-0.45	<0.55	<0.45	<0.15	<0.1	<0.1	<0.05	Bal.

TABLE 2 Chemical composition of the Inconel 718 powder feedstock as given by the supplier

Element	Ni	Cr	Al	Mo	Nb (+Ta)	Ti	Fe
wt%	50-55	17-21	0.2-0.8	2.8-3.3	4.75-5.5	0.6-1.1	Bal.

TABLE 3 Main processing parameters for LPBF of AlSi10Mg and Inconel 718 used in this study

Material	Layer Thickness (t)	Hatch Spacing (h)	Laser Power (P)	Scan Velocity (v)	Substrate Temperature (T_s)
AlSi10Mg	30 μm	97.5 μm	200 W	1200 mm/s	200 °C
Inconel 718	50 μm	120 μm	250 W	805 mm/s	25 °C
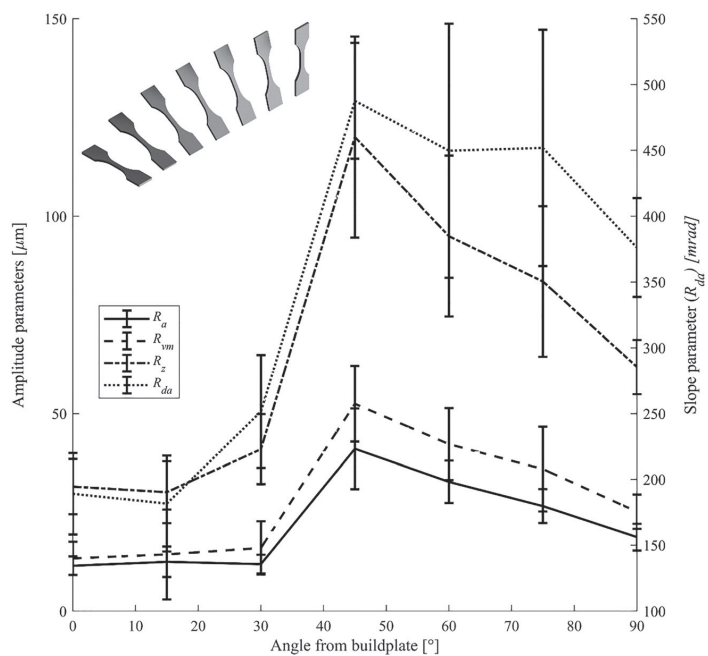
FIGURE 1 Selected WLI roughness measurements for the AlSi10Mg specimens (oriented from 0° (XY) to 90° (ZY) with 15° increments). The inset shows the orientations of each specimen from 0° to 90°. The error bars indicate the standard deviation of the measurement within each measured area

TABLE 4 Specimen annotation according to ISO/ASTM 52921:2013E

| Specimen No.	1	2	3	4	5	6	7
Designation	XY	XY+15B	XY+30B	XY+45B	XY+60B	XY+75B	ZY

and the valleys (R_z), and the average absolute slope measured in radians (R_{da}) all follow the same trend as the arithmetical mean deviation (R_a). Figures 2 and 3 show the same roughness parameters for the Inconel 718 specimens, in the as-built and HIP + ageing heat treatment conditions, respectively.

Our roughness data for the AlSi10Mg (Figure 1) specimens does not match the LPBF roughness data reported by Boschetto et al[25] for AlSi10Mg and by Strano et al for stainless steel,[26] as well as our data of Inconel 718, in which the peak in roughness appears at lower angles. As a result, the surface roughness profile of the AlSi10Mg
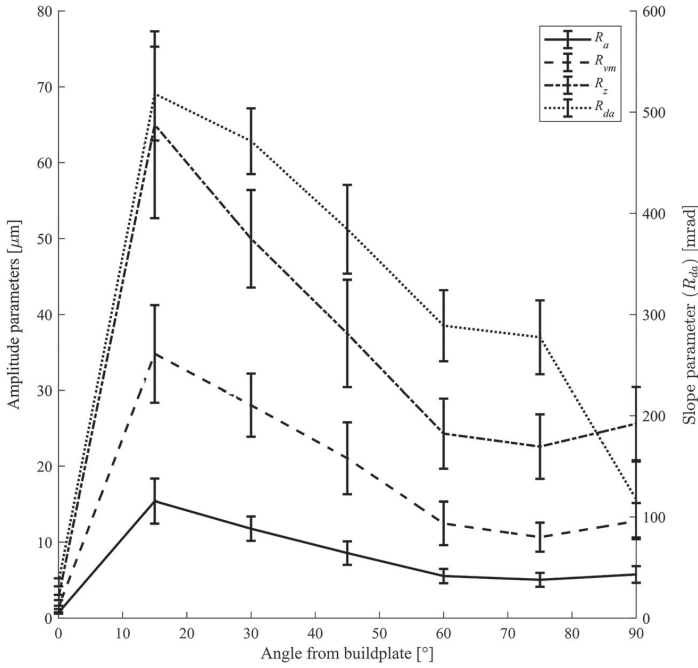
FIGURE 2 Selected roughness measurements for the as-built Inconel 718 specimens (oriented from 0° to 90° with 15° increments)
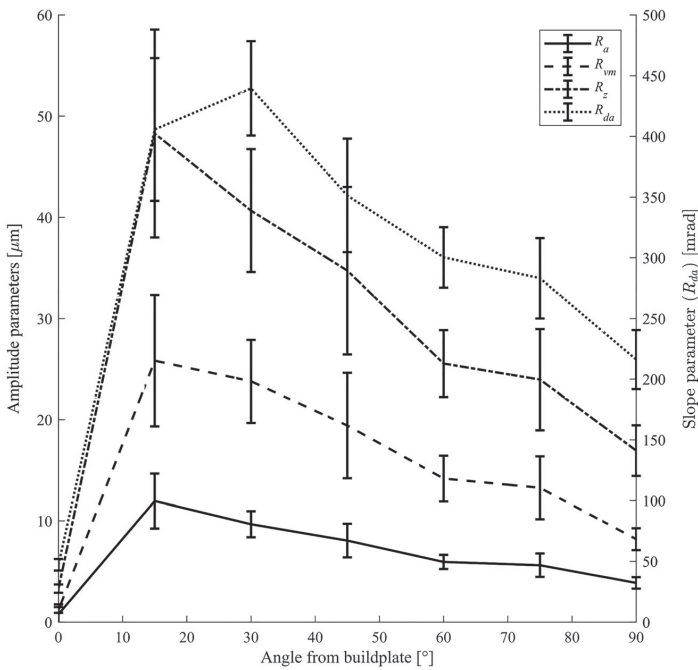
FIGURE 3 Selected roughness measurements for the HIP + aged Inconel 718 specimens (oriented from 0° to 90° with 15° increments)

specimens (Figure 1) fits poorly with the surface roughness model introduced by Boschetto et al. Several factors will determine the final surface roughness during specimen fabrication, such as powder particle size and morphology, layer height, and process parameters.

The surface roughness vs build angle for the Inconel 718 specimens follows the trends reported by other authors for AM materials[25,26]; the surface roughness is lowest for the horizontal specimen (0°), followed by a peak in roughness at 15°, and then a decline as the specimens are raised towards the vertical orientation (90°). For the 15° and 30° specimens, the surface roughness values of HIP plus aged Inconel 718 are lower than those of the as-built specimens. It appears that the highest features of the surface are knocked down in the HIP process. The major difference in scan strategy between the AlSi10Mg and Inconel 718 specimens is that the island scan strategy was used for the former material.

As can be seen in the variation of the results from different studies (Hovig et al[17] and Section1), the machine-to-machine repeatability is low. Therefore, surface characterization for the specific machine and material is necessary in order to predict the fatigue life of a LPBF component.
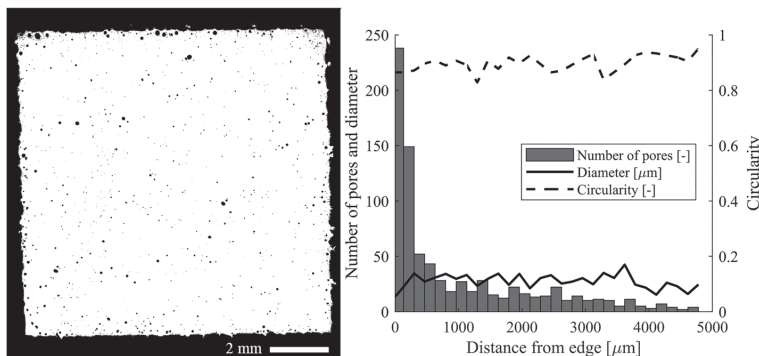
3.2 | Porosity

Figure 4 (left) shows a polished cross section of an AlSi10Mg cube made with the process parameters used in this study. The porosity content is measured to be 0.50 vol%. The distribution, average diameter, and average circularity of the pores as a function of distance from the edge are shown in Figure 4 (right). As can be seen in Figure 4, there is a substantial amount of subsurface porosity, and the closest distance between the surface and a pore is less than 15 μm. The high concentration of subsurface

porosity is believed to be a result of trapped hydrogen during LPBF processing. The laser first melts the cross section of each cube before finishing with a contour scan along the perimeter. This allows the cross section to solidify before the perimeter is melted, effectively creating a physical barrier that limits the hydrogen's ability to diffuse through the outer perimeter during heat treatment. Beevers et al experimented with AlSi10Mg specimens processed with and without contour scans[19] and found that the largest pores were near the surface in both conditions. The specimen processed with contour scan had the largest pores, but the quantity was higher near the surface when processing without contour scan. However, note that Beevers et al did not heat treat the specimen.

The measured diameter of the pores ranges from 8 to 175 μm; the average pore diameter in each histogram bin range from 15 to 42 μm, and the average diameter is 27 μm. The average circularity is 0.88, which indicates that the pores are dominantly spherical.

Figure 5 shows scanning electron microscope (SEM) micrographs of as-built (Figure 5 left) and HIP plus aged (Figure 5 right) Inconel 718. In the as-built condition, two different defects are visible: spherical pores with diameter less than 10 μm and large irregularly shaped defects with size in the order of 100 μm. The spherical pores are believed to be a result of trapped gas during the processing of feedstock or LPBF sample fabrication.[27] The irregularly shaped defects are attributed to suboptimal LPBF processing parameters. In the HIP + aged condition, the irregularly shaped defects are no longer visible. Some of the smaller pores are retained after HIP + ageing, but the quantity is greatly reduced compared with the as-built condition. The relative density of the material also increases from 99.97% for the as-built condition to 99.98% for the HIP + aged condition.[24]

In addition to introducing local stress concentrations, the surface defects and the internal defects disrupt the


FIGURE 4 Optical microscopy image of a cross section of an AlSi10Mg cube cut perpendicular to the build direction (left) and image analysis of the porosity (right)
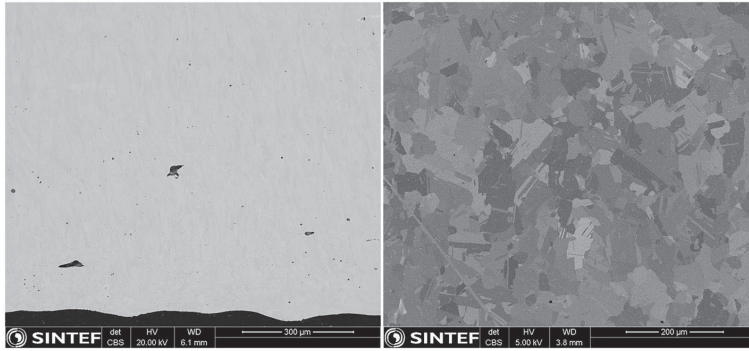
FIGURE 5 SEM micrographs of as-built (left) and HIP postprocessed (right) Inconel 718 cut perpendicular to the build direction. Note that the scales are different

stress distribution around each other. Figure 6 shows a numerically computed SCF for a generic material, with a U-shaped groove on the surface and a spherical pore close to the groove tip, under uniaxial tensile loading conditions. The pores are assumed spherical since the most defect-prone material in this study (AlSi10Mg) has a circularity close to 1. The upper limit for pore size is chosen based on the observed maximum pore size of AlSi10Mg, and the lower limit set to 50 μm, as the distance where the pore becomes independent of the surface defect is approaching the width of the contour scan (150 μm). As can be seen, both the pore diameter and its distance from the groove tip affect the local stress field. The simulation is carried out with d and ρ selected to give a baseline SCF $k_t = 4.5$, but the general trend would be the same if any other baseline was selected. The SCF increases with increasing pore size and decreasing distance between pore and groove tip. Siddique et al[28] expressed the SCF of a pore as a function of the pore diameter and distance from the surface (no surface roughness), with values for
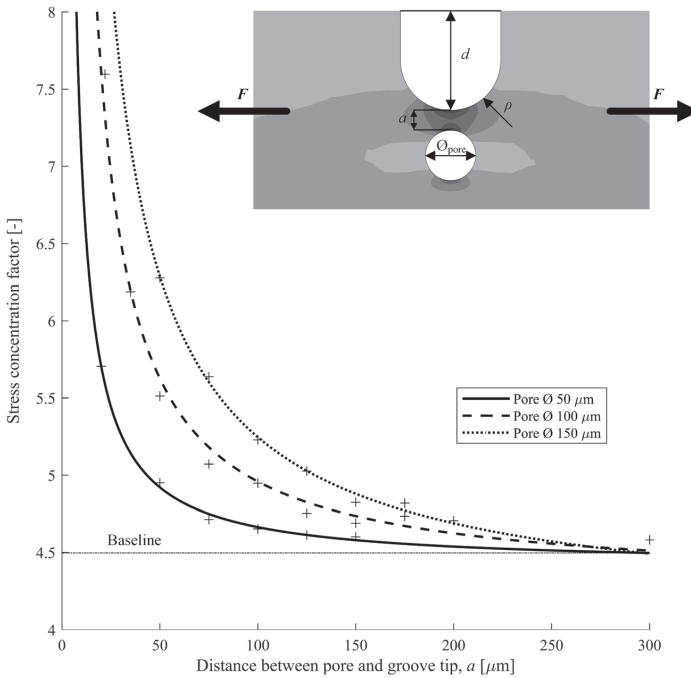
FIGURE 6 The effect of pore diameter and distance between pore and crack tip on the SCF of a U-shaped surface defect with nominal SCF of 4.5. The inset shows the relative geometry of the groove and the pore. F indicates the direction of the applied uniaxial tension

k_t ranging from 1 to 1.178. When comparing the magnitude of the stress concentration from only surface defects (Equation 1 and baseline in Figure 4) and internal pores (Siddique et al), it becomes clear that SCFs from surface defects are far larger than those from only spherical pores.

3.3 | Stress concentration factors

Consider the simplified schematic of an as-built LPBF surface shown as an inset in Figure 7. The schematic shows a cross section of three layers, where the scanning direction alternates with each layer. Each semicircle represents a single laser track. The hatch spacing is indicated with h, the layer thickness with t, and the inclination angle (of the built part) with θ. The surface can then be considered as a periodic row of laser tracks, where the depth of each valley (between two tracks) is the surface roughness measure R_{vm}. The radius at the depth of the valley, ρ, can be calculated with Equation 3;

$$\rho = \frac{L - \tan(R_{da})R_z}{1 - \tan(R_{da})} \qquad (3)$$

The width L is the peak-to-peak distance measured as S (mean spacing between adjacent local peaks). The value

of R_{da}, R_z, and S may be determined by WLI as in this study, or simply with a perthometer. The SCF for surface defects may then be calculated with Equation 2 using R_{vm} as d, and ρ according to Equation 3. This method is referred to as the stylus method in the subsequent discussion.

An alternative approach for calculating the SCF of surface defects is to use the mapped topography from WLI. The surface topography is represented in a matrix, with each element, Z_{XY}, corresponding to the height of the pixel indicated by the row (X) and column (Y). The horizontal radius of curvature at each point may then be obtained based on a quadratic fit through that point and the adjacent points. If the data is fit to $Z(X, Y) = aZ(X, Y)^2 + bZ(X, Y) + c$; the spherical radius of curvature at (X,Y) is approximately $r \cong (2a)^{-1}$. The SCF may then be estimated using Equation 2. This method is referred to as the "WLI method" in the subsequent discussion. The estimated SCFs for the seven specimen orientations were calculated using both the WLI method and the stylus method. The results are shown in Figure 7 for AlSi10Mg and Figure 8 for Inconel 718. As expected, the SCF follows the general trend of the surface roughness parameters (Figures 1, 2, and 3).

Consider the SCF for AlSi10Mg in Figure 7. For specimens oriented at angles below 45°, the SCF is relatively
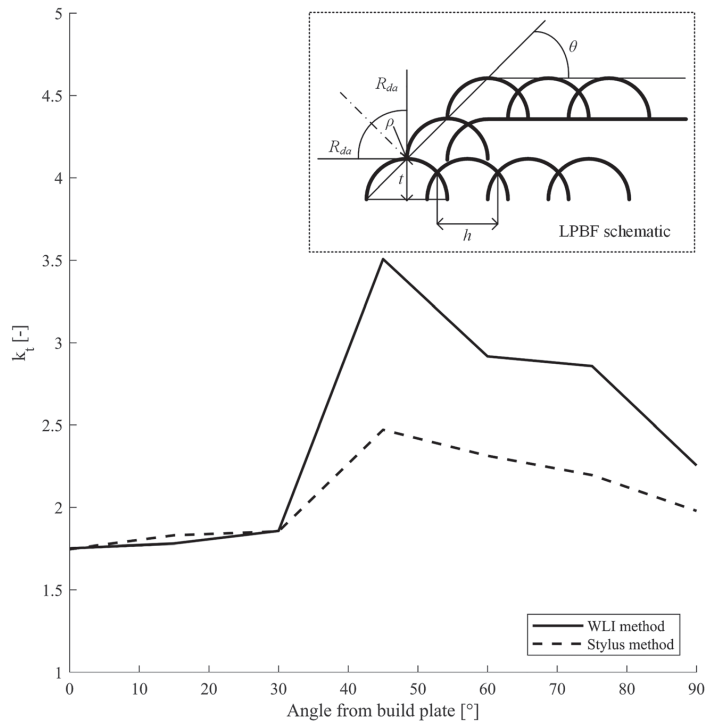
FIGURE 7 Estimated SCF for surface defects in AlSi10Mg for all specimen orientations with both the "WLI method" and the "stylus method". The inset is a schematic of three layers of a LPBF process with the relevant parameters for the stylus method indicated
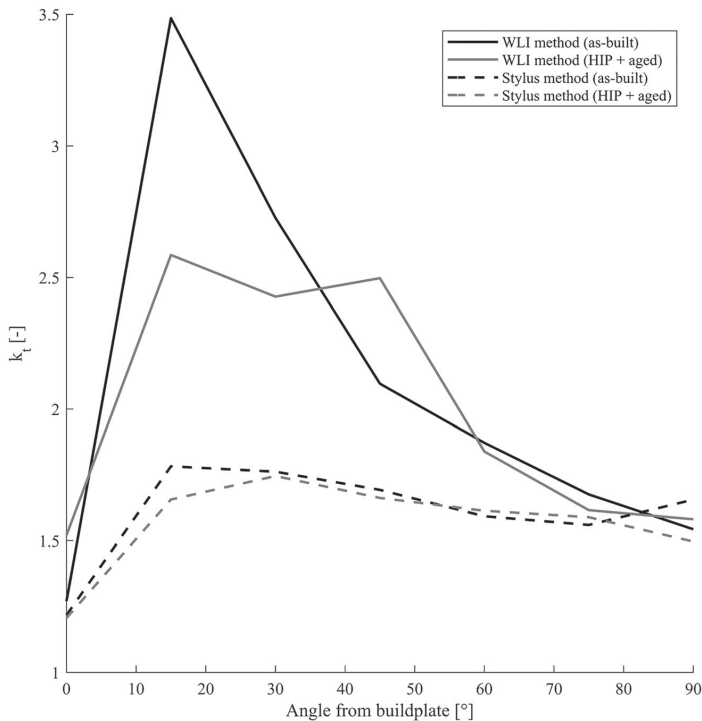
FIGURE 8 Estimated SCF for surface defects in Inconel 718 for both heat treatment conditions and all specimen orientations with both the "WLI method" and the "stylus method"

low and consistent for both methods. When the surface roughness increases for the specimens oriented at 45° and above, the WLI method gives more conservative values. The stylus method considers either a line on the surface (perthometer) or the average surface roughness of the investigated area (WLI) and averages out the extremities. Consequently, the extremities of the peaks and valleys are given less weight than with the WLI method, resulting in a less conservative estimate of the SCF. For smoother surfaces (0°, 15°, and 30°), the discrepancy between the two methods is relatively small and the estimated SCF is conservative for the stylus method. For rougher surfaces, the WLI method will estimate a more conservative SCF than the stylus method.

In the case of Inconel 718 (Figure 8), the discrepancy between the WLI method and the stylus method is large across the entire surface inclination range except for surfaces at 0° and 90°. Figure 9 shows the WLI images of the surface of the horizontal specimens of AlSi10Mg (left), as-built Inconel 718 (middle), and HIP + aged Inconel 718 (right). As can be seen, there is a visible amount of partially fused powder particles on the AlSi10Mg specimen (Figures 9 (left) and 10 (right)), whereas for the horizontal Inconel 718 specimens, there are few if none visible powder particles on the surface. However, when the flat surfaces of the Inconel 718 specimens are built at an angle, the partially fused particles appear (Figure 10 (left)). The presence of particles at the surface will
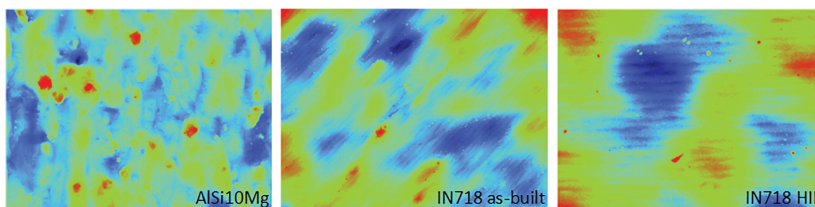
FIGURE 9 Unmasked WLI images of the surface of the horizontally oriented specimens of AlSi10Mg (left), as-built Inconel 718 (middle), and HIP + aged Inconel 718 (right). The area investigated is 1.7 mm × 2.3 mm. Red colour indicate high points, while blue indicate low points [Colour figure can be viewed at wileyonlinelibrary.com]
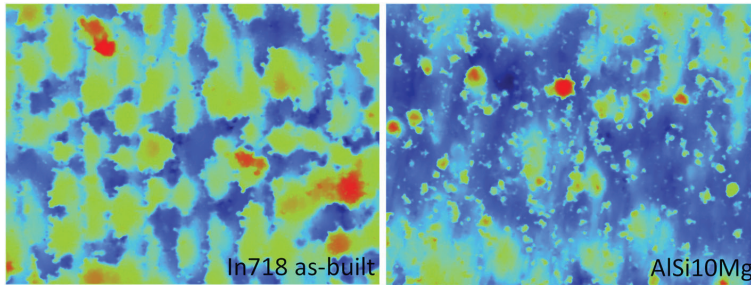
FIGURE 10 Unmasked WLI image of the 15° as-built Inconel 718 (left) and the 45° AlSi10Mg (right) specimens. The area investigated is 1.7 mm × 2.3 mm. Red colour indicates high points, while blue indicate low points [Colour figure can be viewed at wileyonlinelibrary.com]

strongly affect the roughness extremes, the base for the WLI method, but it will not alter the average roughness parameters, the base for the stylus method, to the same extent. This can explain the large discrepancies observed between the methods.

If the material in question contains subsurface pores, a modification of the estimated SCFs might be necessary. As shown in Figure 6, both the pore diameter and the distance between the surface defect and the pore will affect the SCF of the surface defect. If a pore is in close proximity to the surface defect, the local SCF increases, leading to premature crack initiation and reducing the fatigue life. However, as this crack propagates into the pore, the pore will blunt the crack tip. The effective SCF is then the SCF of the pore. Since the SCFs of pores are in the range of 1 to 1.178,[28] further crack propagation will be abated. Statistically speaking, although subsurface porosity might be present, an ordered distribution of pores that will blunt all cracks is quite unlikely. As a result, the cumulative effect of the surface and subsurface defects should be considered when designing components subjected to high cycle fatigue loading. Another finding of modelling the crack-pore interaction (Figure 6) is the distance at which the stress intensity factor becomes independent of pore size and geometry. For the typical range of surface defects, it was found that the pores positioned at 300 μm and farther from the surface defect tip had no effect on the local stress field at the tip. Therefore, in this particular study, subsurface pores will have to be considered only when they are located closer to the surface than 300 μm.

3.4 | High cycle fatigue life estimation

It is widely demonstrated that the specimen build orientation affects the microstructure in terms of texture in Inconel 718 processed by both LPBF[21,22,24,29] and electron beam melting.[30] According to these studies, the variation

in the elastic and shear moduli from the weakest to the strongest orientation does not account for more than 10% and 50%, respectively. Although for a polished sample with $k_t = 1$ the variation of anisotropic properties is quite influential, these effects are considerably lower than the SCF impact that is shown to amplify the externally applies stress by 150% to 350% ($k_t = 1.5$ to 3.5). Consequently, in the present study, it is considered unnecessary to incorporate the anisotropic properties as the aim is to benchmark the effect of surface roughness on high cycle fatigue life. As a final justification, we would also like to remind the reader that the microstructures of LPBF AlSi10Mg and Inconel 718 undergo extensive recrystallization upon heat treatment and HIPing, respectively, which mitigates the traces of textured microstructure and thus mechanical anisotropy.

In order to demonstrate the effect of surface roughness on high cycle fatigue life, a series of simulations were performed using Abaqus and FE-Safe finite element analysis software. A dog bone geometry was loaded in tension and compression at 10% of the material's yield strength in Abaqus. Thereafter, it was subjected to a cyclic load in FE-Safe ($R = -1$). The material properties for AlSi10Mg were selected from a study by Hitzler et al[31] with $E = 62.6$ GPa, $\nu = 0.30$, and $\sigma_y = 198$ MPa. The model is based on an experimentally determined SN curve, and the fatigue life is calculated for the different stress concentration factors measured for the various surface conditions. As a reference SN curve for LPBF AlSi10Mg in T6 condition, the fit from the machined T6 condition in Hovig et al[17] was used. For aged Inconel 718, the material properties were determined in a preceding study by the current authors,[24] with $E = 181$ GPa, $\nu = 0.40$, and $\sigma_y = 1085$ MPa. For aged Inconel 718, published data for machined and aged Inconel 718[23] were used.

According to Figure 11, the fatigue lifetime is reduced by approximately two orders of magnitude for AlSi10Mg and one order of magnitude for Inconel 718, when the
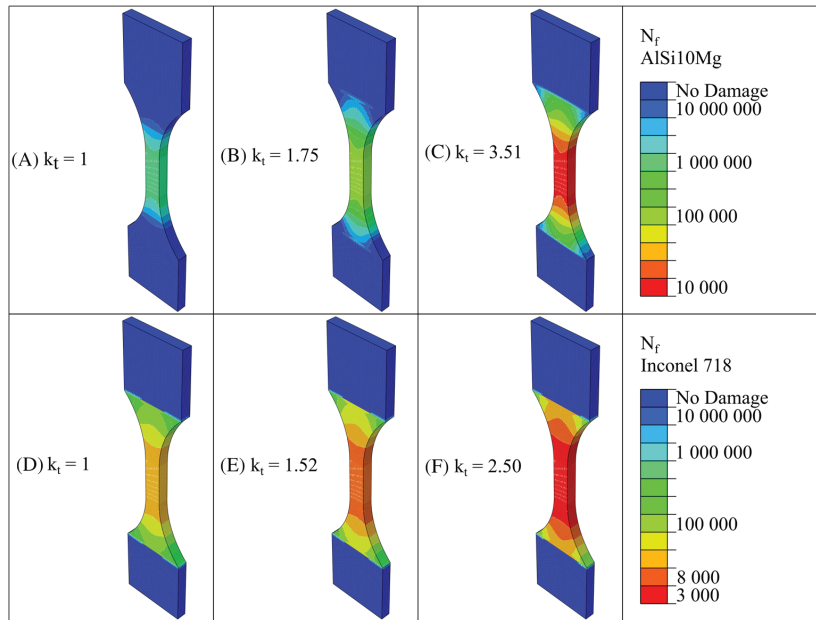
FIGURE 11 Fatigue life simulations of AlSi10Mg and Inconel 718 with different surface conditions. A-C, AlSi10Mg with SCF values according to polished surface, horizontal orientation, and 45° orientation, respectively. D-F, The same for Inconel 718. The legend shows expected number of cycles to failure, N_f. The SCFs were selected from the WLI method [Colour figure can be viewed at wileyonlinelibrary.com]

specimen build inclination changes from horizontal to 45°. Since the processing parameters and scanning strategy for these two alloys were different, it can be inferred that changing the process parameters may also influence the fatigue lifetime of the material. The island scanning strategy that was used for AlSi10Mg seems to have an unfavourable effect on the surface properties, although this must be checked by comparing the two processing methods with the same material and powder. When comparing the resulting surface roughness of LPBF Inconel 718 in this work and previously published studies[21,22] (R_a in the order of 5-17 μm depending on orientation) with published values for surface roughness for AlSi10Mg[12,14,18] (R_a in the order of 10-24 μm depending on orientation), it is apparent that the Inconel 718 alloy generally has a lower surface roughness. Thus, implementing the scan strategy used on the Inconel 718 specimens on the AlSi10Mg specimens does not guarantee comparable surface finishes. In a recent study by Witkin et al,[32] notched fatigue specimens of LPBF Inconel 718 were tested with as-built and machined surfaces. The machined and notched specimens with the highest nominal SCF ($k_t = 3.10$) had a longer fatigue life than as-built (unnotched) specimens with nominal SCFs of $k_t = 2.00$ and $k_t = 2.24$. The results from Witkin

et al implies that even when notched defects with SCFs of three times that of a polished unnotched surface are introduced, the surface roughness is still the dominating effect when it comes to defect induced fatigue life reduction.

In general, the fatigue lives reported here, calculated using Equation 2, are based on SCFs due to uniaxial tension. This should be considered the worst-case loading scenario[2] and gives the most conservative estimate.

4 | CONCLUSIONS

This study presents two methods for estimating stress concentration factors for high cycle fatigue life prediction of AlSi10Mg and Inconel 718 processed by laser powder bed fusion (LPBF). The methods are based on surface roughness data as input. Compared with the WLI method, the stylus method estimates a longer fatigue life for rough surfaces. For smoother surfaces, the difference between the methods is small.

In porosity-free materials, the stress concentration factor, and thus the high cycle fatigue life, is a function of the surface roughness. HIP + ageing was shown to be effective in reducing the surface roughness and the

quantity of internal defects in Inconel 718. Consequently, the stress concentration factor will be reduced. In the case of AlSi10Mg, subsurface defects are present, and their effect must be considered through the methods proposed by, eg, Romano et al,[4] Yamashita et al,[7] or as a multiplier to the SCF based on the worst-case scenario acquired from the surface roughness, average pore size, and distance from the surface anomalies (see Figure 6).

Based on the investigated model in this work, the stress concentration factor of a surface defect is affected by internal defects if the diameter of the internal defect is sufficiently large, and the distance between the surface defect and the internal defect is sufficiently small. Although the maximum stress at the surface defect increases, a resulting crack will be blunted when it propagates into the internal defect. Thus, a more comprehensive model is necessary in order to estimate the fatigue life of components with subsurface defects.

ACKNOWLEDGEMENTS

ORCID

Even W. Hovig https://orcid.org/0000-0002-9071-4458
Amin S. Azar https://orcid.org/0000-0002-6268-7616
Martin F. Sunding https://orcid.org/0000-0002-5632-3381
Erik Andreassen https://orcid.org/0000-0002-4314-5854
Knut Sørby https://orcid.org/0000-0002-8394-5565

REFERENCES

1. Yap C, Chua C, Dong Z, et al. Review of selective laser melting: materials and applications. *Appl Phys Rev.* 2015;2(4):041101.

2. Pilkey WD, Pilkey DF. *Peterson's stress concentration factors.* Hoboken, NJ, USA: John Wiley; 2008.

3. Siddique S, Awd M, Tenkamp J, Walther F. Development of a stochastic approach for fatigue life prediction of AlSi12 alloy processed by selective laser melting. *Eng Fail Anal.* 2017;79:34-50.

4. Romano S, Brückner-Foit A, Brandão A, Gumpinger J, Ghidini T, Beretta S. Fatigue properties of AlSi10Mg obtained by additive manufacturing: defect-based modelling and prediction of fatigue strength. *Eng Fract Mech.* 2018;187:165-189.

5. Romano S, Patriarca L, Foletti S, Beretta S. LCF behaviour and a comprehensive life prediction model for AlSi10Mg obtained by SLM. *Int J Fatigue.* 2018;117:47-62.

6. Yadollahi A, Mahtabi MJ, Khalili A, Doude HR, Newman JC. Fatigue life prediction of additively manufactured material: effects of surface roughness, defect size, and shape. *Fatigue Fract Eng Mater Struct.* 2018;41(7):1602-1614.

7. Yamashita Y, Murakami T, Mihara R, Okada M, Murakami Y. Defect analysis and fatigue design basis for Ni-based superalloy 718 manufactured by selective laser melting. *Int J Fatigue.* 2018;117:485-495.

8. Zhou Z, Xu H, Li C, Chen G. The effect of texture on the low cycle fatigue property of Inconel 718 by selective laser melting. *MATEC Web Conf.* 2018; 165:

9. Aydinöz ME, Brenne F, Schaper M, et al. On the microstructural and mechanical properties of post-treated additively manufactured Inconel 718 superalloy under quasi-static and cyclic loading. *Mater Sci Eng A.* 2016;669:246-258.

10. Chlebus E, Gruber K, Kuźnicka B, Kurzac J, Kurzynowski T. Effect of heat treatment on the microstructure and mechanical properties of Inconel 718 processed by selective laser melting. *Mater Sci Eng A.* 2015;639:647-655.

11. Ni M, Chen C, Wang X, et al. Anisotropic tensile behavior of in situ precipitation strengthened Inconel 718 fabricated by additive manufacturing. *Mater Sci Eng A.* 2017;701:344-351.

12. Aboulkhair NT, Maskery I, Tuck C, Ashcroft I, Everitt NM. Improving the fatigue behaviour of a selectively laser melted aluminium alloy: influence of heat treatment and surface quality. *Mater Des.* 2016;104:174-182.

13. Brandl E, Heckenberger U, Holzinger V, Buchbinder D. Additive manufactured AlSi10Mg samples using selective laser melting (SLM): microstructure, high cycle fatigue, and fracture behavior. *Mater Des.* 2012;34:159-169.

14. Maskery I, Aboulkhair N, Tuck C et al. Fatigue performance enhancement of selectively laser melted aluminium alloy by heat treatment. In: eds. *Proceedings of 26th Annual International Solid Freeform Fabrication Symposium.* Austin, Texas, USA: 2015:1017–1025.

15. Mower TM, Long MJ. Mechanical behavior of additive manufactured, powder-bed laser-fused materials. *Mater Sci Eng A.* 2016;651:198-213.

16. Siddique S, Imran M, Walther F. Very high cycle fatigue and fatigue crack propagation behavior of selective laser melted AlSi12 alloy. *Int J Fatigue.* 2017;94:246-254.

17. Hovig Even W, Azar Amin S, Sunding Martin F, Sørby K, M'Hamdi M, Andreassen E. High cycle fatigue life estimation of AlSi10Mg processed by laser powder bed fusion. *MATEC Web Conf.* 2018; 188:

18. Bagherifard S, Beretta N, Monti S, Riccio M, Bandini M, Guagliano M. On the fatigue strength enhancement of additive manufactured AlSi10Mg parts by mechanical and thermal post-processing. *Mater Des.* 2018;145:28-41.

19. Beevers E, Brandão AD, Gumpinger J, et al. Fatigue properties and material characteristics of additively manufactured AlSi10Mg—effect of the contour parameter on the

microstructure, density, residual stress, roughness and mechanical properties. *Int J Fatigue*. 2018;117:148-162.

20. Scott-Emuakpor O, George T, Holycross C, Bruns J, Zearley A. Bending fatigue life comparison between DMLS and cold-rolled nickel alloy 718. In: eds. *Proceedings of* Virginia Beach, Virginia, USA: 2014:

21. Kelley PF, Saigal A, Vlahakis JK, Carter A Tensile and fatigue behavior of direct metal laser sintered (DMLS) Inconel 718. In: eds. *Proceedings of* Houston, Texas, USA: American Society of Mechanical Engineers; 2015:

22. Konečná R, Nicoletto G, Kunz L, Bača A. Microstructure and directional fatigue behavior of Inconel 718 produced by selective laser melting. In: *eds*. *Proceedings of* Catania, Italy: 2016:2381–2388.

23. Balachandramurthi AR, Moverare J, Dixit N, Pederson R. Influence of defects and as-built surface roughness on fatigue properties of additively manufactured alloy 718. *Mater Sci Eng A*. 2018;735:463-474.

24. Hovig EW, Azar AS, Grytten F, Sørby K, Andreassen E. Determination of anisotropic mechanical properties for materials processed by laser powder bed fusion. *Adv Mater Sci Eng*. 2018;2018:1-20.

25. Boschetto A, Bottini L, Veniali F. Roughness modeling of AlSi10Mg parts fabricated by selective laser melting. *J Mater Process Technol*. 2017;241:154-163.

26. Strano G, Hao L, Everson RM, Evans KE. Surface roughness analysis, modelling and prediction in selective laser melting. *J Mater Process Technol*. 2013;213(4):589-597.

27. Aboulkhair NT, Everitt NM, Ashcroft I, Tuck C. Reducing porosity in AlSi10Mg parts processed by selective laser melting. *Addit Manuf*. 2014;1-4:77-86.

28. Siddique S, Imran M, Rauer M, et al. Computed tomography for characterization of fatigue performance of selective laser melted parts. *Mater Des*. 2015;83:661-669.

29. Gribbin S, Bicknell J, Jorgensen L, Tsukrov I, Knezevic M. Low cycle fatigue behavior of direct metal laser sintered Inconel alloy 718. *Int J Fatigue*. 2016;93:156-167.

30. Kirka MM, Greeley D, Hawkins C, Dehoff R. Effect of anisotropy and texture on the low cycle fatigue behavior of Inconel 718 processed via electron beam melting. *Int J Fatigue*. 2017;105:235-243.

31. Hitzler L, Janousch C, Schanz J, et al. Direction and location dependency of selective laser melted AlSi10Mg specimens. *J Mater Process Technol*. 2017;243:48-61.

32. Witkin DB, Patel DN, Bean GE. Notched fatigue testing of Inconel 718 prepared by selective laser melting. *Fatigue Fract Eng Mater Struct*. 2018;42:166-177.

6.5. Paper 5 - A novel approach for enhancing the fatigue lifetime of the components processed by additive manufacturing technologies

6.6. Paper 6 - Directional fatigue behaviour of maraging steel grade 300 produced by laser powder bed fusion

Directional fatigue behaviour of maraging steel grade 300 produced by laser powder bed fusion

Klas Solberg [*], Even Wilberg Hovig, Knut Sørby, Filippo Berto

Institutt for maskinteknikk og produksjon, NTNU, Trondheim, Norway

ARTICLE INFO

ABSTRACT

Surfaces of metals produced by additive manufacturing (AM) are known to be rough and populated with defects, this is, in particular, true for downward-facing (down-skin) surfaces. When dealing with the fatigue of as-built surfaces produced by AM, fatigue is typically initiating from surface defects. In this work, the fatigue behaviour of maraging steel grade 300 (18Ni300) produced by laser beam powder bed fusion (PBF-LB) is investigated. Fatigue initiation from surfaces built both up- and down-skin are investigated. This is done by using specimens where all surfaces are machined, except the one at interest. Specimens were built in 10 orientation ranging from 0° (horizontal, up-skin) to 135° (down-skin). The surface roughness was measured for all orientations; high surface roughness was found for down-skin surfaces while wavy surfaces were found for up-skin surfaces. The fatigue behaviour was found to be correlated to the build orientation and the surface roughness.

1. Introduction

Additive manufacturing (AM) offers new possibilities in terms of design freedom, lead time and cost reductions [1–3]. Nevertheless, the materials often contain defects deriving from the manufacturing process that are reducing the mechanical performance [4,5]. Typical defects are high surface roughness, lack of fusion, porosity, residual stresses and distortions [5–8]. In addition to this, the microstructure is often aniso-tropic, as a result of the steep thermal gradients in the building process [5]. There are several approaches when designing parts for AM, in some cases, parts are produced near-to-net shape and fully post-processed with machining and heat treatment. This is done to remove defects and achieve the highest possible quality while keeping the costs low by reducing material usage and the amount of tooling. In other cases, geometric complexity, only possible to be achieved by the AM process, is desired in the final design. In this case, it might be impossible to perform machining, and designers are forced to accept the presence of the rough and defect populated as-built (AB) surfaces.

The fatigue behaviour is in particularly sensitive to the above-mentioned defects deriving from the AM process. Many of the mate-rials that are popular in metal AM have high strength and hardness, e.g. Inconel 718, Ti6Al4V, 18Ni300 and 17-4PH steel. From conventionally manufactured metals, high tensile strength and hardness are often correlated to a high notch sensitivity in fatigue loading [9]. In the AB

state, fatigue usually initiates from the rough surface or defects in the surface region [10]. By machining the surfaces, the surface defects are removed, and fatigue initiates from internal defects such as lack of fusion regions or pores [11]. Machining usually enhances the fatigue life, the same is true for chemical etching and other processes that can be used to remove surface defects [12]. Further enhancement of the fatigue behaviour can be achieved by performing hot isostatic pressing, where defects that are not open to a free surface can be closed [13,14]. In addition to these "geometry altering" post-processing methods, heat treatments are used to alter the microstructure. The heat treatments are specific to each alloying system [15], and can also be tailored to the specific AM processes [16].

Maraging steel grade 300 (18Ni300) is one of the alloying systems where mechanical performance can be enhanced by heat treatment. Maraging steel is a FeNi-based alloy with a dominating martensitic microstructure strengthened by precipitation hardening. The martensite in maraging steel is not caused by a high carbon content (like in many other tool steel) but instead by a high Ni-concentration [17]. The lack of carbon leads to good weldability, which makes the material a good candidate for AM [18,19,17,20].

Becker and Dimitrov [21] studied the Fatigue Crack Growth (FCG) of PBF-LB/18Ni300. The study included the effect of crack growth orien-tation (i.e. parallel and perpendicular to the build layers) and the effect of heat treatment. Faster FCG rates were observed for the AB conditions
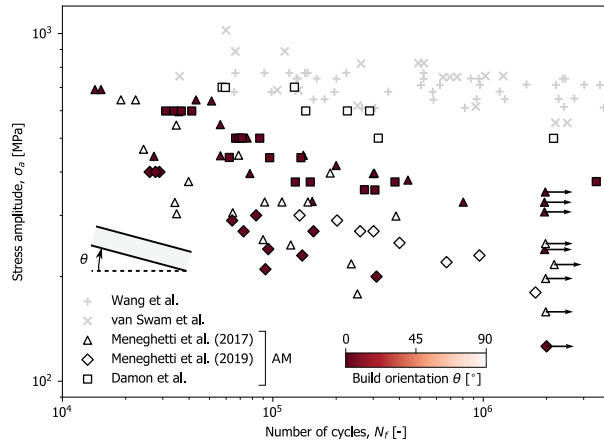

Fig. 1. Comparison of fatigue data from the literature. Wang et al. [22] van Swam et al.[23], Meneghetti et al. (2017) [24], Meneghetti et al. (2019)[26] and Damon et al. (PBF-LB) [27]. All fatigue data were tested at R = −1. Build angles are reported using the conventions of the current article: 0° - horizontal, 90° - vertical..
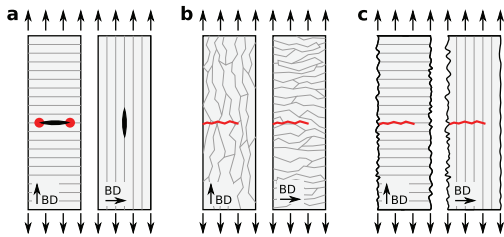

Fig. 2. Different features affecting the directional fatigue behaviour of AM metals. (a) orientation of defects, (b) microstructural anisotropy: orientation of columnar grains and (c) surface roughness dependent on surface orientation. Build directions indicated by BD.

when comparing them to the HT condition. The HT condition displayed the same FCG behaviour for both directions, which also coincided with the FCG for the wrought material. In the AB condition, faster FCG rate was observed parallel to the build layers than for perpendicular to the build layers. The uniaxial fatigue behaviour of AM 18Ni300 has also been studied; a collection of AM 18Ni300 fatigue data from the literature is shown in Fig. 1, compared to fatigue data of vacuum melted 18Ni300 [22,23]. The best fatigue performance is obtained in the

vacuum melted condition, while the AM studies displayed reduced performance. Concerning the directional fatigue behaviour of the AM materials, conflicting results have been reported. Meneghetti et al. [24] found higher fatigue life for the horizontal orientation than the vertical orientation. Croccolo et al. [25] found similar fatigue performance for both horizontal and vertical orientations for bending fatigue. While Meneghetti et al. [26] and Damon et al. [27] found that vertical specimens outperformed horizontal specimens.

Dealing with the directional fatigue behaviour of AM metals, several explanations are given for differences in the fatigue properties. The three most usual explanations are illustrated in Fig. 2; The orientation of internal defects, the orientation of the microstructure and the surface roughness variations based on the surface orientations. Lack of Fusion (LoF) is one example of build direction-dependent internal defects. LoF defects are planar regions which have not been properly fused. As LoFs are planar-like defects, they are most critical when loading is occurring parallel to the build direction [28]. The microstructure of AM metals are in many cases anisotropic due to columnar grain growth parallel to the build direction [29]. When loading occurs parallel to the build direction, the fatigue crack needs to propagate through several grain boundaries than when loading occurs normal to the build direction, this is illustrated in Fig. 2b. Riemer et al. found that the threshold stress intensity factor (for fatigue crack initiation) was higher for 316L built in the vertical orientation than in the horizontal orientation [30], and reasoned for this by stating that the fatigue crack needed to propagate
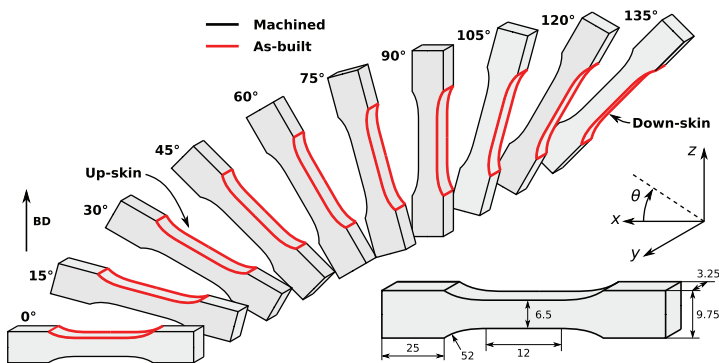

Fig. 3. Specimen orientations and dimensions. BD indicates the build direction.
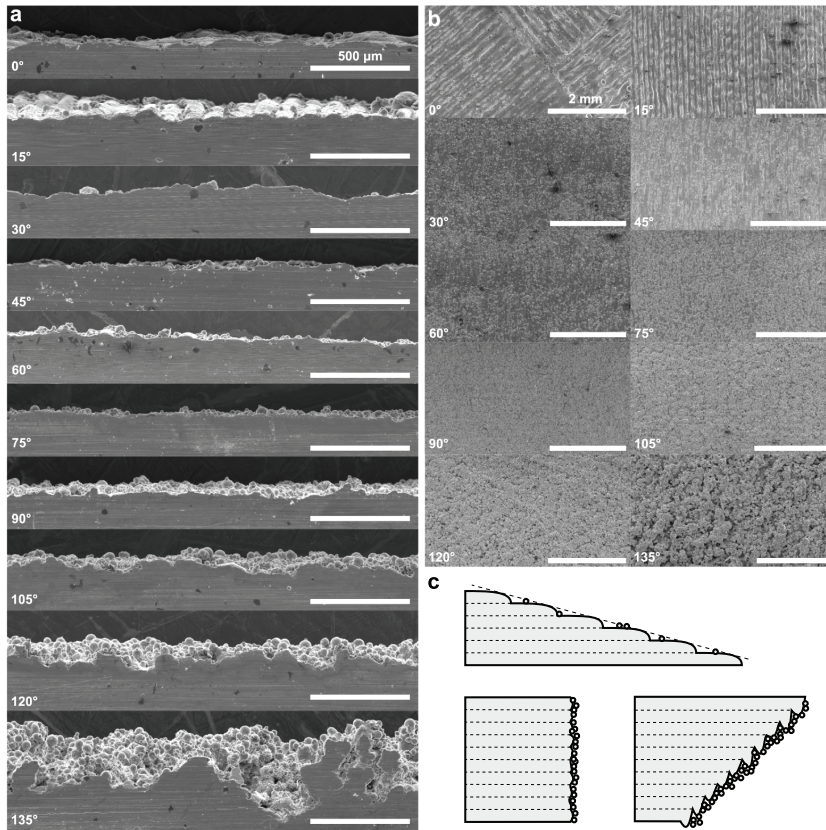
Fig. 4. SEM of surface conditions of specimens. (a) machined cross section (b) as-built surface (c) Schematic illustration of the different surface conditions.

through several grain boundaries. Dealing with uniaxial fatigue behaviour, the research usually shows that the fatigue life is higher for specimens built in the horizontal orientation [31,26,32]. The surface roughness and morphology are also dependent on the build orientations. Typically, down-skin surfaces (i.e. surfaces facing downwards) display higher surface roughness than up-skin surfaces (i.e. surfaces facing upwards). The valleys in the surface roughness profile act as stress risers, making them prone to fatigue initiation. Due to this, the main trend is that when the directional fatigue behaviour is assessed with an as-built surface, fatigue initiates from the down-skin region and not the up-skin region.

The goal of the present work is to evaluate directional fatigue behaviour of PBF-LB/18Ni300 maraging steel and in particular the fatigue behaviour of up- and down-skin surfaces. To do this, a new test specimen is proposed, where all sides of the specimens are machined except one side. Specimens were printed near-to-net shape for different orientations and then machined. To simplify the test scheme, one load level is selected for all the specimens. The fracture surfaces and the surface roughness profiles were investigated. Further, the porosity and microstructure were analyzed. Finally, the fatigue data are discussed in terms of variations in surface conditions and dimensional tolerances.

2. Methods

The specimen geometry is based on ASTM E466-15; Specimens with tangentially blended fillets between a uniform cross-section, the dimensions are shown in Fig. 3. The specimens were built in 10 different orientations relative to the build platform, from $0°$ to $135°$ with steps of $15°$. Three specimens were built in each orientation. The specimens were built in a Concept Laser system using a quadratic island strategy of 5 mm $\times$ 5 mm islands. The islands had an angular shift of $45°$ for each layer in addition to a 1 mm xy-shift in the island locations. The perimeter of each layers was scanned with a single contour track. The hatch spacing of the contour track was the same as the volume hatch. The same parameters were used for up-skin and down-skin surfaces A laser power of 180 W, hatch spacing of 105 μm, scan velocity of 650 mm/s and a layer thickness of 30 μm was used as process parameters. Support structures were used for all down-skin surface except the surfaces left in the AB condition. The support type used was 'block' [33], with a wall thickness of 0.1 mm (one laser line) and a hatching on 1.5 mm between the walls in x- and y-direction. The specimens were heat-treated by direct aging at 500 °C for 5 h prior to removing them from the build platform and machining them.

To be able to observe the fatigue behaviour of the up-skin surfaces, one surface was left in the AB condition, as shown in Fig. 3. First, both sides of the specimens were ground to avoid distortion problems which have been observed for the same material and manufacturing processes [26]. After grinding, the specimens were machined on all sides except one surface.

The fatigue testing was done using a loading ratio R = 0 and a frequency of 30 Hz on an MTS servohydraulic system with a 50 kN load cell. To see the influence of the different build orientations and surface conditions without generating full SN-curves for each orientation, one load level was selected for the tests. The load level was based on
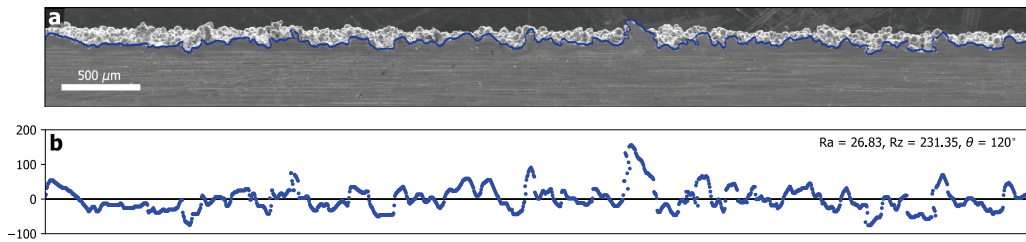
Fig. 5. Example of extraction and calculation of surface roughness parameters in python. (a) SEM with surface profile highlighted, (b) detected points used for calculation, note that Eq. (1) uses equally spaced points in the *x*-direction, which corresponds to the pixels i.n the SEM image.

experimental data on the same alloy from Meneghetti et al. [26] and on some initial trial and error testing of specimens with mistakes in the machining. The load level was determined to correspond to a stress range of 500 MPa, which results in fatigue failures around $\sim 10^5$ cycles. The gauge sections of all the specimens were measured with a caliper before testing.

A Scanning Electron Microscope (SEM) was used for analysing the fracture surfaces and for capturing the morphology of the as-built surfaces. Furthermore, the surface roughness of the as-built surfaces was calculated by extracting the surface profiles as lines in the software InkScape then importing and processing them in python[1]. Two different surface roughness parameters were calculated; the arithmetic mean deviation, *Ra*, and the maximum height of the profile, *Rz*. The arithmetical mean deviation of the assessed profile is given by

$$Ra = \frac{1}{n}\sum_{i=1}^{n}|y_i| \qquad (1)$$

and the maximum height of the profile given by

$$Rz = |\max_i y_i| - |\min_i y_i|. \qquad (2)$$

Where y_i is the distance from the mean line of n equally spaced points at the ith data point. The mean line was calculated by linear regression using `numpy.polyfit`.

The porosity of the material was determined from optical micrographs of polished cross-sections. The micrographs were analysed by a python script using the `cv2.THRESH_BINARY`[2] threshold filter. The threshold was set so that the porosity was captured and scratches and other irregularities were ignored. The microstructure was investigated in SEM, by Back Scattered Electron (BSE) analysis. Before BSE, oxide suspension polishing was done with a particle size of 0.25 μm. Vickers hardness (1 kg) were measured on a Mitutoyo MicroWiZhard system.

3. Results

3.1. Surface roughness

The AB surfaces were investigated by SEM and are shown in Fig. 4. The side-view of the machined surfaces are shown in Fig. 4a and the view normal to the AB surfaces are shown in Fig. 4b. Fig. 4b shows that for the horizontal specimens (0°), the hatching strategy is visible. For low angles (15°-60°), the different build layers are visible, displaying the staircase effect (see e.g. Fig. 4a 15°) which is characteristic for AM [34]. The surfaces built close to the vertical orientation displays a general roughness, which increases as the surface turns to down-skin. In the down-skin surfaces, the surfaces have increasingly higher roughness and
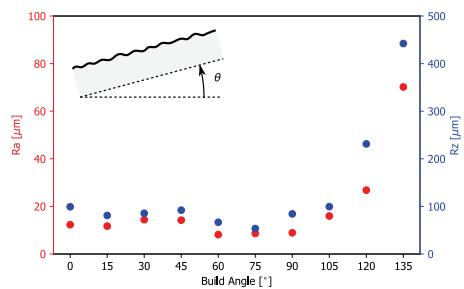
Fig. 6. Correlation between surface roughness (from SEM) and build angle.

high amounts of particles attached. It should be noted that the sharpness of the valleys of the surface in e.g. 135° are not high compared to what has been observed in other works where the melt pool geometry seems to directly dictate the surface morphology and create sharp corners [10].

Based on the SEMs in Fig. 4a and b, three main surface conditions can be identified:

(i) for angles close to zero the stair-case effect is observed. In 0° the hatching pattern is visible and from 15 −45° the stair-case effect is observed with an increased amount of attached powder particles as the angle increases.

(ii) For angles between 45° and 90° a general surface roughness is observed, with an increasing amount of attached powder as the angle increases.

(iii) For down-skin surfaces a strongly increasing surface roughness is observed, high amounts of powder particles are attached to the surfaces.

These three categories are illustrated in Fig. 4c.

Based on the captured SEMs of the surface profiles in Fig. 4a the surface roughness parameters *Ra* and *Rz* were calculated. An example of a surface profile and the extracted profile is shown in Fig. 5a and the data points and the calculation of *Ra* and *Rz* are shown in Fig. 5b. The *Ra* and *Rz* values obtained from all the SEMs are shown in Fig. 6. It should be noted that these data are not taken as the average of several measurements but directly from the SEMs presented in Fig. 4a. The main trend observed in Fig. 6 is that the value of *Ra* and *Rz* is increasing drastically from 105° to 135°. For values between 0° and 90°, the surface roughness values are slightly decreasing. A decrease in surface roughness when going from 0° to 90°, due to the staircase effect, has also been observed in recent literature [35,36]. The surface roughness for case (i) specimens are dominated by the staircase effect and not equal in different directions. I.e. the surface roughness along the length dimension of the specimens is higher than the surface roughness across the thickness of the specimens (See e.g. 15° in Fig. 4b). In the case of (ii) and (iii), the surface seems to be more uniform in the different directions
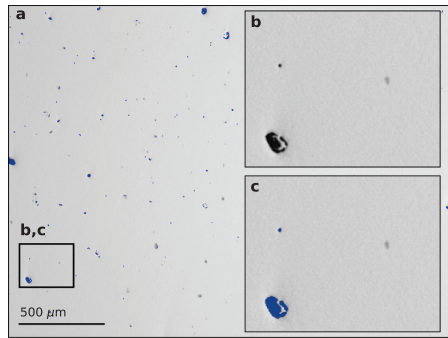
Fig. 7. Example of porosity measurement. (a) Optical micrograph of polished cross section with the detected porosity highlighted in blue. (b) detail of micrograph (c) detail of the micrograph with porosity highlighted.
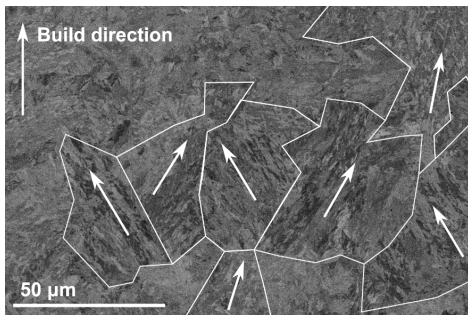

Fig. 8. Microstructure of the material in the *xz*-plane obtained by BSE. Different regions with a clear orientation of the martensite plates are indicated by outlining and arrows.

(See Fig. 4b).

3.2. Porosity

Fig. 7 shows a micrograph of a polished cross-section and the porosity detection. The full micrograph is shown in Fig. 7a and Fig. 7b and c shows a detail of the porosity detection. Note that the black regions with porosity are detected while the grey grinding lines and dirt are neglected. A porosity of $1.68 \pm 0.123\%$ was obtained based on the micrographs.

3.3. Microstructure

The microstructure of the material in the *xz*-plane is shown in Fig. 8 based on BSE analysis. The analysis displays regions of martensite blocks with plates of similar orientations. These regions are indicated by outlining and the direction of the plates are indicated by arrows in Fig. 8. When the material solidifies in the PBF-LB/M process, the high-atomic density vector <110> of the primary α-FCC austenite grains aligns with the direction of the heat flux [37], and the primary austenite grains tend to be elongated in the build direction. As the martensite transformation occurs the martensite plate orientation is dictated by the Kurdjumow-Sachs relationship, meaning that the plates can take any one of 24 orientations. This leads to a weak microstructural texture, much less dominant than what can be observed in other materials such as Inconel 718 [38,39] and AlSi10Mg [40].

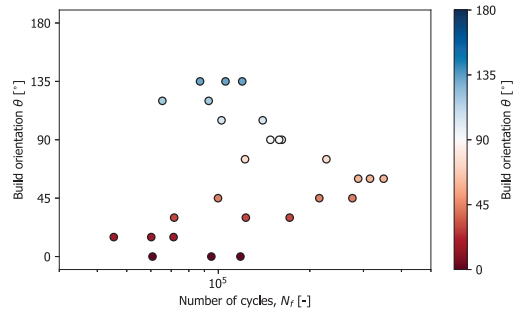The Vickers hardness (HV1) of the material was measured in the *xz*-

Fig. 9. Fatigue data for different orientations.

Table 1
Specimen dimensions and fatigue data. Build angle θ [°], thickness t [mm], width w [mm], stress range $\Delta\sigma$ [MPa], number of cycles to failure N_f [–].

| θ	t	w	$\Delta\sigma$	N_f	Note
0	3.258	6.370	508.9	60760	
0	3.264	6.470	500.1	94862	
0	3.262	6.463	501.0	118234	
15	3.263	6.338	510.7	45314	
15	3.260	6.389	507.1	71265	
15	3.267	6.413	504.1	60186	
30	3.271	6.476	498.6	171628	
30	3.273	6.442	500.9	71586	
30	3.276	6.486	497.1	123178	
45	3.247	6.467	503.0	99761	
45	3.252	6.456	503.1	275975	
45	3.260	6.502	498.3	214804	
60	3.274	6.456	499.7	349644	
60	3.271	6.435	501.8	288333	
60	3.258	6.493	499.3	315357	
75	3.264	6.478	399.6	500000	a
75	3.271	6.500	496.8	122422	
75	3.259	6.498	498.7	226664	
90	3.261	6.620	489.3	148340	
90	3.254	6.547	495.8	161695	
90	3.259	6.529	496.4	158520	
105	3.275	6.557	491.8	139936	
105	3.299	6.531	490.2	102440	
105	3.263	6.388	608.1	66344	b
120	3.252	6.780	479.0	92968	
120	3.245	6.855	474.8	65460	
120	3.248	6.595	789.0	34860	b
135	3.290	7.272	441.5	105578	
135	3.255	7.206	450.3	119832	
135	3.258	7.202	450.1	87085	

a Discontinued.
b Mistake in machining. All sides machined.

plane. The hardness was found to be 634.5 ± 23.4. It should be noted that this is in the same range as what has been reported by Jagle et al. for laser metal deposition and Damon et el. for PBF-LB for similar heat treatment [17,27]. While Meneghetti et al. reported values of HV 367 for AB PBF-LB/18Ni300 [26].

3.4. Fatigue data

The fatigue data are shown in Fig. 9 and summarized in Table 1. In Fig. 9, the number of cycles is plotted versus the build orientation for specimens tested at the same load level (500 MPa). From this plot a clear trend in the fatigue data is visible; the lowest fatigue life is found close to the horizontal orientation, then the fatigue life is increased when approaching the vertical orientation, and decreasing when entering the down-skin region. The highest fatigue life was found for the 60°-specimens. In general, the down-skin specimens displays lower fatigue life
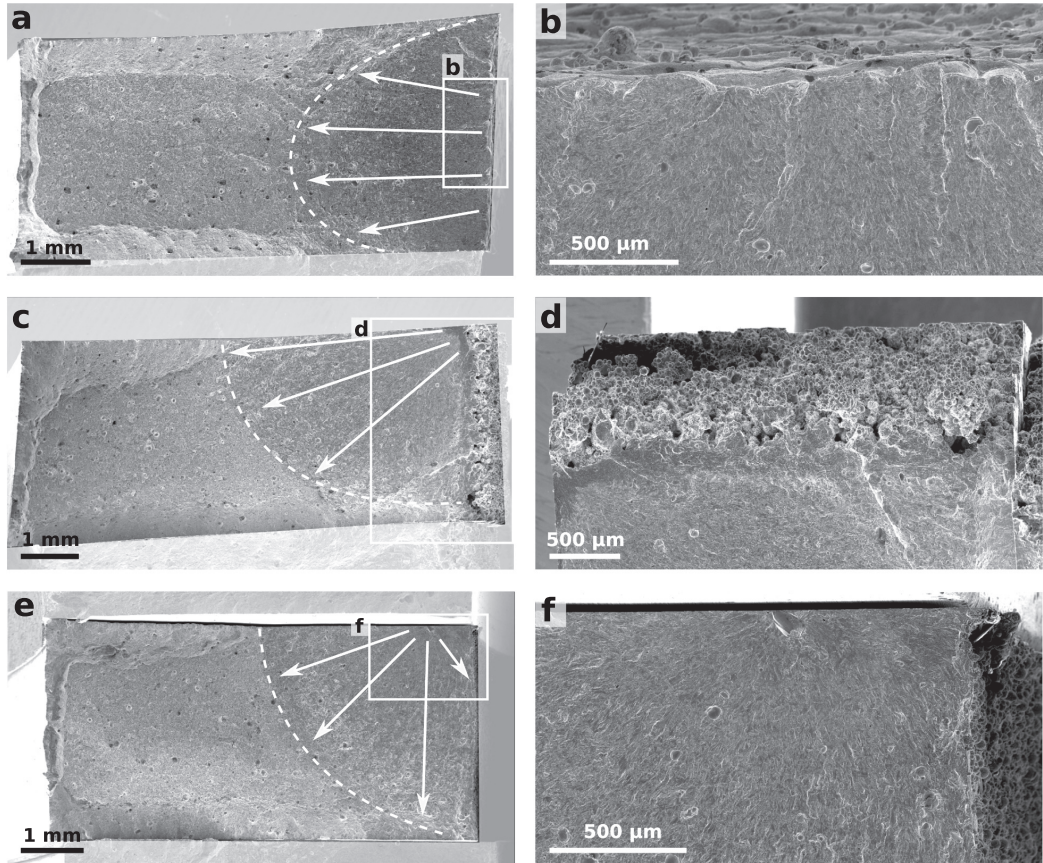
Fig. 10. Fracture surfaces of three different fatigue initiations: (a and b) 0°, fatigue initiation for centre of the AB surface, (c and d) 135°, Fatigue initiation from the corner the AB surface and e and f) 60°, Fatigue initiation from internal defect.

than their up-skin counterparts. Although considering the scatter, the difference is striking, e.g. by comparing 45° and 135°, both orientations display a fatigue life in a similar range. The clearest difference is observed between 60° and 120°.

3.5. Fractography

Fracture surfaces analysed by SEM are shown in Fig. 10. All
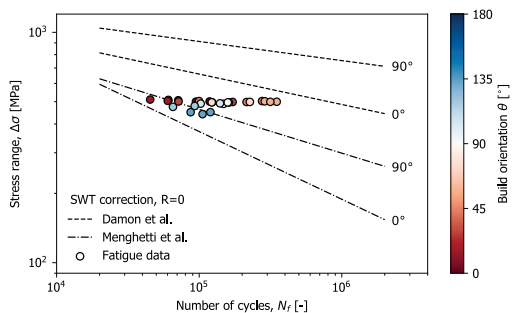
Fig. 11. Comparison of fatigue data.

specimens that were investigated were found to have fatigue initiating from defects followed by a region of fatigue crack growth and a final rupture zone. The final rupture zone displayed shear lips along the edges. Concerning the fatigue initiation sites, all specimens did not fail from the as-built surfaces; some specimens failed from internal voids and defects close to the as-built surface. Three different fracture surfaces displaying different fatigue initiations are shown in Fig. 10: failure from internal defect, failure from the centre of the as-built surface and failure from the corner of the as-built surface.

In Fig. 10a and b, a specimen built with 0° angle is shown. The specimen has fatigue initiation from the centre of the AB surface. Fatigue initiates from a defect that is ∼ 70 μm deep, comparable to the Rz value from Fig. 6, which was measured to be 99.2 μm. In Fig. 10c and d, a specimen built with 135° angle is shown. This specimen is also failing from the AB surface, but fatigue initiated from the corner of the specimen. In this case, the surface roughness, Rz, is higher than the 0° by approximately a factor of 4. In Fig. 10e and f, a specimen built with 60° angle is shown. This specimen does not have fatigue initiation from the AB surface but from a defect close to/at the machined surface. The specimens in this orientation display the highest fatigue life.
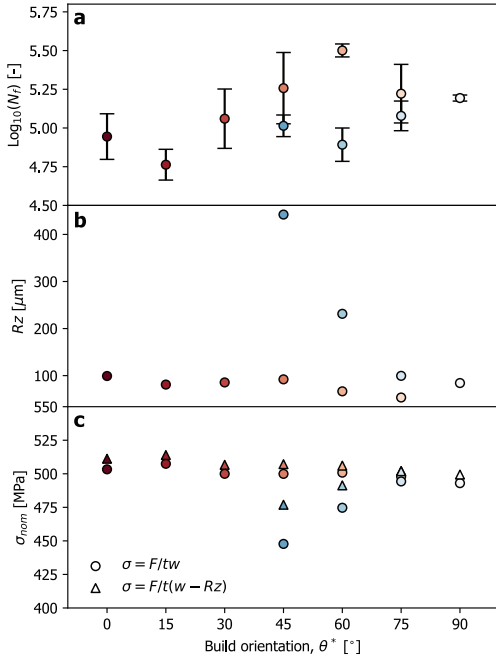
Fig. 12. Comparison of (a) fatigue life, (b) surface roughness and c) nominal stress.

4. Discussion

4.1. Comparison to fatigue data from the literature

In Fig. 11 the fatigue data obtained in this study are compared to fatigue data on PBF-LB from the literature, represented as regression lines. The stress values of the fatigue data from the present work is taken as the applied load divided by the measured cross-section, listed in Table 1. It should also be noted that the fatigue data from literature were tested at $R = -1$ and were therefore corrected by the Smith-Watson-Topper (SWT) mean stress correction [41]. The SWT mean stress correction is given by

$$\sigma\_ar = \sigma\_max \sqrt{\frac{1-R}{2}}, \qquad (3)$$

where σ_ar is the stress amplitude at $R = -1$ and σ_max is the maximum stress during the loading cycle at the given R value. The comparison in Fig. 11 shows that the fatigue data from the present work is in a similar range as the data from the literature. The data from Meneghetti et al. [26] and Damon et al. [27] displayed higher fatigue life for loading in the vertical orientation than the horizontal orientation. A similar trend was observed for the data presented here, specimens close to the horizontal orientation displayed lower fatigue life than the specimens close to the vertical orientation.

From the data in Fig. 11 it is clear that there are variations in the nominal stress due to the specimen dimensions, although the specimens were tested at the same load level.

4.2. Comparison of different build angles

A comparison of the fatigue life, the surface roughness, the nominal stress and the build angle for specimens tested at the same load level is shown in Fig. 12. To compare the up-skin and down-skin surfaces of equal orientation (e.g. 60° and 120°), the build angle is given as

$$\theta^* = \arcsin(\sin(\theta)). \qquad (4)$$

Fig. 12a shows a comparison of the build angles and the fatigue life, where the average and standard deviation of the fatigue life is calculated for each angle. The lowest number of cycles was observed for the 15°-specimens, while the fatigue life increased as the built angle increased towards 60°, then decreased from 60° to 135°. In general, when comparing the corresponding build angles, the down-skin specimens have lower fatigue life than the up-skin specimens.

Variations were observed in the specimen dimensions in particular due to the unmachined surfaces. To take into account these variations, the average stress for each build angle is given in Fig. 12c. Based on the dimensions measured by caliper (given values in Table 1), the stress is calculated by $\sigma = F/tw$. The values show that the nominal stress is decreasing for an increasingly down-skin angle. The caliper, however, does not take into account the surface roughness of the specimens and might give a too low value of the nominal stress in the specimens. To take into account the decrease in the cross-sectional area due to the surface roughness, the cross-section was corrected by the Rz values (shown in Fig. 12b), giving a nominal stress calculated by $\sigma = F/t(w - Rz)$. After correction the nominal stress level for the surface roughness, the nominal stress increase slightly for the values between 0° and 105°, while for 120° and 135° the stress increase. It should be noted that correcting by the full value of Rz might be too conservative, but it indicates the possible additional stress level variations. It is also interesting to remark that not only does the surface roughness depend on the build orientation of the surfaces, but also the dimensional tolerances. Deviations in dimensions due to down-skin surfaces has also been
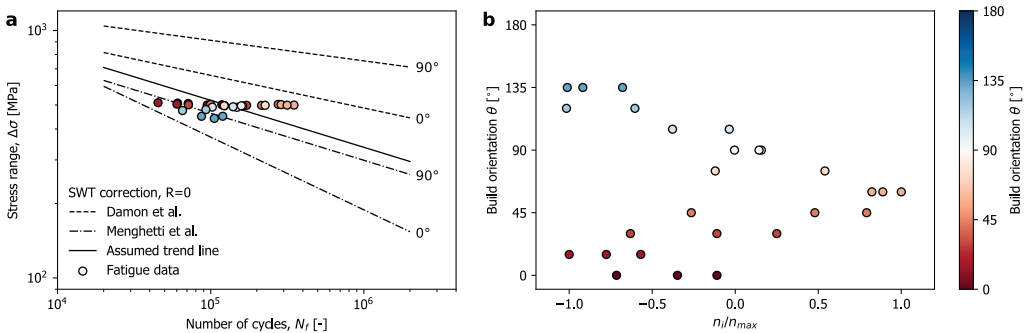

Fig. 13. (a) Comparison of the fatigue data presented in this study and regression lines of the fatigue data of PBF-LB/18Ni300 by Damon et al. and Meneghetti et al. (b) Updated correlation between the build angle and the normalized parameter n_i/n_max.

observed by other researchers in e.g. Refs. [42,43].

The fatigue data presented in Fig. 9 and Fig. 12a assumes the load level to be constant. This is, as discussed above, not the case. To correct for the variations in the stress levels, a comparison was made based on the deviation from an assumed fatigue life curve. Fig. 13a shows fatigue data from this study compared with the linear regression of the fatigue data of Meneghetti et al. [26] and Damon et al. [27] (presented previously in Fig. 12). The data from literature are presented in terms of Basquin curves based on power-law fitting of the data. By assuming that the fatigue data presented in this work follows similar trend lines as the data published by Meneghetti et al. [26] and Damon et al. [27], the trend line was described by Basquin's equation. The slope, B, was assumed to have the same value as the Meneghetti et al. [26] $90°$-data (as the data are close to this curve). Further, a new "assumed" fatigue life curve was created. The vertical shift, A, of the curve was taken so that the trend line (at 500 MPa) intersects with the mean value of the maximum and the minimum number of cycles at tests done around 500 MPa. The deviation for the assumed fatigue life curve is given by

$$n\_i = \log\_10(N\_i) - \log\_10\left(\left(\frac{\sigma\_i}{A}\right)^{\frac{1}{B}}\right). \qquad (5)$$

Further, the deviation from the regression line is normalized by the maximum value, n_max, and the result is shown in Fig. 13b. This comparison gives, perhaps, a more realistic comparison of the corresponding angles, e.g. $45°$ and $135°$ or $60°$ and $120°$. Here, the $135°$ and $120°$ angle displays lower fatigue life than the 45 and 60 orientations. This comparison between the fatigue life (n_i/n_max) confirms that the fatigue life is lower for the down-skin region than for up-skin region.

4.3. Surface morphology

From the correlation between the build angle and surface roughness in Fig. 12b the main shift in the surface roughness conditions is when the surface turns down-skin. Here, the surface roughness increases by over 4 times when comparing the $135°$ orientation to the general values for the up-skin surfaces. When investigating the morphology of the surfaces in Fig. 4a, no sharp features (notch roots) are observed, contrary to what has been found in the down-skin surface in other studies [10]. In addition to this, the up-skin surfaces display a waviness morphology (the $15°$ orientation is the extreme). As discussed in Section 3.1, three main surface conditions were identified; high surface roughness for down-skin surface, general surface roughness for vertical orientation and the staircase-like surface for up-skin surfaces. When the surface roughness is governed by the staircase effect, the surface roughness manifests as notches that are defined along the thickness direction of the sample. On the contrary, in the down-skin region, the notches from the surface roughness are not constant along with the thickness direction of the specimens. This could explain why the $15°$-specimens, which displays a very distinct staircase surface, has the lowest fatigue life.

5. Conclusions

In the present work, the directional fatigue behaviour of PBF-LB/ 18Ni300 maraging steel was studied. Specimens with 10 different orientations ranging from $0°$ to $135°$ were considered. The following conclusions can be drawn:

- A new test specimen for testing both the up- and down-skin fatigue behaviour of AM metals has been proposed. By machining all sides of a specimen except one, fatigue cracks are guided to initiate from the AB surface.
- The surface roughness was evaluated for surfaces built ranging from $0°$ (up-skin, horizontal) to $135°$ (down-skin). The up-skin surfaces

displayed the stair-case effect while the down-skin surfaces displayed high surface roughness.
- The fatigue strength was found to be inferior to wrought 18Ni300 but comparable to other works on AM. Specimens built close to the vertical orientation was found to have longer fatigue life compared to specimens built closer to the horizontal orientation. The same and the opposite trend has been found in recent literature on the same material.
- The specimens with AB up-skin surfaces displayed higher fatigue life than the ones with AB down-skin surface due to the higher surface roughness.

Declaration of Competing Interest

The authors declare that they have no known competing financial interests or personal relationships that could have appeared to influence the work reported in this paper.

Acknowledgement

References

[1] Bourell DL. Perspectives on additive manufacturing. Annu Rev Mater Res 2016;46: 1–18.

[2] Wong K, Hernandez K. A review of additive manufacturing. ISRN Mech Eng 2012; 2012:0–10.

[3] Wiberg A, Persson J, Olvander J. Design for additive manufacturing – a review of available design methods and software. Rapid Prototyp J 2019;25:1080–94.

[4] Singh S, Ramakrishna S, Singh R. Material issues in additive manufacturing: A review. J Manuf Process 2017;25:185–200.

[5] Lewandowski JJ, Seifi M. Metal additive manufacturing: A review of mechanical properties. Annu Rev Mater Res 2016;46:151–86.

[6] Li C, Liu Z, Fang X, Guo Y. Residual stress in metal additive manufacturing. Proc CIRP 2018;71: 348–353. 4th CIRP Conference on Surface Integrity (CSI 2018).

[7] Megahed M, Mindt H, N'Dri N, Duan H, Desmaison O. Metal additive-manufacturing process and residual stress modeling. Integr Mater Manuf Innov 2016;5:61–93.

[8] Mukherjee T, Zhang W, DebRoy T. An improved prediction of residual stresses and distortion in additive manufacturing. Comput Mater Sci 2017;126:360–72.

[9] McKelvey S, Fatemi A. Surface finish effect on fatigue behavior of forged steel. Int J Fatigue 2012;36:130–45.

[10] Solberg K, Berto F. Notch-defect interaction in additively manufactured inconel 718. Int J Fatigue 2019;122:35–45.

[11] Sanaei N, Fatemi A. Analysis of the effect of internal defects on fatigue performance of additive manufactured metals. Mater Sci Eng: A 2020;785:139385.

[12] Jamshidi P, Aristizabal M, Kong W, Villapun V, Cox SC, Grover LM, Attallah MM. Selective laser melting of ti-6al-4v: The impact of post-processing on the tensile, fatigue and biological properties for medical implant applications. Materials 2020; 13:2813.

[13] Molaei R, Fatemi A, Phan N. Significance of hot isostatic pressing (hip) on multiaxial deformation and fatigue behaviors of additive manufactured ti-6al-4v including build orientation and surface roughness effects. Int J Fatigue 2018;117: 352–70.

[14] Tammas-Williams S, Withers PJ, Todd I, Prangnell PB. The effectiveness of hot isostatic pressing for closing porosity in titanium parts manufactured by selective electron beam melting. Metall Mater Trans A 2016;47:1939–46.

[15] Croccolo D, Agostinis M, Fini S, Olmi G, Robusto F, Kostić S, Vranić A, Bogojević N. Fatigue response of as-built dmls maraging steel and effects of aging, machining, and peening treatments. Metals 2018;8(7):505.

[16] Wan H-Y, Zhou Z-J, Li C-P, Chen G-F, Zhang G-P. Enhancing fatigue strength of selective laser melting-fabricated inconel 718 by tailoring heat treatment route. Adv Eng Mater 2018;20:1800307.

[17] Jägle E, Sheng Z, Kürnsteiner P, Ocylok S, Weisheit A, Raabe D, Requena G. Comparison of maraging steel micro-and nanostructure produced conventionally and by laser additive manufacturing. Materials 2017;10.

[18] Turk C, Zunko H, Aumayr C, Leitner H, Kapp M. Advances in maraging steels for additive manufacturing. BHM Berg- und Hüttenmännische Monatshefte 2019;164.

[19] Bajaj P, Hariharan A, Kini A, Kürnsteiner P, Raabe D, Jägle E. Steels in additive manufacturing: A review of their microstructure and properties. Mater Sci Eng: A 2020;772:138633.

[20] Kempen K, Yasa E, Thijs L, Kruth J-P, Humbeeck J. Microstructure and mechanical properties of selective laser melted 18ni300 steel. Phys Proc 2011;12:255–63.

[21] Becker TH, Dimitrov D. The achievable mechanical properties of slm produced maraging steel 300 components. Rapid Prototyp J 2016;22:487–94.

[22] Wang B, Zhang P, Duan Q, Zhang Z, Yang H, Li X, Zhang Z. Optimizing the fatigue strength of 18ni maraging steel through ageing treatment. Mater Sci Eng: A 2017; 707:674–88.

[23] Van Swam LF, Pelloux RM, Grant NJ. Fatigue behavior of maraging steel 300. Metall Trans A 1975;6:45–54.

[24] Meneghetti G, Rigon D, Cozzi D, Waldhauser W, Dabalà M. Influence of build orientation on static and axial fatigue properties of maraging steel specimens produced by additive manufacturing. Proc Struct Integr 2017;7:149–57.

[25] Croccolo D, De Agostinis M, Fini S, Olmi G, Vranic A, Ciric-Kostic S. Influence of the build orientation on the fatigue strength of eos maraging steel produced by additive metal machine. Fatigue Fract Eng Mater Struct 2016;39:637–47.

[26] Meneghetti G, Rigon D, Gennari C. An analysis of defects influence on axial fatigue strength of maraging steel specimens produced by additive manufacturing. Int J Fatigue 2019;118:54–64.

[27] Damon J, Hanemann T, Dietrich S, Graf G, Lang K-H, Schulze V. Orientation dependent fatigue performance and mechanisms of selective laser melted maraging steel x3nicomoti18-9-5. Int J Fatigue 2019;127:395–402.

[28] Yadollahi A, Shamsaei N, Thompson SM, Elwany A, Bian L. Effects of building orientation and heat treatment on fatigue behavior of selective laser melted 17–4 ph stainless steel. Int J Fatigue 2017;94:218–35.

[29] Herzog D, Seyda V, Wycisk E, Emmelmann C. Additive manufacturing of metals. Acta Mater 2016;117.

[30] Riemer A, Leuders S, Thöne M, Richard H, Tröster T, Niendorf T. On the fatigue crack growth behavior in 316l stainless steel manufactured by selective laser melting. Eng Fract Mech 2014;120:15–25.

[31] Mower TM, Long MJ. Mechanical behavior of additive manufactured, powder-bed laser-fused materials. Mater Sci Eng: A 2016;651:198–213.

[32] Edwards P, Ramulu M. Fatigue performance evaluation of selective laser melted ti–6al–4v. Mater Sci Eng: A 2014;598:327–37.

[33] Johannes Lindecke PN, Blunk H, Wenzl J-P, Möller M, Emmelmann C. Optimization of support structures for the laser additive manufacturing of tial6v4 parts. Proc CIRP 2018;74:53–8. 10th CIRP Conference on Photonic Technologies [LANE 2018].

[34] Emmelmann C, Herzog D, Kranz J. 10 - design for laser additive manufacturing. In: Brandt M, editor. Laser Additive Manufacturing, Woodhead Publishing Series in Electronic and Optical Materials. Woodhead Publishing; 2017. p. 259–79.

[35] Strano G, Hao L, Everson RM, Evans KE. Surface roughness analysis, modelling and prediction in selective laser melting. J Mater Process Technol 2013;213:589–97.

[36] Hovig EW, Azar AS, Sunding MF, Andreassen E, Sørby K. High cycle fatigue life estimation of materials processed by laser powder bed fusion. Fatigue Fract Eng Mater Struct 2019;42:1454–66.

[37] Azar AS, Østby E, Akselsen OM. Effect of hyperbaric chamber gas on transformation texture of the API-X70 pipeline weld metal. Metall Mater Trans A: Phys Metall Mater Sci; 2012.

[38] Chlebus E, Gruber K, Kuźnicka B, Kurzac J, Kurzynowski T. Effect of heat treatment on the microstructure and mechanical properties of Inconel 718 processed by selective laser melting. Mater Sci Eng A 2015;639:647–55.

[39] Hovig W, Azar AS, Grytten F, Sørby K, Andreassen E. Determination of anisotropic mechanical properties for materials processed by laser powder bed fusion. Adv Mater Sci Eng 2018;2018.

[40] Brandl E, Heckenberger U, Holzinger V, Buchbinder D. Additive manufactured AlSi10Mg samples using Selective Laser Melting (SLM): Microstructure, high cycle fatigue, and fracture behavior. Mater Des 2012;34:159–69.

[41] Smith KN, Watson P, Topper TH. A stress strain function for the fatigue of metals. J Mater 1970;5:767–78.

[42] Andreau O, Pessard E, Koutiri I, Peyre P, Saintier N. Influence of the position and size of various deterministic defects on the high cycle fatigue resistance of a 316l steel manufactured by laser powder bed fusion. Int J Fatigue 2021;143:105930.

[43] Matache G, Paraschiv A, Condruz R. Edge and corner effects in selective laser melting of in 625 alloy. Manuf Rev 2020;7:8.

NTNU
Norwegian University of
Science and Technology